Self-assembly and On-surface Chemistry of Tetraphenyl Porphyrin

Eleanor S Frampton

A thesis presented for the degree of

Doctor of Philosophy

School of Physics and Astonomy

University of Nottingham

August 2020

Acknowledgements

First I would like to thank my supervisor Alex, for welcoming me into the world of physics and for his support and wisdom throughout this project. I would also like to thank Neil Champness, David Amabilino and Philip Moriarty for their guidance during my PhD. I would like to thank Rob Jones for his support and guidance during the Diamond project. Thanks go to the Nanoscience Group, in particular Chris and Matt for their friendship, patience and coding expertise.

Additional thanks goes to everyone in C20 and C18, but in particular; Maike, Matt, Jemma, Dom, Gary, Joe, Ciaran, Neil, Chris (again) and Matt (again), who made this experience truly unforgettable and magical.

Thanks go to all my friends and colleagues at Coco Tang, who provided so much stress-relieving fun and most importantly cocktails during this time. With a special thanks to Jade Barber for her eternal positivity and friendship and Marta Moreno for her friendship and calming words throughout the duration of this project.

I would like to thank my Mum and Dad and my sisters; Laura and Phoebe, for their support and continuous injection of hilarity and fun into my life.

Finally, I would like to thank my partner Grace Morley, who told me she liked Turner, and never have I turned since then to any other.

This work is dedicated to John Frampton, who loved books and was a particularly gifted writer

Abstract

Self-assembly of molecular building blocks to produce extended two-dimensional arrangements is a first step on the journey towards the design and construction of molecular systems with a predictable structure and functionality. By employing scanning probe techniques such as scanning tunneling microscopy (STM) and scanning tunneling spectroscopy (STS), an understanding of these self-assembled structures on the single-molecule level can be obtained. When combined with other techniques such as x-ray photoelectron spectrocopy (XPS) and x-ray standing wave analysis (NIXSW), the adsorption geometries and reaction pathways can be extracted to give a completed picture of each system.

Within this thesis the self-assembly properties of porphyrin molecules are investigated using scanning probe and photoelectron techniques. Porphyrin molecules have been selected due to their ability to participate in chemical reactions and thier excellent thermal stability

The topography of tetraphenyl porphyrin (TPP) on Au(111) is studied, the local structure and ordering is determined using STM and the average surface arrangement is determined using LEED. The unit cell of the TPP is calculated as well as the commensurability of the lattice with the surface atoms. In addition to an as-deposited close-packed phase, two other visually different phases of TPP on Au(111) are presented and characterised. The arrangement and ordering of the TPP molecules in each phase is quantified using the Voronoi tessellation. The details of the electronic properties of TPP is investigated using STS and kelvin probe force microscopy (KPFM). Using these techniques three electronically distinct species are defined, TPP in the saddle conformation, TPP adsorbing atop a gold atom, and a metalated TPP molecule.

Information on the chemical properties of these porphyrin phases is presented, achieved using XPS, by which an additional phase of TPP is observed and further insight into the chemical composition of each phase is achieved. From the XPS fitting a full structural characterisation of each phase is performed using NIXSW. From this the adsorption sites of each chemical species are defined and the heights above the surface extracted.

In this thesis the experimental details for all three phases of TPP are presented. The use of a combination of methods allows for a complete picture of system to be built and for access to details that would be otherwise inaccessible. This particular combination of techniques, when

used together, can give mechanistic details about the proceedings of chemicals reactions, which has previously been unattainable.

Contents

Chapter 1

Introduction

1.1 Supramolecular Chemistry and Self-Assembly

Supramolecular chemistry is the study of chemistry beyond the covalent bond, focusing on the significance of the intermolecular forces and bonds, such as hydrogen bonding, to form 'supermolecules' through the interaction of synthons. A supermolecule being one which 'possesses features that are as well defined as those of molecules themselves' [1]. This can be extended to the study of supramolecular assemblies- extended poly-molecular arrays with well-defined molecular organisation. These can come in the form of layers, membranes, micelles etc. Self-assembly, in the context of supramolecular chemistry, refers to the spontaneous association of a given number of components, to form either discrete supermolecules or a supramolecular assembly [2]. Work in this field by B. Feringa, J. F. Stoddart and J. P. Sauvage won the Nobel prize for chemistry in 2016, for the 'design and production of nanomachines', which are an assembly of molecular components that are able to move relative to each other in order to perform a given function [3]. These systems are produced using a 'bottom-up' approach, meaning they are pieced together from their individual components to create a new structure with unique functionality. Components may be treated as 'molecular building blocks' and, combined with knowledge of intermolecular forces, used to design systems with specific properties. In chemistry these techniques may be used to create discrete systems *via* synthetic pathways. In nanophysics, they may be used to manipulate single atoms to create surface structures or for the design and production of nanodevices [4]. Between these approaches lies the

interdisciplinary concepts of nanoscience, in which surface-confined molecular architectures may be engineers to possess bespoke functionalities.

In the future it is hoped that these nano-devices will be able to mimic the function of natural processes. In the natural world, these systems are able to assemble themselves using small amounts of energy to perform synthetically energy intensive tasks. Using bottom-up approaches and molecular building blocks it is feasible that similar processes would become available.

The aim of this chapter is to introduce the concepts of self-assembly, with reference to examples within the literature, and to then bring into focus the on-surface properties of molecular assemblies of porphyrins, and to describe the on-surface chemistry that they may undergo.

1.1.1 Van der Waals Forces

There are a number of non-covelent interactions that facilitate the assembly of the ordered molecular arrays within these potential molecular devices. Van der Waals forces are the weakest of all the interactions, with the strength of the interaction being between $0.02 - 0.1$ eV [5]. These interactions occur between dipoles and may be split into three categories; instantaneous dipole/induced dipole, permanent dipole/induced dipole and permanent dipole/permanent dipole. An instantaneous dipole may occur in any molecule, by the random motion of confined electrons, which then induces a dipole in a neighbouring molecule. The latter two types require at least one of the participating molecules to have a permanent dipole moment. These forces can be modelled by the Lennard-Jones potential, which describes the strength of interaction with $(\frac{1}{r})^6$, where r is the distance between the molecules [6]. These forces lack directionality and decrease rapidly with increasing distance. This factor limits their ability to facilitate self-assembly. However, if the participating molecules are significantly large, multiple Van der Waals forces can occur which may sustain an ordered structure.

1.1.2 Hydrogen Bonding

Hydrogen bonding takes place between a hydrogen atoms with a δ^+ charge and an electro-negative atom (O, N, F) with a δ^- charge. When the two partial charges are in close proximity they form a weak interaction (0.05-0.4 eV) [5]. When molecules can form multiple hydrogen bonds the net effect

is a more strongly bound material. These forces are directional, meaning that in terms of creating self-assembled systems, that functional groups that exhibit hydrogen bonding may be chosen to create specific structures.

1.1.3 Metal-organic interactions

Metal atoms and organic molecules interact by the formation of coordinate bonds. These interactions require the organic molecule to possess a lone pair, typically on an O or N atom. These forces are highly directional and are generally stronger than the VDW and hydrogen bonding interactions, with a strength of $0.5 - 2.0$ eV [5]. Metal atoms form coordinate bonds in a number of different geometries, giving the potential the construction of highly bespoke systems. Discrete complexes may be formed using multiple metal atoms to produce molecular cages or squares. [7–10] 1D and 2D assemblies such as molecular wires or self-assembled monolayers (SAMs) may be synthesised or assembled on surfaces [11, 12]. Extended 3D networks, such as metal-organic frameworks (MOFs) with defined pore sizes for use in gas storage or catalysis can be designed and crystallised [13, 14].

1.2 2D Self-assembly

Non-covalent interactions may be used to create nano-scale structures in both solution-based chemistry and additionally on surfaces, where the surface acts as a support for extended self-assembled networks. By selecting molecules with specific potential bonding geometries, the structures of these networks may be predicted and, therefore to a certain degree, designed to posses specific properties, dependant on the optical/magnetic/electronic functionality of the individual molecules. Examples of 2D self-assembled structures and some of their unique properties studied using scanning tunneling microscopy (STM) are discussed below. STM is a particularly useful tool when studying surface architectures as it can be used to study the bonding arrangements of these structures down to a single molecule scale.

1.2.1 Self-assembly of Organic molecules on Surfaces

The formation of an extended 2D network with an open honeycomb structure can be found in reference [15] which uses a combination of molecules to form this network (see Figure 1.1). Two molecules

were adsorbed onto a Ag terminated Si surface, perylene tetra-carboxylic di-imide (PTCDI) and melamine, chosen specifically for their ability to form hydrogen bonds with each other, the bonding motif can be seen in Figure 1.1a. The melamine molecule forms a total of nine hydrogen bonds and forms the vertices of the network, with PTCDI (which may form six bonds) forming the edges.

PTCDI was first deposited to form small islands, at 0.1-0.3 monolayers of coverage. Subsequently, melamine was deposited while the sample was annealed at 100 °C; allowing the PTCDI to diffuse away from the close-packed islands across the surface, and interact with the melamine to produce the hexagonal networks seen in Figure 1.1b

The honeycomb structure of this network shows that there are large hexagonal pores between the interacting molecules. A further study performed on this network utilised these pores to capture C_{60} molecules. Clusters of C_{60} molecules adsorbed within the pores, have sufficient enough size that up to seven C_{60} molecules can adsorb within the pores, however clusters of two, five and six were also recorded.

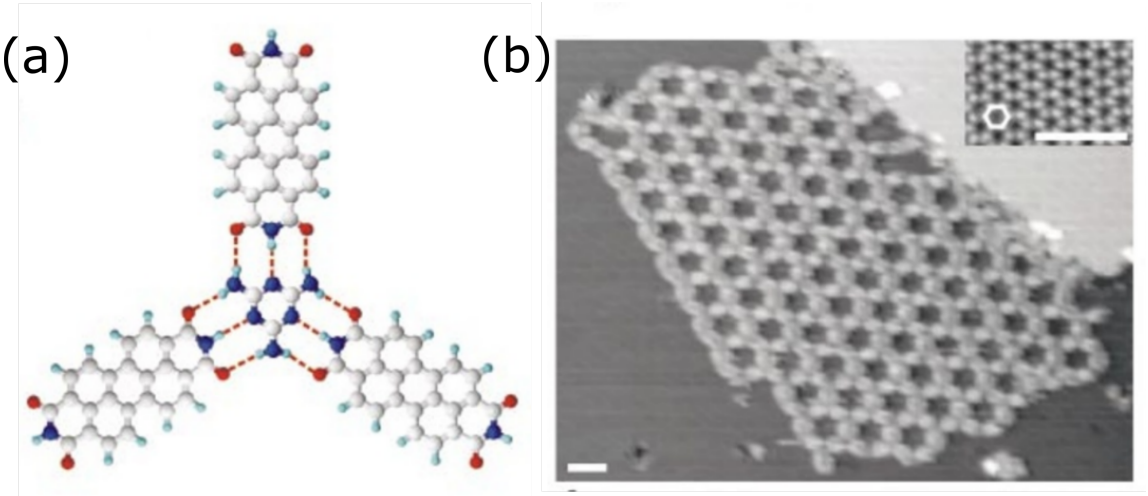

Figure 1.1: (a) PTCDI/melamine hydrogen bonding motif (b) STM image of PTCDI and melamine network on Ag terminated Si surface. Taken from [15]

In another example demonstrating the combination of organic synthesis and self-assembly, pyrene components functionalized at different positions were studied on an Ag(111) surface. [16] The pyrene derivative consists of an aromatic core, made up of four phenyl rings, and pendant groups placed around the core. The pendant groups terminated with a pyridine ring, enabling the molecules to form hydrogen bonds from each leg. The structures of these pyrenes can be seen in

Figure 1.2a.

Initially, only the terra-pyridyl pyrene was deposited and it was found to form a rhombic array on the Ag surface, stabilised by the formation of hydrogen bonds. By only depositing the *cis*-dipyridyl pyrene derivative it was found that a chain like structure, with a crocheted appearance formed on the surface. These molecules also formed aggregates, which were able to form a hydrogen bond between the pyrene core and the pyridine group of an adjacent molecule.

When only the *trans*-dipyridyl pyrene was deposited a Kagome network was formed on the surface which had a knitted appearance, the structure of this can be seen in Figure 1.2b. This structure is also mediated using hydrogen bonding, in which a hydrogen bond is formed from the nitrogen atom on the pendant pyridine group to the pyrene core of a neighbouring molecule.

Similar to the PTCDI and melamine network, the capabilities of these porous networks for hosting guest molecules was explored. Some of the pyrene starting materials were found to be contaminated with iodide, presumably from the CuI catalyst, which enabled the pyrene derivatives to be co-deposited with iodine. The tetra-pyridyl pyrene lattice displayed small bright spots in the cavities which could house up to two iodine atoms. The *trans*-dipyridyl pyrene Kagome netowrk displayed single iodine atoms adsorbed the small cavities but none in the larger pores.

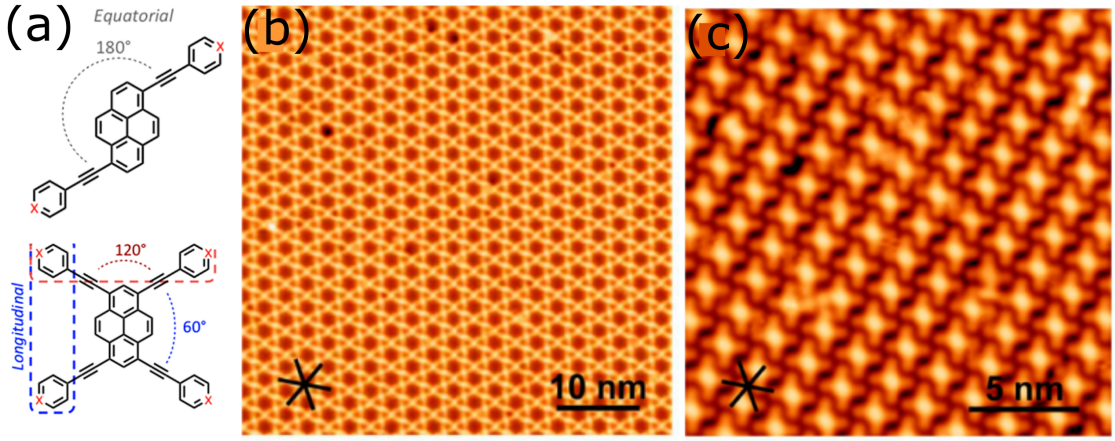

Figure 1.2: (a) molecular structure of di-substituted and tetra-substituted pyrenes. (b) STM image of the structure formed by the *trans*-dipyridyl pyrene on Ag(111). (c) STM image of the structure formed by the tetra-pyridyl pyrene on Ag(111).Taken from [16]

In addition to hydrogen bonding, surface structures have been reported with self-assembly

driven by Van der Waals forces. In a study by G. Velpula *et al.,* molecules with multiple long hydrocarbon chains were selected for their ability to form VDW interactions with each other, to create an interlocking concentric pattern which formed around a central core. [17] This system required four components, the structures of which can be seen in Figure 1.3a, the central core of this network is a coronene molecule, chosen for its six-fold symmetry, around which the shells can form. The inner most shell is formed using isophthalic acid (ISA), which hydrogen bonds with other ISA molecules to form a hexagonal inner ring around the coronene core, which is stabilised using VDW forces. The two outer shells are formed from two different molecules which consist of a central core and six long hydrocarbon chains, which take different length for the different shells. These shells assemble by forming VDW interactions with the inner shells and also with each other, to give interlocking hexagonal rings. These molecule were deposited from solution onto highly-oriented pyrolytic graphite (HOPG) and then imaged using STM. An STM image of the network described above can be seen in Figure 1.3. A number of different structures were reported using these molecular components in differing ratios. The four component system was found to be the most challenging to achieve, however a number of three-component polymorphs were achieved using the three inner shell components. A number of similar structures using this method of a combination of hydrogen bonding and VDW interactions between long alkyl chains have been reported. [16,18,19] Altering the ratios of components on the surface is one route towards designing and controlling these types of structures.

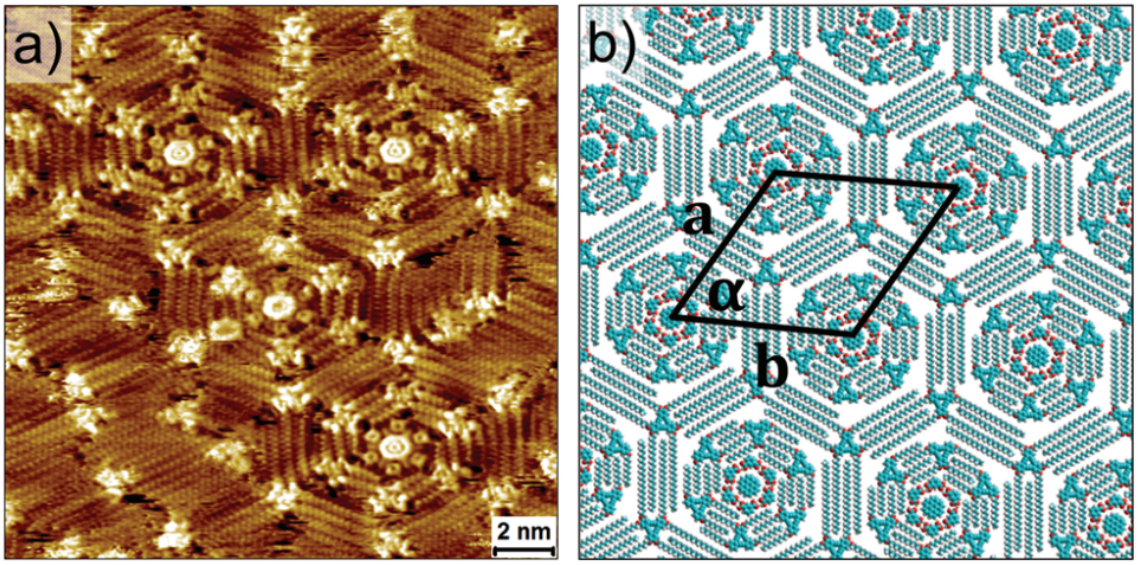

Figure 1.3: (a) STM images of the VDW mediated structure formed by the four components on HOPG. (b) Structure of the network produced, with unit cell highlighted. Taken from [17]

1.2.2 Metal-Organic interactions on Surfaces

Self-assembly of molecules on surfaces is not limited to the use of hydrogen bonding and VDW forces as potential synthons, by utilising metal-organic interactions the formation of highly directional bonds leads to the production of a vast range of surface structures. Metal-organic structures may be selected in favour of hydrogen bonded or VDW mediated structures due to the interactions having a higher strength to form more rigid structures, or to alter the electronic/symmetric/optical properties of the system. Metal-organic structures can form on surfaces by using one of two methods. The first is the the co-deposition of organic molecules alongside metal atoms, the second is by selecting a metal substrate where adatoms are present which can form bonds with organic molecules deposited.

Honeycomb networks of organic molecules with metal atoms at the vertices have been produced using the co-deposition method. In [20] dicarbonitrile-polyphenyl molecules were deposited onto a Ag(111) surface. There molecules consist of three phenyl rings in a linear chain, with terminal carbonitrile groups at either end. Subsequently Co atoms were deposited onto the surface, and interacted with the poly phenyl molecules already present. The positioning of the nitrogen atoms on the polyphenyl molecules allows these molecules to form the edges of the honeycomb network

and the metal atoms to form the vertices. An image of this can be seen in Figure 1.4a.

The formation of this network was then used as a template to direct the formation of Co and Fe metal clusters. By depositing increasing amounts of Co atoms onto the templated surface small clusters of Co atoms formed above the metal-organic lattice, specifically choosing the positions directly above the phenyl rings. The clusters appeared as bright features in STM images. A similar behaviour was observed for Fe atoms whereupon deposited Fe atoms formed clusters nucleated above the phenyl rings of the ligands. However it was found that by increasing the deposition temperature the nucleation points of the Fe clusters shifted from above the ligands to directly above the metal nodes of the lattice below. Both of these structures were observed using STM and the differences can be seen in Figure 1.4, in which 1.4a shows the Co clusters and 1.4b shows the Fe clusters.

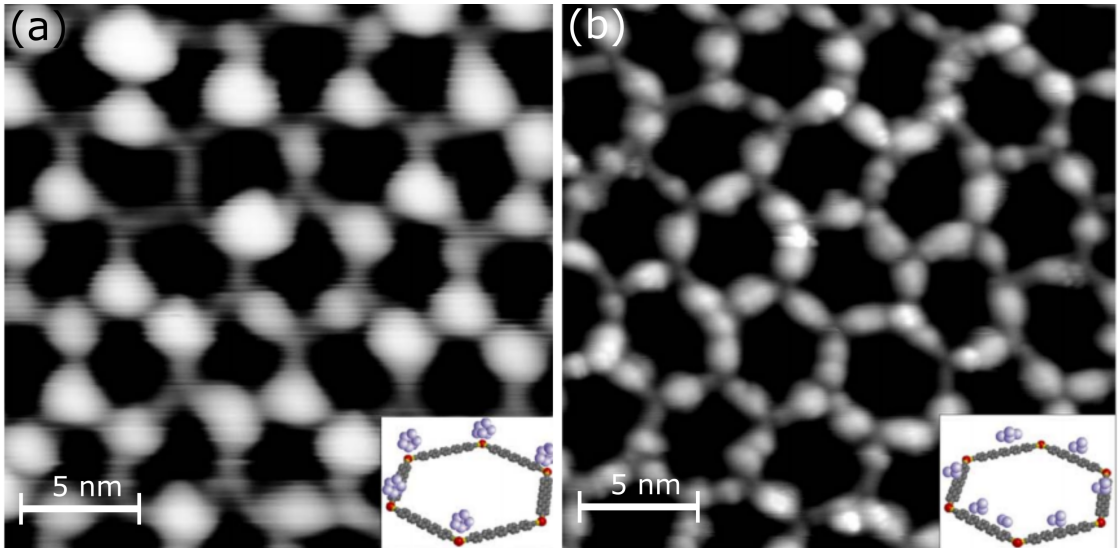

Figure 1.4: Directed assembly of metal clusters using a dicarbonitrile-polyphenyl molecular network as a template. (a) Assembly of Co clusters. (b) Assembly of Fe clusters. Taken from [20]

The formation of metal-organic chains has been reported in [21] which requires the presence of surface adatoms to form interactions. Porphyrin molecules substituted in the *trans-* configuration with pyridin-4-ylethynyl (≡CPyr) groups, were deposited onto a Cu(111) surface while the surface was held at 350 K. This resulted in the production of chains of porphyrin molecules, constructed by the interaction of the pyridyl substituents with surface adatoms. An STM image of this can be seen in Figure 1.5. The metal-organic interactions were found to be strong enough to withstand

manipulation from the STM tip.

Upon heating these molecular wires, it was found that the tails of the chains displayed some degree of flexibility, which increased with increasing temperature (180-210 K). At higher temperatures (240 K), larger sections of the wires, including the inner sections were able to display some movement. When the temperature reached up to 300 K large areas of the chains began to appear fuzzy, which indicates that sections of the chain are rapidly disassembling and reassembling. As the temperature is further increased to 350 K the only sections of chain remaining are those anchored to the step edges, the remainder of the surface displays a fluid phase, which is not resolvable with STM.

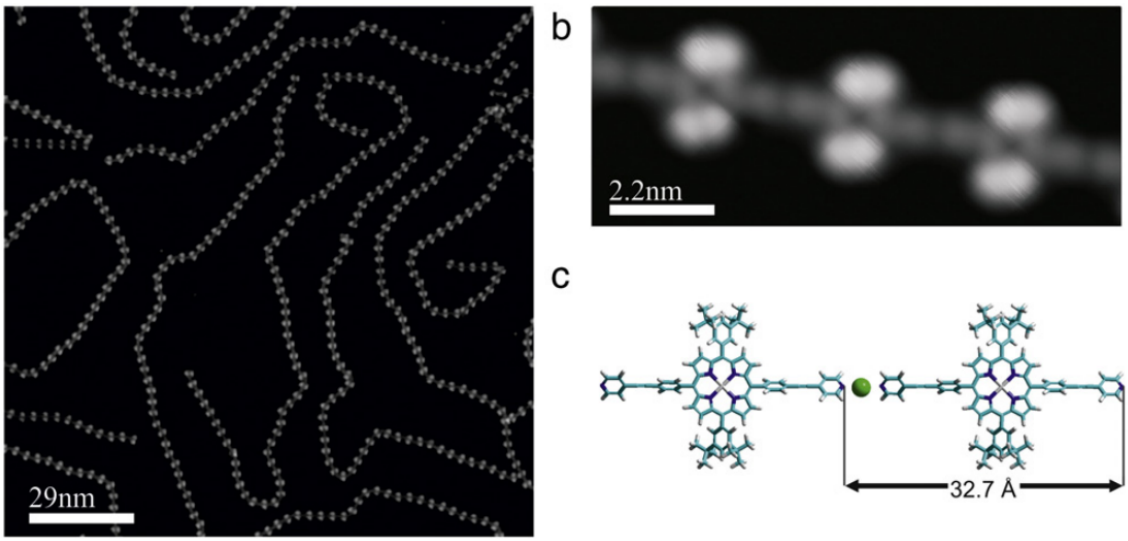

Figure 1.5: (a) STM image of molecular wires formed from substituted porphyrin molecules and surface adatoms. (b) STM image of close-up molecular wire, showing three porphyrin units.(c) Structure of the synthon of the wires.Taken from [21]

1.2.3 Reactions on Surfaces

In addition to self-assembly using non-covelent interactions, molecules on surface can partake in chemical reactions to facilitate the formation of covalent bonds. In these cases the surface can be thought of as a support for the molecules allowing them the proximity required to initiate a reaction, or it can be as much a part of the reaction in the form of a catalyst, which offers the opportunity to explore new reaction mechanisms as an alternative to solution-based chemistry. By being able to form new covalent bonds alternate surface-based synthetic pathways may be utilised.

In addition, covalently bonded structures will provide different functionalities on the surface. Using scanning probe microscopy (SPM) techniques, these reactions may be studied on a single molecule scale, and intermediate structures may also be viewed, giving further insight into the mechanisms which drive these reactions.

The most commonly studied type of on-surface reaction is Ullmann coupling. [22] The Ullmann Coupling, originally performed in solution, requires two aryl halides which are coupled together in the presence of a metal catalyst, originally copper. The first step in the reaction mechanism is the dissociation of the halogen atom from the molecule, which then forms an interaction with either an adatom or a surface atom. The second and final step is the coupling of the two molecules.

In a study performed by W. Wang *et al* 4,4"-dibromo-p-terphenyl Br−$(Ph)_3$−Br (a horizontal chain of three phenyl ring with a Br atom at either end) was deposited onto a Cu(111) surface. [23] STM images taken at 77K show that the molecules formed a honeycomb structure, which can be seen in Figure 1.6a. Upon heating the surface to 300 K the two bromine atoms dissociate and chain-like structures, which displayed a distinct periodicity were seen on the surface (1.6b). This surface was then annealed again to 473 K and another transformation was observed. The chains lost their periodicity and continuous linear chains were observed (Figure 1.6c). Upon further probing into the periodic chains that occurred after the initial anneal, it was found that the chains consisted of the terphenyl units connected by a Cu bridge. The anneal at 300 K is known to release Cu adatoms from the surface which were then incorporated into the organometallic chains. These chains form the intermediate of the Ullmann coupling reactions between the terphenyl units, which eventually react to form C−C bonds. The surfaces presented in this study demonstrate the how different molecular interactions may be exploited to produced a structure with significantly different geometries.

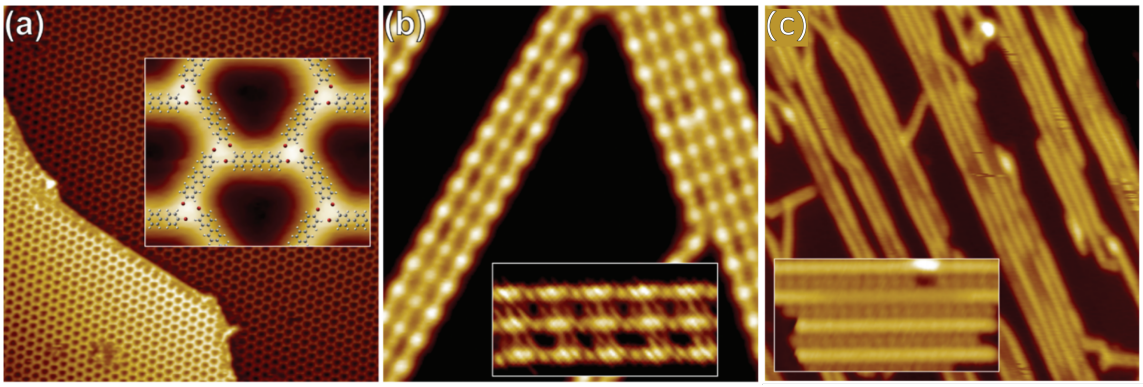

Figure 1.6: (a) STM images of as-deposited 4,4"-dibromo-p-terphenyl Br−$(Ph)_3$−Br forms a honey comb network. (b) STM image of surface after the dissociation of the Br atoms upon annealing, (c) STM image of product of Ullmann coupling, linear covalently bonded chains.Taken from [23]

The principles outlined above can be used to form a number of other surface structures, such as macrocycles, chains of different shapes and discrete surface structures. The *meta-* version of the terphenyl molecules (4,4"-dibromo-m-terphenyl) shown above forms both macrocycles and zigzag chains when deposited onto a Cu(111) surface. [24] By making small changes to the precursor molecules different resulting structures may be achieved on the surface. Additionally, by changing the surface facet different arrangements might be obtained. It can be seen that for 4,4"-diiodo-p-terphenyl (DITP) that when it it deposited onto Ag(110) and Ag(111) different unit cells are seen for both the overlayer of molecule as-deposited and for the covalently coupled overlayer. [25]

On Ag(111) it was seen that the DITP displayed the expected dissociation of its halide atoms and formed a zig-zag chain structure acorss the surface, with the units linked together with Ag atoms, to give the intermediate in the Ullmann coupling reaction. The chains were shown to lay at an angle relative to the crystallographic directions of the surface lattice. The Ag adatoms sit in both 3-fold hollow and atop sites, meaning that the overlayer is not commensurate with the surface lattice below.

When this was repeated using Ag(110) substrate similar zig-zig chains were formed, however they displayed two key differences. The first is that the Ag atoms were found to lie exclusively in four-fold hollow sites, giving the overlayer a commensurate lattice with the surface. The second difference is that the period of the zig-zag chains has extended by 2Å . This was thought to be due to the elongation of C−Ag bonds.

Upon heating both these structures, the Ag atoms are removed, resulting in a compression of the unit cell, and covalent bonds formed to produce zig-zag wires. In the case of the Ag(111) surface the structure was found to have rotated $\sim 30^{\circ}$ to form a commensurate lattice with the surface. In contrast the Ag(110) substrate did not require the overlayer to rotate for the products to display commensurability with the surface.

1.3 Porphyrins on Surfaces

Porphyrins are organic molecules which are found in a number of natural systems and processes, including in red blood cells as oxygen carriers and in chlorophylls as light harvesters. [26] [27] They have a vast variety of potential applications across a range of fields including; catalysis [28,29], light harvesting [30,31], liquid crystals [32], and energy transfer [33], [34].

Porphyrins consist of a central macrocycle, formed from four pyrole rings, linked by methine bridges. Porphyrins are popular molecules for self-assembly and surface studies due to a number of factors, which demonstrates their versatility. The periphery of the porphyrin macrocycle may be functionalised in a number of ways to further tune the properties of the molecules to create bespoke building blocks for self-assembly which form structures with highly defined bonding motifs. They present a high thermal stability which enables them to be deposited onto surfaces with relative ease and crucially, without decomposition. Porphyrin molecules have been selected for study in this thesis for their incredible versatility, as outlined above and due to their ability to participate in chemical reactions and their excellent thermal stability.

1.3.1 STM Studies of Porphyrins on Surfaces

Although porphyrins can be functionalised in many ways, one of the most common porphyrins used for self-assembly studies is Tetraphenyl porphyrin (TPP). Specifically on weakly interacting surfaces, such as Ag and Au, TPP displays attractive molecule-molecule interactions as the dominant driving force for the formation of surface structures. In contrast, strongly interacting surfaces, such as Cu, cause repulsion between TPP molecules, which is discussed further below. [35]

In a study by G. Rojas *et al.,* the self-assembly of TPP on both Ag(111) and Cu(111) was observed using STM. [36]. On Ag(111) TPP was initially deposited at low coverages of $<< 1$

monolayer. STM images of these surfaces, taken at 77 K, show the TPP molecules adsorbing exclusively to the step edges, until the each step-edge was covered, and then as coverage increased small islands began to nucleate on the terraces. The close packed arrangement of these islands showed a tetragonal unit cell with length $a = 13.8$Å . The close-packed TPP molecules are stabilised *via* a combination of VDW interactions and C$-$H$\rightarrow\pi$ interactions (between an H atom on a phenyl ring and the π system of a neighbouring phenyl ring). TPP was found to be highly mobile at lower coverages when imaged at higher temperatures (300 K). A similar behaviour has been seen on Au(111). [37] In these instances, it can be assumed that molecule-molecule interactions dominate the arrangement and that the surface-molecule interactions are weak in comparison. The structure of the overlayer can be seen in Figure 1.7a

In contrast the Cu(111) surface displayed the opposite effect. Upon the deposition of $<<$ 1 monolayer coverage of TPP, STM images showed that the TPP molecules were randomly distributed across the terraces of the surface, isolated from other molecules. The orientation of the molecules mimicked the underlying surface lattice, with the TPP molecules rotated at angles of 120° relative to each other. The surface was then annealed at 350 K, which facilitates the TPP molecules to patially migrate to decorate the step edges. Further annealing, at 450 K was required before all possible step edge sites were occupied. This behaviour is indicative of a strong molecule-substrate interaction. It was also concluded that the Cu(111) surface altered the interactions between the TPP molecules, switching them from attractive to repulsive. It was theorised that this was due to the formations of dipoles on the TPP molecule, caused by charge transfer between the Cu(111) surface and the TPP molecules. The structure of the TPP overlayer on Cu(111) can be seen in Figure 1.7b

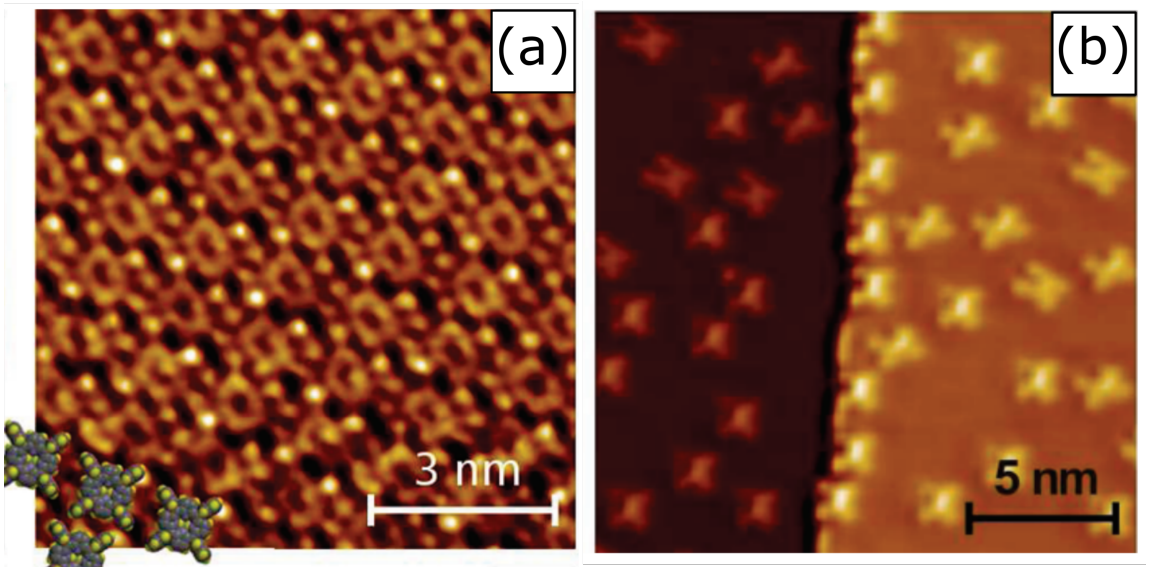

Figure 1.7: (a) STM image of TPP in close-packed arrangement on Ag(111). (b) STM image of discrete TPP molecules on Cu(111). Taken from [36]

The TPP on Cu(111) system has been investigated in greater detail in a study by Stark *et al.*, wherein TPP on Cu(111) was deposited to a full monolayer of coverage on the surface. [38] As previously discussed, at low coverages the TPP on Cu(111) adsorbs as isolated molecules, rotated to align with the crystallographic directions of the surface. At higher coverages the TPP molecules were found to form an ordered checkerboard arrangement, which is stabilized by the formation of attractive CH$-\pi$ and $\pi - \pi$ interactions between the TPP molecules. This arrangement also displayed a height difference between the two types of TPP within the checkerboard. The height difference between the molecules was insufficient for there to be a true second layer of TPP, therefore it was surmised that the height difference was caused by TPP molecules bridging their neighbouring molecules. This caused an elevation of the four TPP molecules surrounding a single first layer TPP molecule. As previously discussed, there is a repulsive interaction between the first layer TPP molecules, however the interactions between the first layer and pseudo-second layer are attractive as the aforementioned CH$-\pi$ and $\pi - \pi$ interactions are able to form.

In the case of the Au(111) surface the supramolecular self-assembly properties of TPP are most comparable to the Ag(111) surface. The TPP molecules form a rectangular islands and then at full monolayer of coverage, they form a close packed arrangement with a square unit cell. [37] An

interesting behaviour of TPP on the Au(111) surface was reported by Grill *et al.*, in which the contrast of TPP molecules, when scanning at different biases was seen to shift. [39] While scanning the same area, as the bias was varied the appearance of the molecules was observed to vary. When scanning at -0.5 V, all TPP molecules displayed the same apparent height, however when the bias was changed to -1.0 V, the contrast of the molecules began to change to include both 'bright' and 'dark' molecules (with the observed molecular contrast being influence by the local density of states (LDOS) associated with the molecule). When scanning at -1.5 V the contrast of the molecules returns to being indistinguishable. By employing a combination of density functional theory (DFT) and STS it was hypothesized that the bright TPP features were caused by TPP molecules sitting atop a surface adatom. Different STS peaks are observed for the 'bright' and 'dark' TPP, with the 'bright' TPP producing peaks at $-1V_t$ and $+1.5V_t$ and the 'dark' TPP producing peaks at $+1V_t$ and $-1.5V_t$ where V_t is the bias voltage applied to the tip. The different spectra and corresponding STM images can be seen in Figure 1.8. The idea of TPP sitting atop an adatoms was probed by using the tip to position single TPP molecules over adatom features in the surface and observing the STM image before and after. It was found that TPP molecules that were formerly dark in colour shifted to bright after being manipulated over the adatoms. The transition was confirmed using STS as the same change in the DOS was observed. In addition, by heating the surface the proportion of bright TPP increased.

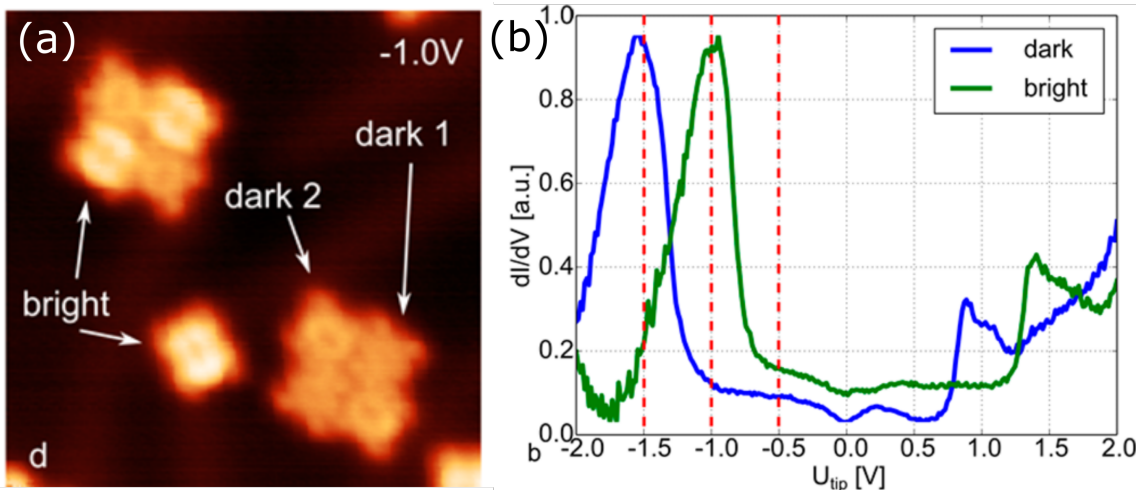

Figure 1.8: (a) STM image of bright and dark TPP molecules on Au(111). (b) STS spectra of each type of porphyrin. Dark was assigned to TPP and bright was assigned to TPP sitting atop an adatom. Taken from [39]

1.3.2 On-surface Reactions of Porphyirns

Porphyrins that have been functionalised to include a halogen atom on the periphery of the central macrocycle may participate in Ullman-type coupling reactions on-surface to form a variety of structures depending on the location of the leaving halogen atom. *Via* the addition of a bromine atom in the *para-* position on the phenyl rings of TPP, a number of structures are possible, depending on the number of substitutions. In a study by Grill *et al.* three different substitution patterns of Br_xTPP (where x= $1, 2, 4$) were used to create different supramolecular assemblies on a Au(111) surface. [40] In each case, the Br_xTPP molecules were deposited onto the surface and then heated to activate the C−Br bond, causing the bromine to dissociate and the TPP molecules to react together to form a C−C covalent bond,(method I). The activation process has also been observed to take place during the sublimation of the molecules if the evaporation temperature is sufficient (method II). In the simplest example, a monobrominated TPP is chosen and reacted using method II. By imaging the surface using STM, it was found that exclusively dimers has formed, due to the single reaction site available. When *trans*-Br_2TPP was selected, the products of the reaction was found to be linear chains, prepared using method I. The two reaction sites allow for the structures to extend in one dimension. Bends in the chains were able to form by the presence of non-covelent interactions such as VDW between the molecules. In the case of the Br_4TPP, there are four possible points at which the molecule may react and form a covelent bond. This resulted in an extended 2D network of porphyrins which were prepared using method I. The different supramolecular structures of these products can be seen in Figure 1.9.

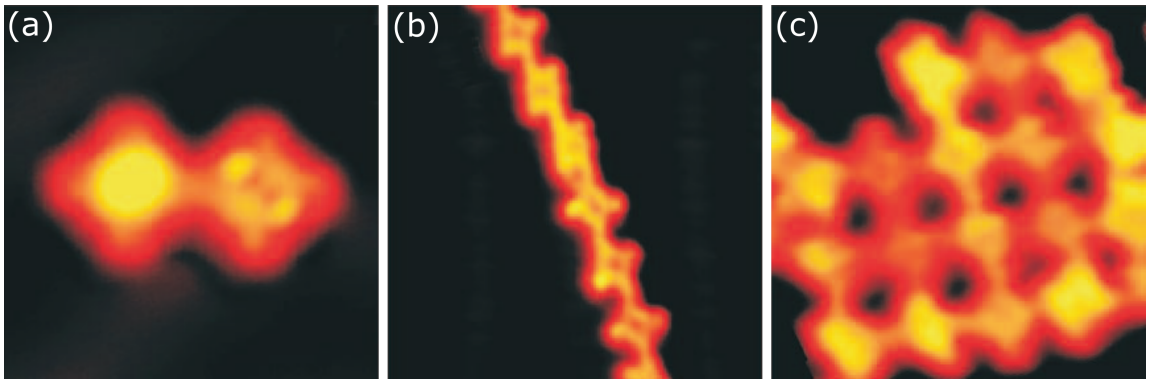

Figure 1.9: (a) STM image of the product of two coupled BrTPP molecules. (b) STM image of the structure of coupled product of Br_2TPP molecules. (c) STM image of the structure of couple Br_4TPP molecules. Taken from [40]

The basis of the this work can be extended to include the option for selective activation, by the inclusion of two different halogen atoms on the TPP molecule.By selecting *trans*-I_2Br_2TPP, the C−Br and C−I bonds can be activated selectively because they have different bond dissociating energies, which allows for step-wise dissociation to create novel structure while demonstrating an increased amount of control over the final product. [41] The monomer *trans*-I_2Br_2TPP was deposited onto a Au(111) surface held at 80 K, the molecules were shown to adsorb intact, and form a close packed arrangement on the surface. Upon heating the sample to 120 °C, the iodine terminals are selectively activated and linear chains form on the surface, which are arranged in close packed islands. The sample was then heated to a higher temperature (200°C), to activate the bromine terminated positions and complete the reaction. The product was a 2D network of TPP molecules, with the same structure as the one produced from Br_4TPP, however the one formed in two sequential steps contained fewer defects and also gave a larger island size indicating that the principles of hierarchical growth can be applied to heterogeneous systems to create a vast range of potential surface structures. [42]

In additional to Ullmann coupling reactions, porphyrins may also undergo intramolecular reactions, in which they will react with themselves and form a new structure. This reaction has been observed in work by A. Wiengarten *et al.*, in which TPP and a ruthenium metalated TPP (RuTPP) were studied individually on Ag(111). [43] In the case of TPP, it was found that the close packed structure formed upon deposition was transformed upon annealing at 250°C, to an irregular

array of molecules distributed across the surface. Similar behaviour was observed for the RuTPP. The reaction that has taken place was attributed to an intramolecular ring closing reaction. This reaction involves first a cyclodehydrogenation, which is followed by an electrocyclic ring closing to yield a planarised porphyrin derivative. The change in arrangement of the surface is likely to be caused by the removal of the CH$-\pi$ interactions which stabilise the close packed arrangement. The planarised porphyrins can no longer form these interactions due to the change in orientation of their phenyl rings, causing the surface to appear disordered. It was found that there were multiple possible products of this reaction, depending on the direction on the ring closing. The ratio of products also differed between the TPP and the RuTPP. The TPP displayed a particular isomer, as the majority product which accounted for 86% of all the products. The second most common isomer was found to be B, consisting of 12% of the mixture, and the remaining isomers C and D accounting for $< 3\%$ each. Conversely in the case of the RuTPP, the ratio of isomers produced displayed less selectivity, with isomers B and C amounting to 30% each, and A and D 20% each of the total.

Upon examining the cause of the discrepancy in ratios of isomers between the metalated and non-metalated porphyrin, it was found that the central hydrogen atoms, present in TPP but not in RuTPP, were pivotal in selective production of isomer A. The central hydrogen atoms provide the two-fold symmetry in TPP, which governs the reaction pathway of the sequential ring closing reactions required to reach the fully planarised final product.

Another example of this type of reaction has been demonstrated by Ciera *et al.*, in which F_4TPP, a fluorine substituted TPP, displays a ring closing reaction to form a porphyrin derivative which is subsequently metalated and polymerized. [44] The F_4TPP species was deposited onto a Au(111) surface, and was seen to form close packed islands, in a similar manner to the TPPs previously discussed. [36–38,40,41] The surface was then heated to 230°C, to facilitate the ring closing reaction. There were multiple possible products of this reaction, which appeared in different proportions, however the product seen in 1.10 was the majority product.

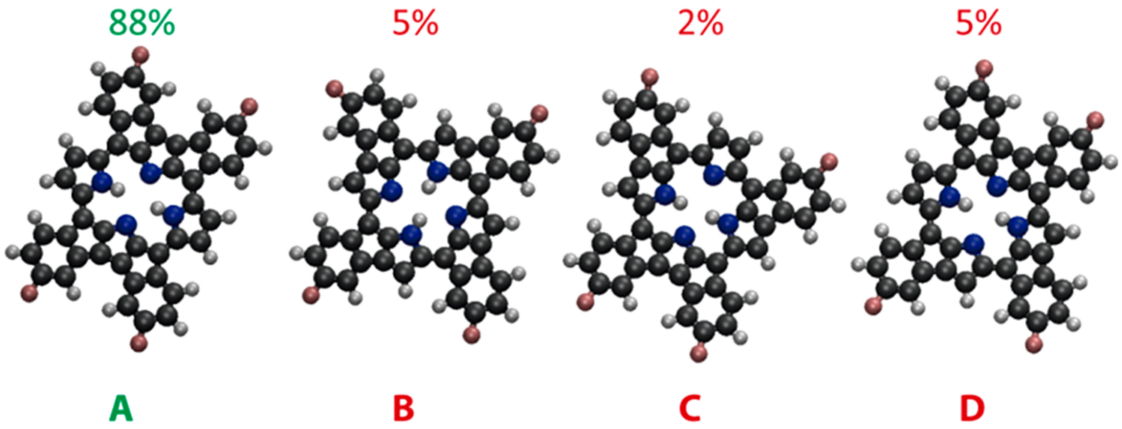

Figure 1.10: Figure showing the different isomers that can be formed during the ring closing reaction of F_4TPP and thier relative proportions

The sample was then heated again, this time to 300°C, to facilitate the self-metalation of the porphyrin derivatives, in which 20% of molecules were seen to incorporate a surface Au atom into their central cavity. The presence of the metal atom was investigated using AFM, in which the Au−N interaction regions were observed. Following this step, the sample was then heated again, to 350 °C, which enabled a polymerisation reaction to take place. The bond dissociation energies of the C−H and C−F bonds are very similar and reactions may occur at either site. The products of this step were found to be oligomer chains of planarised porphyrin derivatives, linked by the formation of C−C covalent bonds, and also defluorinated porphyrin derivatives, in which an activated C−F or C−H bond is passivated by residual atomic hydrogen. The products at each stage of this reaction can be seen in Figure 1.11

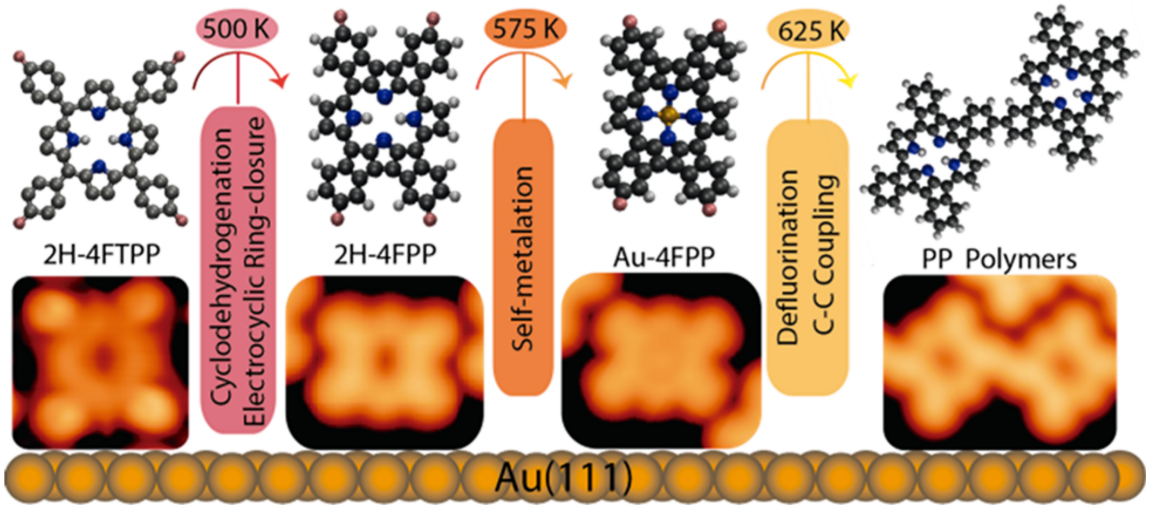

Figure 1.11: Schematic of the reactions of F_4TPP on Au(111), beginning with the ring closeing, followed by metalation and completed by polymerisation. Taken from [44]

The series of reactions discussed above demonstrate the highly customisable nature of porphyrin molecules and their reactions. They may undergo several on-surface processes which, once fully understood, would allow the synthesis and control of molecular devices built from poprhyrin molecules.

1.4 Metalation of Porphyrins

One of the key reactions of porphyrins is metalation, the nitrogen atoms of the pyrole rings are directed towards the centre of the macrocycle, leaving the lone pair present on each nitrogen available for the formation of coordinate bonds. The large size of the pore enables a range of metal atoms to fit comfortably inside the molecule. Metalated porphyrins play an essential role in the natural world and are present in the blood of every animal on the planet. In humans, the iron metalated Protoporphyrin IX performs the essential task of oxygen transport around the body. The Fe_2^+ ion at the centre of the porphyrin macrocycle selectively coordinates to oxygen molecules in the lungs and transports them around the body, releasing them in other tissues where they are required for respiration. The presence of the Fe atom gives blood its characteristic red colour. [45] The only animal to have a different metal present in its blood is the horseshoe crab, which has a porphyrin metalated with a Cu atom instead, giving it blue blood.

Metalloporphyrins can be synthesised using solution-based chemistry, by combining free base porphyrins with a metal ion in solution. [46, 47] However an alternate pathway to achieve a metalloporphyrin is by confining porphyrin molecules to a metal substrate, from which they may take a metal atom from the surface into the macrocycle, or they may be reacted with a metal/metal-containing compound which is deposited onto a surface, with the surface used as a support. [48, 49]

It has been observed that TPP may be metalated with an Fe atom, *via* the evaporation of elemental Fe onto a monolayer of TPP deposited onto Ag(111). [50] The surface was observed before and after the deposition of the Fe atoms. The TPP monolayer displayed the close packed arrangement expected from TPP on a metal surface. After depositing the Fe atoms the surface took on a tiled appearance with some tiles appearing as a protrusion on the surface, STM images of these surfaces can be seen in Figure 1.12. As more Fe was deposited the proportion of these protruded tiles increased. Eventually the number of FeTPP molecules that had formed reached a critical point, at which there were no more TPP molecules that could be metalated. Any additional Fe atoms present at this point formed second layer islands.

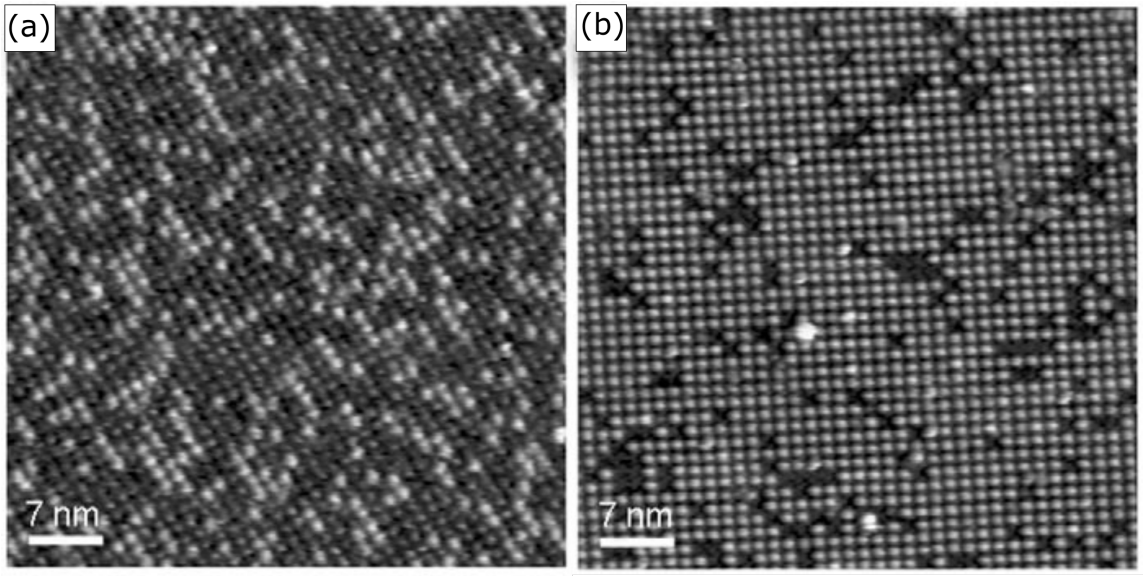

Figure 1.12: (a) STM image of TPP tiling with some protrusions, assigned to FeTPP. (b) As more Fe is deposited the number of protruding tiles increased. Taken from [50]

1.4.1 Spectroscopy Studies of Metalated Porphyrins

STM is a useful tool for gaining insight into the superficial and structural changes that occur on surfaces before and after chemical reactions. To gain further insight into the chemical and electronic transitions that have taken place, a variety of types of spectroscopy may be employed to probe individual molecules or the surface as a whole.

Scanning tunneling spectroscopy can be used to probe the local density of states (LDOS) at specific locations on the surface. TPP metalated with Au(111) has been studied on the Au(111) surface using STS. In an initial study performed by S. Mullegger *et al.,* Au(III)TPP molecules were probed using STS. [51] In this study, TPP molecules had been metalated with gold (Au−TPP) and were deposited onto a Au(111) surface, and studied using STM and STS. TPP was observed at a number of bias voltages, and it was found very little difference in chemical structure was seen across the range. Using STS experiments, the energy of the highest occupied molecular orbital (HOMO) and lowest unoccupied molecular orbital (LUMO) for AuTPP were determined. The spectra produced by holding the tip directing above the AuTPP molecule and sweeping the bias from -2.0 V to +1.3 V displayed peaks at -1.4 V which can be related to the energy of the HOMO and +0.9 V which can be related to the energy of the LUMO, giving a HOMO-LUMO gap of 2.5 V. These experimental results were compared to DFT results. Gas phase AuTPP MOs were calculated, the HOMO-LUMO gap was calculated to be 2.77 V, which is comparable to the experimental result. Using the DFT results the oxidation state of the metal atom could be determined. The DFT result for a Au^{3+} species produced a HOMO-LUMO gap of 2.77 V, while the gap for Au^{+} was found to be less than 1 V, eliminating it as a possibility. It was reasoned that the metal could not be Au^{2+} due to the STM image showing a depression in the centre of the molecule, which is typically associated with doubly occupied d states.

In an second study, performed by Mulleger *et al.*,, of AuTPP on Au(111) in which the frontier orbitals were probed by STS, it was found that an additional peak, not seen in the previous study was present. [52] In this study, the position of the LUMO was found to be 1.12 V, while the position of the HOMO was found to be -1.25 V, giving a HOMO-LUMO gap of 2.37 eV. [51] The discrepancy in the results was concluded to be due to the second study using more optimized tunneling parameters. The optimized STS spectrum displayed a several peaks, the HOMO and

LUMO, as previously stated, but also the HOMO-1 and the HOMO-2 which sat at -1.39 V and -1.68 V respectively, and the LUMO+1, which occurred at +1.31 V. The STS spectrum recorded can be seen in Figure 1.13.

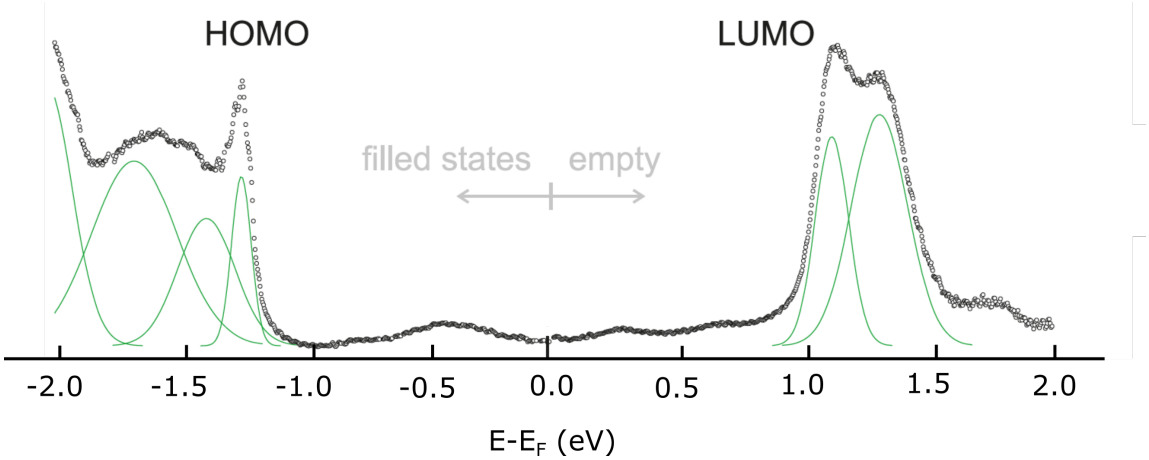

Figure 1.13: STS spectrum of AuTPP with HOMO and LUMO peaks labelled. Taken from [51]

1.4.2 Photoelectron Studies of Metalated Porphyrins

SPM techniques provide a variety of data about on-surface systems and reactions, such as local structural information and information on the electronic states. In conjunction with SPM techniques, X-ray techniques, such as x-ray photoelectron spectroscopy (XPS) and normal-incidence x-ray standing wave (NIXSW), may be used to gain chemical and structural data from molecules on surfaces. XPS experiments may be performed using commercial x-ray sources, however NIXSW requires tunable, high energy radiation which can only be produced using a synchrotron.

XPS can be used to characterise the chemical environments present within a sample and may be employed to monitor changes to these environments during chemical reactions. Both the C1s and N1s environments of porphyrin molecules deposited onto metal surfaces have previously been characterised using XPS.

The chemical environments of the C1s and N1s of TPP on SiO_2 have been reported by Nardi *et al.,* detailing the different chemical environments within TPP molecules when observed experimentally and calculated theoretically. [53]

The N1s spectra showed two main peaks N_A and N_B, which had binding energies of 400.1 eV

and 398.2 respectively. N_A at 400.1 eV was assigned to the pyrrolic nitrogen atoms (−N=, and N_B at 398.2 eV was assigned to the aminic nitrogen atoms (N−H), with an energy gap of 1.9 eV. Two small satellite features (N_{Asat} and N_{Bsat}) were also present at 403.0 and 401.0 eV, which were attributed to shake up processes. The relative weights of the 4 peaks were 42.7% for N_A, 41.5% for N_B, and 7.9% each for N_{Asat} and N_{Bsat}. DFT calculations of the N1s environments for TPP predict two peaks, with energies of 404.4 and 402.6 eV, this gives an energy gap of 1.8 eV which is in excellent agreement with the experimental results.

The C1s spectra displayed one main peak with asymmetric broadening at the base. The asymmetry of the C1s feature indicated that it was comprised of multiple components at similar binding energies. Four different peaks C_A at 285.6 eV, C_B at 286.0 eV, C_C at 286.3 eV and C_D at 285.2 eV and a shake-up feature, C_S located at 288.8 eV, were fit to the C1s spectra. These peaks appeared in a ratio of 51.2%, 17.0%, 8.6%, 17.0% and 6.2% respectively, corresponding to 23, 7, 4, 7 and 3 atoms per peak. The experimental C1s spectrum can be seen in Figure 1.14a. The main peak was assigned to the phenyl carbon atoms of which there are 24 in total. The remaining three peaks C_B, C_C and C_D were assigned to the carbon atoms in the porphyrin ring. C_B and C_D were assigned to the α and β carbon atoms respectively and C_C was assigned to the carbon atoms in the *meso*-positions on the ring. DFT calculations of the C1s environments for TPP predict a similar overall peak structure, with a single main peak, with asymmetric broadening at the base. The difference in assignment is due to the 'perfect' nature of DFT, whereas for the XPS data some of these environments are combined. The main peak, C^{Ph} at 289.9 eV was assigned to the phenyl carbon atoms, five additional peaks, consisting of four carbon atoms each were assigned to the carbon atoms in the porphyrin ring. The α carbon atoms were assigned into two environments, $C^{A-C} - C\alpha$ and $C^{B-D} - C\alpha$ which displayed peaks at 291.1 eV and 290.5 eV respectively. The β carbon atoms were assigned into two environments, $C^{A-C} - C\beta$ and $C^{B-D} - C\beta$ which displayed peaks at 289.9 eV and 289.4 eV respectively. The fifth peak, C^m was assigned to the carbon atoms in the *meso*-positions on the ring, and occurred at 290.4 eV. The spectra for the experimental and theoretical C1s can be seen in Figure 1.14b

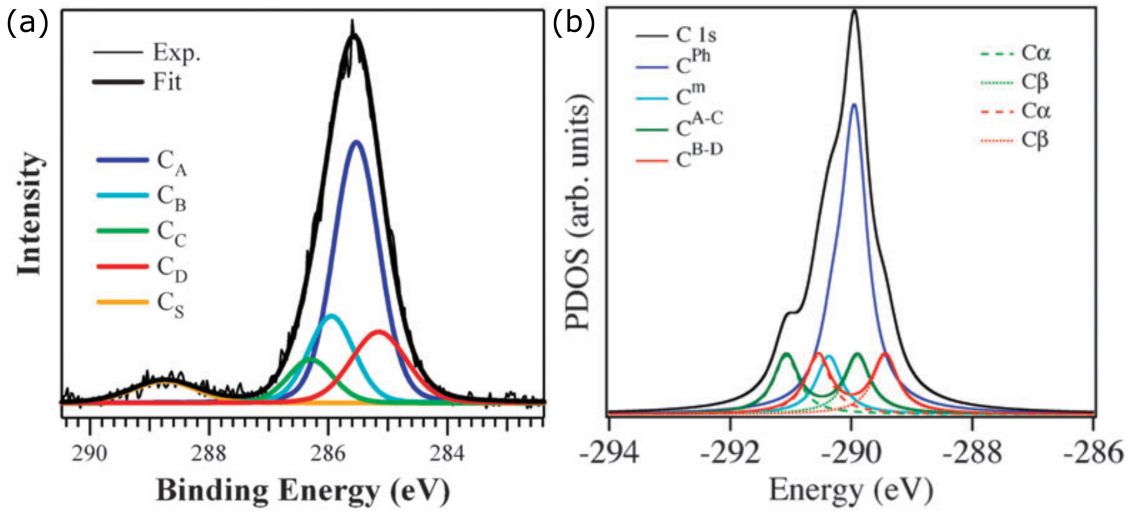

Figure 1.14: (a) Experimentally observed C1s XPS spectrum of TPP on SiO_2. (b) XPS spectrum of the C1s orbital of TPP derived from DFT calculations. Taken from [53]

XPS can be used to observe changes the in chemical environments present in a system during on-surface reactions. Spectra can be taken at various points during the reaction process to provide information on the mechanisms of the reaction and on any new species present. This is particularly relevant to the work presented within this thesis because it demonstrates how XPS can be used to detect the chemical changes and new species on surfaces.

An on-surface synthesis of a metalloporphyrin complex has been reported by J. M. Gottfried *et al.*, in which TPP, deposited onto a Ag(111) surface was exposed to gradually increasing amounts of gaseous Co atoms. [54] Prior to any Co exposure, the monolayer of TPP displayed the characteristic two peaks in the N 1s XPS spectrum, at 398.1 eV and 400.1 eV, which were assigned to the aminic nitrogen and the iminic nitrogen respectively. The monolayer of TPP was exposed to a small amount of gaseous Co (0.022 monolayers (ML) with respect to the surface). The resultant XPS spectrum showed a significant change, even at low levels of Co. A new peak, which was attributed to a Co−N environment, at 398.8 eV was present, alongside the original two peaks. As larger proportions of Co was deposited, the new peak grew in intensity, while the original aminic and iminic peaks diminished. At 0.047 ML of Co, the aminic and iminic peaks has all-but disappeared, and the Co−N peak was the dominant environment present. The presence of only one peak indicated that

the nitrogen atoms were all in the same environment, bonding to the Co atom, implying that the aminic nitrogen atoms had lost thier hydrogen atoms in order to form this bond. The XPS spectra over time can be seen in Figure 1.15

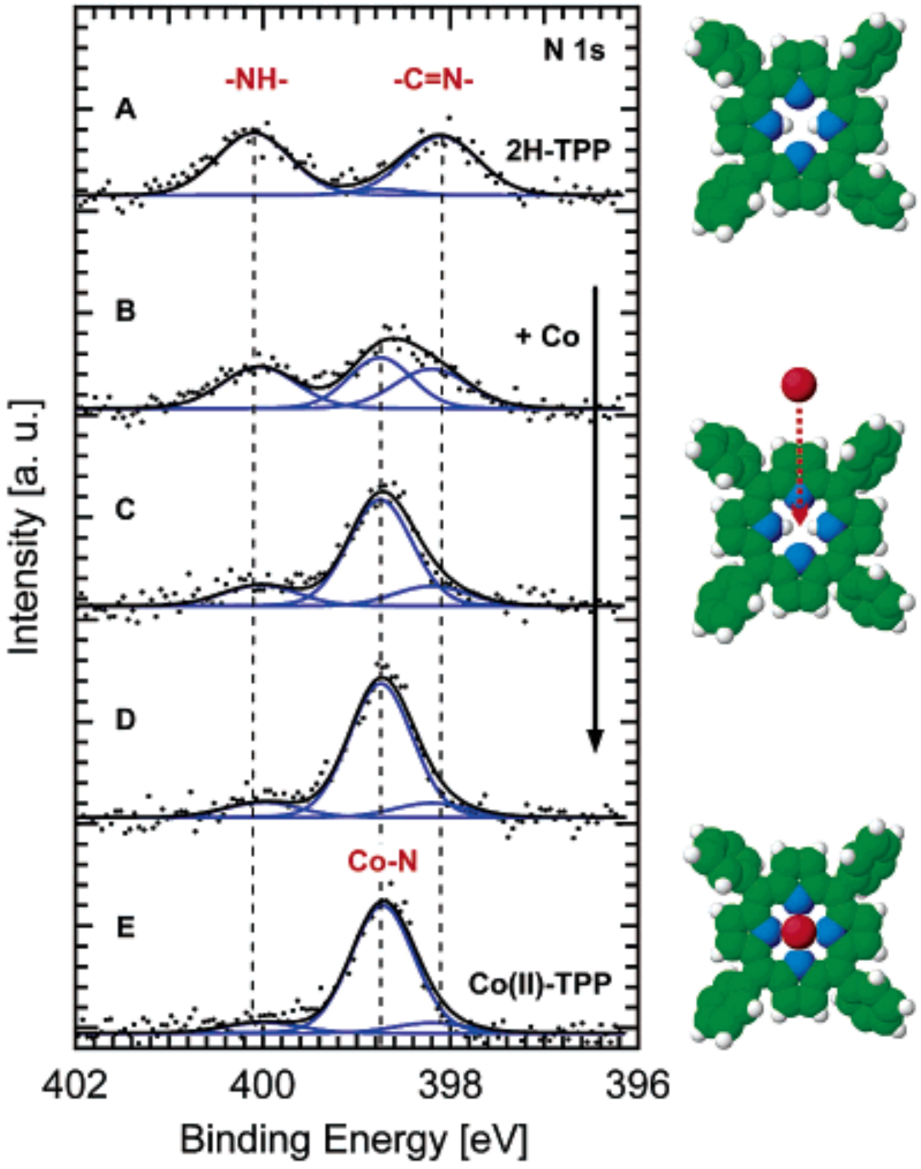

Figure 1.15: XPS spectra taken with increasing depositions of Co onto the surface, showing the metalation of TPP. Taken from [54]

Porphyrins are also known to experience self-metalation *via* the uptake of a metal atom from the surface. This process has been reported by M. Rockert *et al.,* for TPP on Cu(111). [55]

TPP on Cu(111) has been observed to adsorb as individual molecules at low coverages, and as checkerboard structure with alternative molecules elevated above the surface at higher coverages. Prior to annealing the N1s spectra of TPP on Cu(111) displayed two peaks seen at 400.1 eV, assigned to iminic nitrogens, 398.6 eV assigned to aminic nitrogens. Upon heating the surface for 10 minutes at 400 K, changes were observed in the N1s XPS at both high and low coverages.

At high coverage a single large peak was present at 400.1 eV, which was assigned to nitrogen bonding with a Cu atom, representing a metalated porphyrin molecule. This indicated that the metalation of TPP with surface Cu atoms took place rapidly during the anneal, with a high conversion rate. At low coverage the N1s spectra did not show the same change as at high coverage. What had occurred was an increase in intensity of the iminic nitrogen peak, which lies at the same energy as the metalated nitrogen peak, while the aminic nitrogen peak remained present but slightly diminished. This observation was attributed to a slower reaction, which did not go to completion. The origin of the metal atoms was thought to be from surface atoms detaching from step edges and diffusing across the terraces, as opposed to Cu atom being up lifted from the surface below the TPP molecules, to leave behind a vacancy.

Another technique, closely related to XPS, used for determining the structure of molecules on surface is Normal incidence X-ray standing wave (NIXSW). This technique is used for determining adsorption geometries of specific atoms adsorbing at the surface and monitoring changes in adsorbing geometry before and after reactions. This technique enables near-mechanistic detail to be achieved when studying reaction pathways on surfaces. This technique requires chemical environments to be defined by fitting XPS data, such that an XSW profile can be related to each peak. From the XSW profile the relative heights of the atoms in specific chemical environments can be determined.

In an NIXSW study by P. Ryan *et al.,* the adsorption geometry and shape of TPP on the Cu(111) surface was determined and the 'inverted' model of this molecule was confirmed on this surface. [56] Prior to this study TPP was believed to adsorb on Cu(111) in the saddle conformation, however by employing XSW methods the 'inverted' model of TPP could be confirmed as the adsorption conformer over the saddle conformation. TPP displays two distinct nitrogen environments, relating to the iminic and aminic nitrogen atoms. The heights of the N atoms above the surface are directly related to the coherent position values extracted from the XSW profile taken of the (111) reflection.

The heights of the nitrogen atoms above the Cu(111) surface were found to be 1.88 ± 0.08 Å and 2.15 ± 0.15 Å for the iminic and aminic nitrogen species respectively. High coherent fraction C_f values indicated that there was a single absorption site for each type of N atom. By triangulating with the (-111) and (200) reflections the adsorption sites were determined to be the bridge site for the iminic and the atop site for the aminic. This is contrary to the known adsorption geometry for the saddle conformation in which the iminic nitrogen atoms adsorb in an off-atop position, the two conformers of TPP can be seen in Figure 1.16.

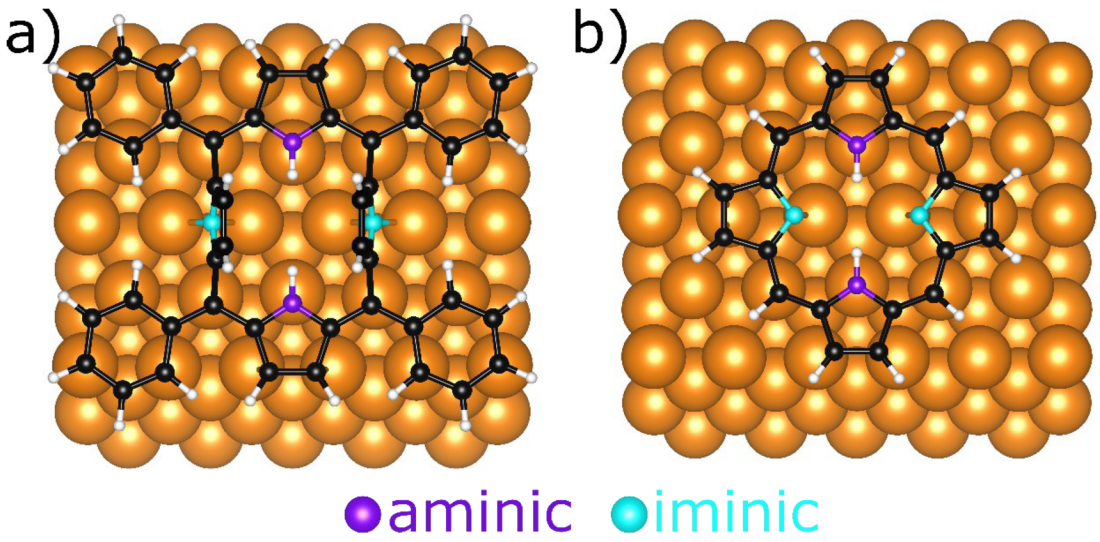

Figure 1.16: (a) The inverted model of TPP, represeting the actual adsorption geometry of TPP on Cu(111). (b) The saddle conformation of TPP which was the previously accepted adsorption geometry. Taken from [56]

NIXSW methods can also be used to study on-surface reactions and the changes in structure associated with them. The self-metalation of TPP molecules on Cu(111) has been studied using these methods, and the presence of a metalated CuTPP species confirmed. [57] As stated in previous examples, TPP displays two N1s peaks, representing the iminic and aminic nitrogen environments. When metalated TPP will only have one distinct nitrogen environment as all N atoms will be bonding to the central metal atom. The XSW analysis gave the heights of the iminic and aminic nitrogen atoms above the surface at room temperature to be 2.23 Å and 2.02 Å respectively. Repeated at low temperature, these heights were found to differ slightly (2.28 Å for the aminic and 1.97 Å for the iminic). The lower height of the iminic nitrogen atoms was attributed to a

stronger interaction between the iminic nitrogen and the surface, consistent with the TPP molecules adsorbing the in the saddle conformation. This has since been disproved in favour of an 'inverted' model. [56] Upon annealing, the nitrogen atoms all coordinate to the central Cu atom, resulting in equal heights above the surface of 2.25 Å.

By combining the N1s and C1s XSW profile data, it was determined that upon annealing and the resulting incorporation of the metal atom, the structure of the porphyrin changes from a distorted model to flattened molecule, in which each atoms takes a similar height above the surface.

1.5 Summary

In this chapter an overview of recent advances in the study of the structural and chemical properties of on-surface systems and reactions by employing a range of surface-based analysis techniques has been presented.

The principles of supramolecular chemistry and the non-covalent interactions that allow for the design and study of supramolecular structures with specific geometries and topologies have been presented. A review of recent developments in the study of porphyrin molecules on surfaces has been presented, with focus on the structures they form and the potential reactions that they can undertake.

SPM and synchrotron methods have been discussed and the types of information that can be extracted from the different types of experiment have been introduced. These concepts will provide a background to the results presented in the remainder of this thesis. Surface imaging techniques such as STM and STS will be used to study assemblies of TPP on a single molecule level, while XPS and NIXSW methods will enable the insight into the average processes and on-surface reactions taking place in the phases of TPP on Au(111)

Chapter 2

Experimental Methods

In this chapter the details of the UHV-based, surface science techniques that are employed in experimental chapters 4-6, are provided. A number of different techniques were used for the collection of experimental data. The scanning probe techniques, scanning tunneling microscopy and spectroscopy were selected for their ability to produce information on nanoscale surfaces in the form of both images and spectroscopic data. Synchrotron techniques, X-ray Photoelectron spectroscopy and Normal Incidence X-ray standing wave, were selected to gain information on both the chemical structural changes that occur at an interface.

2.1 Scanning Probe Techniques

Scanning probe microscopies (SPMs) are a family of techniques that utilise interactions between a tip and a sample to provide information about the properties of nanoscale materials that would otherwise be inaccessible. SPM measurements allow real-space characterisation of individual molecules, in contrast to other methods, which provide information only on the ensemble- average of a system. This SPM family includes techniques such as scanning tunneling microscopy (STM), atomic force microscopy (AFM) and kelvin probe force microscopy (KPFM). The high spatial resolution of these techniques has allowed significant progress to be made in numerous fields, particularly condensed matter physics.

2.1.1 Scanning Tunneling Microscopy

Scanning tunneling microscopy is an imaging technique, which has successfully been employed to study molecules on surfaces. The STM was originally designed in 1982 by G. Binnig and H. Rohrer, who would later win a Nobel Prize in 1986 for this work [58–60]. Their design consisted of a metallic tip, controlled by piezo-electric crystals, and a conductive sample with a small voltage applied between them. The current was measured, and kept at a constant value, as the tip scanned across the surface. This allowed the topology of the surface to be mapped. A schematic of this can be seen in Figure 2.1. They were able to resolve step edges and surface defects in Au(110) and $CaIrSn_4$. Their STM had a lateral resolution of < 10 Å.

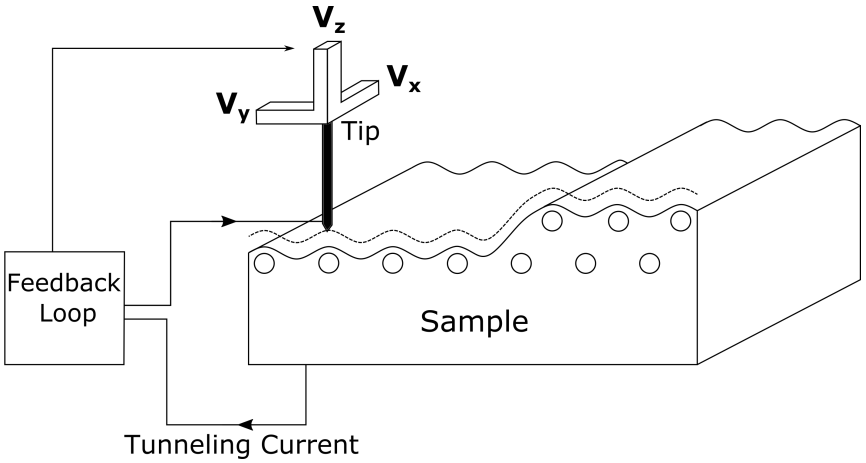

Figure 2.1: Schematic of an STM, showing a surface with a step edge and a tip attached to three piezo-electric crystals to control movement in x,y,z, via the application of a voltage V_x, V_y and V_z respectively.

Modern STMs have a lateral resolution of < 1Å and a vertical resolution on the order of picometers. This allows individual molecules to be studied in a real-space environment. This ability makes STM a uniquely powerful tool as it does not require the long-range order that techniques such as low energy electron diffraction (LEED) and X-ray crystallography rely upon.

Tunneling Theory

The core principle of STM is quantum tunneling, the ability of an electron to pass through a classically forbidden barrier. Consider a large potential energy barrier; in classical physics a particle with a small, relative to the potential, energy will not be able to overcome the barrier. In quantum

mechanics, the particle may traverse this barrier by passing through it rather than over it. Consider a system composed of two conductors, separated by an insulating barrier, of height V_0 and a length of L. In this system is an electron, with mass m and energy, E. This is demonstrated in Figure 2.2. The solution to the time-independent Schroedinger equation for this system can be represented by three wavefunctions, ψ_1, ψ_2 and ψ_3. Before the barrier the electron is represented by the wavefunction, ψ_1. ψ_2 represents the exponential decay of the probability of finding the electron within the barrier. ψ_3 is the wavefunction of the electron when it has tunnelled through to the sample, with a significantly diminished amplitude to be continuous with ψ_2.

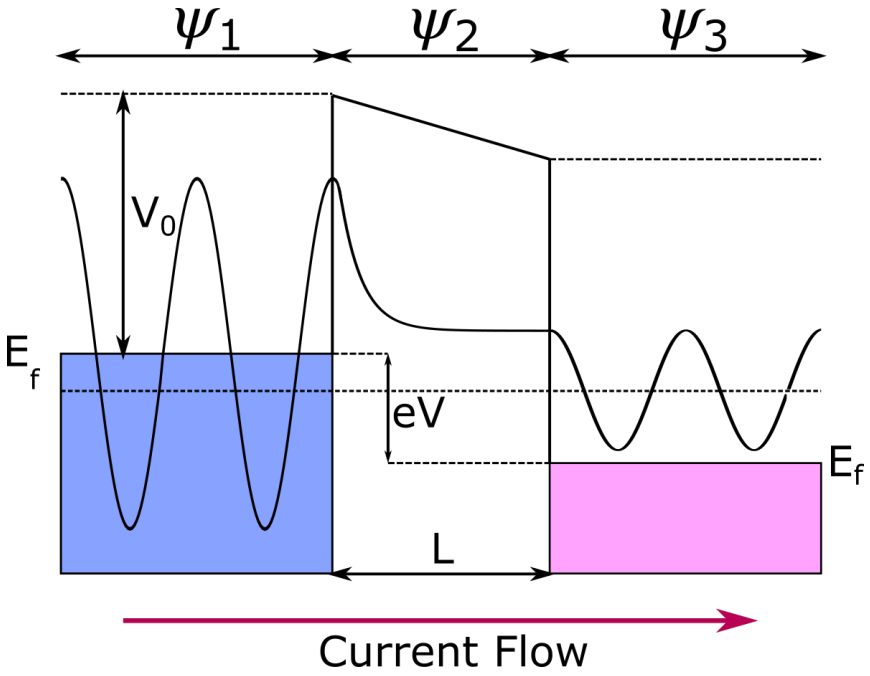

Figure 2.2: Model of electrons tunnelling from an STM tip to a sample. Separated by a distance, L with an energy barrier of height V_0, where E_f is the fermi level in each side of the barrier, divided into unnormalised wavefunctions ψ_1, ψ_2 and ψ_3. Reproduced from [61]

These wavefunctions may be written as,

$$\psi_1 = A_0 e^{ikx} + A_0 e^{-ikx} \tag{2.1}$$

$$\psi_2 = Be^{\alpha x} + Ce^{-\alpha x} \tag{2.2}$$

$$\psi_3 = De^{ikx}. \tag{2.3}$$

where $\alpha = \sqrt{\frac{2m(V_0-E)}{\hbar}}$ and $k = \sqrt{\frac{2me}{\hbar}}$ and e is the elementary charge of the electron and $\hbar$ is the reduced Plancks constant, $\frac{h}{2\pi}$. In Equation 2.1 ψ_1 is composed of two parts, the first representing the incident component and the second representing the reflected component. ψ_2 gives the exponential decay of finding the electron within the barrier, it is more likely to exist close to the left-hand side of the barrier than the right-hand side. Equation 2.3 gives ψ_3, the wavefunction of the electron which has successfully tunnelled through the barrier. This can be used to work out the transmission probability of an electron, T (Equation 2.4) by using the ratio of incident and transmitted wave amplitudes.

$$T = \left| \frac{D}{A_0} \right|^2 \tag{2.4}$$

T is directly proportional to the tunnel current of an STM. Assuming that the barrier is large ($\alpha L \gg 1$), T may be approximated to

$$T \approx 16 \left(\frac{E}{V_0} \right) \left(1 - \frac{E}{V_0} \right) e^{-2\alpha L} \tag{2.5}$$

Equation 2.5 shows that T scales with the inverse exponential of αL component. L being the barrier width and α containing the barrier height $(V_0 - E)$. Therefore, by decreasing the distance between the tip and the surface, the tunnel current increases exponentially.

Tersoff-Hamann

The previous wavefunction treatment of tunnelling is a simplistic approach and does not take into a number of factors when looking at the specific interaction of a surface and STM tip. In 1961 Bardeen developed a general theory of tunnelling, using the transfer Hamiltonian method, in which an electron tunnelled between two metal plates. [62]. Bardeens method was then extended and applied to STM by Tersoff and Hamann some years later. [63] [64] The Tersoff and Hamann model specifies one of the metal plates as the tip and the other as the surface. This gives the tunneling current to be,

$$I = \frac{2\pi}{\hbar} \sum_{\mu\nu} f(E_\mu)[1 - f(E_\nu + eV)] \left| M_{\mu\nu} \right|^2 \delta(E_\mu - E_\nu), \tag{2.6}$$

where; $f(E_\mu)$ is the fermi function of the tip, $f(E_\nu)$ is the fermi function of the surface, V is the applied bias and $M_{\mu\nu}$ is the tunnelling matrix element between the state, ψ_μ of the tip and the state, ψ_ν of the surface. This equation can be considered in three parts. Fermi function, $f(E_\mu)$ represents the probability that a state in the tip, of energy E_μ, is occupied. $[1 - f(E_\nu + eV)]$ represents the probability that a state in the surface, of energy $E_\nu + eV$, is not occupied. $|M_{\mu\nu}|^2$ is the probability that an electron will tunnel from state ψ_μ to ψ_ν. The final part of the equation is the Dirac delta function $\delta(E_\mu - E_\nu)$, this represents the conservation of energy if elastic tunneling was to occur, assuring $I = 0$ if $E_\mu \neq E\nu$. The tunneling matrix, $M_{\mu\nu}$, can be evaluated by integrating the wavefunctions, and their normal derivatives, of tip and the surface over the vacuum barrier between them,

$$M_{\mu\nu} = \frac{-\hbar^2}{2m} \int (\psi_\mu^* \nabla \psi_\nu - \psi_\mu \nabla \psi_\nu^*).d\mathbf{S}, \tag{2.7}$$

where $\mathbf{S}$ is the vector direction of two barrier extremities.

Tersoff and Hamann considered the specfic conditions of low temperature and low bias to simplify equation 2.6 to give the current as,

$$I = \frac{2\pi}{\hbar} eV^2 \sum_{\mu\nu} |M_{\mu\nu}|^2 \, \delta(E_\mu - E_F)\delta(E_\nu - E_F), \tag{2.8}$$

where E_F is the fermi energy. In the limit of small bias, $V \ll 1$, and thus, eV is inconsequential. In the limit of low temperature the lowest unoccupied state in the surface is at the fermi energy and the only available electron to be liberated in tip is also at the fermi energy, thus the probability of both is 1 and the fermi distribution terms can be dropped. Another assumption made by Tersoff and Hamann is that the tip is a spherical point probe, which is spherically symmetric. This reintroduces ψ_ν as a sine-wave that decays outwards, wih no angular dependency. With this, the tunnel current becomes,

$$I \propto \sum_{\nu} |\psi_\nu(r_0)|^2 \, \delta(E_\nu - E_F), \tag{2.9}$$

where r_0 is the centre position of the spherical tip with radius R. This is the local density of states (LDOS) at the surface at the position of the STM tip. In the resultant STM images the features that are visible are the LDOS. In a more realistic approximation there are finite applied

voltages applied to the system. Integrating over all of the states contributing to the tunnel current (between E_F and $E_F + eV$)gives,

$$I \propto \int_{E_F}^{E_F+eV} |\psi_\nu, (r_0)|^2 \, \delta(E - E_F) T(E, eV) dE, \tag{2.10}$$

where $T(E, eV)$ is the transmission coefficient, defined in Equation 2.5, however for small biases this is assumed to be constant.

Current Flow

The direction of current flow between an STM tip and surface and consequently the states being imaged, can be controlled by the altering the applied bias. The bias can be applied to either the tip or the surface, however in this thesis the bias will be applied to the sample only. At zero applied bias there will be no current flow and the fermi levels (E_F) of the tip and surface will be at equal energy. Figure 2.3 shows the two possible arrangements of current flow. If a positive bias is applied (2.3a) to the sample, the fermi level of tip tip becomes raised. Current will flow from filled states in the tip into empty states in the surface of equivalent energy. Images produced in this manner will show the empty states of the surface. Alternatively, if a negative bias is applied (2.3b) to the sample the fermi level of the surface will rise. Current will now flow from filled states in the surface to empty states in the tip. This will produce images showing the filled states of the surface.

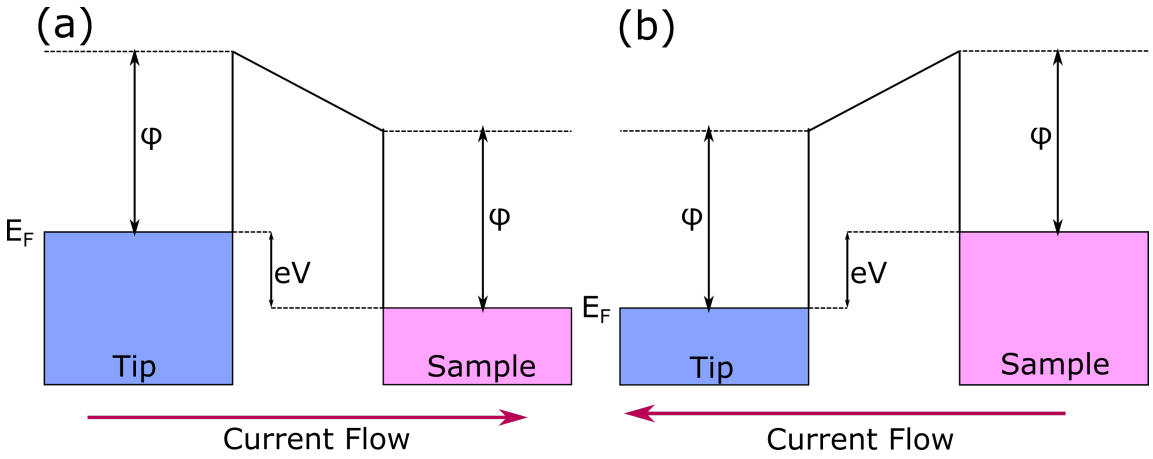

Figure 2.3: Diagram of energy levels in the tip and the sample showing the directions of current flow between them at different biases. (a) A positive bias is applied to the sample, consequently the Fermi level of the tip is raised relative to the sample. Current flows from the tip to the sample. (b) A negative bias is applied to the sample, consequently the Fermi level of the tip is lowered relative to the tip. Current flows from the sample to the tip.

When molecules are deposited on the surface it is possible to image their molecular orbitals (MOs). By varying the bias different MOs will become visible. This can be thought of as electrons tunneling in two steps, from the tip to the adsorbed molecules and then from the molecules to the surface (or vise versa), however it is more appropriate to think of the surface and adsorbate as one. This is acceptable because the adsorbed molecules are in close proximity to the surface so it is likely that it will strongly couple with the surface states, resulting in hybrid orbitals. This causes the MOs of the adsorbate to be tied to the surface orbitals relative to the Fermi level. [65] A diagram of this can be seen in Figure 2.4. If a positive bias is applied to the sample, the fermi level of the tip becomes raised and electrons tunnel from the tip into the LUMO of the molecules (and LUMO+1, LUMO+2, etc depending on the value of the bias). If a negative bias is applied to the sample the fermi level of the sample raises and subsequently, so do the MOs of the adsorbate, and electrons tunnel from the HOMO (and HOMO-1, HOMO-2 etc) into the tip.

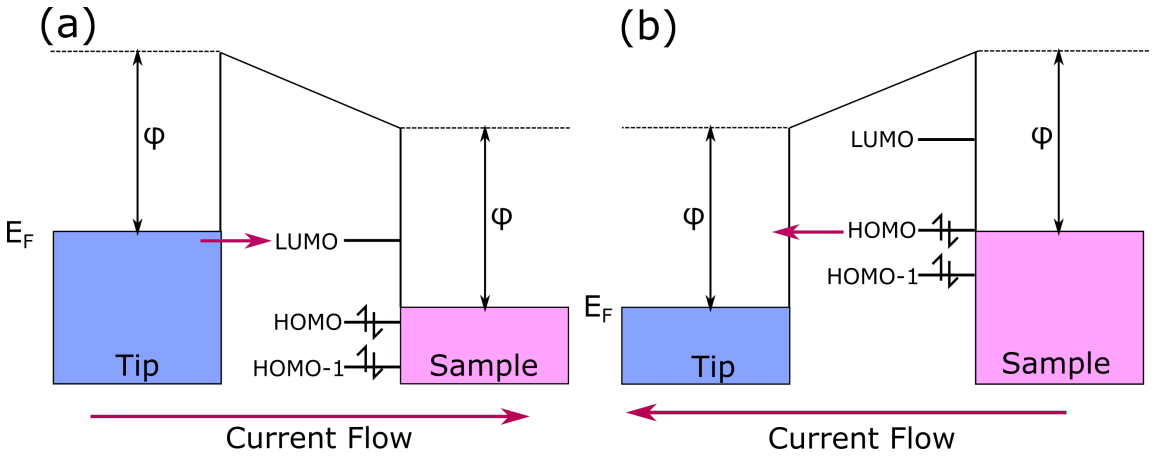

Figure 2.4: Diagram of energy levels in the tip and the sample showing current flow when molecules are present on the surface. (a) A positive bias is applied to the sample, the Fermi level of the tip raises relative to the surface and electrons flow into the LUMO of the molecules. (b) A negative bias is applied to the sample, the Fermi level of the tip lowers relative to the surface and electrons flow from the HOMO of the molecules into the tip.

STM Operation

An STM forms an image by scanning across the surface, line by line and taking discrete measurements for each pixel and gradually building up the image. There are two modes in which an STM can operate, constant height and constant current.

In constant height mode the tip is kept at a constant z value above the surface as it moves in x and y. As the tip moves the tunnel current fluctuates in accordance with the local density of states (LDOS) at that point, its value is measured for each point and then assigned to the corresponding pixel. This can be seen in Figure 2.5a. The greatest disadvantage of this mode of operation is that there is a significant chance of the tip crashing into the surface. This can be caused by the presence of large surface features or a large number of step edges, therefore, large atomically flat areas of surface are required for this mode of operation.

In constant current mode the tunnel current is set to a chosen value and a feedback loop is used to maintain the same current as the image is taken. The tip height then varies with the position, dependant on the LDOS at that location, this is shown in Figure 2.5b. When the tip moves between points the z position is adjusted by the feedback loop to maintain the current set point. As the tip moves in x and y across the surface the z position is recorded for each point corresponding to the pixel value.

There are two factors which contribute to the assigned pixel values, the height and the conductivity of the surface features. For most surface species, a greater height will correspond to a greater z position or tunnel current. This will appear as a bright feature in the image. If there is an insulating species present this will cause the tunnel current to drop, or the z position to decrease, appearing as a depression in the image, for example, the blue atom in Figure 2.5.

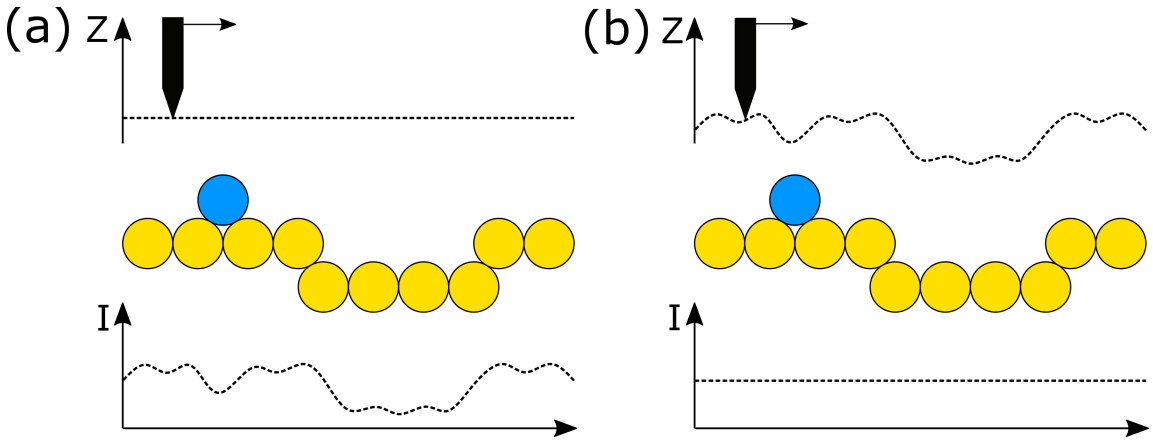

Figure 2.5: Modes of Operation of an STM. (a) Constant height mode, tip remains at constant Z, while I varies with the heights of surface features. (b) Constant current mode, I is fixed and the Z position of the tip fluctuates using a feedback loop to maintain the current as it moves across surface features.

2.1.2 Scanning Tunnelling Spectroscopy

STM can be used to probe the local electronic structure of surface features by performing Scanning Tunnelling Spectroscopy (STS). By differentiating the tunnel current I, defined in equation 2.10, with respect to voltage V, you can obtain the density of states at the surface,

$$\frac{dI(V)}{dV} \propto \rho_s(E_F - eV) \tag{2.11}$$

where $\rho s(E)$ is the density of states at the surface. This is done by holding the tip in a fixed position above a point of interest on the surface. The bias is then swept across a range of values and the current is measured. $\frac{dI}{dV}$ can be measured indirectly, by measuring $I(V)$ and taking the differential of the resultant curve, however spectra acquired in this manner are often exhibit higher levels of noise. $\frac{dI}{dV}$ can also be obtained directly by applying a small sinusoidal oscillation, dV, to

be the bias, which returns an oscillating current signal, dI. The current modulation is recorded using a lock-in amplifier, with the bias modulation used as a reference. When the bias is swept across a range of voltages, an STS spectrum can be acquired. STS spectra will show peaks at the voltages that correspond to filled and empty states in the surface and any deposited species [66].

2.1.3 Kelvin Probe Force Microscopy

Kelvin probe force microscopy (KPFM) is technique related to atomic force microscopy (AFM), that can be used to measure local contact potential difference (LCPD) between the tip and the sample. It can be used to study the electronic properties of materials. This can be done on a macroscopic level, to find the averaged LCPD over the whole sample, using methods first developed by Lord Kelvin in 1898 [67], it can also probe local environments on the scale of nanometers, to take a single measurement.

To do this experimentally, a small oscillation must be applied to the tip, which in turn generates an AC current. This AC current may then be cancelled out by applying a DC voltage, which corresponds to the LCPD between the tip and the sample. Assuming that the material of the tip is known, then the work function of the tip is also known and can be used as a reference. The unknown work function of the sample may then be calculated using the work function of the tip and the LCPD [68] [69].

Contact potential difference (V_{CPD}) may be defined by,

$$V_{CPD} = V_{dc} = \frac{|\phi_t - \phi_s|}{e} \tag{2.12}$$

where ϕ_t and ϕ_s are the work functions of the tip and the sample respectively. V_{dc} is an external DC voltage put across the tip and sample to nullify V_{CPD}. When the tip and sample are in close proximity, there is a large electrostatic force between them, which is proportional to the difference between their work functions. Current will flow from the lower work function material to the higher to align their Fermi levels, and hence, misalign their vacuum levels. This is demonstrated in Figure 2.6a, where ϕ_t, ϕ_s and V_{CPD} are shown. The effect of the DC voltage is such that the vacuum levels realign and the V_{CPD} is counteracted.

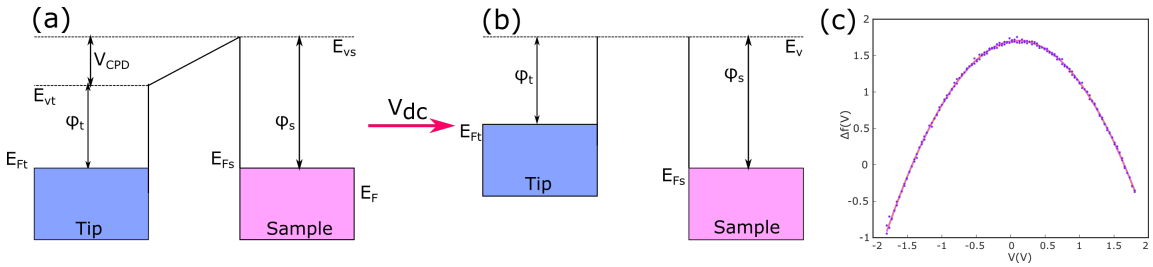

Figure 2.6: Diagrams showing the energy levels in the tip and sample during KPFM. (a) Energy levels showing equated Fermi levels (E_{ft} and E_{fs}) and the LCPD (V_{CPD}) between the tip and sample. (b) DC voltage compensates for LCPD and shifts energies of Fermi levels to remove it. Reproduced from [69]

The product of this is a spectrum in the form of a parabola, see Figure 2.6c, that comes to a peak at the point where the frequency shift is minimised. The top of the parabola is that point at which the electrostatic interactions between the tip and the surface, caused by the difference in work function, have been minimised or are at zero. The frequency shift can be used as a measure of the strength of the interaction between the tip and the surface, if the peak of the parabola shifts to a more negative value, the attractive interaction is stronger, whereas if there is a more positive frequency shift, the interaction is more repulsive. By sweeping the bias the interaction across a range of values can be measured, coming to a peak where the forces equate. Where the CPD is zero no bias is required to align the Vacuum levels of the tip and the sample as they should already be aligned, hence a gold tip and a gold surface theoretically have a CPD of 0. Experimentally this value does not always come out as zero, due to other factors effecting the CPD, such as the shape of the tip and local surface structures.

2.2 Ultra-high Vacuum

STM experiments are often carried out under ultra-high Vacuum (UHV) conditions, which is defined as pressures of $< 10^{-9}$ mbar. This is achieved by employing steel chambers where the vacuum is maintained by a range of pumps. Rotary and scroll pumps give a pressure of $\approx 10^{-3}$ mbar, turbo-molecular pumps take the pressure down to $\approx 10^{-8}$ mbar. Ion pumps are used to achieve pressures between 10^{-9} and 10^{-12} mbar (following the baking of the system to remove water). A UHV environment is crucial as these experiments require sample surfaces to be clean and free of

contaminants, to ensure successful imaging of only the intended species. Contaminant species may also interact, and potentially react with the deposited molecules to be studied, which compromises the acquired data. Under atmospheric pressure surfaces may be covered with contaminants in less than one second, however under UHV they can remain contaminant free for hours to days at a time.

2.2.1 Surface Preparation

The surface employed in this thesis is the Au(111) surface. Two different forms were used, a single crystal and a thin film on mica, both exhibit the expected (111) morphology for gold. The single crystal consists of a button heater mounted behind a single crystal of the desired surface, in this case Au(111), approximately 1 mm thick. The crystal is attached to the heater with a tantalum spider. The gold on mica is formed by growth of the thin film onto the mica to a thickness of approximately 200 nm. The sample plate is then constructed using a piece of gold on mica, layered over a piece of low resistivity silicon wafer which is clamped onto the sample plate.

Crystal planes can be described using miller indices, a set of three integer numbers, denoted by the letters h, k and l. Crystals can be cleaved along these planes such that the top layer has a specific unit cell. When cleaved along the (111) plane the ideal surface has the hexagonally close-packed (HCP) unit cell. A diagram of this can be seen in Figure 2.7. The Au(111) surface is unique, compared to other coinage metals, in that it exhibits a $22 \times \sqrt{3}$ surface reconstruction. The herringbone reconstruction causes 23 surface atoms to compress into the space of 22 lattice spacings. This gives the characteristic corrugated patterning of the Au(111) surface, known as the herringbone reconstruction, an example of this can be seen in Figure 2.7. The herringbone reconstruction has alternating regions of FCC and hexagonal close packed (HCP). The bulk of the crystal remains in the FCC lattice.

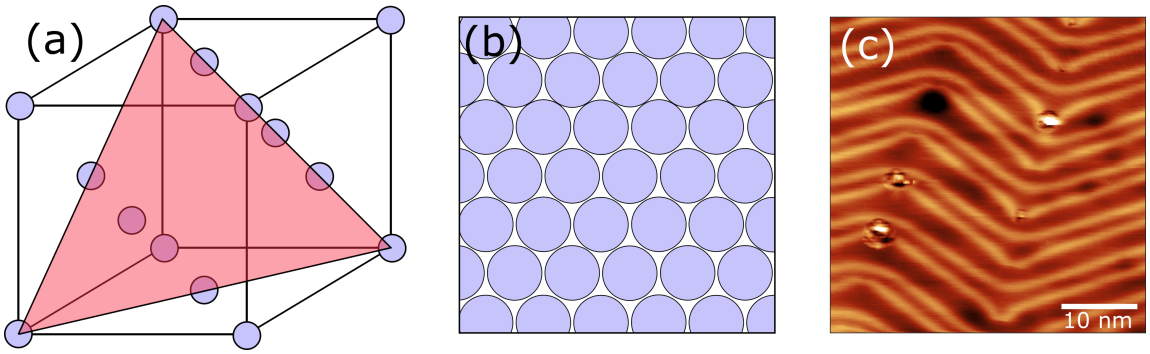

Figure 2.7: (a) FCC Unit cell with the (111) crystal plane indicated. (b) Model of the (111) surface. (c) STM image of the Au(111) surface, showing the characteristic herringbone reconstruction. Bias = -1.4 V, Setpoint = 20 pA

Before performing experiments the surface must be thoroughly cleaned such that there are large, atomically flat terraces, free of any debris. To remove any contaminants, or remnants of previous experiments, the sample is first bombarded with argon ions in a process known as sputtering. Ar gas is leaked into the system until a pressure of 5×10^{-5} is reached. They are then ionised to Ar^+ and accelerated towards the sample with the impact removing any contaminating species that might be present. This leaves the surface rough and cratered. To reform and smooth the surface to create the large flat terraces the sample must then be heated to high temperatures, $500°C$. This is done by passing a current across a piece of low resistivity silicon, to heat the Au(111) on mica sample plate or by using the button heating in the case of the single crystal sample plate. These two steps are performed in cycles until the surface exhibits the expected reconstruction

2.2.2 Molecule Deposition

The molecules studied within this work were deposited onto the surface using thermal evaporation. The molecules, in the form of a powder, are placed in Knudsen cell. The Knudsen cell consists of a metal or ceramic crucible which is heated by a metal coil. Current is passed through the coil to heat the crucible. The heat causes the molecules to sublime into the gas phase and are then free to diffuse across the UHV chamber before impinging on the sample.

2.3 Synchrotron Based Techniques

A synchrotron is a particle accelerator which can be utilised to produce a range of polarised electromagnetic radiation which gives a large range of frequencies, of which specific ones may be selected for different experiments. Synchrotron radiation is produced by firing an electron beam into a vacuum. Bending magnets are used to direct the beam around a large polygon. The bending magnet causes the beam to loose energy, in the form of photons. The photons can be directed to beamline hutches tangential to the polygon, where they enter the system to be studied. The energy of the photons within the beam can be controlled by the use of 'undulator' and 'wiggler' magnets.

Undulators and wigglers are insertion devices within the beamline to cause a large change in the acceleration of the beam, causing it to emit energy. Wigglers consist of arrays of magnets of alternating poles. The first magnet bends the beam away from its path, the middle magnet is a more powerful magnet and returns the beam the other way. The final magnet of the trio brings the beam back onto its course. This device is used to generate shorter wavelengths, while preserving the broad range of frequencies also generated. An undulator functions in a similar manner, however it uses lower magnetic field strengths and the radiation emitted is allowed to interfere, constructively or destructively. Undulators are particularly useful in this context as they can be set to give radiation at a particular photon energy.

2.3.1 Low Energy Electron Diffraction

Low energy electron diffraction (LEED) is a technique used for the determination of surface structure. Although LEED does not require synchrotron radiation, in the thesis all LEED measurements were taken alongside synchrotron studies and as the diffraction theory underlying LEED is similar to other synchrontron techniques it has been introduced here. LEED may be used to determine the unit cell of a crystalline surface, and then to find the unit cell of the adsorbate species relative to the unit cell of the surface. This may be used to determine whether there is a preferential adsorption site.

LEED, similar to X-ray diffraction, follows Braggs Law [70], however in the case of LEED, Braggs law may be written,

$$n\lambda = asin\theta \tag{2.13}$$

where λ is the wavelength of the electrons, a is the atomic spacing, θ is the angle between the incident beam and the reflected beam and n is an integer representing the diffraction order. In LEED, the reflected beams are directed at a fluorescent screen, and appear as spots which represent the reciprocal lattice of the crystalline surface. In Figure 2.8 the difference between LEED and X-ray diffraction is depicted, with the components of their respective Bragg equations labelled.

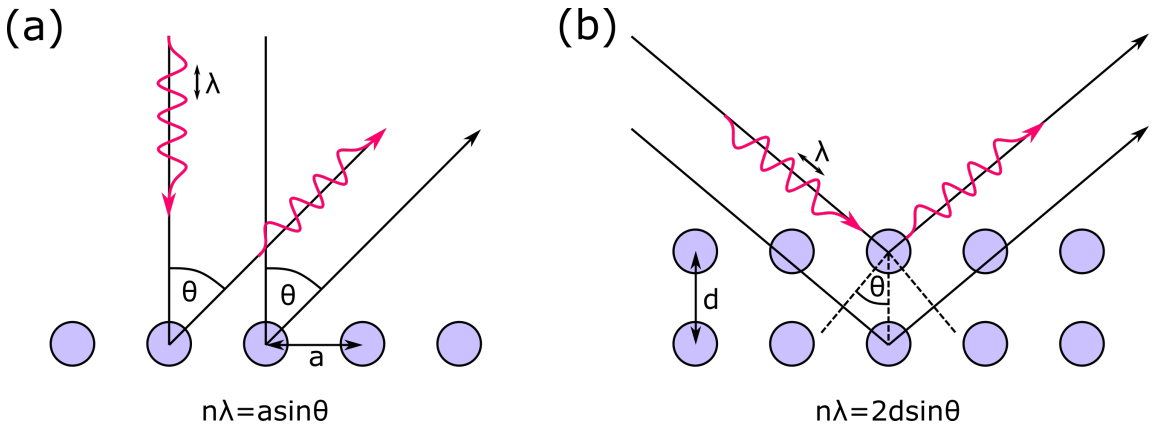

Figure 2.8: Side by side comparison of electron diffraction and X-ray diffraction. (a) Electron diffraction; incident electrons, with wavelength λ, are at a normal to the surface and are reflected at an angle θ to the surface. (b) X-ray diffraction

Both LEED and X-ray diffraction require a samples that exhibit a reasonable amount of long-range order, LEED is a surface sensitive technique and may be used to study adsorbed species and X-ray diffraction is predominantly used to find the bulk structure. Overlayer adsorbates must posses long-range order to give a defined LEED pattern, amorphous overlayers do not have defined LEED patterns.

A LEED measurement is taken by positioning the sample such that its surface is oriented towards the electron beam and the reflected waves are observed. The position of the sample is not changed during the measurement process but the energy of the beam may be varied (between 5 and 200 eV in the work described here). The reflected waves are directed towards the fluorescent screen to produce the LEED pattern. This is contrary to X-ray diffraction, where the position of the sample is varied while the wavelength is kept constant. The LEED pattern is then used to measure the dimensions of the unit cell of the surface. The spots on the LEED pattern represent a to-scale version of the reciprocal lattice of the surface atoms. This can be extended to adsorbate species, a LEED pattern may be measured after molecules have ben deposited on the surface, and provided

that they form a regular lattice, a LEED pattern may be measured for this overlayer. The LEED pattern for the overlayer will also represent the lattice of the adsorbed molecules in reciprocal space, meaning their unit cell may be calculated. Using the pattern from the clean surface and the pattern for the overlayer, the position of the overlayer relative to the surface atoms may be calculated.

2.3.2 X-ray Photoelectron Spectroscopy

X-ray Photoelectron spectroscopy (XPS) is a technique commonly used for identifying elemental components of a material, or surface, and their chemical environment. As suggested by its name, XPS requires an X-ray source, which may be lab-based (e.g. Al K-alpha), or from a synchrotron. XPS utilises the photoelectric effect, in which atoms may emit photoelectrons when hit with radiation. [71]

To record a spectrum, a beam of photons, with a known energy, hv (where v is the photon frequency) are directed at a sample. The incident photons transfer their energy to electrons found in the core levels of surface atoms. When the energy transferred by the photon is higher than the binding energy (BE) of the electron, the electron may be ejected. The binding energy describes the amount of energy required to remove an electron from one of the core levels of the atom, it can be described using

$$E_{BE} = E_{photon} - (E_{KE} + \phi) \tag{2.14}$$

where E_{BE} is the binding energy of the electron, E_{photon} is the energy of the photon, E_{KE} is the kinetic energy of the emitted electron and ϕ is the work function for the specific photoelectron detector. A diagram of this process can be seen in Figure 2.9. The core level energies are unique for each element meaning XPS can be used to characterise the composition of an unknown sample. A spectrum may be recorded and then compared to a table of reference peaks.

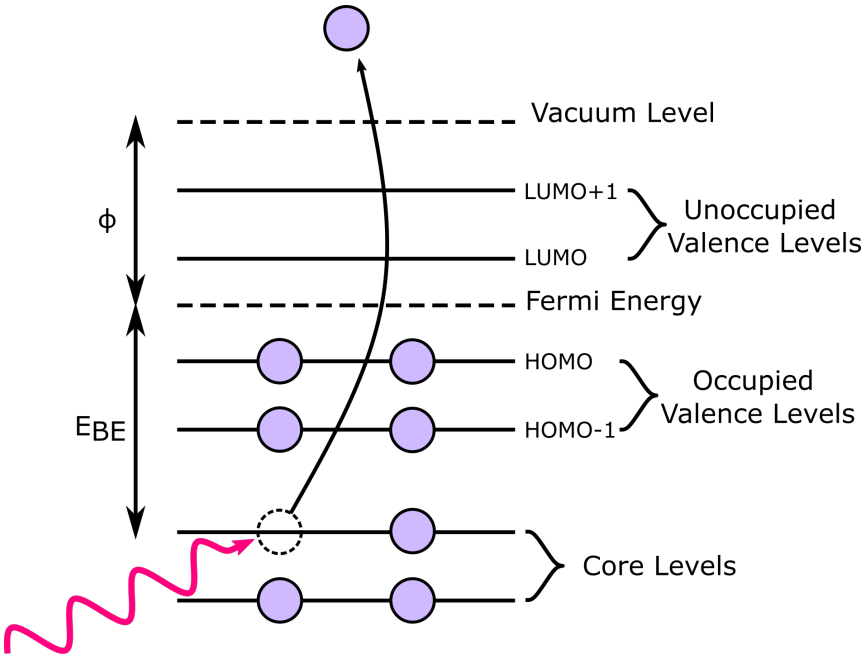

Figure 2.9: Diagram of photoelectron being ejected from the core levels of an atom into the vacuum. A photon (pink) penetrates the core levels of the atom, ejecting an electron and leaving behind a hole. The binding energy E_{BE} can be calculated using the photon energy, the kinetic energy of the electron and the work function ϕ

XPS is not only able to give the identity of the elements present, but also information about their chemical environment. [72] Energy levels in atoms are sensitive to neighbouring atoms, causing their binding energy to shift. The direction and magnitude of the shift varies depending on the neighbouring species. This can be demonstrated using the example of ethyl trifluoroacetate ($F_3CO_2C_2H_5$), which has four carbon atoms, each in a different chemical environment. Therefore the C1s spectrum, seen in Figure 2.10, shows four separate peaks. The spectrum in Figure 2.10 shows the amount the peaks deviate from the expected BE of 294 eV. The first peak, belonging to the CH_3 group is at 0, with the remaining three peaks shifted relative to it. These remaining peaks are attached to increasingly electronegative atoms, causing the BE of these carbon atoms to increase, with the tri-fluorinated carbon having the largest shift in BE.

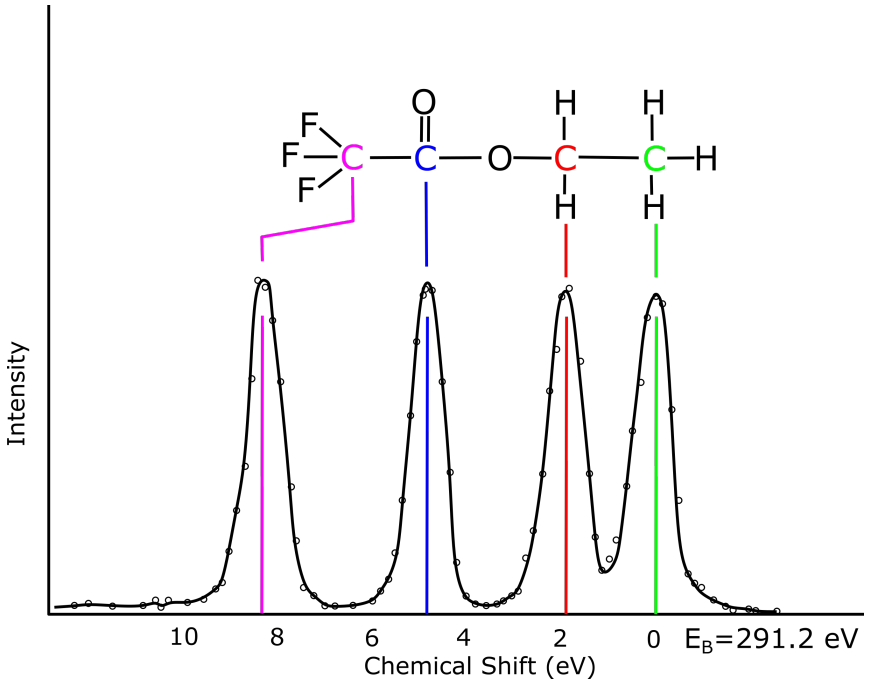

Figure 2.10: Example of how chemical shifts differ with chemical environment in XPS measurements. Ethyl trifluoroacetate has four different carbon environments, each producing a unique signal in an XPS spectrum, due to their different binding energies. Reproduced from [73]

There are a number of other effects that are visible in XPS spectra. Peaks due to Auger electrons, shake-up and shake-off features are often present in spectra. These peaks are caused by the re-arrangement of the electrons remaining in the atom to stabilise the hole left in the core when the photoelectron is emitted. Auger peaks are caused by an electron from an upper level falling into a hole in the core level. When this electron falls into the core level, energy is released, causing an electron from the upper level to be emitted. Shake up features are caused by the outgoing photoelectron losing a small amount of energy, which then allows an electron within a high-lying occupied state to be promoted to an empty state (HOMO to LUMO). Shake-off features are similar, with the promoted electron emitted into the vacuum.

The signals acquired during an XPS experiment are predominantly from atoms in the top layers of the sample, in any deposited species and in the surface layers of the bulk. This is due to the low mean free path of the photoelectrons. However, this also means that the total signal may be reduced as the electrons travel between the sample and the detector, to reduce this effect XPS experiments are performed in UHV.

2.3.3 Near Edge X-ray Absorption Fine Structure

Contrary to XPS, which provides information of the core orbitals of atoms, near-edge X-ray absorption fine structure (NEXAFS) is a technique used to probe the unoccupied frontier orbitals of atoms and molecules. From it, information about the oxidation state of molecules and orientation of the unoccupied orbitals relative to surface may be obtained.

In XPS an electron is ejected from the core orbitals of the atoms, in NEXAFS an electron is promoted from the core orbitals to the low-lying unoccupied orbitals of the atom, this process can be seen in Figure 2.11. Both processes require an X-ray source, XPS requires high energy X-rays to eject the core electron, NEXAFS requires the X-rays energy to be tuned such that it may be promoted but not fully removed.

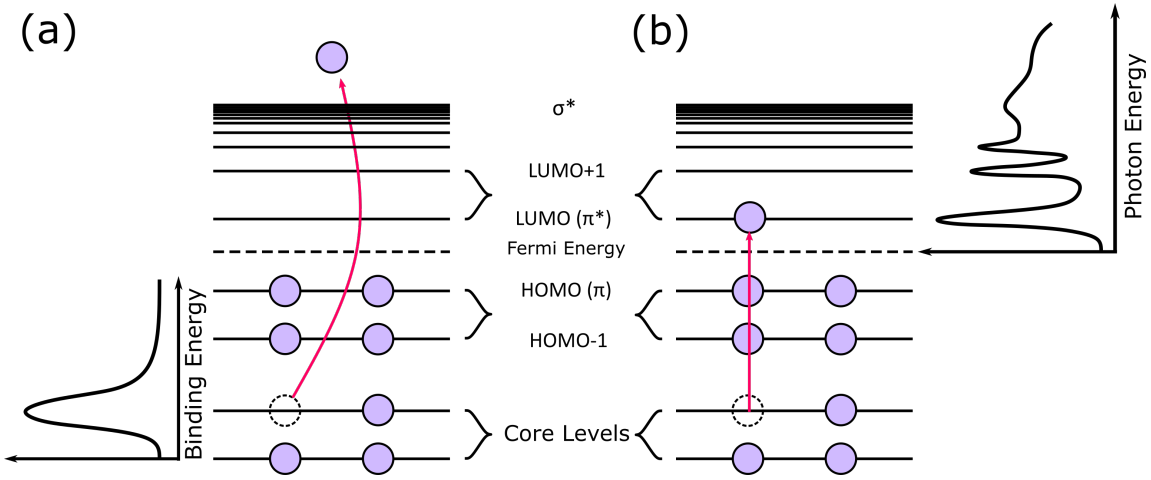

Figure 2.11: Comparison of XPS with NEXAFS. (a) Diagram of photoelectron being ejected from the core levels of an atom into the vacuum, which occurs during XPS. (b) Diagram of an electron being promoted from the core levels to an unoccupied level of a molecule. The peaks present in the NEXAFS spectrum correspond to the unoccupied levels.

When taking a NEXAFS spectrum of an isolated single atom the result is very different to that of a pair of bonding atoms in a molecule. The single atom would be expected to give a predictable spectrum showing peaks at the energies of the transition from the core levels to the unoccupied levels. It will also show the transition from the core levels into the continuum of states, where each state does not have a discrete energy level, this appears on the spectrum as a broad 'tail'.

When looking at a bonded atoms the orbitals of the two atoms combine using the linear combination of atomic orbital (LCAO) theory to give a set of MOs. These molecular orbitals include the

unoccupied anti-bonding states, including π^* and σ^* states. The spectrum for bonding atoms will include two new features corresponding to these orbitals. The π^*, which is likely to contribute to the LUMO, will be the lowest energy transition and appear on the left hand side of the spectrum. The σ^* orbital resides in the continuum of states and will appear as a broad peak in the higher energy, right hand side.

2.3.4 Normal Incidence X-ray Standing Wave

Normal incidence X-ray standing wave (NIXSW) is a surface sensitive technique used for determining the structure of molecules on a crystalline surface. NIXSW is chemically specific, meaning the position of individual atoms, with a specific electronic signature, within an adsorbed molecule may be determined. This method of analysis utilises XPS to determine the chemically specific environments, and then X-ray diffraction properties of the crystal planes of the surface to determine the positions of the atoms, without requiring the over-layer to display long-range order in all directions. By directing X-rays at a sample and then varying the wavelength, a signal composed of the reflected X-rays will be produced, which is specific to the chemical environment and position of atoms above the surface. NIXSW experiments generally require synchrotron radiation to achieve the high energy and precisely varied wavelengths of X-rays required for these measurements. [74] [75]

The fundamental principle of NIXSW is that an X-ray standing wave, perpendicular to a set of bulk crystal planes, may be generated. The incident X-rays, with wavelength λ, must meet the Bragg condition,

$$n\lambda = 2d\sin\theta \tag{2.15}$$

where n is a positive integer, d is the interplanar spacing and θ is the angle of incidence, which, for NIXSW, is 90°. In order to meet the Bragg condition the X-rays must be high energy because the interplanar distances are very small, typically 2-3 Å. The wavefield of this standing wave extends outwards from the surface, such that the X-ray absorption sustained by any adsorbates present is effected by the specific position within the period of the standing wave. To understand fully the information collected from this technique there is another factor to consider. Upon entering the crystal the incident X-ray intensity may become attenuated, due to multiple scattering events, reducing the the depth it penetrates the crystal. Because of this there is only a finite range

of wavelengths that may satisfy Equation 2.13, and thus, meet the Bragg condition. This can be visualised by measuring a Darwin reflectivity curve, which measures the reflectivity with wavelength (2.12b), the curve peaks into a flat top over the range where reflectivity is at its maximum. In 2.12a it can be seen that between standing waves, E_1 (red) and E_2 (pink), there is phase change of π to the standing wave.

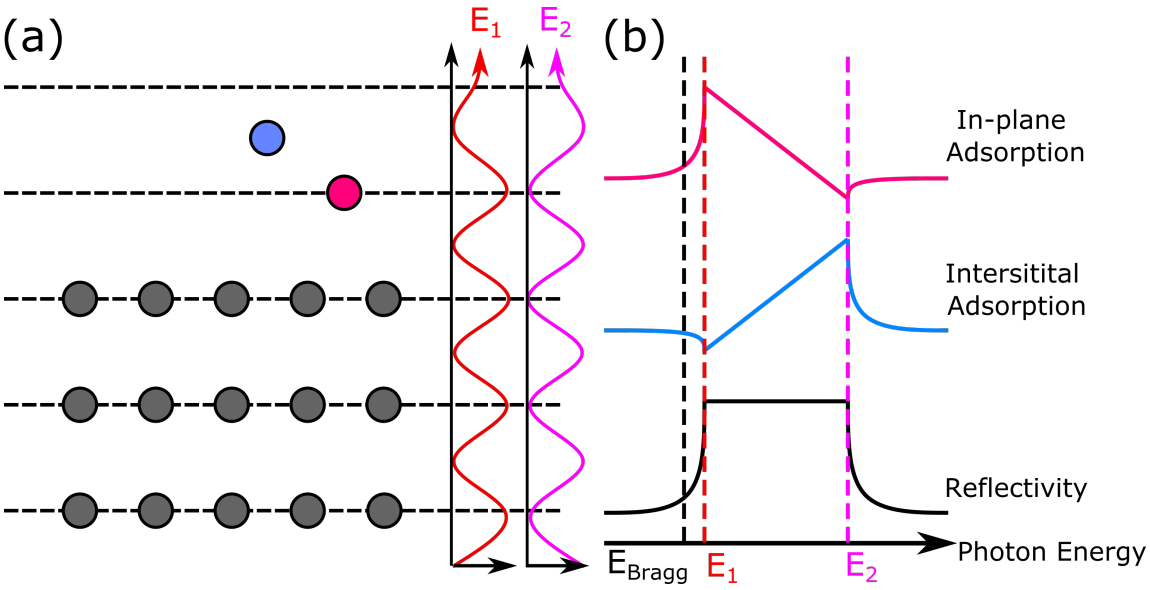

Figure 2.12: (a) Reflecting planes of a crystal surface with bulk atoms shown in grey. Two adsorbing atoms (blue and pink) are shown at different positions between the crystal planes. Standing waves at E_1 and E_2 are shown in red and pink. E1 has nodes located at each reflecting plane. E_2 has anti-nodes located at the reflecting planes. (b) Reflectivity curve for the bulk surface (black), absorption profile for the pink atom (pink), absorption profile for the blue atom (blue), across a range of energies with E_1 and E_2 marked in red and pink respectively. Reproduced from [74]

By depositing molecules on the surface the shape of the absorption profile will change, depending on their position. This is shown in Figure 2.12. The surface atoms (grey) sit along reflecting planes, which extend into the crystal, and also into the vacuum. Incident X-rays of energy E_1 are used to generate a standing wave, with nodes at each of the reflecting planes (red). During the experiment the energy is swept from the lower energy end of the reflectivity curve (E_1) to the higher end (E_2) (magenta).

Absorption profiles are measured for each species present on the surface. For the pink atom that lays directly on one of the reflecting planes, at E_1, where the standing wave is at a node it will show maximum X-ray intensity as it has maximum absorption at this point. As the energy

is swept towards E_2 the intensity gradually decreases until it reaches a minimum at E_2, at which point the phase of the wave will have changed by π, and the atom is positioned at an anti-node. The opposite is true for the blue atom, which sits half way between two planes. At E_1 it is at an anti-node, and its X-ray absorption is at a minimum. As the energy is swept, its absorption increases and reaches a maximum at E_2 where it is at a node. This shows that atoms at different heights between the planes produce unique absorption profiles. From these profiles NIXSW can be used to determine the heights and adsorptions geometries of the adsorbed atoms.

2.3.5 Basic Theory

To fully engage with the results of NIXSW experiments, and calculate absorption geometries, the underlying theory must be appreciated. Firstly, the intensity of the standing wave, I, may be calculated using,

$$I = \left| 1 + \frac{E_r}{E_0} \exp\left(-2\pi i z \mathbf{H}.\mathbf{r}\right) \right|^2 \tag{2.16}$$

where E_0 and E_r are the incident and reflected wave amplitudes, respectively, and $\mathbf{H}$ is the reciprocal lattice vector of the Bragg reflection being studied, and $\mathbf{r}$ is a real-space vector giving the position from which the intensity is measured. By taking the scalar product of $\mathbf{r}$ and $\mathbf{H}$, this equation can become,

$$I = \left| 1 + \frac{E_r}{E_0} \exp\left(-\frac{2\pi i z}{d}\right) \right|^2 \tag{2.17}$$

which has be written in terms of d, the layer spacing of the sample and z, the perpendicular distance above the sample. The wave amplitudes, E_0 and E_r, can be used to define reflectivity, R,

$$\frac{E_r}{E_0} = \sqrt{R} e^{i\phi}, \tag{2.18}$$

where ϕ is a phase factor which varies by π over the reflectivity range. This allows Equation 2.16 to be re-written as,

$$I = \left| 1 + \sqrt{R} \exp\left(i\phi - \frac{2\pi i z}{d}\right) \right|^2, \tag{2.19}$$

and then evaluating the modulus squared,

$$I = 1 + R + 2\sqrt{R}\cos\left(\phi - \frac{2\pi z}{d}\right). \tag{2.20}$$

This assumes that there is only one type of adsorbing atom in a single adsorption site, z, present on the surface. However, this model is too simplistic to account for the complexity of the type of experiments being performed.

2.3.6 Coherent Fractions and Coherent Positions

A more useful and realistic treatment is assuming that the adsorbing atoms have a position, z, distributed with probability $f(z)$, over a range, dz, defined by,

$$\int_0^d f(z)dz = 1. \tag{2.21}$$

This takes into account that atoms can positioned in more than one adsorption site above the surface, as well accounting for thermal vibrations. From this, the standing wave intensity can be calculated by,

$$I = 1 + R + 2\sqrt{R}\int_0^d f(z)\cos\left(\phi - \frac{2\pi z}{d}\right)dz. \tag{2.22}$$

By evalcuating this integral, the standing wave intensity can also be written as,

$$I = 1 + R + 2C_f\sqrt{R}\cos\left(\phi - 2\pi C_p\right), \tag{2.23}$$

introducing two new terms, the coherent fraction, C_f, and the coherent position. C_p. These are structural fitting parameters which describe the fraction of atoms at a particular position, and are the values which are revealed by analysing the experimental data. Relating these parameters to the actual distribution of positions gives

$$C_f \exp\left(2\pi i C_p\right) = \int_0^d f(z)\exp\left(\frac{2\pi i z}{d}\right)dz. \tag{2.24}$$

Coherent fraction and position values are a combination of the range of adsorption sites present on the surface. The X-ray absorption signal from each different chemical environment can be plotted

and Equation 2.23 can be used to fit an absorption profile to the data, from which the coherent fraction and position values can be extracted. Models of different possible absorption geometries are then evaluated using Equation 1.23 to try and obtain C_f and C_p values measured from the data. The idealised case, where there is only one adsorption geometry, the coherent fraction will be 1 and the coherent position is the z position of the atoms divided by the layer spacing. However, the more likely scenario is that there will be multiple adsorption sites across the surface. This can be visualised using the diagrams in Figure 2.13

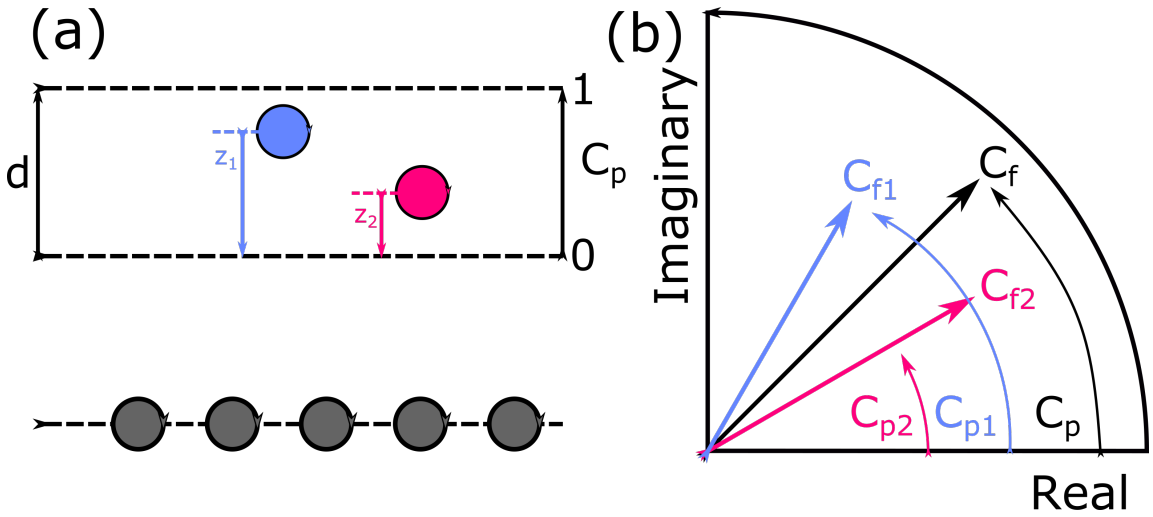

Figure 2.13: (a) Two atoms adsorbed at different heights on the surface (z_1 and z_2). Layer spacing, d shown on the left and corresponding C_p value shown on the right. (b) Argand diagram plotting C_f and C_p values of atoms in (a). Blue and pink vectors represent the position and amount of each atom present in (a). Black vector shows the sum of the pink and blue vectors, positioned at the polar coordinates of the C_f and C_p values that would be produced by this experiment.

The two atoms in 2.13a different z positions, z_1 (blue) and z_2 (pink) between the reflecting planes. The fractional occupation of these two sites can be described by C_{f1} and C_{f2}, which in this case is $C_{f1} = C_{f2} = 0.5$. The position of each atom may be described by C_{p1} and C_{p2}, which is its z position divided by the layer spacing, d. It can be seen in 2.13a that there are two axes, one showing the layer spacing and one showing the equivalent coherent position. These values may be plotted in complex space as vectors on an Argand diagram, where C_f and C_p correspond to r and θ respectively. This can be seen in 2.13b, where C_{f1} and C_{p1} are represented by a blue arrow and C_{f2} and C_{p2} are represented by a pink arrow. Their sum, represented by a black arrow, would be

the measured C_f and C_p values. This can be calculated using,

$$C_f \exp\left(2\pi i C_p\right) = C_{f1} \exp\left(\frac{2\pi i z_1}{d}\right) + C_{f2} \exp\left(\frac{2\pi i z_1}{d}\right) = C_{f1} \exp\left(2\pi i C_{p1}\right) + C_{f2} \exp\left(2\pi i C_{p2}\right) \tag{2.25}$$

The same treatment may be given in more complex systems where there might be 3 or more z positions, all with nonequivalent fractions of atoms.

2.3.7 Measuring and Analysing Data

Measuring X-ray absorption directly to obtain these measurements is challenging, however it may be overcome by utilising an XPS-type set-up to generate photoelectrons from the core levels of atoms. The flux of these photoelectrons may then be measured to provide a value for X-ray absorption. The advantage of this method is that by measuring the photoelectrons binding energy it is possible to determine the binding site for atoms in specific chemical environments.

2.3.8 Reflecting Planes

Obtaining the heights of the adsorbed atoms is performed by using the same reflecting plane as the orientation of the surface. However, there are multiple different planes which can be used, each giving a different piece of information about the location of the atoms. By combining information from each plane, exact adsorption geometries may be calculated by a process of triangulation. For example, when using the (111) surface, reflecting from the (111) plane will give the heights of the atoms relative to the projected planes. If, instead, reflections from the (-111) were measured then the coherent position value could be relative to the lateral position between the planes instead. This is shown in Figure 2.14.

Figure 2.14a shows the (111) surface and reflecting planes can be seen, with the adsorbed atoms located between the horizontal planes. 2.14b shows the (-111) surface and the (-111) reflecting planes, adsorbed atoms lateral position will be between these planes.

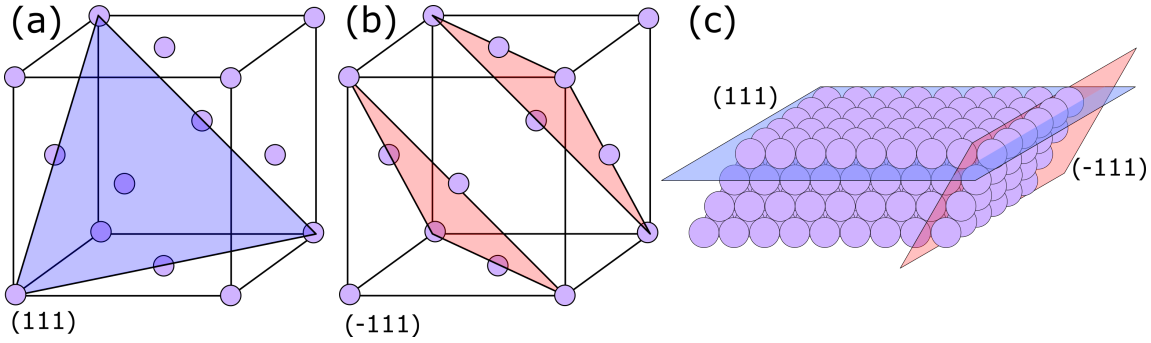

Figure 2.14: (a) Unit cell for (111) crystal plane. (b) Unit cell for the (-111) crystal plane. (c) Example (111) crystal with the bisecting (111) plane shown in blue and the bisecting (-111) plane shown in pink.

2.4 Summary

In this chapter the techniques (STM, STS, KPFM, LEED, XPS, NEXAFS and NIXSW) used throughout the remainder of this thesis have been explained and summarised. The topic of UHV has been introduced, alongside the procedures required to operate within it. The Au(111) surface, which is used throughout this work has been described. These methods are used to characterise the systems presented here on in, for their structural, chemical and electronic properties.

Chapter 3

Synthesis of Porphyrins

3.1 Introduction

In this chapter the synthesis of the porphyrin products studied in this thesis is presented. Two methods of asymmetric porphyrin synthesis are presented alongside a single method of symmetric poprhyrin synthesis. The products of each reaction have been characterised using nuclear magnetic resonance (NMR) and mass spectrometery.

3.1.1 Porphyrins

Porphyrins are omnipresent molecules, commonly found in nature, they have been extracted, synthesised and studied since the late 19^{th} century. They are present in a number of biological systems such as, heme, found in red blood cells, chlorophylls, used as part of process of photosynthesis, and in vitamin B12, a crucial component of the human metabolism [76] [77]. There are a broad range of potential applications for these molecules, in semiconductor devices [78], chiral sensors [79], molecular memory storage [80], cancer therapies [81] and alternative energy sources [82].

The name 'Porphyrin' comes from the ancient Greek word, *porphura*, which means purple. This describes one of the most characteristic features of porphyrins, which is their brilliant purple colour. Porphyrin is a macrocycle, consisting of four pyrrole-type rings, linked by bridging methine ($=CH_2-$) groups. Its appearance is as a lustrous deep purple crystalline solid, however, with the addition of substituents, its colour may vary towards red/brown hues [83]. The macrocycle has a

large conjugated 18 π electron system, which causes intense absorption bands in the visible range. The specific transitions occur at between 400-450 nm for the $\pi - \pi^*$ transition and 500-700 nm for the Q bands. These transitions result in the characteristically intensely coloured compounds. In their most basic form, porphin, (seen in Figure 3.1a) no substituents are present, and the central cavity is empty. However, in order to alter the electronic or chemical properties of porphyrins, they may be functionalised in one of three ways (3.1b-d).

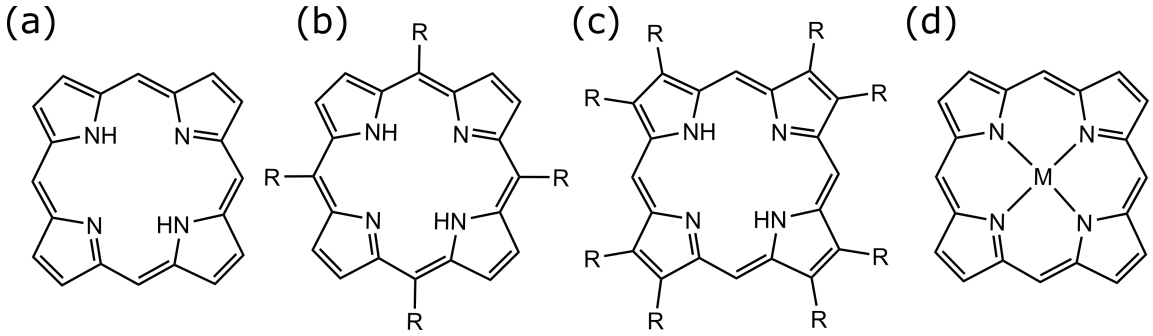

Figure 3.1: (a) The structure of Porphin, the simplest of of the family of porphyrins. (b) Functionalisation at the *meso*-positions ($\alpha, \beta, \gamma, \delta$). (c) Functionalisation at the β-pyrrolic carbons. (d) Functionalisation *via* metalation.

Figure 3.1b shows functionalisation at the *meso*-positions of the core, numbered 5,10,15,20- in the IUPAC numbering system, or labeled $\alpha, \beta, \gamma, \delta$ in the Fischer system [84]. The second method of adding peripheral functionality is to substitute at the β-pyrrolic carbons, IUPAC numbers; 2,3,7,8,12,13,17,18 and Fischer numbers; 1-8 (3.1c). The final method, is by capturing a metal atom in the central cavity of the molecule by forming coordinate bonds with the nitrogen atoms (3.1d).

3.2 Synthetic Routes to Porphyrins

The first synthesis of a porphyrin took place in 1929, by H. Fischer, who reported the multi-step synthesis of a number of structures, including protoporphyrin IX and the free base porphyrin of hemin [85], for which he won a Nobel Prize in 1930. There are many different methods to synthesise porphyrins, either by combining pyrrole with an aldehyde and acid catalyst, or by building step-wise from dipyrromethanes and aldehydes. Between 1935 and 1941 P. Rothmund reported a number of 'one-pot' syntheses of porphyrins [86] [87]. In 1936 he reported the structure of porphin, and also

the structures of 5 *meso*-substituted porphyrins. [88] His reaction required pyrrole to be heated to 90-220 °C with an aldehyde inside a sealed tube. Then, in 1939 the formation of Tetraphenyl porphyrin (TPP) was achieved using this method, which can be see in Figure 3.2 [89].

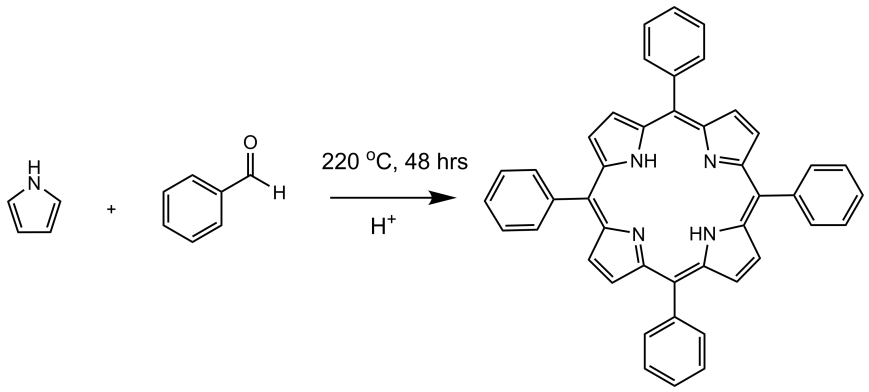

Figure 3.2: The Rothmund Synthesis of Tetraphenyl porphyrin, using pyrrole, benzaldehyde and an acid catalyst.

This method was progressed by A. D. Alder and F. R. Longo, whose synthesis improved upon the 11% yield to values in excess of 20%. In addition, they were able to reduce both the temperature, to 150°, and duration of the reaction, to 24 hours. Their method used an acetic acid catalyst but produced a tar-like impurity that was challenging to remove. This method can be seen in Figure 3.3 [90]

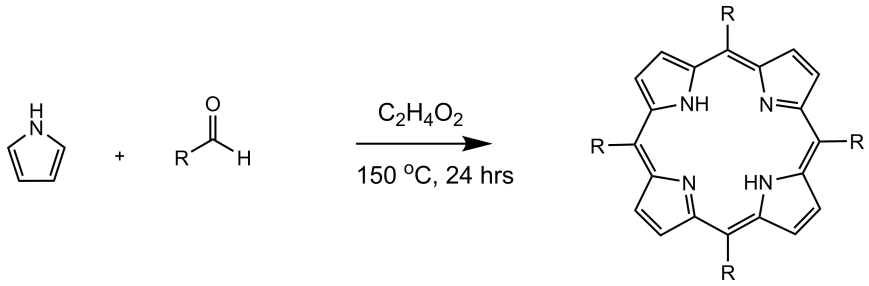

Figure 3.3: The Alder-Longo Synthesis of a *meso*-substituted porphyrin, using pyrrole, benzaldehyde and an acetic acid catalyst.

Porphyrins may now be made under relatively mild, equilibrium conditions and in good yields, using a reaction developed by J. Lindsey. It requires an acid catalyst such as trifluoroacetic acid (TFA) and an oxidant, such as 2,3-dichloro-5,6-dicyanobenzoquinone (DDQ). The acid forms a porphorinogen, which is a fully protonated porphyrin, which is then oxidised to the final porphyrin

product. [91]

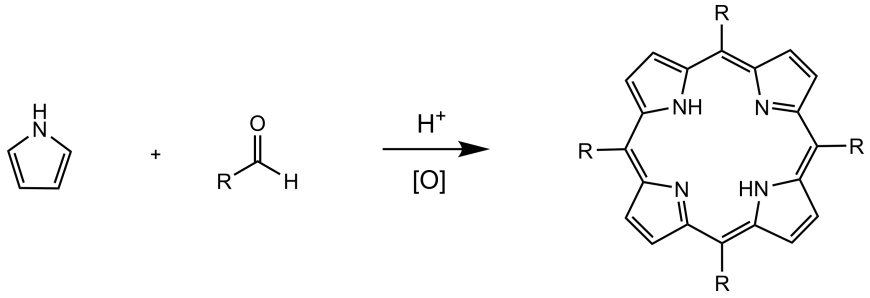

Figure 3.4: The Lindsey Synthesis of a *meso*-substituted porphyrin, using pyrrole and benzaldehyde, with an acid catalyst followed by an oxidant

The previously described methods are useful when then product required has the same functional groups at each *meso*-position. The following method, developed by S. F. MacDonald, may be used to make porphyrins with multiple different peripheral functionalities, including asymmetric porphyrins. This reaction is between a dipyrromethane and an aldehyde under acidic conditions and may be carried out at room temperature [92]. This reaction can be customised to produce porphyrins with a number of different functionalities. It can be seen in Figure 3.5 that there are 3 possible positions to introduce new functional groups, R_1 and R_2. This reaction has very low yields, in the region of $< 10\%$.

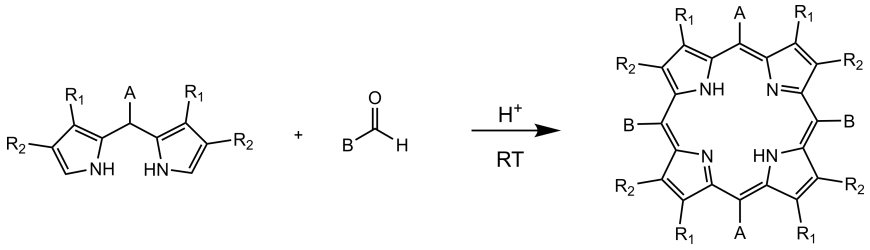

Figure 3.5: The MacDonald synthesis of a *trans*-porphyrin, using a functionalised dipyrromethane, and an aldehyde, under acidic conditions

Synthesis of porphyrins with multiple different functionalities in the *meso*- positions can be achieved by first acquiring the relevant dipyrromethane, and then performing an acylation. This can be done symmetrically or asymmetrically to achieve different functionalities in the final product, a diacylated dipyrromethane. There are a number of possible syntheses of these molecules. An example of this type of reaction can be done in one or two steps with the use of Grignard reaction.

In a single step a symmetrical diacylated dipyrromethane can be produced, this requires an acyl chloride and the relevant dipyrromethane in a 2:1 ratio. The dipyrromethane reacts with the Grignard reagent in two locations to form a dipyrromethane-Grignard species. This species then undergoes an electrophilic substitution to attach the acyl chloride. This process can be seen in Figure 3.6a. The final product can be purified *via* column chromatography. To produce the mono-acylated version the method is the same however the ratio of reagents is 1:1 instead of 2:1, the product of this reaction can be seen in Figure 3.6b. To complete the diacylation this step must then be repeated with a different acyl chloride in order to create the desired asymmetry.

To complete the macrocycle, the diacylated dipyrromethane is then combined with another dipyrromethane. This procedure requires the diacylated dipyrromethane to first being reduced, to form a bicarbinol species, which is then reacted with the second dipyrromethane to produce a porphyrinogen species, which then requires oxidation to give the final porphyrin product. This reaction can be seen in Figure 3.6c. The product of each step requires purification *via*- column chromatography [93]

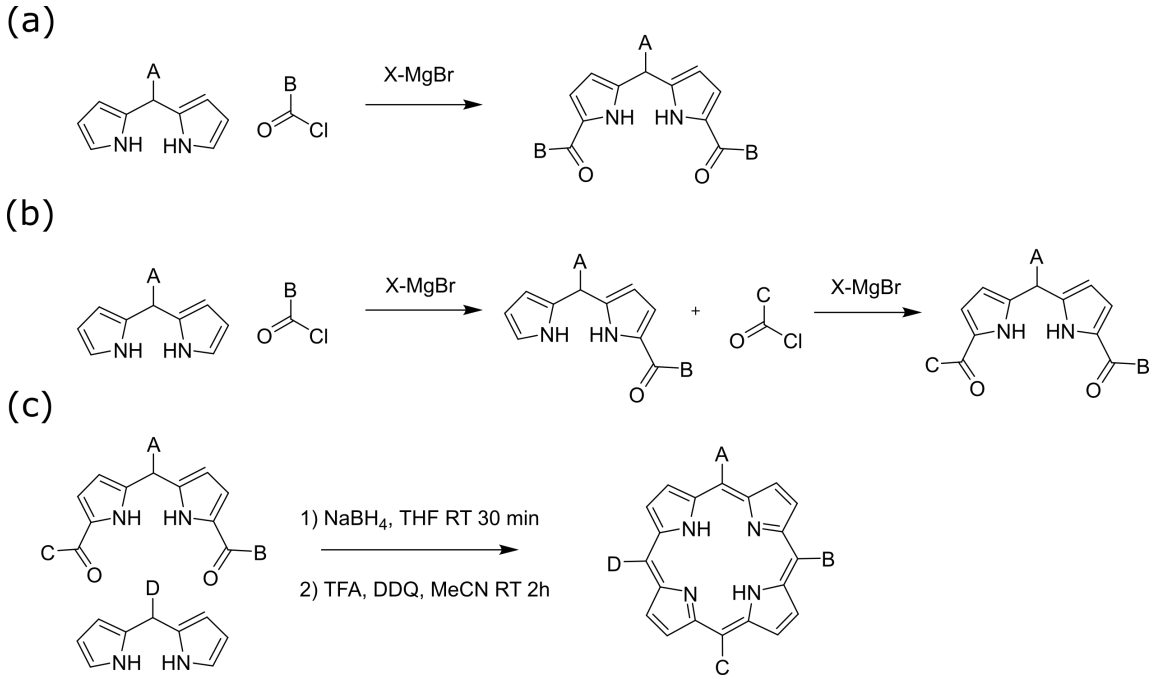

Figure 3.6: Synthetic route to asymmetric porphyrins. (a) Synthesis of diacylated dipyrromethane. (b) Synthesis of mono-acylated dipyrromethane and asymmetric diacylated dipyrromethane. (c) Synthesis of asymmetric porphyrin from diacylated dipyrromethane.

3.3 Synthesis of Porphyrins

3.3.1 Tetraphenyl Porphyrin

Tetraphenyl porphyrin for use in STM experiments was synthesised by freshly distilling pyrrole, before refluxing it with benzaldehyde in propionic acid for 2 hours. Cold methanol was added to induce crystallisation and the product then collected by filtration. The product appeared as a shiny purple powder. It was characterised by nuclear magnetic resonance (NMR) and mass spectrometry. Producing the characteristic singlet ^{1}H NMR peak at -2.75 δ/ppm for the pyrrolic proton and the molecular ion at $610.18^+ m/z$ in the mass spectrum.

3.3.2 Brominated Tetraphenyl Porphyrins

Functionalising TPP enables on-surface reactions to be performed and studied. By using a mixture of porphyrin isomers, a range of surface structures may be produced, from small di-mers and tri-mers, to extended chains or networks. On-surface chemistry opens the door to reactions that would not be feasible in solution and grants us the ability to view reactions steps and intermediates in a way that is off-limits in traditional synthetic practices. Brominating porphyrins is one way of doing this, with the bromine acting as a leaving group such that a cross-coupling reaction may occur.

Producing a mixture of isomers may be achieved in two ways, the first, a multi-step process, where the porphyrin is built up to reach the desired product, as discussed previously in this chapter, and the second is a single-step, statistical process in which aldehydes with the required functionality are mixed together to produces a range of isomers. The second method then requires separation. If the reactivity of the two aldehydes is assumed equal, the distribution of isomer products should be similar to the distribution shown in Table 3.1 [94]. However, if the reactivities of the aldehydes are significantly different or an 1:1 ratio is not used then the isomers produced will not follow this pattern.

Isomer	**Statistical Amount %**
A_4	6.25
A_3B	25
cis-A_2B_2	25
trans-A_2B_2	12.5
AB_3	25
B_4	6.25

Table 3.1: Statistical amounts of isomers produced in a reaction of pyrrole with a 1:1 ratio of aldehydes A and B to form porphyrins

A mixture of Br_xTPP isomers (3.7) were synthesised with the intention of observing and reacting them on a surface. Two mixtures of Br_xTPP, where $0 \leq x \leq 4$, isomers were prepared, using different ratios of 4-bromobenzaldehyde and benzaldehyde to achieve different ratios of isomers. The first of these mixtures was using a 1:1 ratio of 4-bromobenzaldehyde:benzaldehyde and the second using a 1:4 ratio. Both reactions were carried out by freshly distilling pyrrole, before refluxing the pyrrole and aldehydes in propionic acid. Cold methanol was added to induce crystallisation and the products then collected by filtration. In both cases the product was a crystalline purple solid. Isomers may be separated by column chromatography, using DCM/hexane as an eluent, however due to the similarity of solubilities of these molecules, particularly in the *cis* and *trans* isomers, this was not able to be achieved [95]. However as all isomers were to be required for on-surface synthesis, separation was not pursued. It was for this reason that synthesis of the individual components was not explored.

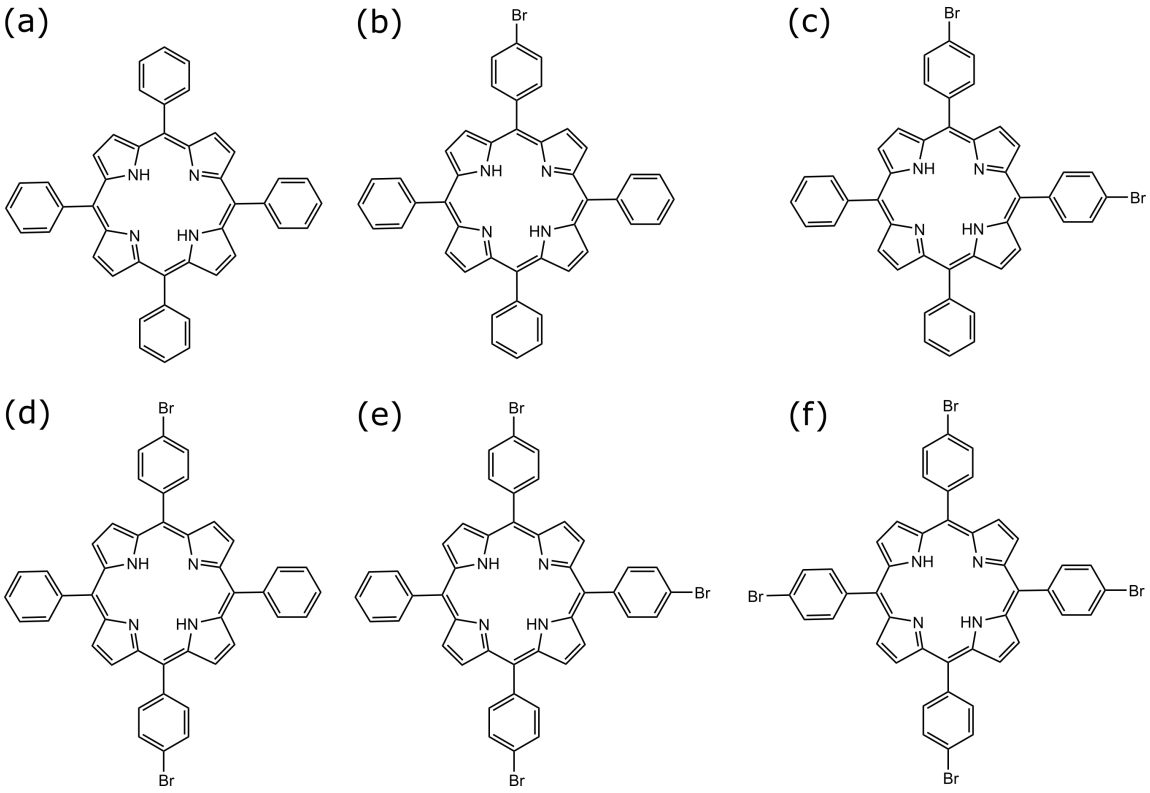

Figure 3.7: Structures of brominated porphyrin isomers produced in mixtures 1 and 2. (a) TPP, (b) BrTPP, (c) *cis*-Br_2TPP, (d) *trans*-Br_2TPP, (e) Br_3TPP, (f) Br_4TPP

The approximate distribution of isomers produced in these mixtures was determined *via* a combination of mass spectrometery and ^{1}H NMR spectroscopy. Mass spectrometery was used to determine which isomers were present in each mixture. In mixture 1, isomers (b)-(f) were found to be present, by the presence of their molecular ion peaks in the mass spectrum. Mixture 2 was found to contain (a)-(d) using the same method. The ratio of isomers was then determined using ^{1}H NMR. Porphyrin molecules display a characteristic chemical shift, corresponding to the aminic proton, located in the core of the molecule. It appears as a singlet peak at approximately $-3\delta/pmm$. The expected chemical shift for an N−H group is between 0.5 - 5 δ/ppm [96], however in a porphyrin molecule this peak is found at a significantly higher field due to being located in a heavily shielded position, in the core of the ring [97]. The position of this singlet peak can vary slightly depending on the peripheral functionalities of the porphyrin. The mixture of isomers will produce one peak for each isomer present, which can be assigned by comparing with previous data

for these molecules [93]. The statistical amounts of each type can then be determined by integrating over the peaks to find the number number of H atoms in each environment, which can be used to work out an approximate ratio. These results are summarised in Table 3.2. The NMR spectrum of Mixture 1 can be seen in 3.8, the four peaks corresponding to the four components of the mixture can be seen with their integrated value below.

BrC_6H_4CHO: C_6H_5CHO	**Isomer**	**This Work** δ/ppm	**Reference*** δ/ppm	**Peak Area (arb. units)**
1:1	Br_4TPP	-2.87	-2.87	3
	Br_3TPP	-2.84	-2.85	10
	Br_2TPP	-2.82	2.77	14
	BrTPP	-2.79	-2.76	10
1:4	Br_2TPP	-2.80	2.77	2
	BrTPP	-2.77	-2.76	3
	TPP	-2.75	-2.77	3

Table 3.2: NMR peak positions for porphyrin mixtures. *Reference peak positions reported from [93]

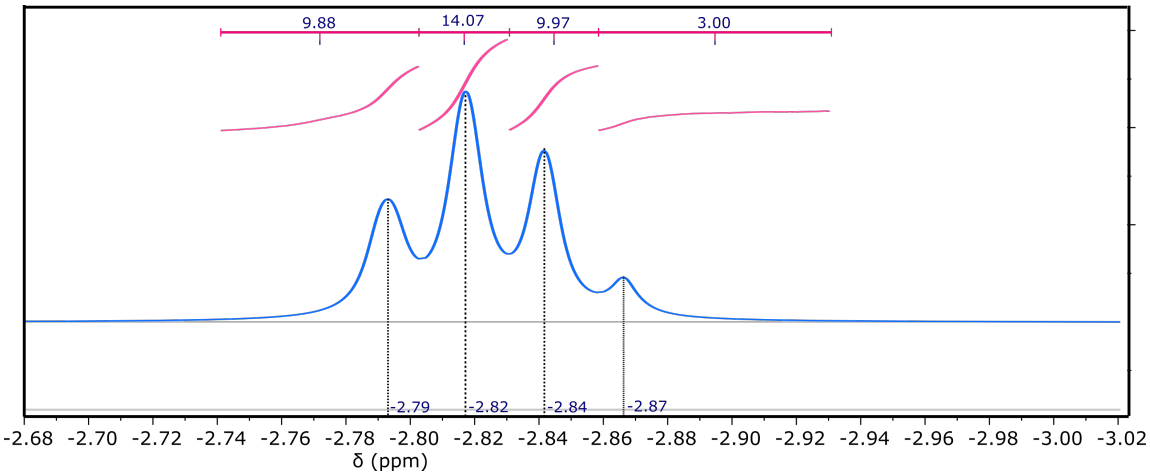

Figure 3.8: Close up of the Aminic Proton peaks in the NMR of Mixture 1, with peaks at -2.79, -2.82, -2.84 and -2.87 δppm, representing BrTPP, Br_2TPP, Br_3TPP and Br_4TPP respectively. The peak integration is showing in pink above the spectrum

3.4 Conclusion

In this Chapter the synthesis of porphyrin molecules for the purpose of surface studies has been presented.

The direct method is compared to the statistical method for synthesising halogenated porphyrin isomers. The statistical method of synthesising BrxTPP (where x =0-4) isomers was selected over the direct approach, which is a non-trivial, highly intensive multi-step procedure as opposed to the statistical which is a straightforward single-step reaction. The statistical method was deemed appropriate in this case as all the isomers were required to be deposited on a surface so separation was not an issue.

The ratios of mixtures 1 and 2 were calculated using the ratio of the pyrollic hydrogen NMR peaks. Mixture 1, a 1:1 of 4-bromobenzaldehyde:benzaldehyde, gave proportions of 8% Br_4TPP, 27% Br_3TPP, 38% Br_2TPP and 27% BrTPP. Mixture 2, a 1:4 of 4-bromobenzaldehyde:benzaldehyde, gave proportions of 25% Br_2TPP, 37.5% BrTPP, and 37.5% TPP. The synthesis of TPP has also been presented.

In the following four chapters, the properties of these molecules on the Au(111) surface are studied, focusing on TPP, using STM, STS, KPFM, XPS and NIXSW techniques.

3.5 Experimental

3.5.1 Porphyrin Mixture 1

Pyrrole was freshly distilled prior to reaction at 70 °C, 30 mbar. 4- bromobenzaldhyde (2 g, 10.5 mmol), benzaldehyde (1.112 g, 10.5 mmol) and pyrrole (1.45 g, 21 mmol) were refluxed in propionic acid (50 mL) for 2 hours and then left to cool overnight. Cold methanol (40 mL) was added and the sides of the flask were scratched to induce crystallisation. The product was collected by vacuum filtration as a lustrous purple powder. 1H NMR (400 MHz, $CDCl_3$) d ppm = 8.90-8.84 m, 8.64-8.57 m, 8.5-8.47 m, 8.25-8.22 m, 8.12- 8.08 m, 7.94- 7.91 m, 7.84-7.76 m, 1.29 s, 0.92-0.86 m, -2.77—2.84 m. MS: (ESI) m/z calculated for C44H30N4 = 610.18+, $C_{44}H_{29}N_4Br$= 684.20+, $C_{44}H_{28}N_4Br_2$ = 773.07+, $C_{44}H_{27}N_4Br_3$ = 855.22+, $C_{44}H_{26}N_4Br_4$ = 929.22+

3.5.2 Porphyrin Mixture 2

Pyrrole was freshly distilled prior to reaction at 70 °C, 30 mbar. 4- bromobenzaldehyde (1 g, 5.25 mmol), benzaldehyde (1.112 g, 10.5 mmol) and pyrrole (1.45 g, 21 mmol) were refluxed in propionic acid (50 mL) for 2 hours and then left to cool overnight. Cold methanol (40 mL) was added and the sides of the flask were scratched to induce crystallisation. The product was collected by vacuum filtration as a lustrous purple powder. 1H NMR (400 MHz, CDCl3) d ppm = 8.89-8.83 m, 8.64-8.58 m, 8.25-8.22 m, 8.13- 8.09 m, 7.94- 7.91 m, 7.83- 7.75 m, 1.28 s, 0.92- 0.87 m, -2.75- -2.80 m. MS: (ESI) m/z calculated for $C_{44}H_{30}N_4$ =610.18+, $C_{44}H_{29}N_4Br$= 684.22+ $C_{44}H_{28}N_4Br_2$ =781.18+

3.5.3 5,10,15,20- Tetraphenyl Porphyrin

Pyrrole was freshly distilled prior to reaction at 70 °C, 30 mbar. Benzaldehyde (1 mL, 10 mmol) and pyrrole (0.7 mL, 10 mmol) were refluxed in propionic acid (50 mL) for 2 hours and then left to cool overnight. Cold methanol (40 mL) was added and the sides of the flask were scratched to induce crystallisation. The product was collected by vacuum filtration as a lustrous purple powder. 1H NMR (400 MHz, CDCl3) d ppm = 8.89 s, 8.11-8.09 d, 7.94- 7.91 d, 7.77 s, -2.77 s. MS: (ESI) m/z calculated for $C_{44}H_{30}N_4$ =610.18+

Chapter 4

STM Characterisation of Porphyrin Structures on Au(111): Order and Disorder

4.1 Introduction

In this chapter experimental results are presented on the characterisation of the structure of TPP on the Au(111) surface, in its close packed arrangement, and also in its 'diffuse' arrangement, which is observed upon heating. Two different coverages are presented (a monolayer and 'island' coverage), with an order to disorder transition observed upon heating in each case. This order-disorder transition for both samples was investigated using a combination of techniques, including; STM, LEED and the implementation of a Voronoi tessellation approach. STM and LEED provide a structural characterisation of the surface in the ordered and disordered phases, while the Voronoi tessellation is used to qualify the change in the ordering of the molecules when moving from the close packed phase to the diffuse phase.

4.1.1 On-Surface Porphyrin Reactions and Structures; As Studied by STM

A number of studies of porphyrin reactions on various surfaces have previously been conducted, with STM frequently employed as a characterisation technique. STM is a particularly powerful tool for observing molecular processes since it allows reactions to be studied in 'real' space and the structural and electronic properties of individual molecules to be probed. The self-assembly behaviour of TPP on Ag(111) and Cu(111) surfaces has previously been observed by STM [36]. These experiments demonstrated that the porphyrin molecules are free to diffuse and self-assemble when deposited on the metal surface, however their ability to do so is dependant on the strength of (i), their interactions with the surface and (ii), with each other. Different arrangements are observed for Ag(111) and Cu(111). On the Ag(111) surface the TPP molecules displayed an extended 2D network, driven by Van der Waals forces and C−H→π interactions. This is contrary to the Cu(111) surface, where the TPP molecules are observed to repel each other. This repulsion is attributed to the dipoles that form on the TPP molecule as a result of charge transfer between the Cu(111) surface and the TPP molecules, preventing an extended network from forming, as seen previously in Figure 1.7.

Reactions of porphyrins may also be observed by employing these methods, by using a porphyrin that has been functionalised with a reactive group (eg. a halogen), with an on-surface coupling reaction facilitated by heating the sample. In this work, by Grill *et al*, three brominated TPP isomers were studied, BrTPP, *trans*-Br_2TPP and Br_4TPP, each producing a different product when reacted. By studying these reactions using STM it was shown that the products of these reactions were; a porphyrin dimer, a 1D porphyrin chain and an extended 2D grid [40]. Porphyrins may also undergo intramolecular reactions, in which they will react within the molecule to form a new structure. An example of this is the ring-closing reaction. This intramolecular ring-closing reaction has been studied in F_4TPP, in which a dehydrogenation, followed by an electrocyclic ring-closing to yield a planarised porphyrin-like molecule, seen previously in 1.11. Following this ring closing reaction, a self-metalation may also take place, in which the adsorbed molecule uptakes a metal atom from the surface into the centre of the macrocycle [44].

4.1.2 Characterisation of the Au(111) Surface

Prior to depositing any molecules, the clean Au(111) surface characterised via STM, which can be seen in Figure 4.1. The Au(111) surface is unusual in that it exhibits a surface reconstruction, known as the herringbone reconstruction. It is caused by the compression of 23 surface atoms into 22 lattices spacings, creating alternating regions of FCC and HCP packing on the surface. This gives the surface a unit cell of $22 \times \sqrt{3}$ atoms, and can be seen in Figure 4.1c, with the regions of FCC and HCP indicated. The inclusion of an additional atom in the surface unit cell causes the surface atoms to buckle and form undulations, which appear in STM images as bright parallel lines running across the surface (4.1a). The reconstruction is caused when the crystal is cleaved along its 111 plane and the surface atoms rearrange to minimise the surface free energy. Atomic resolution of the Au(111) surface was also achieved (4.1b), showing the predicted atomic spacing of 2.88 Å, and the predicted angle of 60° between the atoms.

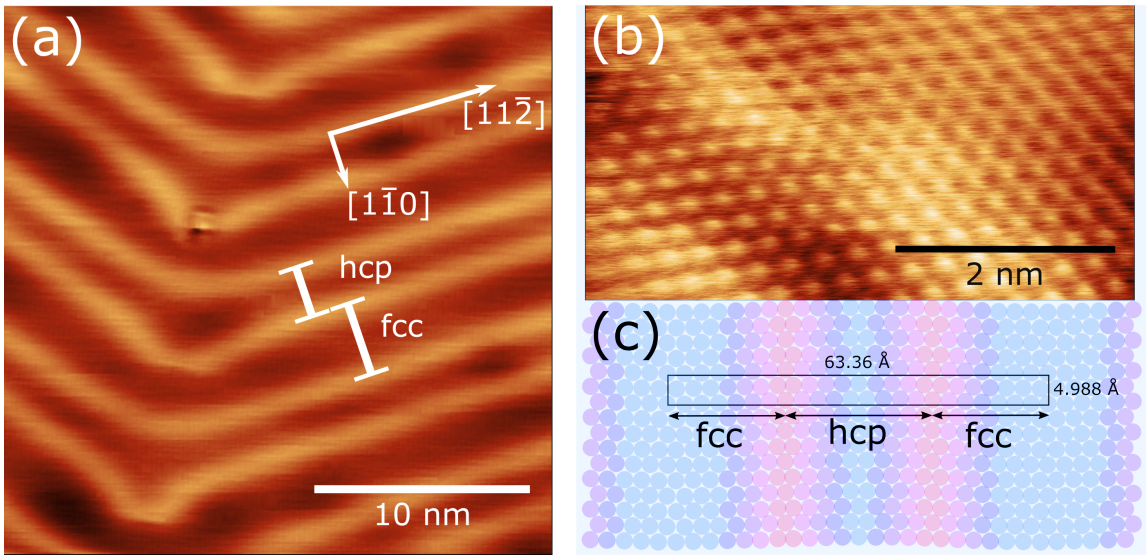

Figure 4.1: (a) STM image of Au(111) with herringbone reconstruction, with regions of HCP and FCC and lattice directions highlighted. Bias = -1.4 V, Setpoint = 20 pA. (b) STM image of atomic resolution on Au(111). Bias = -0.8 V, Setpoint = 940 pA. (c) Arrangement of atoms in the herringbone reconstruction, with the unit cell and regions of HCP and FCC highlighted.

4.2 Close Packed Domains of TPP on the Au(111) Surface

4.2.1 Room Temperature Studies

The synthesis of mixtures of Br_xTPP isomers (where $0 \leq x \leq 4$) was previously discussed is Chapter 3. Mixture 2 was selected for depositing on the surface, as it contained a smaller range of products; TPP, mono-brominated and the *cis*- and *trans*- di-brominated TPP isomers. The smaller range of compounds limits the range of possible structures that may be produced during an on-surface reaction.

Br_xTPP was deposited on a clean Au(111) surface, by evaporation from a knudson cell (k-cell). A number of depositions were performed until evidence of island formation was seen. In Figure 4.2 three successive depositions are shown, with increasing temperature of evaporation (from 4.2a to 4.2c). In the first deposition (4.2a) it can be seen that bright features are decorating the step edges of the gold surface, with the herringbone reconstruction still clearly visible on the exposed terraces. Subsequently, more molecules were deposited, and in 4.2b, it can be seen that there are molecules covering the step edges, and also sitting in some of the elbow sites and FCC regions of the herringbone. The third and final deposition, (4.2c) shows that the porphyrin molecules are at a near monolayer coverage, with some internal structure of the large island visible in the bottom right corner of the image, however no individual isomers could be identified.

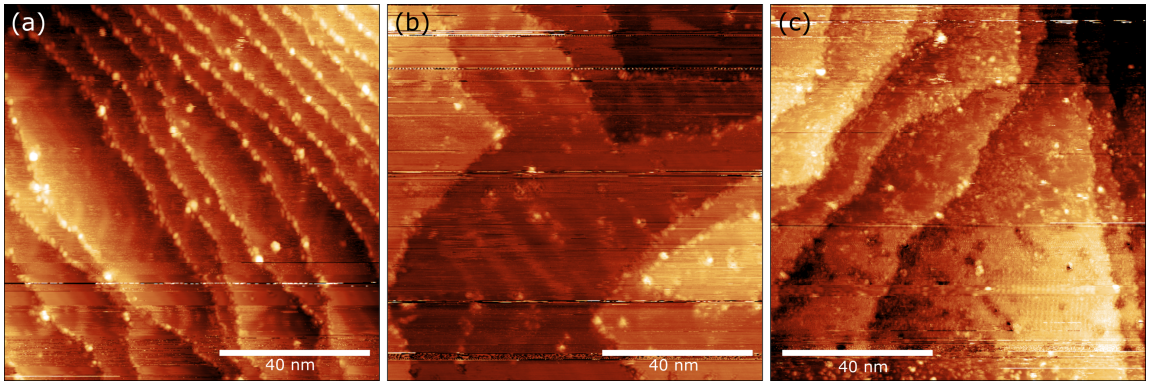

Figure 4.2: Images of Br_xTPP deposited at room temperature, with increasing coverage L-R. (a) Bias = -1.8 V, Setpoint = 50 pA. (b-c) Bias = -1.8 V, Setpoint = 20 pA .

Another image of the islands can be seen in Figure 4.3a, appearing as bright blocks with square edges, consistent with the expected shape a porphyrin island would produce. When taking a line

profile across the island, the size of the each component is in agreement with the dimensions of TPP molecules, 1.54 nm. Over 6 molecules, the distance measured was 8.46 nm, giving the average size of the molecules within the island to be 1.41 nm. This process was repeated a number of times and the results were consistent each time.

After annealing the surface at approximately 300 ± 50°C for 30 minutes the island structure is no longer visible and has instead transitioned to a 'chain-like' structure, as shown in Figure 4.3b. It should be noted that if carbon chains had formed, the angles between each component would be 120° or 109.5°. These chains have angles at 90°, which supports the idea of on-surface coupling reactions occurring between the porphyrin isomers after annealing.

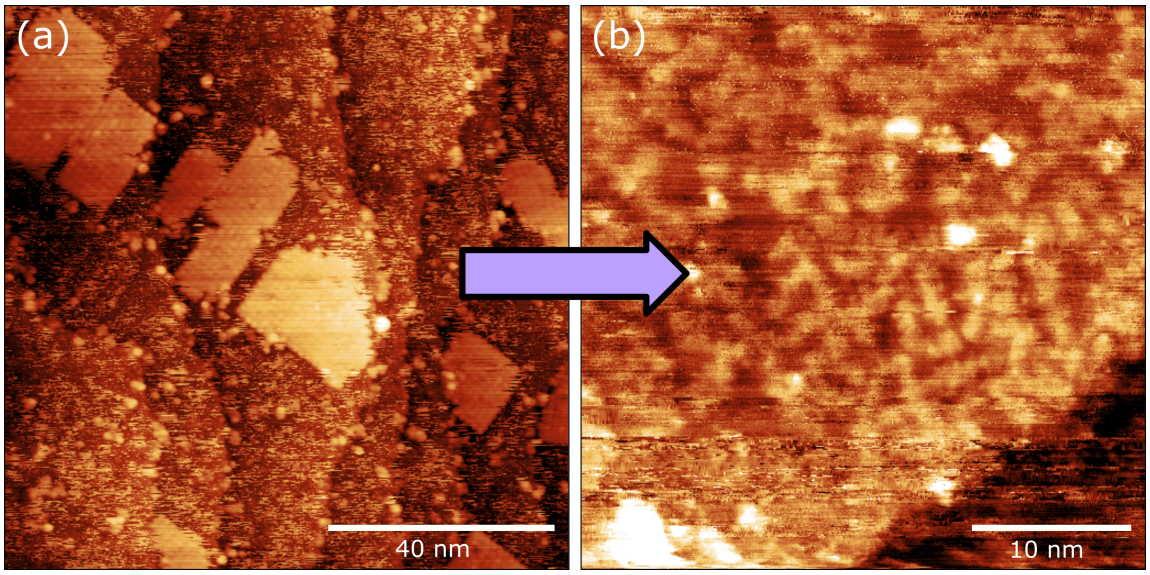

Figure 4.3: Change in structure of surface molecules upon annealing. (a) Showing the surface pre-anneal, with large rectangular islands. Bias = -1.8 V, Setpoint = 20 pA. (b) Showing the surface after annealing, islands are no longer visible and 'chain-like' structures can be seen. Bias = -1.8 V, Setpoint = 20 pA.

Studies at low temperature have shown that TPP is highly mobile at room temperature at coverages lower than a monolayer, at which point the close-packed arrangement can be seen. In the higher coverages (4.2b and c) small islands can be seen, which indicates that the coverage is nearing a monolayer, and though some TPP molecules are beginning to close pack, a large number are still highly mobile and diffusing across the surface.

4.2.2 Low Temperature Studies

At room temperature the transition from the ordered islands to the 'chain-like' structures was observed, however it was not possible to resolve single molecules or identify individual isomers. The ordered arrangement of the porphyrins on Au(111) was investigated further at 77 K. A monolayer coverage was achieved by exposing the clean gold surface to a sublimed porphyrin material for 4 minutes by heating the material to $\sim 300 \pm 50^{\circ}C$. The porphyrin molecules were deposited from a quartz crucible heated using a coil of tantalum wire. In Figure 4.4a the coverage of the surface can be seen to be nearing a monolayer, with the herringbone still visible through the layer of molecules. There are several dark patches on the surface, corresponding to areas that are not covered by the porphyrins. A smaller scale image of the packing of the molecules can be seen in 4.4b. The core of the porphyrin appears a toroidal shape, with bright features positioned around the core representing the peripheral phenyl rings. These shapes have an approximate four-fold symmetry which is consistent with the TPP structure. The packing of TPP can be seen more clearly in 4.4c, which shows overlaid, scaled images of the TPP structure onto the image in 4.4b that have been aligned with the core of the porphyrins on the STM image.

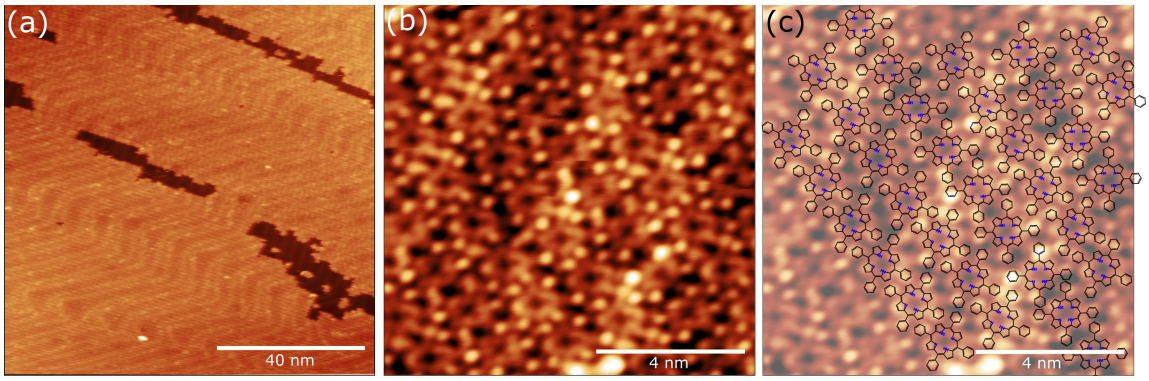

Figure 4.4: (a) Overview of TPP on Au(111) at monolayer coverage (Sample temp 77 K). Bias = -0.8 V, Setpoint = 30 pA. (b) TPP in close packed arrangement on Au(111). Bias = 1.2 V, Setpoint = 50 pA. (c) TPP molecules overlayed onto (b).

A closer look at the individual adsorbed molecules can be seen in Figure 4.5. In 4.5a, a small scale STM image of the porphyrins can be seen, similar to the area shown in 4.4b. The dimension of these molecules were measured along both long axes of the porphyrin (see 4.5). To do this, line profiles were taken in two directions across the molecule, which are shown in 4.5a by the purple

and blue lines. These specific lines correspond to the two profiles in 4.5b. The two profiles have a similar shape, with larger peaks at each end, corresponding to the pendant phenyl rings. There are two smaller secondary peaks in the inner region of the profile, assigned to the core of the porphyrin molecule. The blue profile, however appears ~ 0.4 nm shorter than the purple one. The dimensions of the porphyrins were then measured from peak to peak (see dotted line in Figure 4.5b). Repeating over 60 molecules produced the graphs in 4.5c and d. Direction 1 gave consistently higher distances than direction 2, with a mean of 1.49 ± 0.002 nm in direction 1 and 1.23 ± 0.002 nm in direction 2. The anticipated diameters of TPP, BrTPP, *cis*-Br_2TPP and *trans*-Br_2TPP are 1.54 nm [98], 1.86 nm, 1.86 nm, and 1.94 nm, [99] respectively. Comparing these with the dimensions measured using the STM image, it can be assumed that only TPP is present on the surface as none of the dimensions corresponding to the brominated poprhyins are observed. The inner peaks have an average separation of 0.633 ± 0.007 nm, which is comparable with the expected diameter of the porphyrin core, 0.688 nm. TPP is a symmetrical molecule, meaning directions 1 and 2 ought to give the same distance, however in this case direction 1 gave a consistently longer distance. This is likely due to thermal drift in the STM. The STM has a fast scanning direction where the tip moves horizontally across the surface, and a slow scanning direction, where the tip moves up, line by line. Thermal drift in the slow scanning direction lead to the artificial shortening of these dimensions. This would also skew the size and shape of the unit cell.

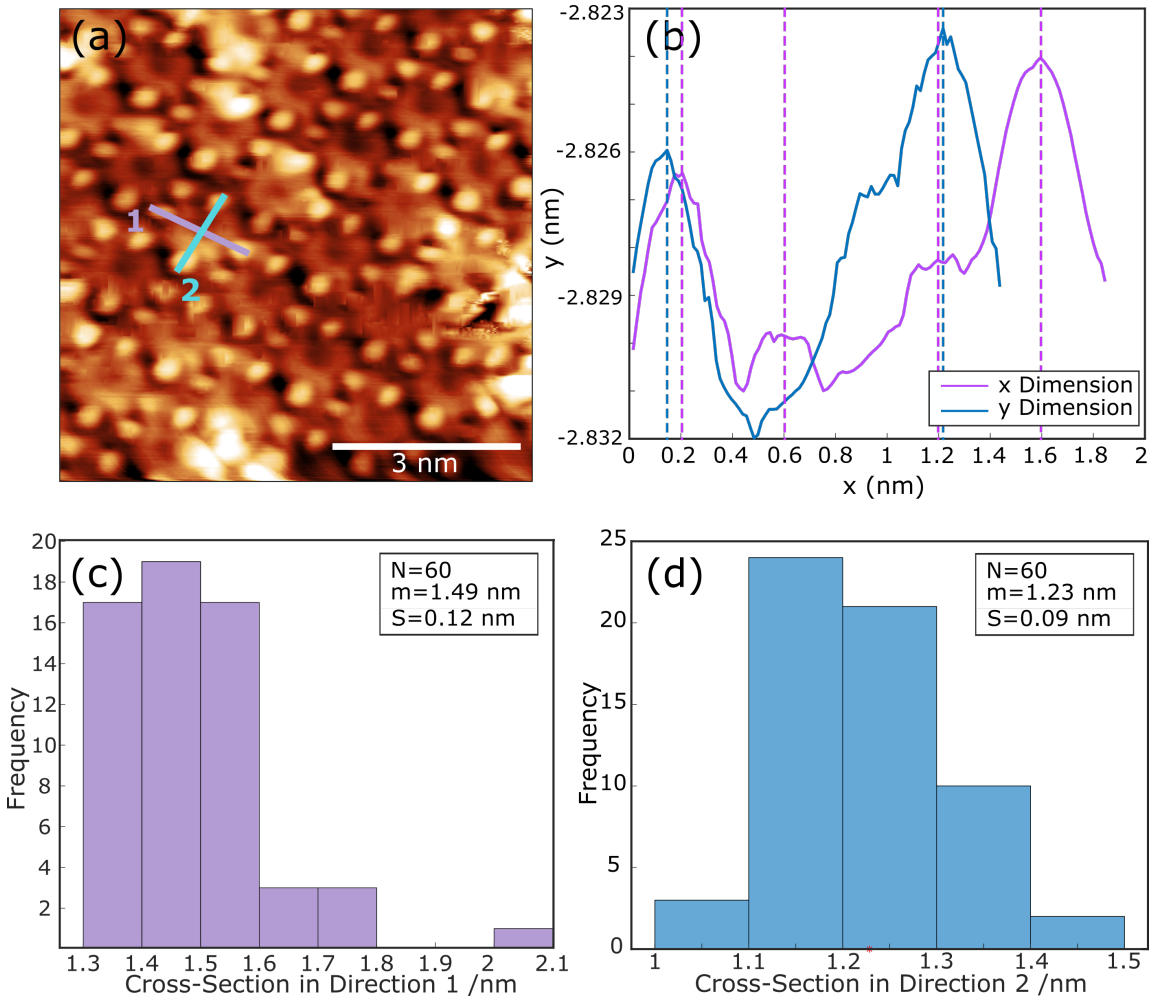

Figure 4.5: (a) STM image of close-packed TPP on Au(111) with lines showing the positions of the measured line profiles. Bias = 0.3 V, Setpoint = 100 pA. (b) Line profiles along lines 1 and 2. (c),(d) Histograms showing distribution of dimensions measured in the two directions respectively. (N = number of measurents, m = mean distance, S = standard deviation on the mean)

In this close packed arrangement, a number of different packing motifs were observed. TPP may be found in two possible orientations, with one rotated at 30° relative to the other. These two orientations are defined as A and B, and they appear in a number of different combinations. In some images, only one orientation of porphyrin was present, for example, the image in Figure 4.5a shows only one orientation. In other images both can be seen to be present, in Figure 4.6a both A and B can be seen. The packing of A and B varies throughout this image, in 4.6b orientation A is represented by a blue square and orientation B is represented by a green square. In this image

it can be seen that the structure is formed in a pattern of two rows of A, one row of B, two rows of A etc. However, in the top right corner, the packing changes, skipping a row of A, giving an A B A B pattern. In some images only the alternating A B A B was observed. Owing to the different packing motifs it is challenging to define one unit cell for this surface structure, as there is no long-range repeating pattern present.

A unit cell for the image seen in Figure 4.6a can be defined in one of two ways, firstly, looking at the two neighbouring rows of A and defining a unit cell for those, and second, by disregarding the positions of the phenyl rings and only looking at the porphyrin core. Using the first method, a unit cell for the two rows of A can be defined as $1.62 \pm 0.06 \times 1.44 \pm 0.01$ nm, with an angle of 105.6°. For the second method, defining a repeat unit from the porphyrin centres only, a unit cell can be defined between a row of A and a row of B, giving the unit cell to be $1.90 \pm 0.01 \times 1.43 \pm 0.01$ nm, and an angle of 123.5°. The shorter distance is only along the rows, while the longer distance represents the inter-row separation. However, measurement of angles from STM can be challenging and the absolute values quoted here should be taken with a reasonable error of ±20°.

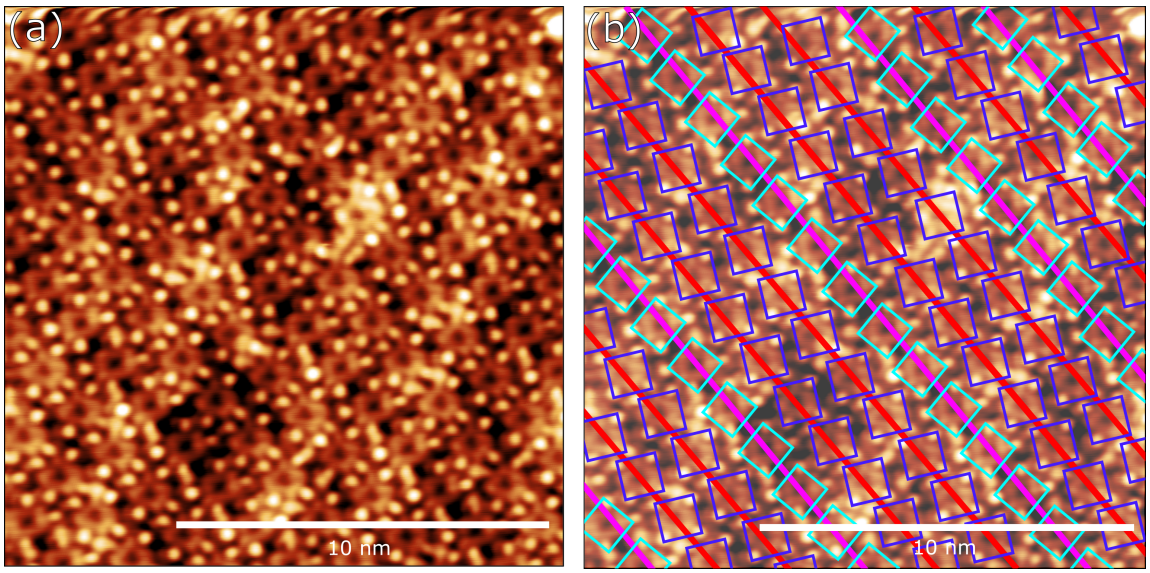

Figure 4.6: (a) STM image of close-packed TPP arrangement. Bias = 0.6 V, Setpoint = 50 pA. (b) Red and magenta lines showing direction of TPP rows, blue and cyan square showing the rotation of the TPP molecules overlayed onto (a).

The packing of the TPP molecules is likely to be driven by a combination of VDW interactions and C−H→π interactions between the face of the peripheral phenyl rings and the hydrogen atoms

in the *para-* position on the phenyl ring of a neighbouring molecule. These interactions are caused by charge transfer from the π system to an empty orbital associated with the CH species. Each TPP molecule is able to form four such interactions with its neighbours, resulting in the 2D network seen in Figure 4.6

4.2.3 Br_xTPP Mixture

In section 4.2.2 it was concluded that only TPP was present on the surface from the dimensions of the molecules. The measured dimensions of the molecules were not consistent with the expected distances for the brominated isomers. The expected distances for the brominated isomers were 1.89 nm and 1.94 nm, calculated from a simulated structure [99], however the measured distances, 1.49±0.02 nm, were not comparable to these numbers and much more comparable to the dimensions for TPP, 1.54 nm. In addition, the appearance of the porphyrins in the STM images does not support multiple isomers being present. The molecules on the surface appear symmetrical, each of the four pendant group appears the same size and shape. Previously, studies have been performed on brominated TPP, [40] where the brominated phenyl rings are clearly visible in the STM images. Examples of BrTPP and *trans*-Br_2TPP can be seen in Figure 4.7a, where BrTPP shows one of the phenyl groups is significantly larger and is clearly asymmetric. The *trans*-Br_2TPP has obvious 2-fold symmetry as opposed to the 4-fold symmetry that TPP would display. Figure 4.7b unambiguously shows all deposited molecules look identical and possess 4-fold symmetry, implying that only TPP is present on the surface. Therefore, it can concluded that sublimation from a BrxTPP/TPP mixture results in, under these conditions, the deposition of only the TPP species. These findings may be attributed to the higher sublimation temperature expected for the brominated TPP.

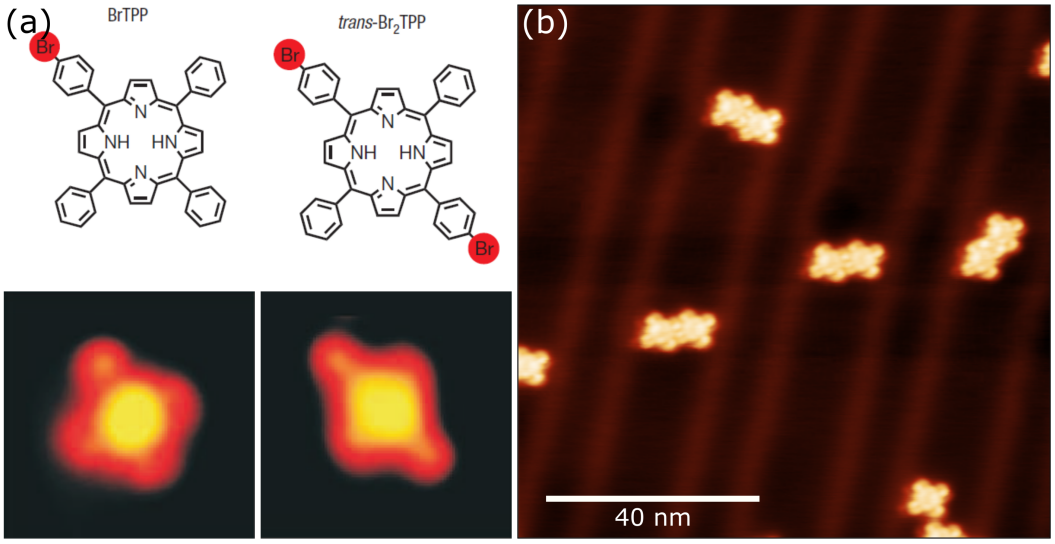

Figure 4.7: Comparison of known BrTPP and trans$-Br_2$TPP STM image and an image of molecules deposited from Br_xTPP mixture. (a) BrTPP and trans$-Br_2$TPP isomers with corresponding STM images below, from [40]. (b) TPP islands showing only one isomer present (TPP). Bias = -1 V, Setpoint = 15 pA.

4.3 Formation of a Diffuse Phase of TPP on the Au(111) Surface

4.3.1 Annealing a Monolayer

When TPP is deposited on the Au(111) surface to a monolayer coverage it forms the close packed arrangement as previously seen in this chapter. Upon annealing, this close-packed structure undergoes a phase transformation to form a new arrangement on the surface.

The annealing process consisted of heating the surface at 300 ± 50°C ($\sim$ 600 K) for 20 minutes, by passing a current through a piece of low resistivity silicon. Images of the surface were then recorded at a temperature of 5 K. It can be seen in Figure 4.8a that the TPP structure has changed from its ordered, close-packed structure to an amorphous diffuse phase, where there is a no long-range order. It is clear from this loss of order, that the close-packed arrangement is no longer the most energetically favourable state. From Figure 4.8 it is apparent that coupling reactions

between individual TPP molecules have not occurred, as no extended 1 or 2D small structures have formed on the surface, with the TPP molecules appearing as discrete units. Additionally, the appearance of the individual TPP molecules has changed, before annealing they appeared as a ring with four evenly spaced, peripheral bright features, following annealing, the majority of TPP molecules appear as elongated shapes, with a small depression in the centre. There is also a loss of the four-fold symmetry displayed by the TPP before annealing. From Figure 4.8a-b it can be seen that a large number of the TPP molecules appear as an 'H' shape, with an approximate 2 fold symmetry, while others have reduced symmetry and appear irregular (4.8c).

A possible explanation for the difference in their appearance is that planarisation of TPP has occurred. TPP is known to adsorb onto the surface in the saddle conformation, where the five-membered rings point alternately up and down, and the phenyl rings the exist out of the plane at an angle of $\sim 45^{\circ}$ relative to the core. [100] This planarisation reaction is known to take place in F_4TPP but has not been recorded for TPP [44]. Similar to the reaction seen in [44], there is evidence in Figure 4.8a have undergone a dehydrogenation, followed by an electrocylic ring-closing reaction, to form a planar, porphyrin-like species.

The ring-closing reactions can occur at four places on the TPP molecule, at each of the substitutions in the *meso-* positions. The dehydrogenation removes a hydrogen atom at the *ortho-* position on phenyl ring and also from the β position the pyrolic ring and a bond formation occurs between them to facilitate the ring closure, forming a new five-membered ring. A number of possible isomers can be produced this way. Two of these isomers can be seen in Figure 4.8b-d. In some of the molecules, peripheral bright spots can still be seen, such as in 4.8d, this is thought to be owing to incomplete planarisation reactions, as the phenyl ring would be out of plane with the rest of the molecule, creating a raised spot on the ring This may be present on one more more of the substituent phenyl rings.

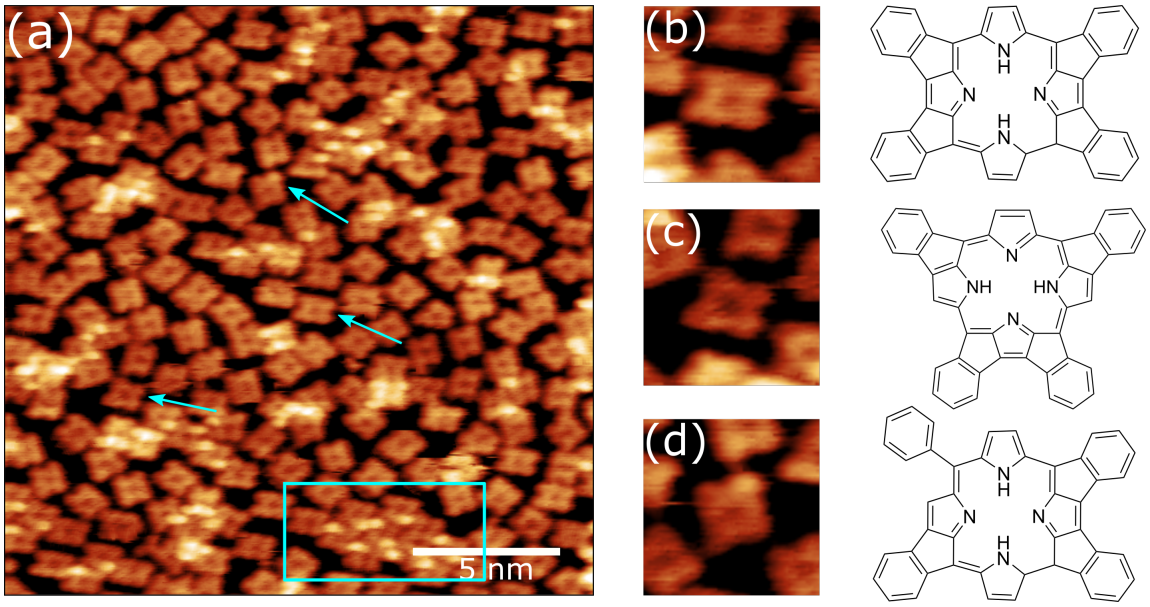

Figure 4.8: Change in structure of TPP monolayer upon annealing. (a) 'Diffuse' phase of TPP on Au(111) that occurs upon annealing. Bias = 1.3 V Setpoint = 5 pA. (b-c) Structures of a ring closed TPP-derivatives and corresponding STM images. (d) Structure of incomplete ring closed TPP-derivative where one phenyl ring remains unreacted and the corresponding STM image.

As previously discussed in this chapter, the driving force for the organised structure of the close-packed TPP is a combination of VDW and the formation of C−H→π interactions. These interactions are able to form in the close-packed phase due to the saddle shape of the TPP, and the rotation of the phenyl rings. The rotation means that the π electrons in the phenyl rings are facing a hydrogen atom on a neighbouring phenyl ring, enabling an interaction to form. When the TPP molecules undergo the ring closing reaction, and consequential planarisation of the molecule, the phenyl rings are no longer in a position to interact with the neighbouring hydrogen atoms in the *para*-position on the phenyl rings, thus removing a driving force for close-packing. It can be seen in Figure 4.8a that in the bottom right corner of the image there is a small close-packed island highlighted in the blue box, each molecule in this island possesses a bright peripheral feature, which can be assigned to an incomplete ring-closing, allowing for the C−H→π interaction to form, and the formation of a small close-packed island to occur.

4.3.2 Studying the Order-Disorder Transition for Sub-Monolayer Coverages

Previously in this chapter, the observations following annealing a full monolayer coverage of TPP on Au(111) have been presented. An additional data set was acquired for sub-monolayer coverage of TPP. These images were collected at 5 K, due to the diffusion rate of TPP at higher temperatures (ie. 77 K), being incompatible with STM image acquisition. In this experiment the Au(111) surface was exposed to the flux of sublimed TPP for 1 minute, this surface was then characterised *via* STM at 5 K. The images obtained showed that the TPP had adsorbed to the step edges and formed small islands on the surface.

The TPP appears to adsorb in small, close-packed, clusters of between two and nine units. They appear to be preferentially located in the FCC region of the herringbone, with the width of such islands limited by the size of this region. However the island size does not appear to be limited in the other direction, with longer rows of TPP forming in the direction of the herringbone. These observations suggest that the arrangement of TPP when the coverage of the surface is low is driven by a combination of surface-molecule interactions as well as molecule-molecule interactions as there is clearly a favourable adsorption position on the surface. STM images of this surface can be seen in Figure 4.9. 4.9a shows a large area of the surface, with islands running down the direction of the herringbone on both visible terraces. The dominant island size in this image appears to contain 2 TPP molecules, suggesting that the critical island size is two molecules.

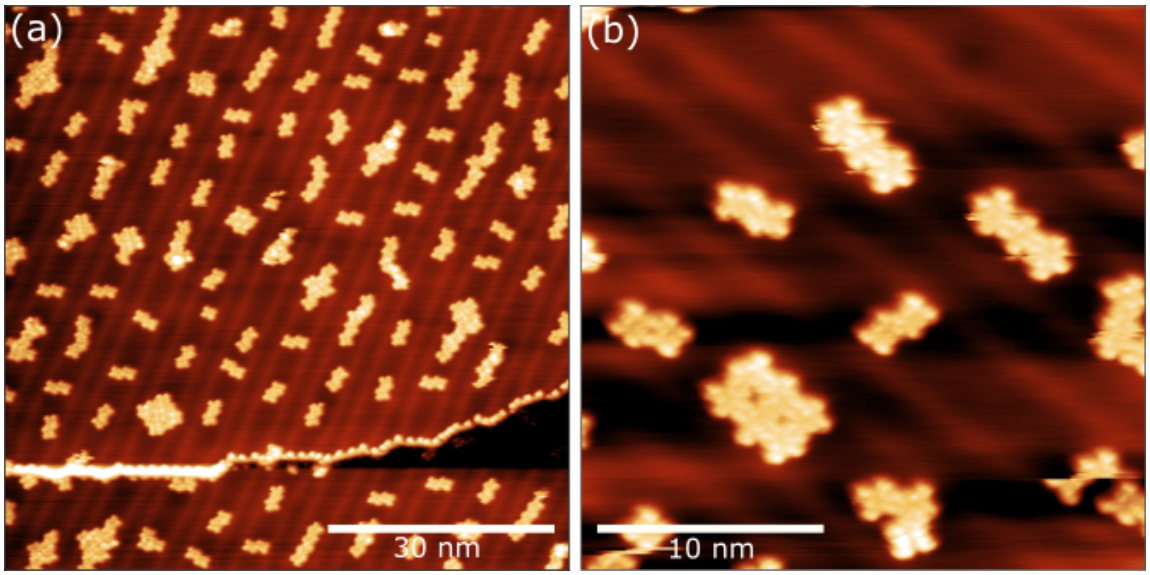

Figure 4.9: (a) STM image of a sub-monolayer coverage of TPP on Au(111). Bias = -1.3 V, Setpoint = 25 pA. (b) STM image showing a close up of islands of TPP. Bias = -1.3 V, Setpoint = 50 pA.

The TPP molecules that make up the islands pack together in the same motif (AA rows) as the TPP in the close-packed arrangement in the monolayer. The interactions that hold the islands together can be assumed to be the same C−H→π interactions that are present in the close-packed phase. The separation of the islands along the herringbone was measured and the results plotted as a histogram, Figure 4.10a. It was found that the average separation between the islands was 7.15 ± 0.24 nm. It should be considered that the TPP molecules will be diffusing at a similar rate to each other, and once an island begins to nucleate the molecules will stop diffusing and the island will begin to grow. The dimension and components of the islands was also investigated, the number of TPP units in each island was counted and plotted as a histogram. The average number of molecules per island was found to be two, but islands were observed to have up to nine TPP components.

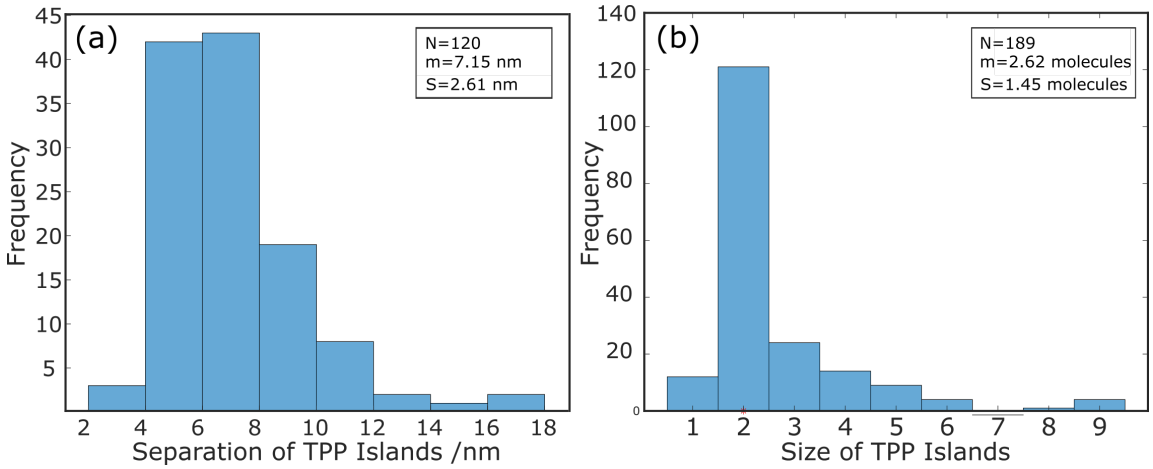

Figure 4.10: Histograms showing distribution of island separation (a), and island size (b).(N = number of measurements, m = mean distance, S = standard deviation on the mean)

Annealing the Sub-Monolayer Coverage (Islands)

The monolayer coverage of TPP when annealed produced the 'diffuse' phase of TPP, where it was proposed that the TPP molecules have likely undergone a ring closing reaction to form porphyrin derivatives which are planar and, hence, no 300 ± 50°C ($\sim$ 600 K) for 20 minutes and afforded a similar effect on the arrangement of TPP molecules.

The formerly close-packed islands of TPP have been redistributed across the surface and appear as individual TPP units. Following annealing, no island structures are present, indicating that the formation of dimers and other small islands is no longer an energetically favourable arrangement. The preferred adsorption position, however, has remained in the FCC region of the herringbone. The similar behaviour of monolayer and sub-monolayer coverages upon annealing suggests that a similar transition has occurred in both cases.

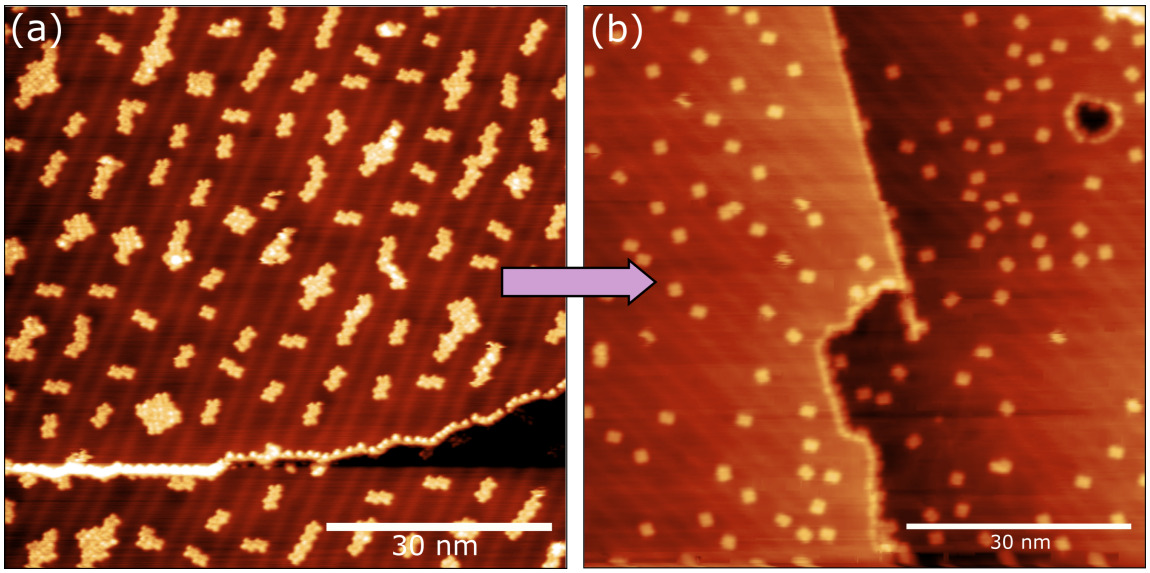

Figure 4.11: STM images showing the change in structure of surface confined molecules upon annealing. (a) Sub-monolayer coverage of TPP on Au(111) before annealing. Bias = -1.3 V, Setpoint = 25 pA.(b) Low coverage 'diffuse' phase of TPP on Au(111) that occurs upon annealing. Bias = 1.3 V Setpoint = 25 pA.

4.4 Low Energy Electron Diffraction of TPP on Au(111)

Low energy electron diffraction (LEED) is a technique used for studying the diffraction properties of surfaces and any adsorbed overlayers that may be present. The LEED patterns presented in this chapter were taken prior to the XPS and XSW measurements discusses in Chapter 6 and are used to support the STM based characterisation detailed above. LEED can be used a a qualitative surface analysis technique for determining the coverage of the surface and the unit cell of the overlayer.

4.4.1 Characterising the TPP Unit Cell with LEED

Prior to taking any measurements, the Au(111) surface was cleaned *via* sputter and anneal cycles. A LEED pattern was recorded for the clean surface with a beam energy of 66.5 eV, this pattern consisted of six bright spots seen at the edges of the fluorescent screen, which can be seen in Figure 4.12a These spots arise from the incident diffracted beams on the screen. The hexagonal shape reflects the three-fold symmetry of the FCC lattice of the Au(111) crystal. The diffraction pattern is expected to contain a central spot as the beam reflects at a normal to the surface, however in this

case it is occluded. The dimensions of the unit cell for Au(111) is known to be 2.885×2.885 Åwith an angle of 120°, which can be seen in reciprocal space in Figure 4.12b, using this information the unit cell for the overlayer of TPP can be calculated. It should be noted that the (111) surface was used to calculate the TPP overlayer, without considering to the herringbone reconstruction.

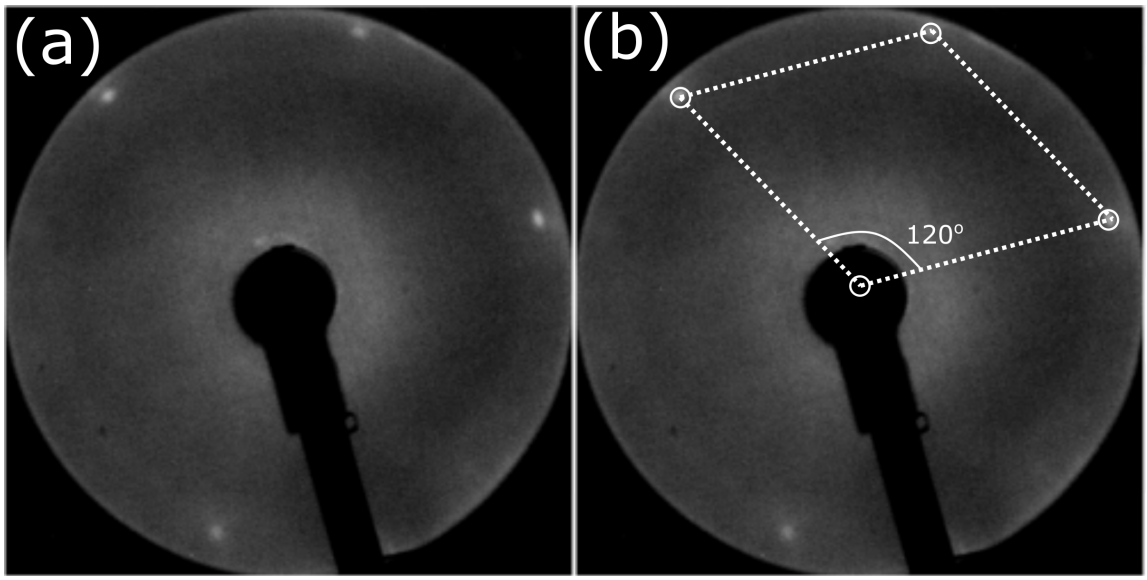

Figure 4.12: (a) LEED pattern of clean Au(111), showing six spots representing the FCC lattice in reciprocal space, at 66.5 eV. (b) LEED pattern of TPP on Au(111) at 15.5 eV

After the TPP molecules were deposited another LEED pattern was recorded (the LEED pattern, taken at a beam energy of 15.5 eV, for TPP on Au(111) can be seen in Figure 4.13a). This pattern consists a square lattice, rotated over three domains. The square lattice can be seen in Figure 4.13c and the three domains can be seen in 4.13b, with the red, blue and green colours each corresponding to a different domain. The positions of the lattices for the different domains can be seen in 4.13d. The square lattice shown in 4.13b can be translated onto the Au(111) FCC LEED pattern taken at 66.5 eV, by scaling it using $E_1^{\frac{1}{2}}/E_2^{\frac{1}{2}}$ (where, in this case $E_1 = 15.5$ eV and $E_2 = 66.5$ eV). The square net from the TPP on Au(111) LEED pattern taken at 15.5 eV must be shrunk by a factor of 0.48 to be overlayed onto the Au(111) LEED pattern taken at 66.5 eV. Both the square net for the TPP overlayer and the unit cell for the Au(111) FCC lattice can be seen in Figure 4.13e.

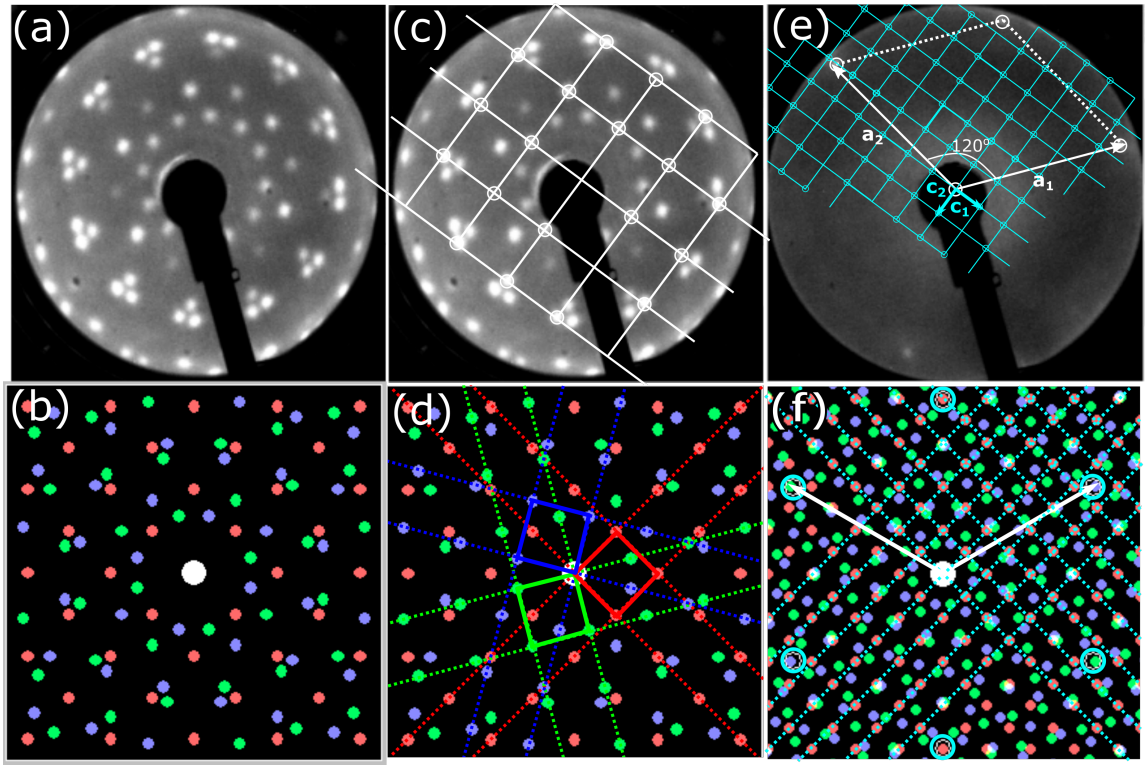

Figure 4.13: (a) LEED pattern of TPP on Au(111) at 15.5 eV (b) LEED pattern for TPP on Au(111) calculated in LEEDpat (c) LEED pattern of TPP on Au(111) at 15.5 eV with overlayed lattice mesh (white lines) (d) LEED pattern for TPP on Au(111) calculated in LEEDpat, showing the unit cell of the Au(111) in each of its three domains (blue, green, red squares) (e) LEED pattern of Au(111) surface with unit cell of surface highlighted (white lines) and the lattice mesh of the TPP overlayed superimposed onto the image (blue lines) (f) LEED pattern for TPP on Au(111) calculated in LEEDpat with underlayer of Au(111) highlighted in blue rings and blue dashed lines highlighting a single domain of TPP.

The unit cell of the TPP overlayer was calculated using the vectors $\mathbf{a_1}$, $\mathbf{a_2}$, $\mathbf{c_1}$, and $\mathbf{c_2}$. Vectors $\mathbf{a_1}$ and $\mathbf{a_2}$ describe the unit cell of the gold in reciprocal space, and vectors $\mathbf{c_1}$, and $\mathbf{c_2}$ describe the TPP overlayer in reciprocal space. $\mathbf{a_1}$ and $\mathbf{a_2}$ can be expressed in terms of $\mathbf{c_1}$, and $\mathbf{c_2}$,

$$\mathbf{a_1} = 3.96\mathbf{c_1} + 3.96\mathbf{c_2}, \tag{4.1}$$

$$\mathbf{a_2} = -1.45\mathbf{c_1} + 5.41\mathbf{c_2}, \tag{4.2}$$

where the values of $\mathbf{c_1}$, and $\mathbf{c_2}$ were found by manually measuring the distances. These equations may then be solved simulataneously to give $\mathbf{c_1}$, and $\mathbf{c_2}$ in terms of $\mathbf{a_1}$, and $\mathbf{a_2}$. From there, these

equations may be written as a Matrix, **M**, which can be converted from reciprocal space to real space by taking the inverse transpose of **M**. This returns a matrix, $\mathbf{M}^*$, which has gives c_1^* and c_2^* in terms of a_1^* and a_2^*.

$$M = \begin{pmatrix} 0.1457 & -0.1457 \\ 0.1991 & 0.0534 \end{pmatrix} \text{ and } M^* = \begin{pmatrix} 3.96 & 5.41 \\ -3.96 & 1.45 \end{pmatrix} \tag{4.3}$$

Matrix M* was then used to find the unit cell of the overlayer of TPP on Au(111). The unit cell of the TPP overlayer in real space and reciprocal space can be seen in Figure 4.14a and b respectively. In Figure 4.14c the unit cell of TPP can be seen superimposed over an STM image of close packed TPP. It can be seen that the close packed lattice observed by STM is can be accurately described by LEED. From analysing the LEED patterns produced by TPP the close-packed overlayer is shown to be incommensurate, meaning there is no preferential binding site for TPP on Au(111), and TPP may sit in any number of different positions on the surface.

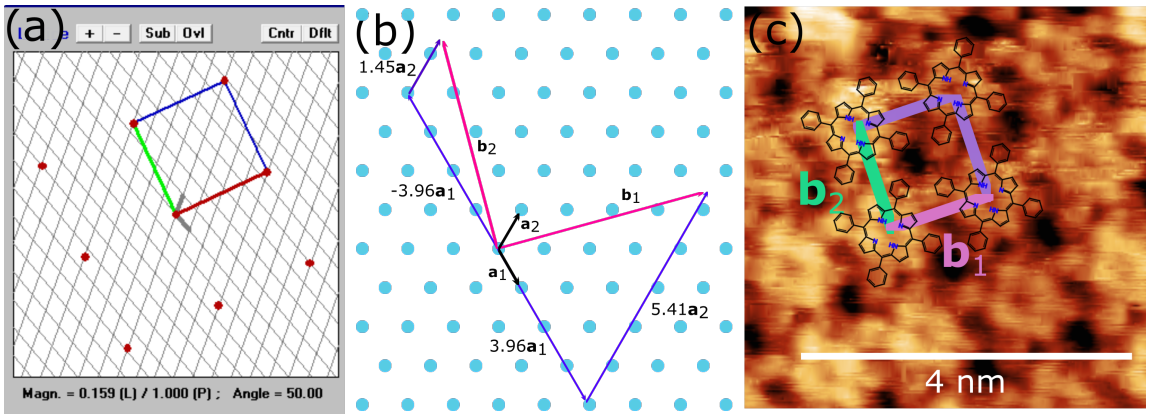

Figure 4.14: (a) Unit cell calculated in LEEDpat, with inset TPP LEED pattern. (b) Unit cell calculated using LEED pattern. (c) Unit cell observed by STM. Bias = 1.8 V, Setpoint = 100 pA

In Figure 4.15 the 2D Fourier transform of an STM image (Figure 4.15a) is displayed. The 2D Fourier transform of an STM image should be equivalent to its LEED pattern. However, a LEED pattern is an average over all possible domains of TPP on the surface, while each STM image may only show one domain, with the resultant Fourier transform describing only one particular domain. In Figure 4.15b an inset of the calculated LEED pattern for a single domain of TPP on Au(111) is compared to the Fourier transform of the image seen in Figure 4.15b (close up in 4.15c). The

square lattice is highlighted in 4.15c with dotted white lines, the spacing between the points was measured to be $0.77 \pm 0.15 nm^{-1}$, which translates to 1.29 ± 0.24 nm, this is ~ 0.1 nm smaller than the values calculated from the LEED pattern for the unit cell.

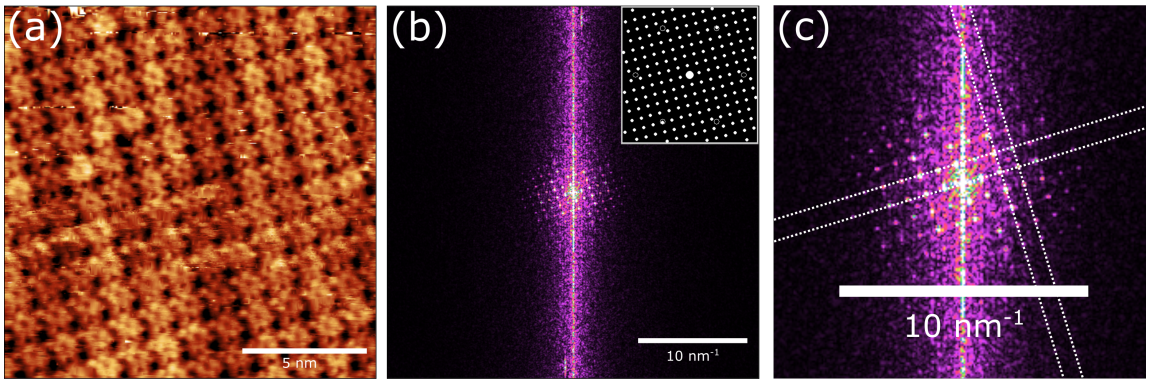

Figure 4.15: (a) STM image showing close-packed TPP on Au(111). Bias = 1.8 V, Setpoint = 80 pA. (b) Corresponding 2D Fourier Transform of close-packed surface, with inset of calculated LEED pattern of a single domain of TPP on Au(111). (c) Close-up of Fourier Transform, with dotted lines showing the rows of spots.

4.4.2 LEED Analysis of the Diffuse Phase

LEED was also used to provide information on the diffuse phase, following the annealing of the Au(111) sample. The diffuse phase is known to be mobile at room temperature, and therefore, would not be expected to produce a clear diffraction pattern when studied with LEED. The pattern produced by the diffuse phase is a blurred ring around a large, bright central spot, these can be seen in Figure 4.16a and b, taken at 6.5 eV and 22.5 eV respectively. This pattern confirms that the TPP structure now exhibits diffuse characteristics as the close packed LEED pattern is no longer visible. The diffuse LEED pattern shows that there is no ordering of the TPP molecules, and therefore no well-defined unit cell. From this data the intermolecular distances can be approximated by using the diffuse ring and central spot as to measure from and than converting the result from reciprocal space to real space. The inner and outer limit of the ring were calculated, and taken to be the error on the central point, the bright hexagon in the centre was also used as a measuring point, taking the distance from one side the other. Using the ring, the intermolecular distance was calculated to be 0.83 ± 0.10 nm and using the inner hexagon it was found to be 1.52 ± 0.10 nm.

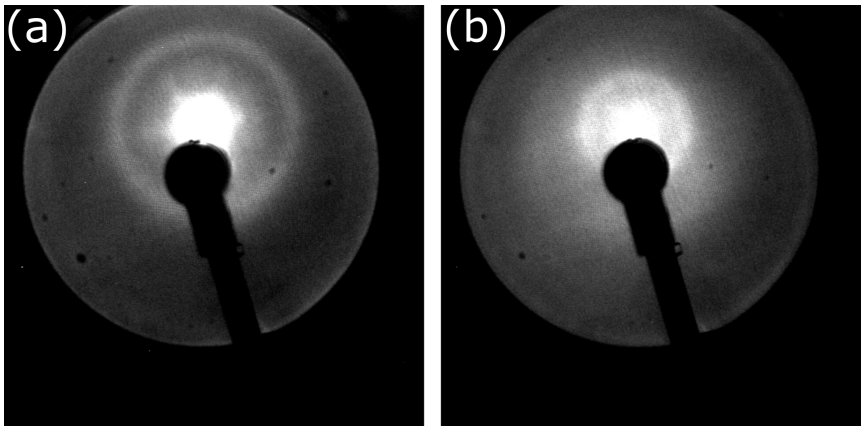

Figure 4.16: LEED pattern of Diffuse phase TPP on Au(111) at 6.5 eV (a) and at 22.5 eV (b). Close packed spot pattern has disappeared and ring structure seen in LEED shows no clear unit cell for diffuse phase.

This LEED pattern can be compared to the 2D Fourier transform of an STM image of the diffuse phase. In Figure 4.17a an STM image of the diffuse phase can be seen, with its corresponding 2D Fourier transform in 4.17b. The 2D Fourier transform of the diffuse phase also takes the form of a blurred ring with a bright central spot. The intermolecular distance can be found by taking a line profile across the 2D Fourier transform to obtain the 1D Fourier transform.

To find the intermolecular distance, the distance between the peaks can be taken and then transferred from reciprocal space to real space. In the line profile of this image there are a number of pairs of peaks to choose from, see dashed lines in 4.17c. The distance between the lines was found to be $0.7 \pm 0.18 nm^{-1}$ for the pink lines, $1.23 \pm 0.25 nm^{-1}$ for the blue and $2.09 \pm 0.33 nm^{-1}$ for the green. When transformed from reciprocal space gives distances of 1.43 ± 0.21 nm, 0.81 ± 0.59 nm and 0.48 ± 0.08 nm respectively. The intermolecular distance (unit cell dimension) is the largest distance, 1.43 ± 0.21 nm, while the other two values correspond to intramolecular distances. The second measurement of 0.81 ± 0.59 nm corresponds to the outer macrocycle, measured between opposite pyrrole rings. The thrid figure 0.48 ± 0.08 nm corresponds to the inner macrocycle, as measured between pairs of nitrogen atoms.

These values are in good agreement with those calculated using the LEED data indicating that the surface is likely to have a very similar structure. The inner values, calculated from the pink lines in Figure 4.17c and from the inner hexagon of the LEED pattern, are comparable to the dimensions of the Unit cell calculated for TPP on Au(111), which was 1.39 nm. This could correspond to small

areas in which TPP is still in the close packed arrangement (see the bottom right corner of the STM image in Figure 4.17a, or indicate that while the surface is disordered, (hence the loss of the ordered pattern seen in the LEED taken in close-packed phase) a similar amount of material remains on the surface and the intermolecular distance remains similar.

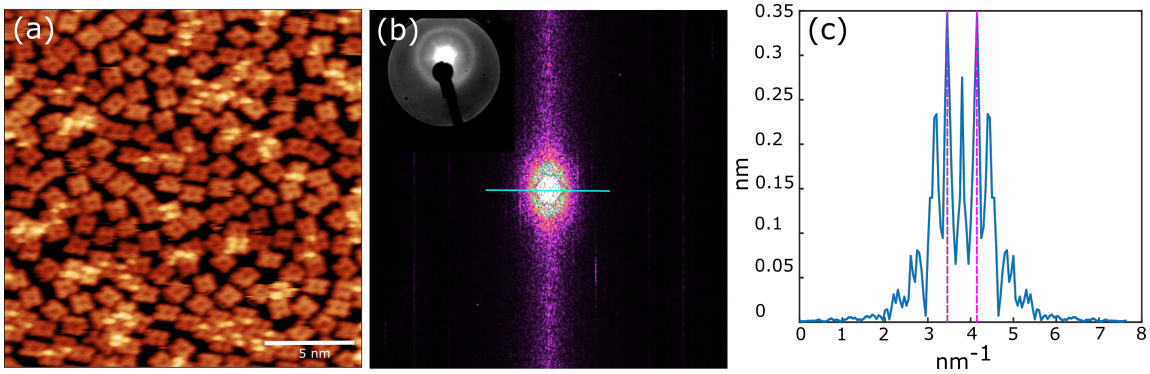

Figure 4.17: (a) Diffuse phase TPP Bias = 1.3 V, Setpoint = 5 pA. (b) 2D Fourier transform of (a), with inset LEED pattern of Diffuse phase at 6.5 eV. Ring pattern of LEED is mirrored in 2D Fourier transform. (c) Line profile of line in (b).

4.4.3 Summary

In summary, a combination of STM and LEED have been used to characterise the close-packed and diffuse phases of TPP on Au(111). The close-packed phase displays a number of packing motifs which have been characterised *via* STM. The TPP molecules have been seen to sit in one of two orientations on the surface, which can either form blocks of a single orientations (AAAA), alternating the two (ABAB) or a selection of each (ABBABA). The unit cell for the close-packed phase has been determined using STM, FFT of an STM image and LEED, which gave three slightly different results. Using STM the unit cell of a full monolayer of TPP molecules on Au(111) has been defined to be $1.62 \pm 0.06nm \times 1.44 \pm 0.01$ nm with an angle of 105 $\pm 20°$, to account for the drift in the image. The unit cell can also be defined by taking the FFT of an STM image, which gives a unit cell of 1.29×1.29 nm and an angle of 90°. Using LEED the unit cell of 1.39×1.39 nm with an angle of 90°, which is comparable to the FFT result. The structures of these TPP assemblies are thought to be the same, however each method is extracting different information, resulting in different unit cell parameters. The unit cell calculated from STM images taken at 77 K displayed a significant amount of thermal drift, which caused the elongation of the image in a

specific direction, giving an angle with a large error and parallelogram shaped unit cell. The unit cell calculated from the LEED data gives an average across the surface and is likely to be the most appropriate measure of the unit cell of the extended structure because of this. The FFT method depends upon the quality of the STM image it was taken from, which makes it a highly variable method.

The close-packed phase was found to be non-commensurate with the gold surface at high coverage, which indicates that the structure is dictated by molecule-molecule interactions rather than surface-molecule. At low coverage the close-packed phase displays preferential adsorption of the small islands in the FCC region of the herringbone. It was found that the average separation of the island was 7.15 ± 0.24 nm and the average island size was two TPP molecules.

In the remainder of this chapter the ordering of the different arrangements of TPP will be quantified using the Voronoi tessellation, which provides a value for the statistical entropy of the surface.

4.5 Quantifying Order - Voronoi Tesselation

4.5.1 Calculating Statistical Entropy

Analysis of surface structures typically involves defining a unit cell, which requires long range order. Previously discussed was the unit cell and packing of the close packed phase of TPP and its transition to the diffuse phase upon heating. However, it is difficult to quantitatively compare these surfaces, due to the disorder of the diffuse phase, therefore a metric to quantify order is needed.

An additional technique that may be used to characterise the observed changes in the arrangement of TPP is based upon the Voronoi tessellation. This analysis method does not require long range order, however it does require that the surface can be defined in terms of a cellular structure. This type of analysis was first used in the 17^{th} century by Johannes Kepler and Rene Descartes, and then went through a revival in 1908 upon the publication of work by Georgy Voronoi [101] [102]. The Voronoi tessellation may be used to determine the statistical entropy of a cellular network; a quantity that defines the level of order or disorder within a network, and highlights any faults or deviations within the structure [103].

A Voronoi diagram is generated by defining a set of points, or 'generators', from which cells may be grown outwards, such that the cell bounds are equidistant from the surrounding points. [104] In the case of a molecular network, the centre of each molecule may be assigned as the 'generator point' and the cells grown around the molecule. If the molecules are in a close packed arrangement, the cells may be viewed as the Van der Waals radii of the molecules. The properties of the cells, including vertices, edges, and generators may then be analysed and compared against a Poisson (random) distribution to quantify the entropy's of the system. This is done using,

$$S = -\sum_{n} P_n \ln P_n, \tag{4.4}$$

where S is the statistical entropy, P_n is the probability that a Voronoi cell has n sides [105]. For a set of 100 perfectly ordered points, all equidistant, the cells that grown will all be the same size and shape, this can be seen in Figure 4.18a. In this case, the ordered set of points produces a set of square cells, all with 4 equal sides, due to the initial arrangement of the 'generators' (4.18b). The statistical entropy of the system is therefore zero ($S = 0$), which is to be expected as every cell

is identical. For a set of 100 points that have been randomly generated (Poisson distribution) the resultant Voronoi diagram is very different. It can be seen in Figure 4.18c that the cells produced using these points are all different shapes and sizes. The distribution of cell sides can be seen in 4.18d, and shows that the number of cell sides varies between 3 and 9 and follows an approximate Poisson distribution. This system has a statistical entropy of $S = -1.69$, which is comparable to the theoretical value for a random system, $S = -1.71$ [106].

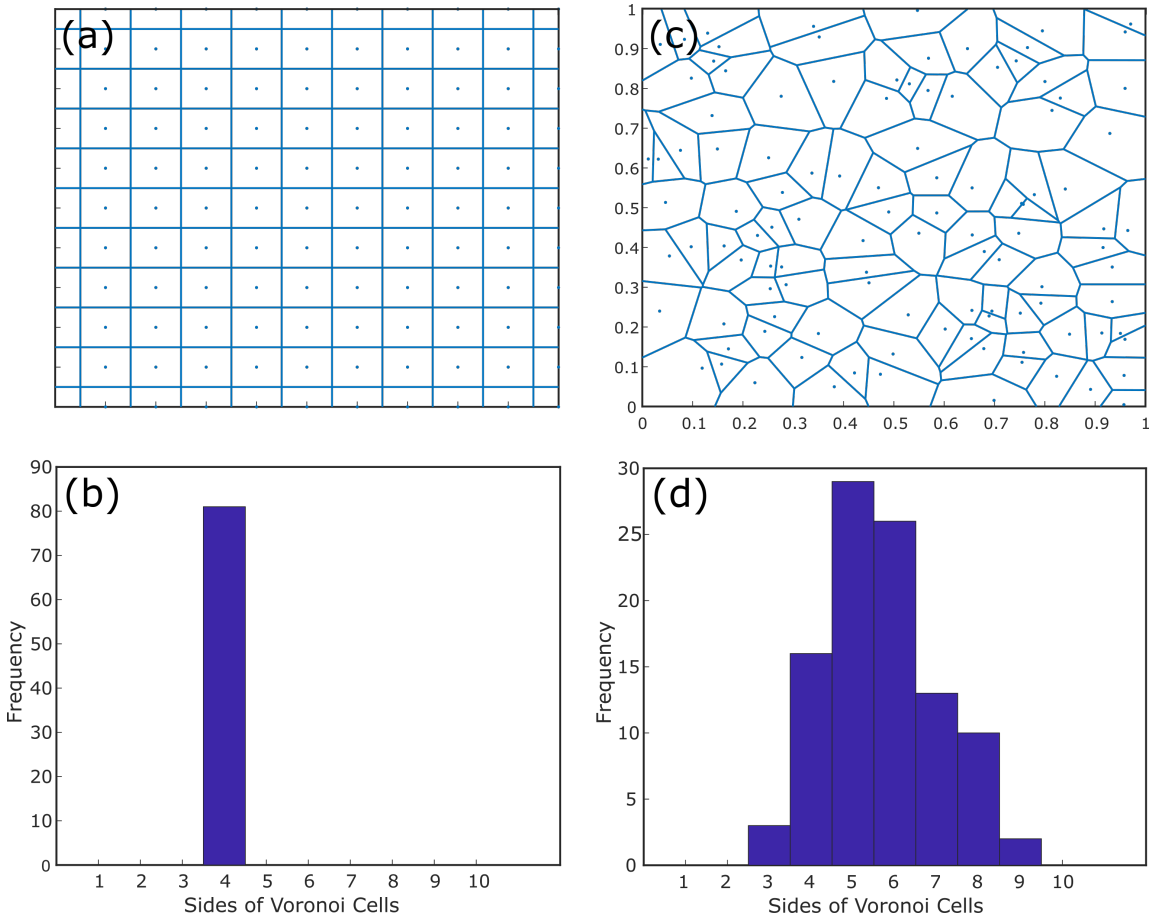

Figure 4.18: (a) Ordered network of points, resulting in identical cell shapes. (b) Histogram of corresponding cell sizes, showing all cells have the same number of sides. (c) Poisson distribution of random points, resulting in cells of various shapes and sizes. (d) Histogram of corresponding cell sizes, showing approximate Poisson distribution of cell sizes, ranging between 3 and 9 sides.

This method of analysis can be applied within nanoscience to quantify the entropy of structures seen in STM and AFM images. In work by C. P. Martin *et al.*, it is reported that the Voronoi tessellation was used to analyse the morphology of thiol-passivated gold nanoparticles during the

dewetting process. The particles are dissolved in toluene and as the solvent evaporates the nanoparticles are left on the surface in a cellular formation. The resulting structure was analysed using a Voronoi tessellation and the statistical entropy was found to be $S = -1.38$, lower than the expected value for a Poisson distribution (1.71), and therefore a more ordered structure. In this case it was concluded that this was due to coalescence of cells during the dewetting process. [106].

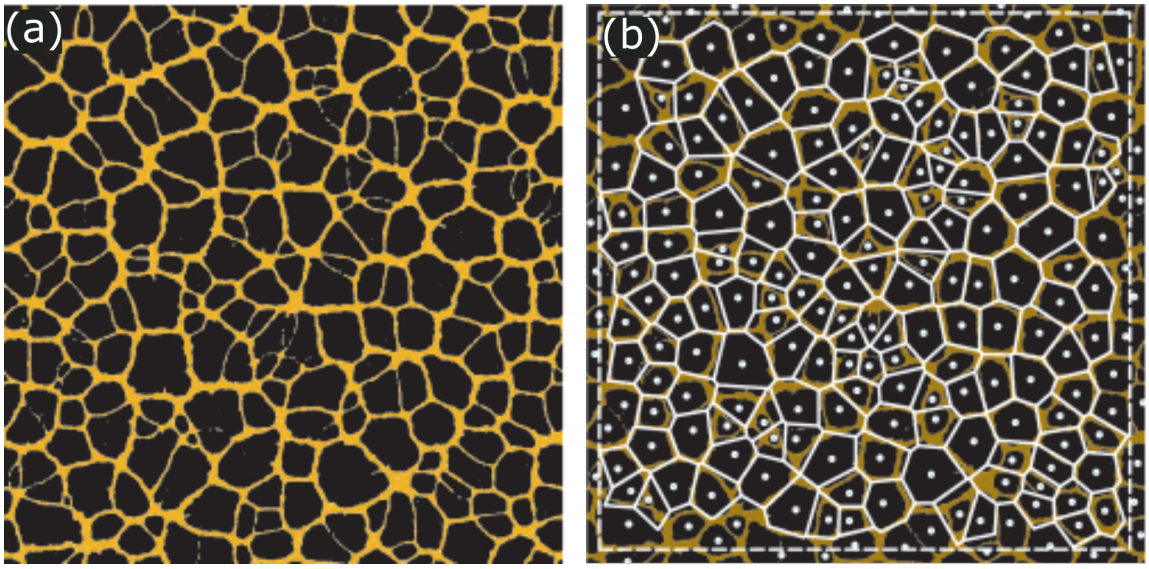

Figure 4.19: Cell network formed by dewetting of thiol-passivated gold nanoparticles (a) and resultant Voronoi tessellation using cell centres as generators (b). Images taken from [106]

4.5.2 Voronoi Tesselation of Close Packed and Diffuse Phases of TPP on Au(111)

Applying this methodology to the structures of TPP seen on Au(111) allows a way to quantitatively differentiate between these two phases. The generator points were placed at the centre of the TPP molecules, appearing in the STM images as a small dark circle in the middle of the molecule. The voronoi cells were grown outwards from these points to generate Voronoi diagrams for each phase, with points existing at the edges of the images were removed as their cells are able to grow indefinitely. For the close packed phase the resultant Voronoi diagram, seen in Figure 4.20a with the corresponding STM image underneath and b, with the image removed, shows an ordered arrangement of hexagonal cells, with a small number of pentagonal cells (4.20c) showing a small number of defects in the surface structure. The statistical entropy for this system was calculated

to be $S = -0.08$, which, is close to zero, indicating an ordered arrangement of TPP. The same procedure was applied to images from the diffuse phase and the resultant Voronoi diagram showed a broader distribution of cell shapes, with the number of sides varying from four to seven, with six being the most common, these results are shown in Figure 4.20d-f. The statistical entropy for this arrangement of TPP was found to be $S = -1.09$, a significantly more negative value, indicating that there is a larger degree of disorder amongst the TPP in this phase.

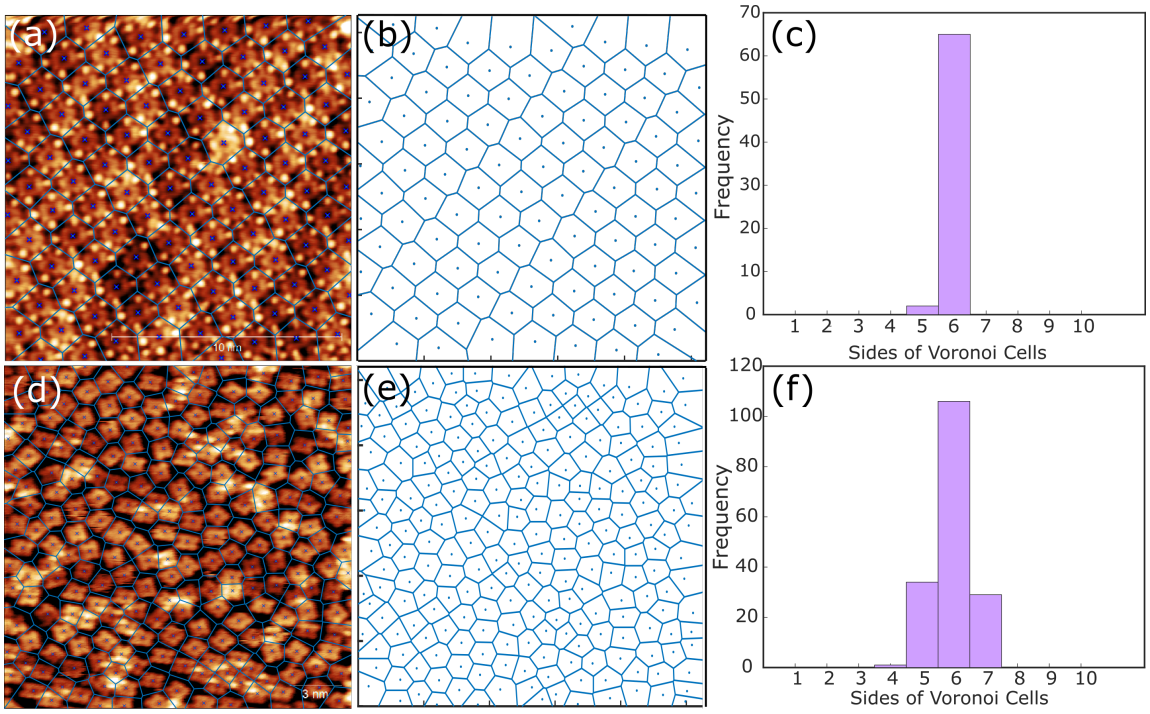

Figure 4.20: Comparison of close-packed and diffuse phases using Voronoi Tessellation. (a) Close packed TPP STM image with overlayed Voronoi tessellation. (b) Voronoi tessellation of the close packed phase, with STM image removed. (c) Corresponding histogram of cell sizes, showing predominantly 6 sided cells.(d) Diffuse phase TPP STM image with overlayed Voronoi tessellation. (e) Voronoi tessellation of the diffuse phase, with STM image removed. (f) Corresponding histogram of cell sizes, showing cells with sides varying from 4 to 8 in number.

By using the Voronoi tessellation the ordering of TPP molecules on Au(111) has been quantified for both the close-packed and the diffuse phase. By defining the Voronoi cells using the centre of the TPP molecules the statistical entropy for each different phase was calculated In the close-packed phase the TPP molecules are arranged in a regular order, which is represented by a low statistical entropy. In the diffuse phase the TPP molecules don't not possess long range order, which is

represented by a higher statistical entropy value. This method would be applicable to any system in which a cell could be defined, to find the statistical entropy possessed by the system.

4.6 Conclusion

In this chapter, two phases of TPP on Au(111) have been characterised using STM, LEED and the Voronoi tessellation. The unit cell of TPP on Au(111) has been defined using three methods, STM, LEED and FFT of STM images, these methods all given slightly different results. Using STM the unit cell of a full monolayer of TPP molecules on Au(111) has been defined to be $1.62 \pm 0.06 \times 1.44 \pm 0.01$ nm with an angle of 105 $\pm 20°$. The unit cell can also be defined by taking the FFT of an STM image, which gives a unit cell of $1.29 \pm 0.11 \times 1.29 \pm 0.11$ nm and an angle of 90°. Using LEED the unit cell of 1.39×1.39 nm with an angle of 90°, which is comparable to the FFT result. SPM techniques give very high lateral resolution, particularly in the 'fast-scan' direction, however due to thermal drift (or piezo electric creep) SPM can be unsuitable for angular measurements. These factors would affect the measurement of the unit cell of the overlayer, causing a stretching in a given direction and distortion of the angle between molecules, hence the large error on the angle measurement. LEED can be used to find a more accurate unit cell, as the result will not be distorted in a specific direction however, the LEED pattern gives an average of the surface but does not account for local variations, for example in the instance in which the two orientations of the TPP molecule were seen in alternating rows. The two techniques should be used in tandem to gain access to all of the information, the more accurate unit cell deduced from the LEED pattern, and the local information gained from the STM images. Each method gives a value which is correct, and the surface structures are not believed to be different, however what each method is measuring is slightly different due to the factors outlined above.

From the LEED patterns it was found that the overlayer of TPP was non-commensurate with the gold surface, implying there there is not a preferential adsorption site, and that the structure of the close-packed phase is more driven by molecule-molecule interactions than molecule-surface interactions. It has been observed that upon heating the sample the close-packed phase of TPP undergoes a transformation and forms the diffuse phase. The diffuse phase has been characterised using a combination of STM and LEED. The average separation between the TPP molecules was

calculated using both techniques, from the STM images it was calculated to be between 0.81 and 1.43 nm, while from the LEED it was calculated to be 0.93 and 1.52 nm which are in good agreement with each other. The phase change is likely to be caused by the triggering of an intramolecular ring-closing reaction, which consists of a dehydrogenation, followed by an electro-cyclic ring closing to form a flattened TPP derivative. There are a number of possible products form this reaction which accounts for the variety of molecular shapes seen in the diffuse phase. The flattening of the molecule removes the molecule-molecule interactions which stabilise the close-packed phase, which contributes to the disordered appearance of the surface.

To further characterise this transition from the close-packed phase of TPP to the diffuse phase, and identify the species produced in the diffuse phase, STS and KPFM were employed to gain information on the energies of the MOs and the LCPD of the system. The results of these experiments are discussed in the following chapter.

Chapter 5

Investigating the Origins of the Order to Disorder Transition: SPM as a Single Molecule Probe of Electronic Structure and Charge

5.1 Introduction

In this chapter experimental results are presented on the characterisation of the order-disorder transition displayed by TPP on Au(111) upon the annealing of the surface. Two different techniques for analysing the change that occurs in the TPP molecules are presented. Kelvin probe force spectroscopy (KPFS) was used to probe the contact potential difference (CPD) of the TPP molecules, while scanning tunneling spectroscopy (STS) was used to investigate the change in electronic structure of the TPP molecules. In these techniques the STM tip is used as a point probe, to study individual molecules.

5.1.1 KPFS Studies of Porphyrins

KPFS is a method for measuring the local contact potential difference (LCPD) between the tip and the sample, which as discussed in Chapter 2, is achieved by holding the tip in a fixed position above the surface, and sweeping the bias while measuring the frequency shift. The LCPD observed is expected to be different when the spectrum is taken over areas of the clean gold surface as compared to the spectra acquired above deposited molecule or species. This is particularly useful for observing information on the charge of species at a surface. In a study performed by L. Gross *et al.,* the charge state of gold and silver adatoms on a NaCl film was probed using KPFS. [107] It was found that the LCPD curve for a neutral Au atom(Au^0) shifted towards a negative voltage compared to the curve for the (Au^-). In the case of neutral silver atoms (Ag^0) and positively charged silver atoms (Ag^+), it was found that the positively charged Ag adatom shifted the curve to a more negative value than the neutral Ag adatom, consistent with the results for the Au adatoms. These results demonstrate that this technique can be used to effectively quantify changes in the charge of atoms or species before and after applying specific processes to a sample.

As well as measuring CPD of single points on a surface KPFM methodologies can also be applied to a small area of a surface, to produce a charge distribution map of that area, this is commonly used over single molecules. In a study performed by T. Niu *at al.,* naphthalocyanine (Npc) molecules on thin film NaCl on Cu(111), were imaged in a number of different ways, including using KPFM. [108] NPc molecules display a tautomerization process in which the two inner hydrogens can swap between oppoiste pairs of N atoms. The two fold symmetry of the molecule is visible in STM images, in which a nodal plane can be seen along the iminic (=N−) nitrogen direction. Using KPFM to image the charge density of the system before and after the tautomerization process it is possible to observe the shift in electron density on the molecule. It can be seen that the asymmetry between the iminic (=N−) and aminic (−NH−)nitrogen atoms of the molecule in the KPFM image switches before and after the tautomerization process. Using KPFM to produce an image of charge density is a useful tool for observing molecules on surfaces, however in this thesis KPFM is only used to take single point measurements.

5.1.2 STS on Porphyrins

STS is a useful technique for probing the electronic states and studying the HOMO-LUMO gap in molecules that have been deposited on surfaces. STS spectroscopy has been previously used to study TPP on Au(111), in order to probe and understand the difference between the 'bright' and 'dark' appearance TPP molecules within STM images. [39] It was thought that the 'bright' appearance of TPP may be caused by molecules sitting atop a gold adatom. Characteristic STS peaks are observed for the 'bright' and 'dark' TPP, with the bright TPP giving rise to peaks at -1.0 V_t and +1.5 V_t and the dark TPP producing peaks at +1.0 V_t and -1.5 V_t, where V_t is the applied bias at the STM tip. Metalated porphyrins have also been studied using this method, including TPP metalated with a gold atom. The spectra combined with corresponding STM images can allow the oxidation state of the metal atom in the central cavity to be interpreted. Two studies on AuTPP have shown that the observed HOMO-LUMO gap is 2.4 eV, when the oxidation state of the gold atom is Au^{3+}. The HOMO-LUMO gap was measured from the peaks in experimental STS spectra and compared to the predicted HOMO-LUMO gap calculated using DFT (2.77 eV). The oxidation state of the metal was reasoned to be 3^+ as the HOMO-LUMO gap for a TPP species containing an Au^+ ion was less than 1 eV, and the corresponding STM images showed a depression in the centre of the molecule, caused by doubly occupied d states, which indicates that Au^{2+} is not present [52] [51].

5.1.3 TPP on Au(111) - Low Coverage Regime

In this chapter, spectroscopy results from the close-packed phase of TPP and the diffuse phase of TPP are presented. The close-packed phase previously seen in Chapter 4 was characterised at a full monolayer coverage, and at a sub-monolayer coverage in which small islands of TPP were produced. In this set of experiments, a Au(111) single crystal was exposed to sublimed TPP, to produce a sub-monolayer coverage on the gold surface. The surface was then characterised at 5 K using STM, with the resultant images showing large islands of 10+ molecules across the surface (STM image shown in Figure 5.1a). There are significant number of TPP molecules in this image that are not part of a close-packed island. To facilitate additional characterisation a number of KPFM and STS spectra were taken on this surface and are presented in this chapter.

Annealing the Au(111)/TPP surface for 30 minutes and then characterising at 5 K reveals that the close-packed structure of the surface had undergone a similar change that was described in Chapter 4. Within the new phase of TPP, the large islands have broken apart and formed small islands consisting of one or two TPP molecules. These molecules are preferentially adsorbed in the FCC region of the herringbone, similar to the small islands seen previously, in Chapter 4 Figure 4.9. The appearance of the TPP molecules does not show the 'flattened' appearance previously seen (Chapter 4 Figure 4.8), as internal structure is still visible within the molecules, indicating the anneal is likely to be at a lower temperature. An STM image of this surface can be seen in Figure 5.1b. Although the flattening of the molecules in not readily discernible, the transformation from 'large' to 'small' islands is similar to the previously observed temperature-dependant transition. A number of KPFM and STS spectra were taken in this phase of TPP to be compared with the close-packed phase of TPP.

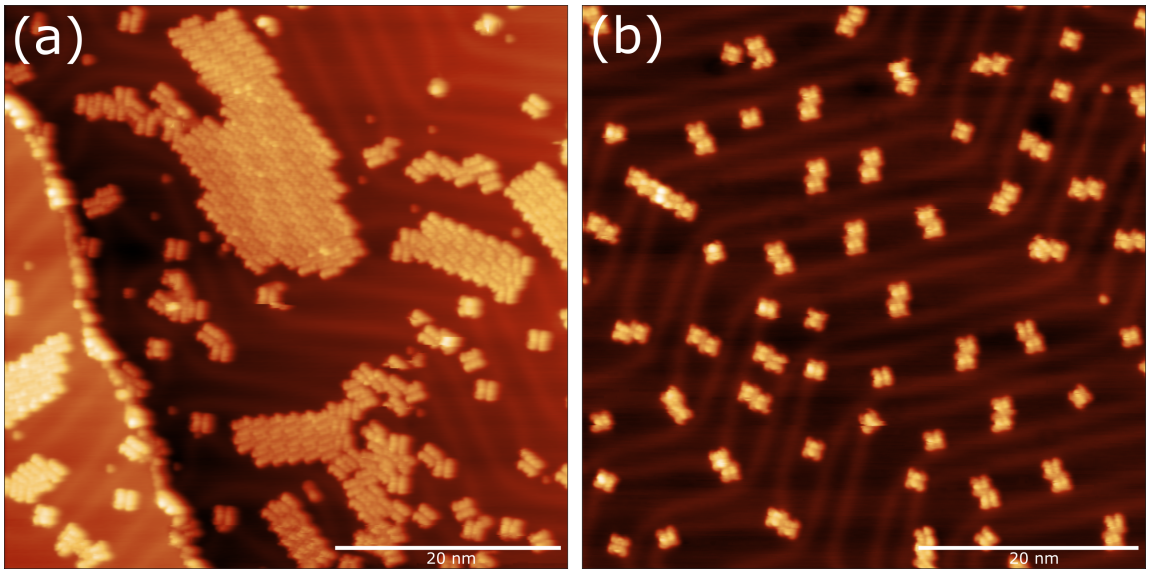

Figure 5.1: STM Images of the surface before and after annealing. (a) Islands of TPP on Au(111). Bias = -1.8 V, Setpoint = 100 pA. (b) 'Diffuse' phase of TPP on Au(111) that occurs upon annealing. Bias = -1.8 V Setpoint = 110 pA.

5.2 Kelvin Probe Force Microscopy of TPP on Au(111)

Kelvin probe force microscopy (KPFM) was used to probe the local contact potential difference (LCPD) between the tip and the TPP molecules before and after annealing, such measurements

may provide information on the charge state of the molecular species. In order to accquire KPFM spectra, measurements are taken in a dynamic-STM set-up. Therefore a qPlus sensor is used in place of an STM tip, allowing a small (pm) oscillation to be applied to the tip. This mode of operation allows the shift in resonant frequency (df) to be measured. [109] To take a kelvin probe spectrum the tip is held at a fixed height above the surface and the sample bias is swept, over a range of +2.0 V to -2.0 V, in this case. As the bias is swept the frequency shift ($\Delta f(V)$) is measured to produce a spectrum. The spectra are in the shape of a parabola, where the peak of the curve represents the applied bias at which the CPD is minimised.

5.2.1 KPFM on Clean Gold

Initially spectra were accquired over flat, clean areas of the gold surface. When recording a Kelvin probe spectrum of the metal surface it is assumed that the tip is formed from the same material as the surface, in this case gold. Here, it could be expected that the kelvin probe spectrum would show the peak of the parabola at 0 V. A spectrum taken of clean gold is pictured in Figure 5.2a, where the blue dots represent the raw data. An equation of the form $\Delta f(V) = c(x-a)^2 + b$, where a, b and c are constants, was fitted to the raw data to give the red line and the maximum point of the curve was found. The peak of the curve is at 0.48 ± 0.03 V) and the location of the spectrum is marked in Figure 5.2b with a purple dot. The range of peak values for the clean gold spectra can be seen in the histogram in Figure 5.2c. The average peak position was calculated to be 0.39 ± 0.15 V (see Table 5.1), which is significantly higher than the expected 0 V, this is potentially due to a number of factors. If the tip does not comprise entirely of clean gold, and contains some additional contaminant species, there would be an offset in the spectrum peak. In addition, local structure can effect the observed frequency shift, with the flat surface and a faceted tip exhibiting a non-zero CPD, and therefore the frequency shift will not be at exactly 0 V.

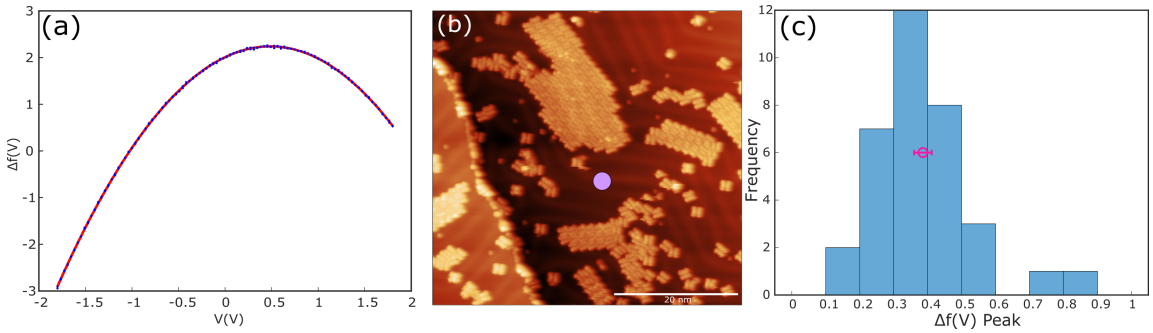

Figure 5.2: (a) KPFM data acquired above clean gold (blue dots showing raw data and red line showing fitted curve), maximum value = 0.48 ±0.03 V. (b) Islands of TPP on Au(111) with spectra site marked with a purple spot. Bias = -1.8 V, Setpoint = 100 pA. (c) histogram displaying the distribution of peak positions for Kelvin probe measurements of clean gold.

5.2.2 KPFM on phases of TPP

In order to investigate the change in CPD due to the presence of TPP under the probe, Kelvin probe spectra were taken on areas of clean gold and over TPP molecules alternatively, this assisted in ensuring the tip was clean before each TPP measurement. In Figure 5.3a an example Kelvin probe spectrum taken over the close-packed phase of TPP can be seen, with Figure 5.3b showing the position that the spectrum was taken. The peak of this particular spectrum is at 0.30 ±0.03 V, shifted in the negative direction compared to the peak of the clean gold spectrum shown in 5.2, thus indicating that the TPP is potentially positively charged with respect to the Au(111) substrate (although the magnitude of the charge is not determined here). The distribution of peak positions for pre-annealing TPP can be seen in Figure 5.3c, with the average and standard error, 0.32 ± 0.11 V (Table 5.1) marked by the red circle.

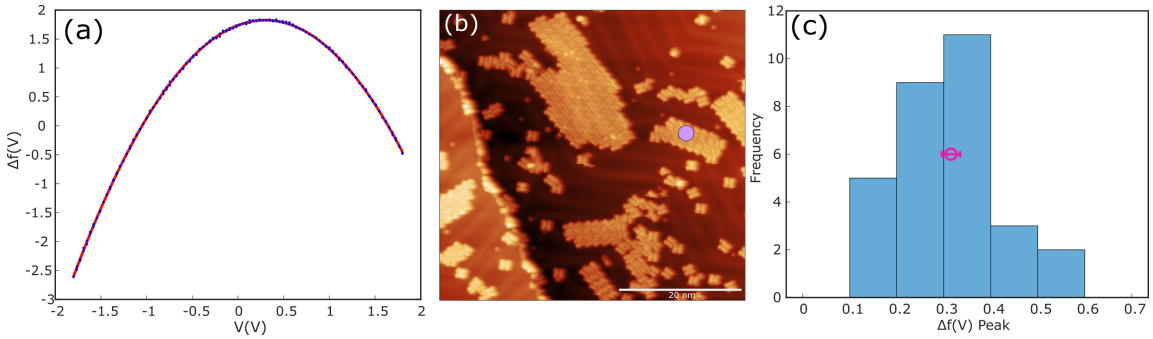

Figure 5.3: (a) Kelvin Probe Curve for TPP (blue dots showing raw data and red line showing fitted curve), maximum value = 0.30 ±0.03 V. (b) Islands of TPP on Au(111) with spectra site marked with a purple dot. Bias = -1.8 V, Setpoint = 100 pA.(c) histogram displaying the distribution of peak positions for Kelvin probe measurements of TPP prior to annealing.

To produce the diffuse phase of TPP the surface was annealed at 250±50 °, and the same procedure of taking spectra on areas of clean gold and TPP molecules, as outlined above, was performed on the diffuse phase. In Figure 5.4a a Kelvin probe spectrum taken over the diffuse phase TPP can be seen, with Figure 5.4b showing the position that the spectrum was taken. The peak of this particular spectrum is at 0.11 ±0.03 V, which shifted in the negative direction compared to the peak of the clean gold spectrum shown in Figure 5.2 (again indicative of a positive charge on TPP). The distribution of peak positions for the diffuse phase TPP can be seen in Figure 5.4c, with the average and standard error, 0.14 ± 0.11 marked by the red circle. This is a significant difference from the average peak position in the close-packed phase of TPP, with the average for the diffuse phase being shifted by -0.14 V compared to the close-packed phase. The shift in the negative direction indicates that TPP within the diffuse phase may have a more positive charge, as compared to TPP within the close-packed islands. However care must be taken when comparing the absolute and average peak values, as is discussed below.

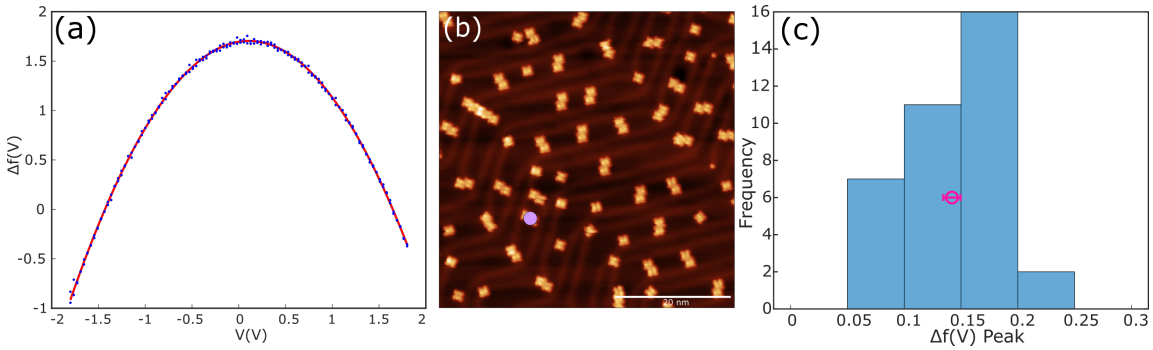

Figure 5.4: (a) Kelvin Probe Curve for Annealed TPP (blue dots showing raw data and red line showing fitted curve), maximum value = 0.11 ±0.03 V. (b) Annealed TPP on Au(111) with spectra site marked with a purple spot. Bias = -1.8 V, Setpoint = 110 pA.(c) Histogram displaying the distribution of peak positions for Kelvin probe measurements of TPP after annealing

Comparing the Average Values for Peak Position

Multiple spectra were taken for both clean gold and TPP in the close-packed and diffuse phases. These were then used to compare the average shift of TPP relative to clean gold for each phase, as well as a comparison of TPP in each phase. The average peak position for clean gold in the close-packed phase was found to be 0.39 ± 0.15 V, while the average peak position of TPP in the close-packed phase was found to be 0.32 ± 0.11 V. Comparing these values, the average shift for TPP relative to clean gold is -0.07 ± 0.15 V. A shift in the negative direction indicates that TPP may have a slight positive charge compared to the gold surface. The average peak position for clean gold in the diffuse phase was 0.18 ± 0.05 V. This is significantly different to the average calculated for the close packed phase. This discrepancy is likely to be caused by changes in the apex structure of the tip between the phases of TPP. The average peak position for TPP in the diffuse phase was 0.14 ± 0.11 V, displaying a shift in the negative direction of -0.04 ± 0.11 compared with clean gold, indicating a slight positive charge.

Close-packed TPP displays a more negative shift from clean gold ($- \pm 0.15$ V) than diffuse TPP (-0.04 ± 0.11 V), which suggests that close-packed TPP has a more positive charge than diffuse TPP. Due to the overlapping errors of these values it is challenging to draw a particular conclusions using this method of analysis. A second method comparing sequential gold and TPP values only is discussed below.

	Au	TPP	Difference
Close-Packed	0.39 ± 0.15	0.32 ± 0.11	0.07 ± 0.15
Diffuse	0.18 ± 0.05	0.14 ± 0.111	0.04 ± 0.11

Table 5.1: Kelvin Probe data: Average peak positions for pre-anneal clean gold and TPP and post-anneal clean gold and TPP.

Comparing Sequential Peak Positions

An alternate method for analysing this data is to only look at subsequent clean gold to TPP measurements. To do this, only TPP spectra that were taken directly after a clean gold spectrum were used, the peak position of the clean gold directly before was subtracted from the peak value from the TPP spectrum to obtain a $\Delta f(V_{CPD})$ 'shift'. This method ensures that the two spectra are taken using a tip with the same structure.

Two consecutive spectra can be seen in Figure 5.5a, with the difference highlighted by showing the peak positions for each spectrum and highlighting the difference between the peaks. The maximum in the TPP spectrum is clearly shifted in the negative direction with respect to the maximum in the clean gold spectrum (indicating a positively charged TPP). The histograms in Figure 5.5b show the distribution of the difference between the clean gold and TPP peak positions. The close-packed phase (shown in blue) shows and average shift of -0.11 ± 0.02 V, while the diffuse phase (shown in pink) displays an average shift of -0.059 ± 0.02 V, the average for each of these data sets are marked on the histograms in blue and pink respectively. Both close-packed and diffuse TPP have shifted to a more negative value than clean gold, with the close-packed TPP shifting more negative than the diffuse, giving a difference of 0.051 V between the phases.

KPFM Summary

Using these results, the following statements can be made, firstly, it is apparent that care must be taken when comparing KPFM measurements as small changes in tip structure between readings can present a significant effect on CPD measurements. Secondly, by processing the KPFM data in different ways, different interpretations may be highlighted. In both methods it can be seen that TPP in both the close-packed and diffuse phases is more positively charged than the gold surface. By comparing the absolute CPD measurements (average for two phases) the observed frequency shifts

would suggest that TPP is more positively charged in the diffuse phase relative to in the close-packed phase. However, by taking into account tip structure, and using only sequential measurements to measure frequency shift, the diffuse phase TPP displays slightly negative frequency shift, implying that it has a slight positive charge. The close-packed phase also has a negative frequency shift, but it is of greater magnitude, which indicates that close-packed phase TPP has a greater positive charge. Importantly this is a change, from which it can be stated that there has been a shift in LCPD facilitated by annealing. It is likely that the sequential measurements are the more accurate interpretation. Therefore, the close-packed phase can be stated to be more positively charged than both the diffuse phase and the gold surface. This may be due to enhanced hybridisation between close-packed TPP and the Au surface compared with the diffuse TPP. The 'flattening' of TPP (discussed further in Chapter 7) may lose the interaction with gold compared with saddle-shaped TPP in the close-packed phase. Interpretation in terms of CPD exclusively is a simplification of this change as other effects, such as the formation of dipoles may be relevant. [110]

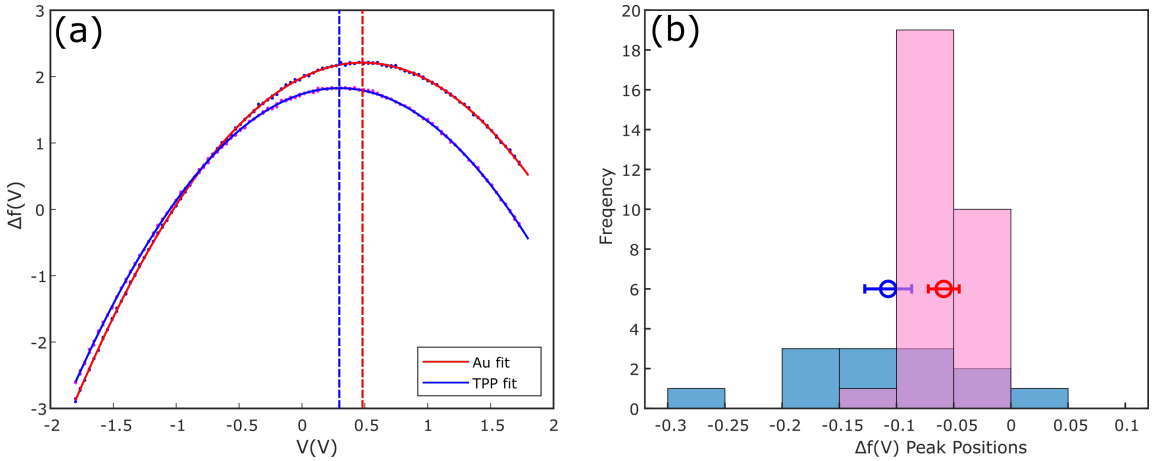

Figure 5.5: (a) Overlayed spectra of clean gold and TPP taken consecutively before annealing. Au spectrum blue dots representing raw data, red line showing fitted curve. TPP spectrum pink dots representing raw data, blue line showing fitted curve. (b) Histograms of difference in Au peaks and TPP peaks before and after annealing. close-packed phase histogram is shown in blue with the average difference shown by the blue circle. Diffuse phase histogram showing in pink with the average difference shown by the red circle.

5.3 STS of the Close-packed Phase of TPP on Au(111)

In order to facilitate further investigation of the change in properties of the TPP molecules caused by this order-disorder transition, scanning tunneling spectroscopy (STS) was used to probe the electronic structure, and identify molecular orbitals (MOs) of TPP on Au(111). An STS spectrum is produced by holding the tip at a fixed point above the surface and measuring the differential conductance (dI/dV) while the applied sample bias, (V_s), is swept over a range of values (see Chapter 2.1.2). In this section the STS spectra have been produced in one of two ways; the first requiring a small sinusoidal oscillation to be applied to the bias and the use of a lock-in amplifier to record the returned oscillating current, and the second by numerically differentiating the I(V) signal.

5.3.1 STS of Clean Gold and TPP

Initially, background spectra were taken above the clean Au(111) surface to ensure the tip is clean and metallic. In Figure 5.6a a spectrum for the clean gold surface is pictured, it displays a peak at -0.38 V which is attributed to the gold surface state [111]. The blue and pink lines refer to the forwards and backwards bias sweep. The position at which the spectrum was taken on the STM image can be seen in Figure 5.6b and is illustrated by a purple spot. This particular STM image displays a 'double-tip' artefact in the top half of the image.

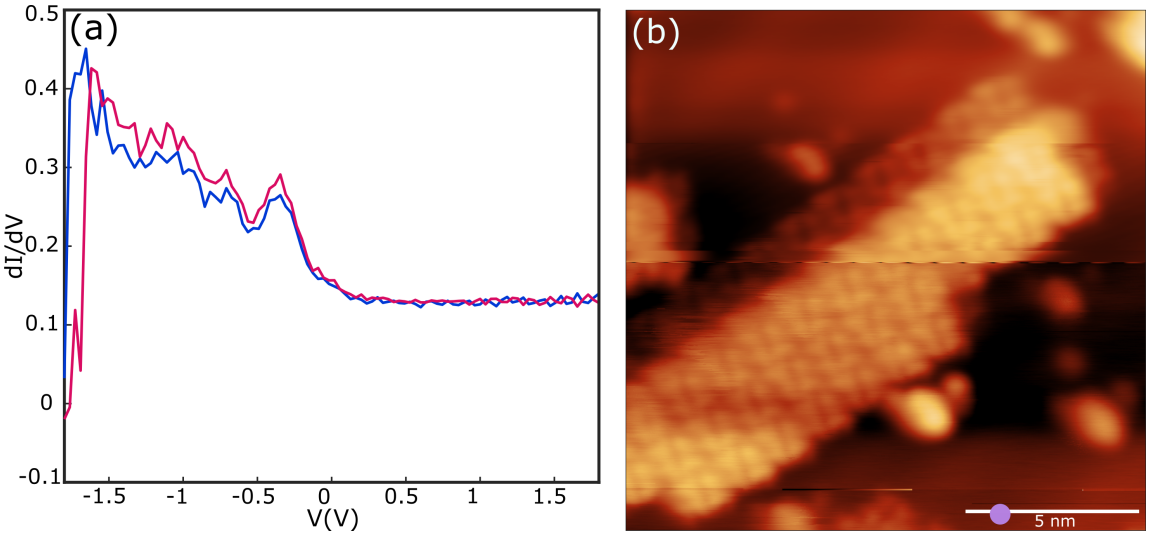

Figure 5.6: (a) STS spectrum for Clean Gold, with peak at -0.38 ±0.03V for surface state. (b) STM image of TPP on Au(111) with spectra site marked with a purple dot. Bias = 1.8 V, Setpoint = 200 pA

Spectra were then taken above clean gold and islands of TPP alternatively. In Figure 5.7a a spectrum taken above a TPP island is pictured, with the pink and blue lines representing the forwards and backwards scan as the bias is swept. There are peaks seen at 1.55±0.03, -0.31±0.03, -1.07±0.03 and -1.69 V±0.03, and a shoulder at -0.89±0.03 V. The peak at 1.55±0.03 V can be assigned to the HOMO of TPP and the peak at -1.07±0.03 V with the shoulder at -0.89±0.03 V can be assigned to the LUMO of TPP, based on previous studies of TPP on Au(111). [39] The peak at -0.31±0.03 V can be assigned to the gold surface state. This state is likely present due to hybridisation between the TPP and the Au(111) surface, as well as a contribution from direct tunneling, however the intensity is significantly lowered (the point at which the spectrum was acquired on the TPP island is indicated in Figure 5.7b by a purple dot).

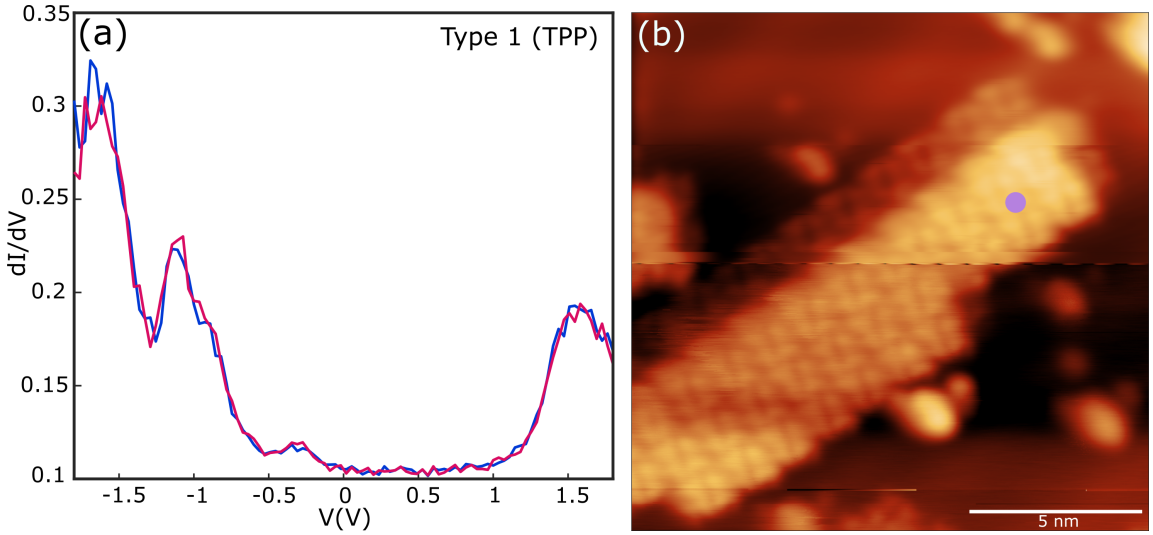

Figure 5.7: (a) STS spectrum for TPP, with peaks at -1.07 ±0.03V and 1.55 ±0.03V. (b) STM image of TPP on Au(111) with spectra site marked with a purple dot. Bias = 1.8 V, Setpoint = 200 pA.

Two different categories of peak positions were seen in the STS spectra of the close-packed phase of TPP. The first showed the HOMO and LUMO peaks to be at approximately -1 and +1.5 V respectively, which will be referred to as type 1. The second showed the HOMO and LUMO peaks to be at approximately -1.5 and +1 V respectively which will be referred to as type 2.

Based upon previous work, type 1 was assigned to a TPP molecule sitting on the Au(111) surface in its saddle conformation. [39] The peaks at -1 V and +1.5 V gave a HOMO-LUMO gap of 2.5 V. Type 2 was assigned to TPP sitting on top of a gold adatom. The peaks at -1.5 V and +1 V gave a HOMO-LUMO gap of 2.5 V. Figure 5.8a shows a histogram of every peak position measured in the dataset, it can be seen that there are peaks at -1.8 V, -1.0 V, -0.5 V and +1.5 V, an additional small peak can be seen at +1.0 V. Type 1 was found to account for 92% of the spectra with type 2 accounting for 8%.

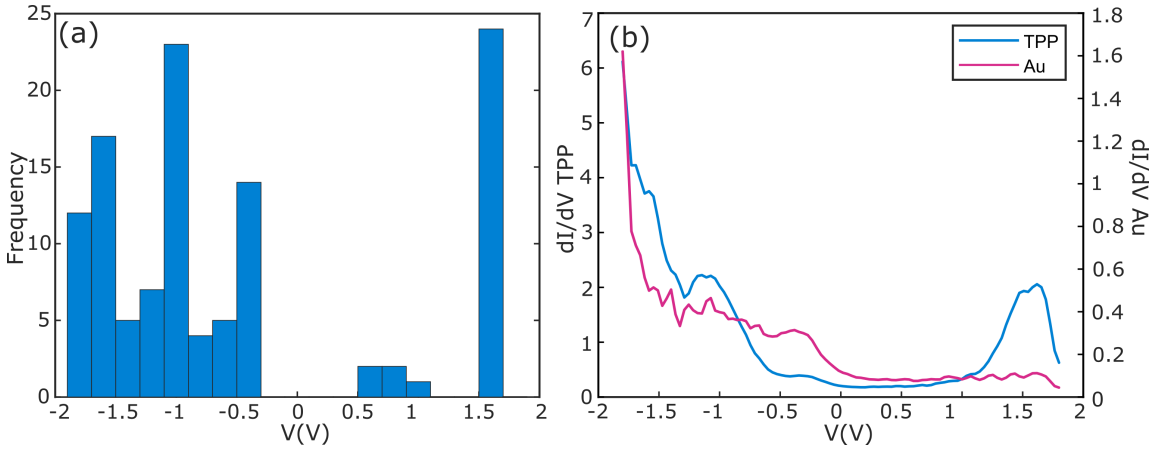

Figure 5.8: (a) Histogram of peak positions from $\frac{dI}{dV}$ spectra taken before annealing. (b) STS spectra for clean gold (pink line) with peak at -0.38±0.03 V, and TPP (blue line) with peaks at -1.11 ±0.03 V and 1.55 ±0.03 V.

5.3.2 Obtaining $\frac{dI}{dV}$: Numerical Differentiation vs a Lock-In Amplifier Technique

The spectra shown in Figures 5.6 and 5.7 were produced using a lock-in amplifier method. In this method, a small sinusoidal oscillation is applied to the bias, dV, which returns an oscillating current signal, dI. When the bias is swept across a range of voltages, an STS spectrum can be acquired by feeding the dI signal into a lock-in amplifier with the bias modulation used as a reference, and a signal proportional to the amplitude of the oscillation is returned. The advantage of this technique is that the level of noise in the resultant spectra is greatly reduced compared to a numerical differentiation of an I(V) signal. The disadvantage of this technique is that it takes a long time to produce each spectrum. An alternative method to acquire STS data is to record the current as the bias is swept over a range of values to give a curve of I(V). By taking the differential of this curve an STS spectra can be calculated. This method is significantly faster as the I(V) spectra can be taken rapidly in comparison to taking the dI/dV signal from the lock-in. However this is only a viable method if the I(V) spectrum is good quality as any noise in the I(V) spectrum will be transferred into the STS spectrum.

This set of experiments reported upon here includes spectra produced using both the lock-in method and the numerical differentiation method. The spectra acquired using the numerical

differentiation of I(V) were made by holding the tip at a fixed position above the surface and sweeping the bias over a range of values, typically -1.8 and 1.8 V. This gave a set of data points representing current as a function of voltage. A line was fitted to this data and then smoothed using a smoothing spline function [112] to reduce the noise in the data, (data smoothed over 199 points to produce a smoothly varying dataset). An equation of this line was determined and the differential, $\frac{dI}{dV}$, calculated to give a graph equivalent to an STS spectrum. These steps can be seen in Figure 5.9, where the I(V) data points (blue dots) with the smoothed line fitted to them (red line) can be seen in Figure 5.9a, the differentiated line can be seen in Figure 5.9b and the signal from the lock-in amplifier taken at the same point can be seen in Figure 5.9c. The two spectra give comparable values for the peak positions, so it was concluded that both methodologies can be implemented to acquire $\frac{dI}{dV}$ spectroscopic data.

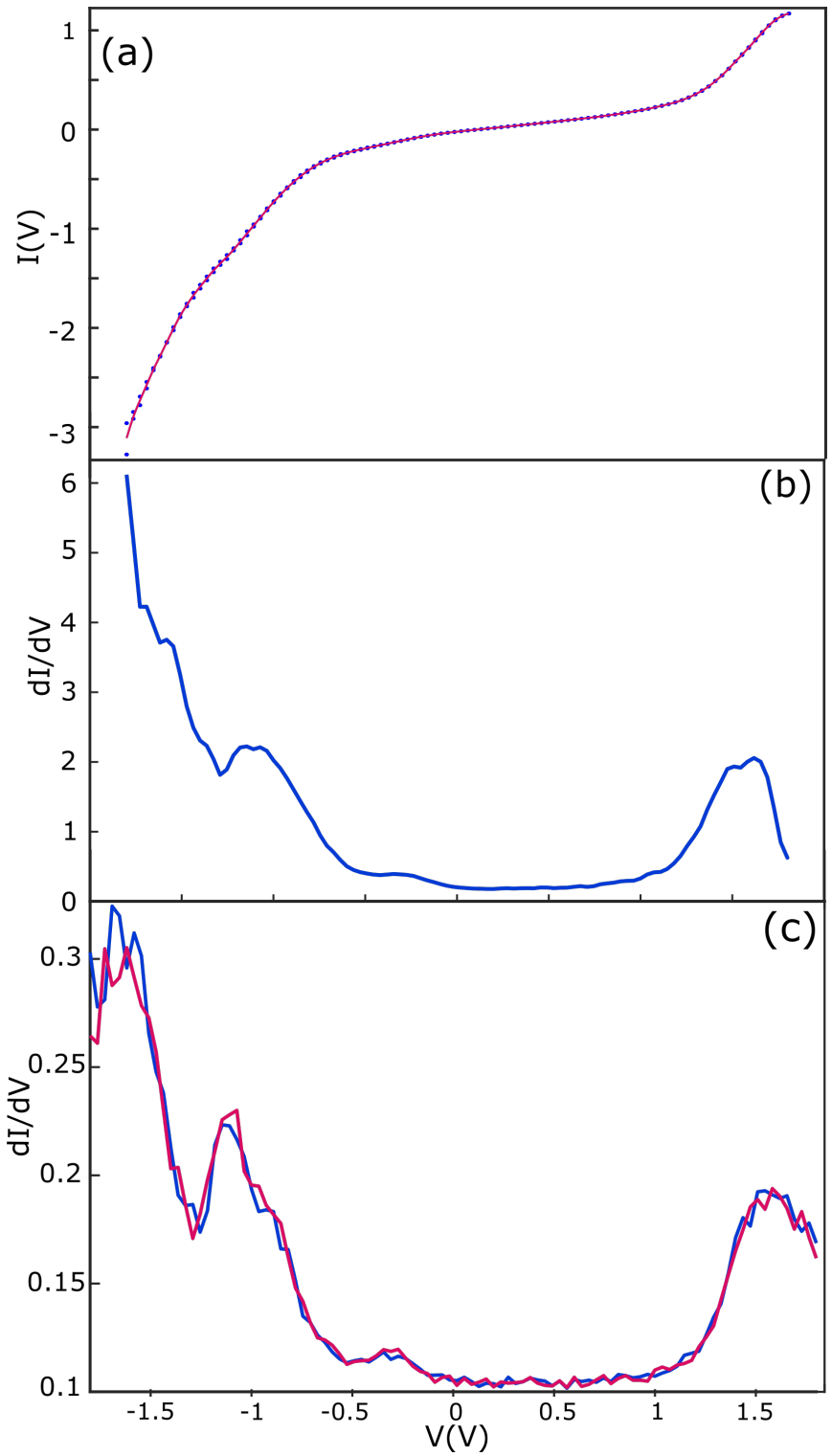

Figure 5.9: (a) I(V) data for TPP (blue dots) and curve fitted using smoothing spline (red line). (b) dI/dV for TPP acquired via numerical differentiation of smoothed data (a). (c) dI/dV signal for TPP acquired using a lock-in amplifier.

5.4 STS Characterisation of the TPP Diffuse Phase on Au(111)

The surface was heated to 250 ± 50 °to facilitate the formation of the diffuse phase of TPP, which was then studied using STS. In the close-packed phase, two types of spectra were seen for TPP, type 1, with peaks at -1.0 V and +1.5 V and type 2 which displayed peaks at -1.5 V and +1.0 V. The majority species before annealing was the type 1 TPP, which was 92% of the TPP spectra. After annealing a different ratio of types of TPP, and a new type of TPP spectrum was seen. These spectra were produced using the numerical differentiation of I(V).

Spectra taken on the TPP diffuse phase produced one of three distinct sets of peak positions. In Figure 5.10a a spectrum of a type 1 TPP molecule can be seen, with peaks at -1.1 ±0.03V for the HOMO and +1.6 V for the LUMO, and a small peak at ∼ 0.4 V, corresponding to the surface state. This spectrum was taken on a TPP molecule that was part of a small island of three TPP molecules. Figure 5.10b shows the corresponding STM image, with a purple dot showing where the spectrum was taken. Previously, this spectrum was assigned to TPP in its saddle conformation on the gold surface.

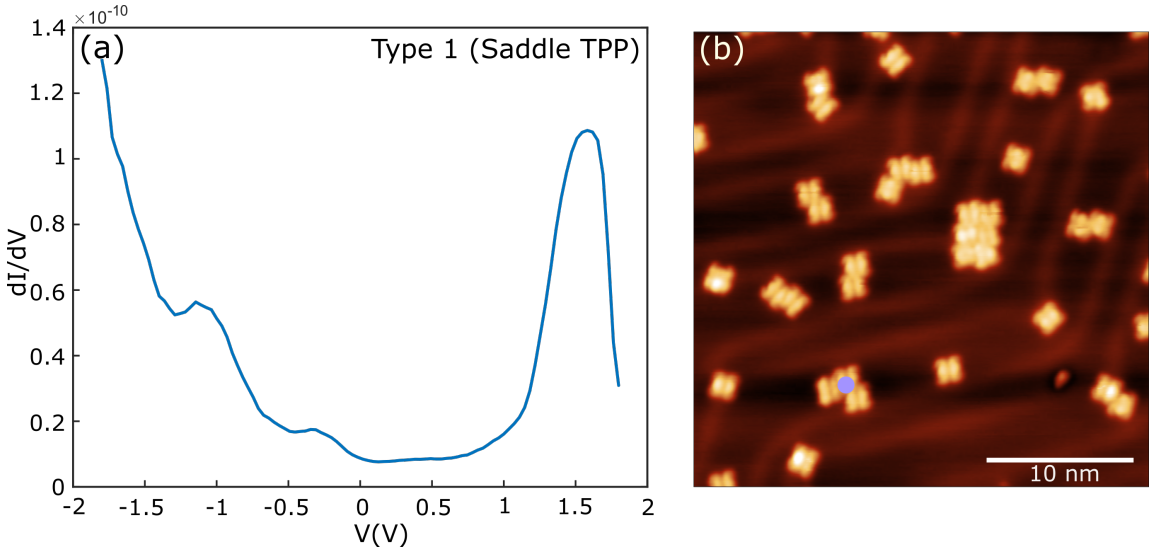

Figure 5.10: (a) STS spectrum for TPP after annealing, with peaks at -1.15 ±0.03V and 1.58±0.03 V assigned to TPP. (b) Annealed TPP on Au(111) with spectra site marked with a purple dot. Bias = -1.8 V, Setpoint = 80 pA.

The second type of TPP seen on in the diffuse phase is the previously described type 2 TPP. Figure 5.11a shows the STS spectrum for this type, displaying peaks at -1.66 ±0.03 V and +0.96±0.03

V corresponding to the HOMO and LUMO respectively. A small peak at ∼-0.4 V can also be seen, which is assigned to the surface state. This spectrum was taken over a single TPP molecule, the corresponding STM image can be seen in Figure 5.11b, where the position the spectrum was taken is marked by a purple dot. This type of spectrum was previously assigned to a TPP molecule sitting on top of a gold adatom (aaTPP) as previously reported. [39]

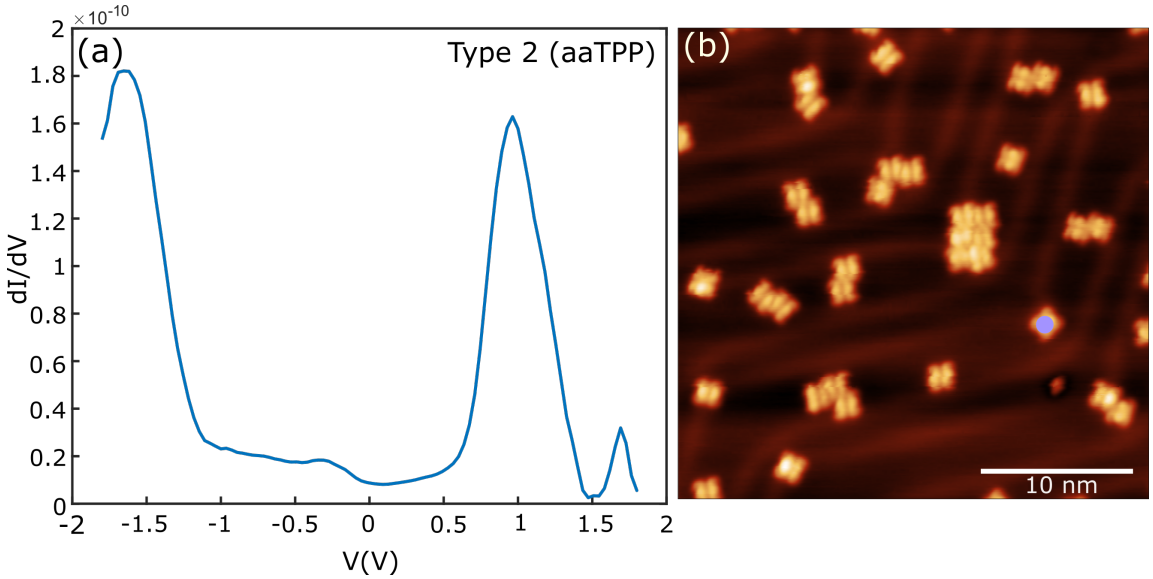

Figure 5.11: (a) STS spectrum for TPP after annealing, with peaks at -1.66±0.03 V and 0.96 ±0.03 V, assigned to AATPP (b) Annealed TPP on Au(111) with spectra site marked with a purple dot. Bias = -1.8 V, Setpoint = 80 pA.

An additional spectrum type was seen for TPP within the diffuse phase. An example of this spectral type can be seen in Figure 5.12a, with peaks at -1.07 ±0.03V and +1.0 ±0.03V for the HOMO and LUMO respectively. There is an additional small peak at ∼-0.4 V. This type of porphyrin has a smaller HOMO-LUMO gap of ∼2.0 V compared to the previous two types of spectra which both displayed a gap of ∼2.5 eV. This spectrum was taken on an isolated TPP molecule sitting on the gold surface, the corresponding STM image can be seen in Figure 5.12b, with a purple spot showing the position the spectra was taken. A tentative assignment of this spectrum is to a TPP species that had taken a gold atom into its central cavity to form metalated TPP (AuTPP), which is discussed further below.

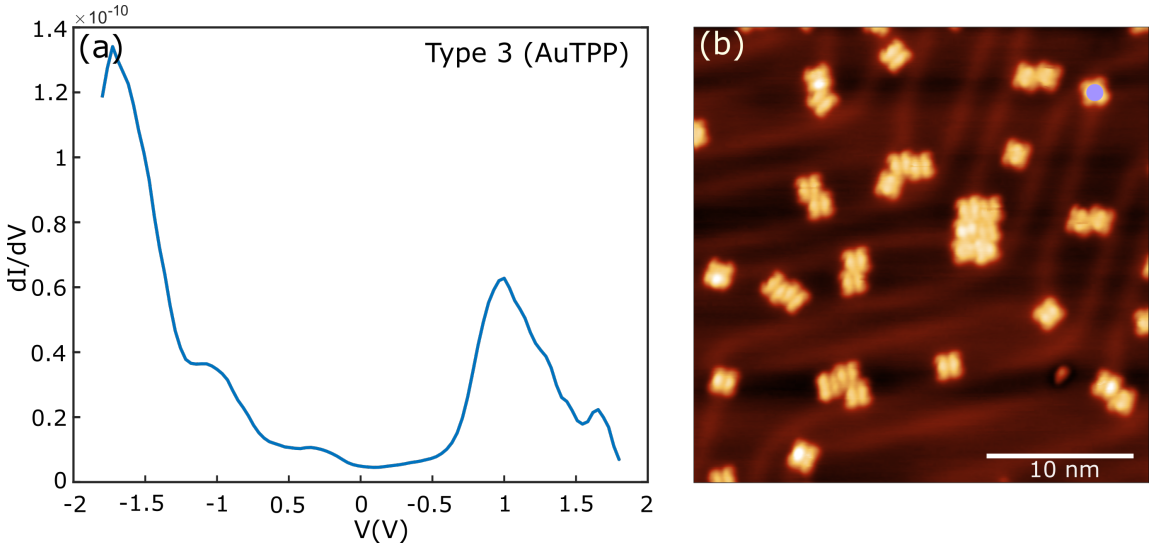

Figure 5.12: (a) STS spectrum for TPP after annealing, with peaks observed at -1.1 ±0.03 V and 1.0±0.03 V, assigned to AuTPP. (b) Annealed TPP on Au(111) with spectra site marked with a purple dot. Bias = -1.8 V, Setpoint = 80 pA.

In the diffuse phase the three types of porphyrins, assigned to TPP, aaTPP and AuTPP were found with relative abundance of at 31%, 52% and 17%, respectively. The percentage of TPP present has decreased from that present within the as-deposited close-packed phase, while the percentage of aaTPP has significantly increased and become the dominant species. This implies that the annealing process facilities the formation of the aaTPP. The AuTPP is a new species that was not previously seen in the close-packed phase and only appears in a small quantity in this data set. The distribution of all the peaks can be seen in the histogram in Figure 5.13a, four peaks can be seen, at approximately -1.7 V, -1.0 V, -0.4 V, +1.0 V and +1.5 V. The three types of spectra can be seen overlayed in Figure 5.13b, with their peaks at comparable positions to those in the histogram.

The spectra assigned to TPP and aaTPP have the same HOMO-LUMO gap (2.5 eV), and are shifted 0.5 eV relative to each other. The spectrum assigned to AuTPP is different in that it has a smaller HOMO-LUMO gap of 2.0 eV, with an additional occupied state at -1.0 V. The reduction in HOMO-LUMO gap can be attributed to metal to ligand charge transfer (MLCT) from the gold atom to the TPP, which is acting as a ligand. [113] TPP posesses energetically low lying π^* orbitals allowing for charge transfer from the d-orbitals of the gold to occur. The charge of the gold atom at

the centre of the metal complex can be estimated by looking at a combination of STM images and STS spectra. The STM images taken of the metalated TPP molecules show a small depression in the centre, suggesting the metal atom must have doubly occupied states, this excludes Au^{2+} as the central ion as it is a d9 ion and would give a bright centre. Looking at the STM images, Au^{+} and Au^{3+} are plausible candidates as they are d10 and d8 ions. The DFT calculations state that the HOMO-LUMO gap for the Au^{+} ion is less than 1 eV, which is significantly less than the observed HOMO-LUMO gap for this system, 2.0 eV, leaving Au^{3+} as the most likely oxidation state of the gold atom. [51] The HOMO-LUMO gap for Au^{3+} was calculated to be 2.77 eV which is higher than the experimental value, but this could be due to the DFT being performed on gas phase TPP as opposed to TPP on a gold surface (which would be a significant increase on the computational expense of the calculation) Furthermore, when deposited on a surface, the orbitals of the molecule may hybridise with surface states, shifting them to slightly different energies. Additionally, when looking at energy of LUMO in gas phase DFT the orbital is unoccupied, hence LUMO, but during STM experiments, a tunneling electron is being transferred into the LUMO, meaning that the orbital being probed is actually an excited state of the molecule, whereas DFT is for ground state, the discrepancy may also contribute to the observed difference.

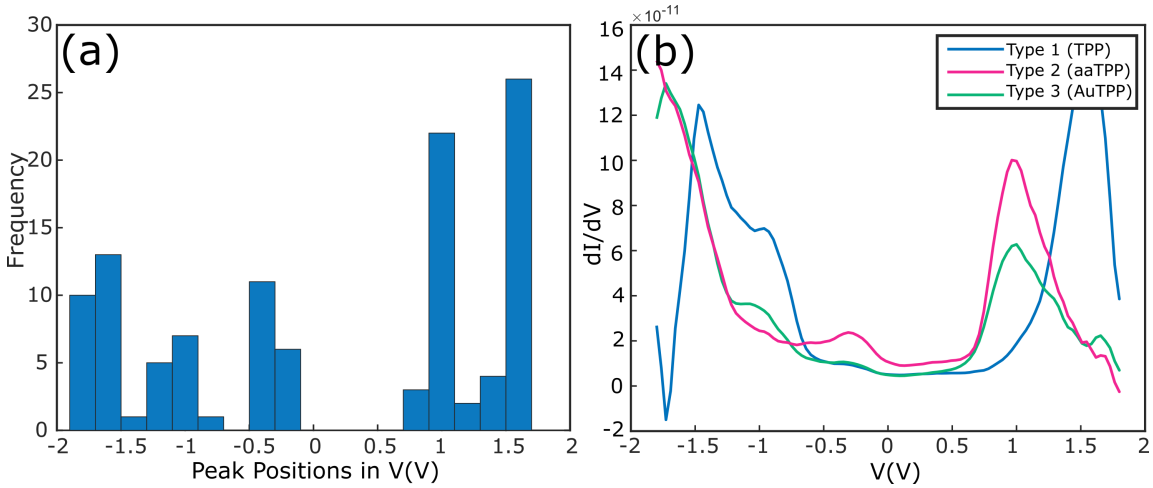

Figure 5.13: (a) Histogram of peak positions from spectra taken after annealing. (b) STS spectra of three 'types' different TPP molecules after annealing, TPP (blue line), aaTPP (pink line) and AuTPP (green line).

The TPP and aaTPP STS spectra are comparable to data previously presented by J. Meilke

et al. [39], in which STS spectra were measured for TPP molecules on Au(111). In the previous work the TPP molecules appeared at two different contrasts, bright and dark, with the bright TPP molecules corresponding the aaTPP spectra and the dark ones the TPP spectra. In Figure 5.14a the spectra acquired by J. Meilke *et al.,* for TPP and aaTPP are shown along side the spectra shown in Figure (5.14b). [39] The same peaks are present in the 'bright' and 'dark' TPP spectra in 5.14b as in the data presented in 5.14a, and the HOMO-LUMO gap and peak positions are the same. However, the observed colour contrast, reflecting the difference in apparent height, for the different types of TPP molecules was not present in the STM images acquired here. This can be rationalised as the STM images presented here were taken at a bias of -1.8 V, with the spectra for TPP and aaTPP both showing a peak at approximately this value, so the contrast isn't expected to be visible in the STM images.

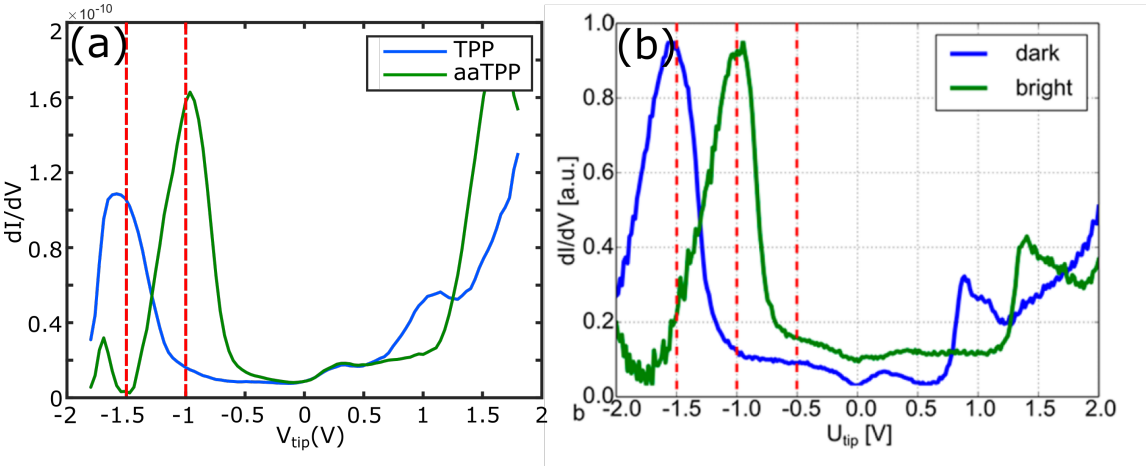

Figure 5.14: Comparing STS spectra with data from [39]. (a) Spectra for two types of TPP from this work, one with peaks at -1.15 V and 1.58 V, assigned to TPP (blue) and one with peaks at -1.655 V and 0.9636 V, assigned to AATPP (green). (b) Spectra from [39] for TPP (blue) and for TPP sitting atop an adatom (green).

Despite not displaying the clear colour contrast that the TPP molecules have in Ref. [39], the TPP and aaTPP may show some small differences in their internal structure. In Figure 5.15, the two different types of TPP can be seen, with the difference in their internal structure highlighted using pink ovals and blue circles. These two types were found to correlate with the spectra assigned to TPP and aaTPP, with the pink ovals belonging exclusively to the TPP and the blue circles to the aaTPP. The heights across these two different types of TPP were also measured by taking

line profiles of the STM image, however no quantifiable difference was found. The proportion of aaTPP on the surface is expected to be heavily dependant on the availability of gold atoms, which in turn will be dependant on the substrate temperature. During the annealing process it is possible that gold atoms detach from step edges and allow for the formation of more of the aaTPP species. Different sample preparation and deposition parameters may lead to different amounts of aaTPP in the pre-annealed (close-packed) phase.

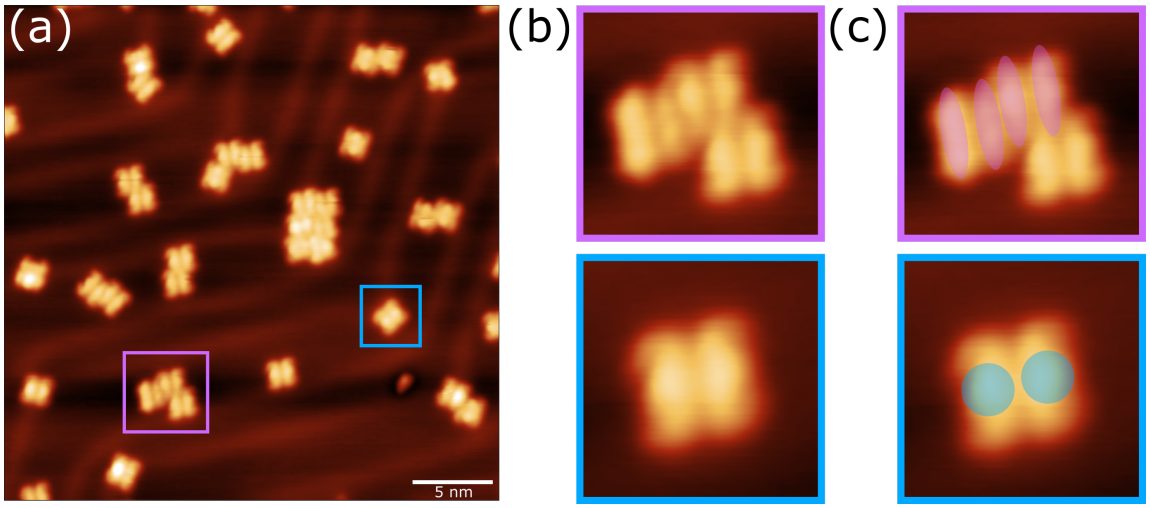

Figure 5.15: (a) STM image of the diffuse phase of TPP on Au(111) in which two different types of TPP internal structure can be seen. (b) Close up of TPP molecules displaying different internal structure. (c) Catagorisation of TPP molecules based on thier internal structure, with differences highlighted using translucent shapes. Bias = -1.8 V, Setpoint = 80 pA

Due to the complexities of accurately calibrating temperatures in a UHV environment, the anneal temperature in this set of experiments may not have reached the required temperature to activate the ring closing reaction discussed in Chapter 4. This is evidenced by the observation that, the individual TPP molecules do not have the same 'flattened' appearance as in the diffuse phase observed in Chapter 4. Additionally, some small islands of TPP molecules remained, having not fully broken apart.

STS performed on ring-closed TPP derivatives in a study by B. Ciera *et al.* has been previously reported. [44] In this study it was found that the F_4TPP, in its as-deposited state, prior to experiencing intramolecular reaction facilitated by annealing, displayed the characteristic STS peaks for a TPP molecule, with the HOMO peak at -0.9 V and the LUMO peak at 1.6 V, giving a HOMO-

LUMO gap of 2.5 V. After annealing, the planarised molecules were then probed again, revealing a change in energy of the HOMO and LUMO peaks, to -0.75 V and +0.65 V respectively and a reduction in HOMO-LUMO gap to 1.4 V. Comparing these results with the data presented here, it is unlikely that the anneal temperature was high enough to activate the ring-closing reaction.

5.5 Conclusion

Within this chapter SPM has been used to characterised single TPP molecules on Au(111) by employing KPFM to probe the charge state of individual molecules, and STS to determine the energy of the frontier orbitals and therefore, changes in electronic structure facilitated by annealing. By employing these techniques has enabled the mechanism which underlies the order-disorder transition which occurs when moving from the close-packed phase to the diffuse phase to be further understood. KPFM measurements indicated that the TPP molecules in both phases potentially possess a slight positive charge, with the close-packed phase being more positive relative to the diffuse phase. However as these measurements seem to be very sensitive to tip shape, linking to CPD is likely to be an over simplification. Using STS three distinct TPP species have been characterised. In the close-packed phase the majority of TPP species has been assigned to TPP (92%), with the minority being assigned to the aaTPP species (8%). In the diffuse phase it was observed that the proportion of TPP had decreased to account for 31%, while the proportion of aaTPP had increased to be the majority species (52%). A small amount of a new species, 17%, was also found to be present wich was assigned to AuTPP.

In order to further study how these three species relate to the order-disorder transition, XPS, NEXAFS and NIXSW were utilised to gain structural and chemical information on the underlying mechanisms that drive this transition. These experiments are discussed in the following two chapters.

Chapter 6

A Chemical Characterisation of the Order to Disorder Transition of TPP on Au(111)

6.1 Introduction

In this chapter experimental results are presented on the chemical characterisation of the order-disorder transition displayed by TPP on Au(111), this characterisation if faciliated by employing X-ray Photoelectron Spectroscopy (XPS) and Near Edge X-ray Absorbtion Fine Structure (NEXAFS) techniques.

In Chapter 4 it was shown that two different structural phases of TPP may be produced, by first depositing TPP molecules on a Au(111) surface, to give the ordered close-packed phase and then annealing the surface to observe the transition to the disordered diffuse phase.

This process was investigated further in Chapter 5, by measuring the spectroscopic properties of these phases. Three 'types' of TPP were identified, with the relative abundance of those species changing significantly after annealing. The different 'types' of TPP displayed different energies for the molecular HOMO and LUMO, (relative to the fermi level of the system) and different energies for the observed HOMO-LUMO gap.

In this chapter, XPS is used to probe the chemical environments and core orbitals of the nitrogen and carbon atoms of TPP and NEXAFS is used to probe the frontier orbitals of the nitrogen atoms.

6.1.1 XPS on Porphyrins

XPS is a technique frequently employed to characterise the chemical environments present within a sample and may be employed to study changes to these environments induced by chemical reactions. TPP has previously been studied on a variety of surfaces using XPS. In its as-deposited state, spectra detailing the C 1s and N 1s core levels have been discussed for a number of systems.

The C 1s core level of TPP on SiO_2 has previously been studied both experimentally and theoretically, using XPS and DFT [53]. The experimental XPS C1s spectrum was deconstructed into five peaks, which can be assigned to each different carbon environment in TPP; assigned as C_A, C_B, C_C and C_D and a shake-up feature, C_S (see Figure 2.9). These peaks appeared in a ratio of 51.2%, 17.0%, 8.6%, 17.0% and 6.2% respectively, corresponding to 23, 7, 4, 7 and 3 atoms per peak. DFT calculations for the same system showed a similar overall shape, but with some differences in terms of the individual peaks. The dominant peak C_A remains in the same position and corresponds to 24 carbon atoms. However, the remaining carbon atoms are assigned into four peaks of the same intensity, each corresponding to 4 carbon atoms each, this calculated spectrum can be seen in Figure 2.9. DFT allows for the consideration of very small differences which are not oberserved experimentally, which explains the difference in the theoretical and experimental spectra. The N 1s core level of TPP on Ag(111) has also previously been studied [54]. In this experiment XPS was used to monitor a metalation reaction as the film of TPP was exposed to Co, which was deposited *via* sublimation. The monolayer of TPP showed two peaks in its N 1s XPS spectrum, at 398.1 eV and 400.1 eV, which are assigned to the aminic nitrogen and the iminic nitrogen respectively. As the substrate was exposed to impinging Co atoms a third peak began to grow in the N 1s spectrum, assigned to metalated CoTPP. The third peak, positioned at 398.8 eV increased in intensity as more TPP molecules became metalated (due to the flow of Co atoms), while the other two peaks diminished proportionally, these XPS spectra can be seen in Figure 1.15.

6.2 Chemical Characterisation of TPP via X-Ray Photoelectron Spectroscopy

Here, XPS was employed to characterise the chemical environments of specific atoms within TPP for each phase observed. TPP was deposited on an Au(111) single crystal *via* sublimation until the close-packed phase was observed. This was achieved by monitoring the structure using LEED, previously discussed in Chapter 4, when a well defined LEED pattern is produced it was taken to be an indication that there is at least a monolayer of coverage, with the molecules forming a close-packed ordered network.

Initially a low-resolution overview XPS scan was recorded across a large energy range, 0-800 eV (Binding energy, BE), to show the chemical environments of all the atoms present on the surface. The overview scan of the close-packed monolayer of TPP is shown in Figure 6.1, where peaks corresponding to gold, carbon and nitrogen atoms can be seen. The fermi energy for this scan was measured to be 4.92 eV and all binding energies quoted for this scan have been corrected relative to this energy. At 84.1 eV and 87.6 eV two intense peaks are present, which represent the $Au4f_{7/2}$ and $Au4f_{5/2}$ levels respectively. The two larger peaks at 335.1 eV and 353.1 eV correspond to the $Au4d_{5/2}$ and $Au4d_{3/2}$ energy levels, while the $Au4p_{3/2}$ peak appears slightly smaller, at 545.6 eV. These Au peaks are characteristic of the gold substrate. The TPP molecule contains only nitrogen, carbon and hydrogen (which doesn't appear on the XPS spectra). The C1s peaks are visible in the overview spectrum, and appear as a small peak at 284.1 eV. There are multiple carbon environments present in TPP, however they are not distinguishable in this scan. The N 1s peaks are not clearly visible in the overview scan due to its low resolution, however they are magnified and are shown in the inset in Figure 6.1. There are two peaks in the N 1s region, which are due to the two chemical environments of the nitrogen atoms in TPP, aminic (−NH−) and iminic (=N−), the iminic peak appears at 397.1 eV and the aminic peaks appears at 399.1 eV. All of the values quoted here are comparable with literature values from the NIST.gov data base and are all in agreement with previously published XPS analysis of TPP. [114]

The XPS spectra have are fitted using a combination of Gaussian and Doniach-Sûnjiċ line shapes, which are shown by the coloured lines in each of the fits. The Shirley background applied to the spectra is linear, and a step function is then applied to each peak, centred on the maximum

of the peak (not shown). These are then combined to produce the black line which represents the sum of the background, the peaks and the step function.

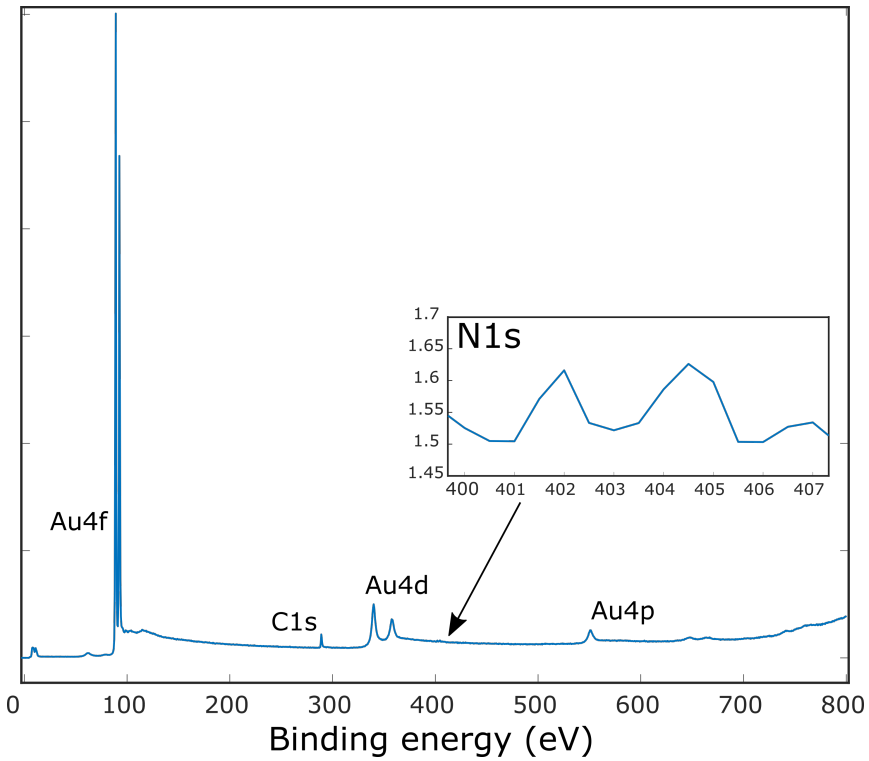

Figure 6.1: Low resolution overview XPS Scan where the Au4f 7/2 and 5/2, Au4d 5/2 and 3/2, Au4p 3/2 and C1s peaks are clearly visible, with the N 1s peaks shown in an inset graph due to their low intensity.

6.2.1 XPS Characterisation of the Close-Packed TPP Structure

The close-packed phase of TPP, which has been discussed previously in Chapters 4 and 5, displays an ordered network of TPP molecules (observed using both STM and LEED). The STS studies, discussed in Chapter 5 have shown that two types of TPP (TPP and adatom TPP (aaTPP))are present. Using knowledge of the structure of TPP to define several distinct chemical environments, it can be assumed that within the close-packed phase there will be at least four C1s environments and two N 1s environments, In addition, aaTPP may have slightly different chemical environments leading to an expectation that additional peaks will be observed within the XPS spectra. From measurements reported on by Nardi *et al.* [53] for TPP on SiO_2 it can be expected that there will be four peaks within the C1s spectrum, appearing over a range of 1.5 eV, with a shake-up

feature +3 eV from the dominant peak. From measurements taken by J. Gottfried *et al.,* [54] it can be expected that the N 1s will display two peaks with binding energies 398.6 and 400.1 eV corresponding to the aminic and iminic respectively.

Details of the C1s XPS Analysis

The fitting of the C 1s spectra was performed by PhD student M. Edmondson, but as discussion of this data is relevant to this work, my analysis of this data is included here.

The C 1s XPS spectra for the close-packed phase of TPP were fit in accordance with the data presented in [53], with an expectation of four peaks, one for each carbon environment. In Figure 6.2a the structure of TPP is presented, with each of the distinct carbon environment highlighted. There are twenty four carbon atoms in the four pendant phenyl rings, (highlighted in green) which are assigned to a single carbon environment, C_a. In the core of the TPP molecule there are three seperate environments, two with eight carbon atoms each, C_b and C_d (highlighted in pink and blue) and the third with 4 carbon atoms, C_c (highlighted in cyan). The C1s XPS spectrum acquired for TPP in the close-packed phase can be seen in Figure 6.2b. There is a main peak at 284.1 eV, with asymmetric broadening at the base, and evidence of a small shake-up feature on the left hand side, based upon previous experimental and theoretical studies. Four peaks have been fit to the spectra, as well as the small shake up feature, C_s (red). The positions of the peaks fit to the XPS spectrum are $C_a = 284.2$ eV, $C_b = 284.7$ eV, $C_c = 285.5$ eV and $C_d = 283.9$ eV. The shake up feature, C_s appears at 286.9 eV, shifted by 2.7 eV from the main peak.

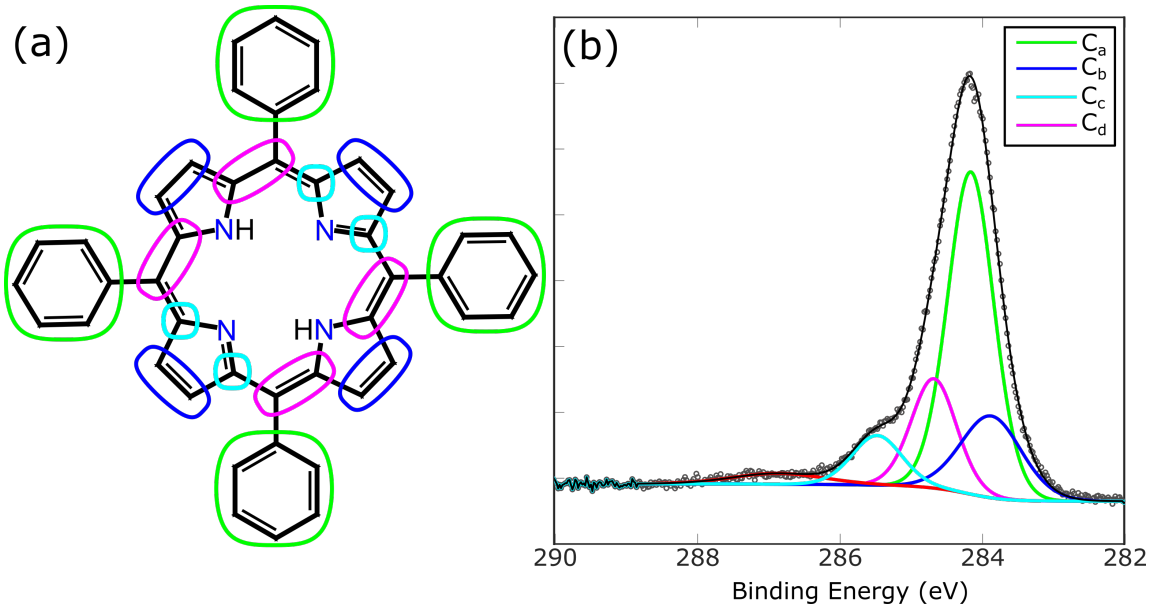

Figure 6.2: XPS fitting for C1s peaks for the close-packed arrangement. The coloured lines are summed to fit the points, with the curve showing the overall fit. (a) Different chemical environments for the carbon atoms in TPP. (b) Corresponding peak positions for environments highlighted in (a), Photon Energy= 900 eV.

These peak positions are comparable to those indentified by Nardi *et al.* [53], where the peak positions for C_a-C_d where 285.6, 286.0, 286.3, and 285.2 eV respectively, with shake-up feature, C_s at 288.75. The C 1s spectra of TPP on Au(111) displayed binding energies approximately 2 eV lower, attributed to interactions with the Au(111) surface. The peak fitting was achieved by constraining the peak areas according to the number of carbon atoms in that environment, to give a ratio of 54.5 %, 18.2 %, 9.1 % and 18.2 % for C_a, $C-b$, C_c and C_d (as expected based on the strcuture of TPP).

Details of the N1s XPS Analysis

In addition to C 1s spectra, the N 1s core level was also studied. In the close-packed phase of TPP two distinct peaks were visible in the N 1s XPS spectrum, as to be expected from the two different nitrogen environments, aminic (−NH−) and iminic (=N−) nitrogen. Multiple preparations of this surface were performed and each yielded a slightly different XPS spectrum. Two different preparations of the sample and their N 1s signals can be seen in Figure 6.3, both spectra have had four peaks fitted to them, N_α (green), NH_α (pink), N_β (cyan) and NH_β (blue), where N_α and N_β

refer to the iminic nitrogens and NH_α and NH_β refer to the aminic nitrogens. In Figure 6.3a the α environment, N_α and NH_α, gives rise to the dominant peaks, while the β environment peaks (N_β and NH_β) are of relatively low intensity in comparison; with an area ratio of 41.7 %, 44.4 %, 5.0 % and 8.9 % respectively. The positions of the peaks fit to this spectrum are 397.2, 399.3, 397.8 and 400.0 eV for N_α, NH_α, N_β and NH_β respectively. Figure 6.3b also shows four peaks, assigned in the same manner, however the intensity of the N_β and NH_β peaks are significantly larger. The peak positions are 397.2, 397.8, 399.4 and 400.0 eV for N_α, NH_α, N_β and NH_β respectively, with an area ratio of 20.0 %, 28.8 %, 34.4 %, and 16.8 %. There is 2.1 eV difference in binding energy between the α peaks and 2.3 eV between the β peaks. The details for all the peaks and thier ratios can be seen in Table 6.1.

It was anticipated that there would only be two peaks for the close-packed N1s core level from looking at data in [115], however it is clear that up to four peaks can be fit to the spectra in this data set. Previous studies have shown that there is a difference in binding energy for mono-layers and multi-layers of TPP, with the multi-layer displaying a higher binding energy [116]. However, the two sets of peaks in this data set are attributed to TPP molecules interacting more strongly with the gold substrate and causing two sets of peaks, one for TPP and one for a TPP species which is interacting with the gold substrate. The α peaks are assigned to the TPP and the β peaks are assigned to the TPP species interacting with the gold substrate, one each for Au−N and Au−HN. The interaction between TPP and the Au substrate could be altered by heating the sample, meaning that the proportion of the TPP molecules interacting with the gold would be highly dependant on the sample preparation, specifically the temperature of the sample plate. The nature of the TPP−Au interaction is not immediately apparent, and could be a direct interaction with the (111) surface or with an adatom species (discussed further below).

The spectrum in Figure 6.3a was prepared by depositing the TPP molecules onto the Au(111) crystal and then recording spectra, whereas the spectrum in 6.3b was prepared by first depositing the TPP molecules and then annealing the surface at a low temperature (∼400 K), which was not observed to produce the diffuse phase, (confirmed using LEED). In 6.3b the intensity of the β peaks is larger than in 6.3a, which suggests that the proportion of interacting molecules can be increased by gently heating. The increase in intensity of the peaks at higher BE following annealing, also suggests that these features are not due to the presence of multi-layer TPP growth.

These observations have similarities to the STS data presented in Chapter 5, where it was seen that the close-packed phase consisted of two different types of TPP, which were assigned to TPP and TPP sitting atop a gold adatom (aaTPP). TPP accounted for 92 % of the molecules probed using STS and aaTPP accounted for the remaining 8 %. Upon annealing the proportion of aaTPP increased, to give 52 % aaTPP and 31 % TPP. Heating the sample is thought to increase the availability of the gold atoms which has previously been discussed in [39] which is in agreement with the difference in sample preparations for these spectra, and hence by comparing these two data sets the TPP species interacting with the gold substrate is assigned to aaTPP.

Data set		N_α	NH_α	N_β	NH_β
Set 1	**BE (eV)**	397.2	399.3	397.8	400.0
	%	41.7%	44.4%	5.0%	8.9%
Set 2	**BE (eV)**	397.2	399.4	397.8	400.1
	%	20.0%	28.8%	34.4%	16.8%

Table 6.1: XPS Peak Positions in the close-packed phase of TPP

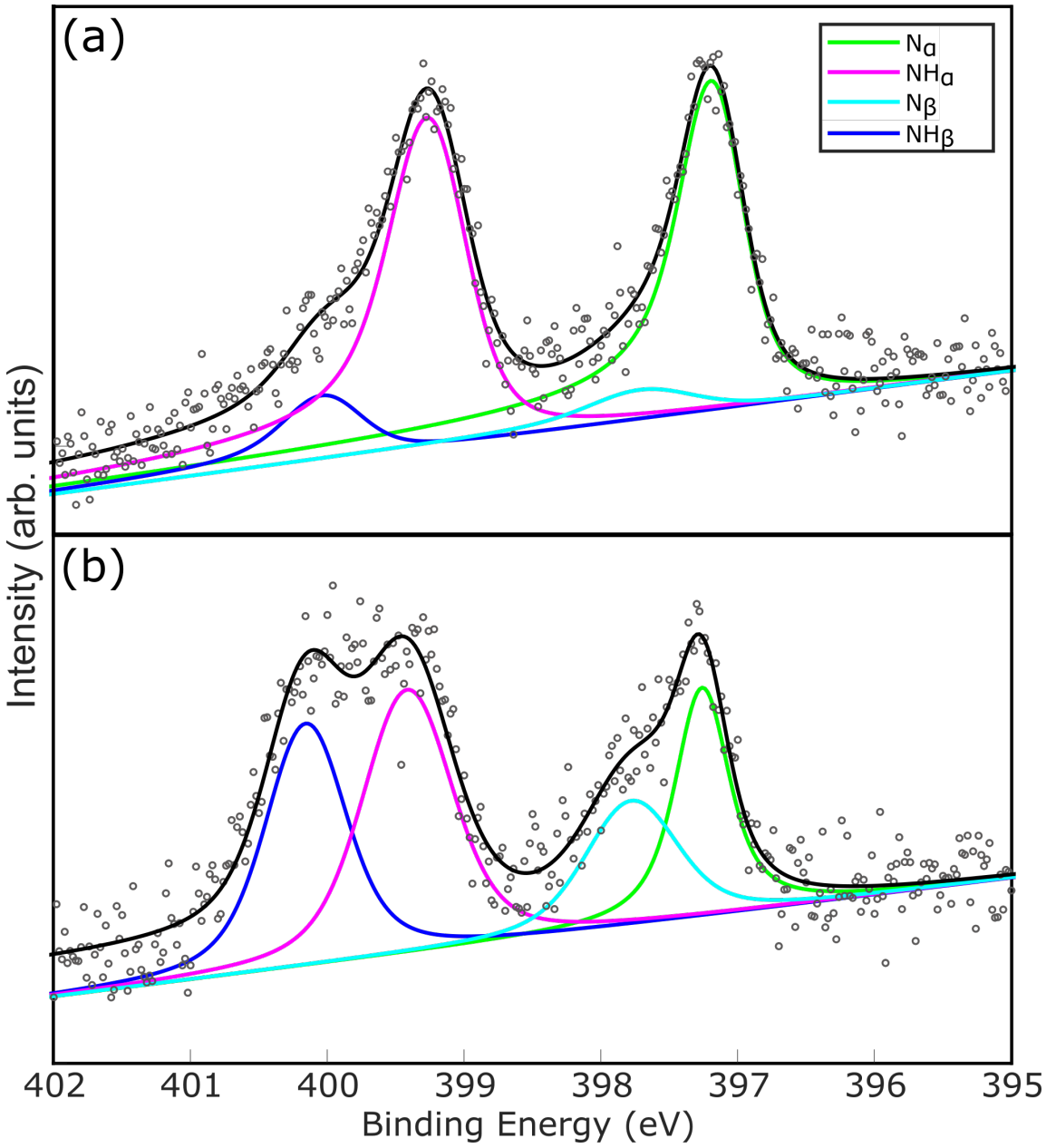

Figure 6.3: XPS fitting for two N1s spectra taken of the close-packed TPP arrangement, the coloured lines are summed to fit the points, with the curve showing the overall fit. (a) N1s spectra of close-packed arrangement of TPP, showing the fitting of 4 peaks to the data. Photon Energy = 900 eV (b) N1s spectra of close-packed arrangement of TPP, showing the fitting of 4 peaks to the data, however peaks N_β and NH_β have a significantly higher intensity than in (a) Photon energy = 900 eV.

6.2.2 Transition from a Close-Packed to a Diffuse phase: XPS Characterisation

The diffuse phase of TPP on Au(111) was produced by heating the sample plate to $\sim 260 \pm 50°C$ and monitoring the surface structure using LEED. The close-packed phase displayed a distinctive LEED pattern, with an ordered array of diffraction peaks (see 2.8), related to the arrangement of TPP on the surface. The diffuse phase is an amorphous phase of TPP, and does not have a defined LEED pattern, rather appearing as a fuzzy circle, with no clear spots, which can be seen in Figure 4.16. It may be inferred from the STS data, presented in Chapter 5 that the diffuse phase N 1s XPS spectrum will have a similar appearance to the N 1s spectra taken in the close-packed phase, and comprise of a mixture of TPP peaks and aaTPP peaks. The ratio of peaks can be expected to change to favour the aaTPP peaks, as the proportion of aaTPP STS spectra increased upon annealing. Following on from this, a peak for the metalated TPP may also become visible in this phase, however it can be expected to make only a small contribution as it accounts for a minor fraction (12%) of STS spectra. From measurements taken in [54] a peak for a metalated TPP molecule would appear at a binding energy between the aminic and imminic peaks. In the C 1s spectrum there may be a change related to the ring-closing reaction that was observed in Chapter 4 as this will change the carbon environments present in the TPP molecule.

C 1s XPS

Following the anneal at $260 \pm 50°C$, the C 1s core level spectrum for the diffuse phase showed two major differences to the spectrum of the close-packed arrangement of TPP.

Firstly, the number of peaks fitted to the spectrum is reduced. One interpretation is that as C_a and C_d are combined into a single 'main' peak, with C_b and C_c combined into a smaller secondary peak. The combination of C_a and C_d can be understood as a shift placing them at the same energy. Figure 6.4b shows the C1s XPS spectrum with three peaks fit to it, the main peak, C_a (green), a smaller peak C_b (blue) and a shake up feature, C_s (pink), with positions 284.0 eV, 284.9 eV and 286.3 eV respectively. The new carbon environments are depicted in 6.4a, and are shown in the colour of the corresponding peaks. The C_a environment now contains 32 carbon atoms, and has a proportion of 72.7% of the total peak area, the C_b environment now contains 12 carbon atoms,

and has a proportion of 27.3% of the total peak area. The proportional areas of the peaks are in agreement with the ratio of carbon atoms in the different chemical environments of the 'flattened' TPP.

Secondly, the position of the main peak has shifted from 284.2 eV in the close-packed arrangement to 284.0 eV in the diffuse phase, having shifted -0.2 eV. It is likely that this change is caused by the ring closing reaction. The reaction changes the aromaticity of the porhyrin ring, and therefore the electronic states and the environments of the carbon atoms within the molecule. The negative shift is consistent with the ring-closing reaction having taken place, as the planar species is less able to interact with the surface and also other molecules, reducing the binding energy of electrons within it. The 'lost' C_c peak will be due to these carbon atoms related to the ring closing undergoing a significant change in environment.

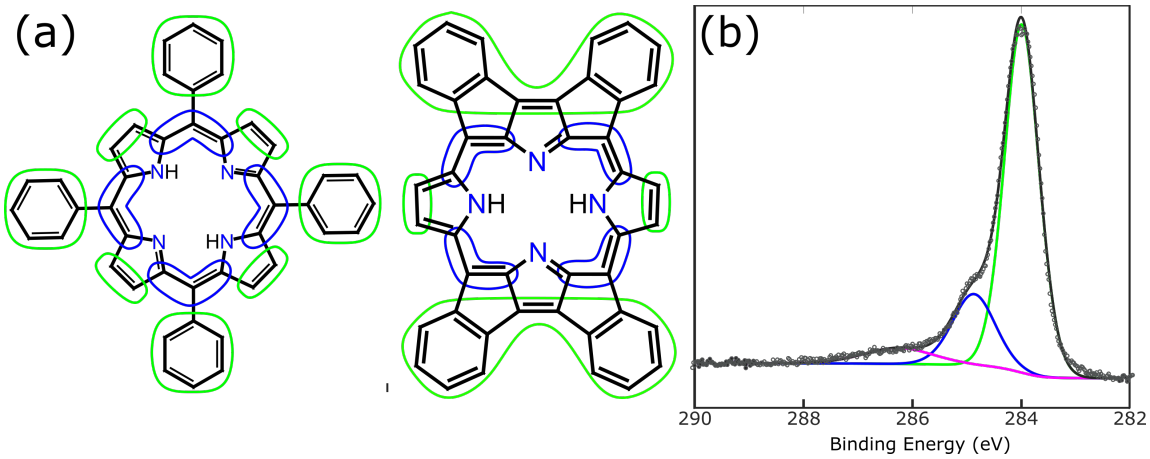

Figure 6.4: XPS fitting for C1s peaks for the diffuse phase of TPP. The coloured lines are summed to fit the points, with the black curve showing the overall fit. (a) Different chemical environments for the carbon atoms in TPP and also in the ring closed structure of TPP (b) Corresponding peak positions for environments highlighted in (a), Photon Energy= 900 eV.

N1s XPS

The N 1s core level in the diffuse phase shows different spectra to those taken in the close-packed phase, indicating some chemical change has occurred. A range of different spectra were acquired in this phase of TPP, which had varying numbers of distinct peaks, ranging from two to four peaks. The intensity of the peaks also varied, similar to the spectra seen in the close-packed phase. A set of N 1s XPS spectra taken in the diffuse phase from two different sample preparations can be seen

in Figure 6.5, 6.5a shows a spectrum with two environments, 6.5b shows three environments and 6.5c shows four environments.

Figure 6.5a has two peaks fit, N (green) and $N-H$ (blue) which are positioned at 397.4 eV and 399.2 eV respectively, with a difference of 1.8 eV in their binding energies. Both peaks are of similar intensity and have an area proportion of 49.8 % and 50.2 %. The presence of only two peaks indicated that only one type of TPP is the dominant species within this particular spectrum.

Comparing with the N_α and NH_α peaks in the close-packed phase, the difference in binding energy between the peaks has decreased, from 2.1 eV to 1.8 eV and the position of the imminic peak (N) has shifted by 0.2 eV, from 397.2 eV to 397.4 eV. These observations are potentially due to the ring-closing reaction inducing a change in the electronic state of the 'flattened' TPP.

Figure 6.5b has three peaks fit, N (green) and NH (blue) and N_μ (pink) which are positioned at 397.4 eV, 399.2 eV and 397.9 eV respectively. The N_μ peak has a significantly lower intensity than the N and NH peaks, with area proportions 43.9 %, 47.0 % and 9.1 % respectively. Assuming that the peaks labels N and NH still belong to the same species of porphyrin, the third peak would belong to a second species, with only one nitrogen environment. The third peak could be tentatively assigned to a metalated TPP molecule, which would have all the nitrogen atoms bonding to a central gold atom, and therefore would all be in the same environment. It is possible that there is also a small amount of the aaTPP species present, however the presence of only one obvious additional peak would indicate that it is such a small proportion that the peaks assigned to it do not have significant intensity

Figure 6.5c has four peaks fit, N_α (green), NH_α (blue), N_β (pink) and NH_β (cyan) which are positioned at 397.3 eV, 399.1 eV, 397.7 eV and 400.1 eV respectively. The peak positions here match the ones reported in the close-packed phase, suggesting the same two TPP species are present, TPP and aaTPP. The β peaks are at a higher intensity than the α peaks, implying that there is a larger proportion of the aaTPP species. The area proportions of the peaks are 15.1 %, 18.6 %, 22.7 % and 43.5 % for the N_α, NH_α, N_β and NH_β respectively. Details of all the peak positions and ratios can be found in Table 6.2 The peak previously assigned to AuTPP may also be present but due to its position being very similar to the N_β peak, it is likely being masked by it. In this spectrum, the aaTPP peaks have a higher intensity than in previous spectra, supporting the idea that the annealing process stimulates the formation of the aaTPP species. However, due

to the range of spectra seen in both the close-packed phase and the diffuse phase, prehaps a more accurate interpretation would be that the proportion of aaTPP on the surface has more to do with the sample preparation, and the number of available adatoms in different areas. The number of adatoms available will be highly dependant on the area of surface and local features (eg. step edges), thus explaining the different spectra seen when probing different locations on the sample. These peaks were assigned using the STS data reported in Chapter 5, in which spectra for both TPP and aaTPP were seen, this suggests that the shift in peak positions between the α and β peaks is caused by a change in electronic state. [39] The proportion of the metalated species however, is highly likely to be dependant on the anneal temperature/time, as small proportions of this species were seen the in diffuse phase of both the XPS and STS study, but not in the close-packed phase, indicating this species is produced upon heating.

Diffuse Spectra		N_α	NH_α	NH_β/N_μ	NH_β
2 Peaks	**BE (eV)**	397.4	399.2		
	%	49.8%	50.2%		
3 Peaks	**BE (eV)**	397.4	399.2	397.9	
	%	43.9%	47.0%	9.1%	
4 Peaks	**BE (eV)**	397.3	399.1	397.7	400.1
	%	15.1%	18.6%	22.7%	43.5%

Table 6.2: XPS Peak Positions in the Diffuse phase of TPP

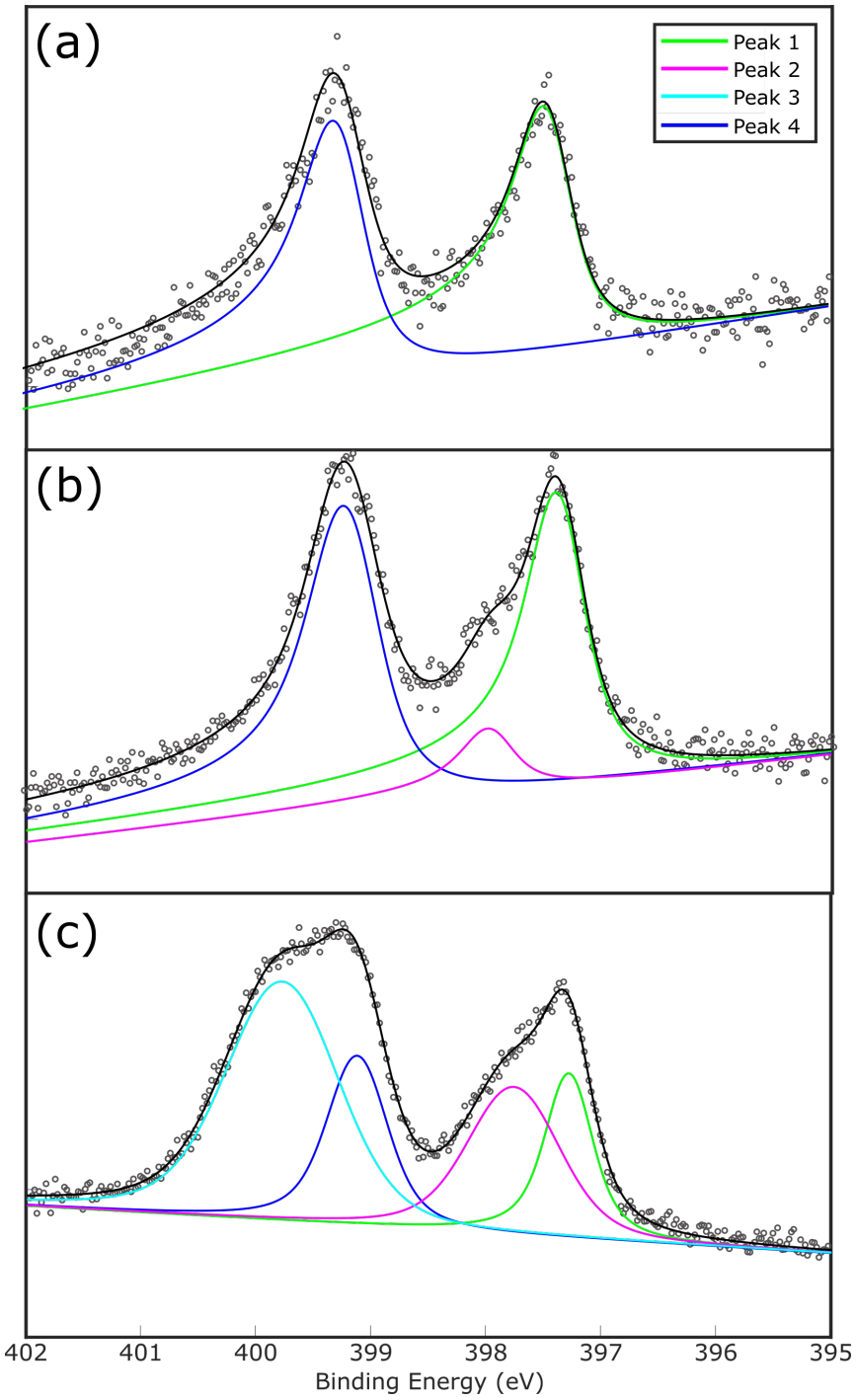

Figure 6.5: XPS fitting for three N1s spectra taken of the Diffuse phase. The coloured lines are summed to fit the points, with the curve showing the overall fit (a) N1s spectra of Diffuse phase of TPP, showing the fitting of 2 peaks to the data. Photon energy = 900 eV. (b) N1s spectra of Diffuse phase of TPP, showing the fitting of 3 peaks to the data. Photon energy = 900 eV (c). N1s spectra of Diffuse phase of TPP, showing the fitting of 4 peaks to the data. Photon energy = 600 eV.

6.2.3 Transition from the Diffuse Phase to the Metalated phase: XPS Characterisation

The metalated phase of TPP has not yet been discussed thus far as no evidence for a fully metalated phase of TPP was observed in the STM and STS studies in Chapters 4 and 5. Some partial metalation was observed within the diffuse phase that was probed by STS in Chapter 5, however the spectra assigned to metalated TPP (AuTPP) only occured in 17 % of the spectra in this phase. If metalation was to occur however, it can be expected that the XPS would change from displaying two peaks to a single peak as all available nitrogen atoms would be bonding to the gold metal. [54]

The sample was subsequently annealed to a higher temperature of $440 \pm 50°C$ and XPS data reveals than an additional phase of TPP may be achieved. The C1s and N1s spectra of this new phase both indicated that significant chemical changes have occurred. Both spectra can be seen in Figure 6.6. The C1s spectrum (6.6a) after the anneal shows one broad peak, with the minor peak at 284.9 eV (which was present in the diffuse phase) being lost. The peaks fit to this spectrum are labelled C_a (green), C_b (blue), and C_c (pink) with a small shake up feature C_s (cyan), with their positions being 283.9 eV, 284.4 eV, 285.0 eV and 286.4 eV respectively. The number of carbon atoms assigned to each peak is as follows; 32 in C_a, 8 in C_b and 4 in C_c, giving area proportions of 72.7%, 18.2% and 9.1% respectively.

The N1s spectrum (6.6b) now shows one new peak, having lost both the peaks at 397.2 and 399.1 eV which were previously present. The new single peak is at 398.0 eV, which is at the same energy as the N_μ peak that was seen in diffuse phase. The presence of a single peak indicates that there has been a chemical change amongst the TPP molecules to go from two nitrogen environments, amminic ($-$NH$-$) and imminic (=N$-$), to a single environment. A possible explanation for this behaviour would be that dehydrogenation and metalation has occurred, with all four nitrogen atoms coordinated to a metal atom (therefore in a single environment). The metal atom could be a gold atom removed from the surface layer, or an adatom species. As the diffuse phase is likely to be a flattened TPP derivative, the metalated phase would therefore be the metalated version of this molecule, which is a process that has been reported previously by B. Ciera *et al.*

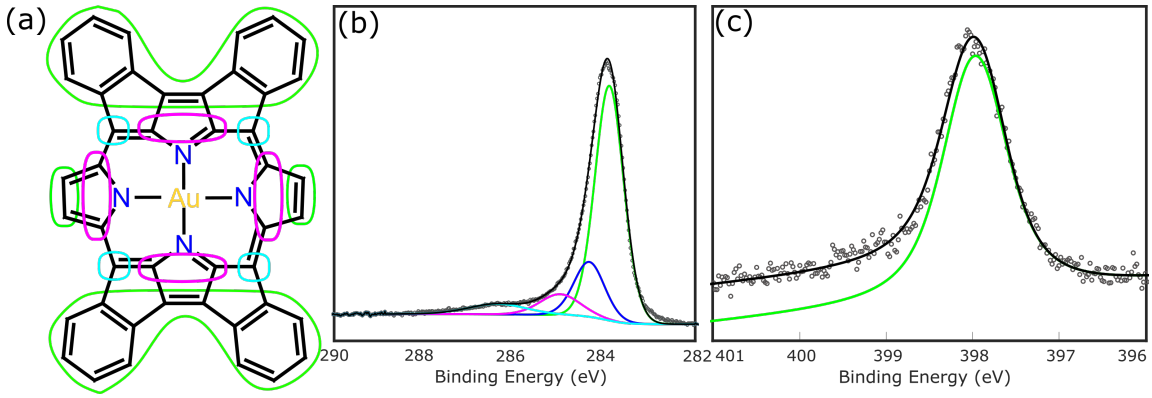

Figure 6.6: XPS fitting for Metalated phase of TPP.(a) C1s XPS spectrum showing three peaks. Photon Energy = 900 eV (b) N1s XPS spectrum, showing one peak at 397.97 eV. Photon Energy = 900 eV

6.2.4 Monitoring an On-surface Reaction: Temperature Programmed XPS on the Diffuse to Metalated Phases

The transition from the diffuse phase to the new metalated phase was studied further using temperature programmed XPS (TP-XPS), acquiring spectra while the reaction takes place. The sample is exposed to a reduced flux of 'soft' x-rays in an effort to limit beam damage and in the event that evidence for beam damage was seen (in the loss/formation of unexpected peaks) the sample was moved such that a new area was being illuminated. Based upon the XPS spectra acquired for the diffuse and metalated phases the anticipated result is that the two aminic and iminic peaks (located at 397.4 eV and 399.2 eV) will reduce, while a peak between them with an energy of 398.0 eV grows.

This is consistent with XPS spectra of TPP taken during a metalation with a Co atom. where a TPP molecule was metalated with Co and the reaction monitored with XPS, showing two peaks reducing and a third peak growing between them as more TPP molecules up-took the Co atoms. [54]

XPS spectra were taken continuously (each acquisition cycle taking 2 minutes) while the surface was heated from room temperature (300 K) to 480 ± 50 K. During this time the N and NH peaks were observed to decrease in intensity while a third peak grew between them, which is in agreement with our data above (sections 6.2.2 and 6.2.3). The change in intensity of the three peaks is presented in Figure 6.7, where the spectra are stacked according to the order in which they were

taken to produce a colour map. The increasing intensity of the peaks is mapped by increasing brightness in the colour gradient, where dark patches are areas of low intensity and white features are areas of high intensity. This colour map shows that the peaks at 399.2 and 397.4 eV (N and NH) begin to diminish, as a third peak at 398.0 eV grows, until the N and NH peaks no longer appear, and a single bright feature related to the metalated phase is present.

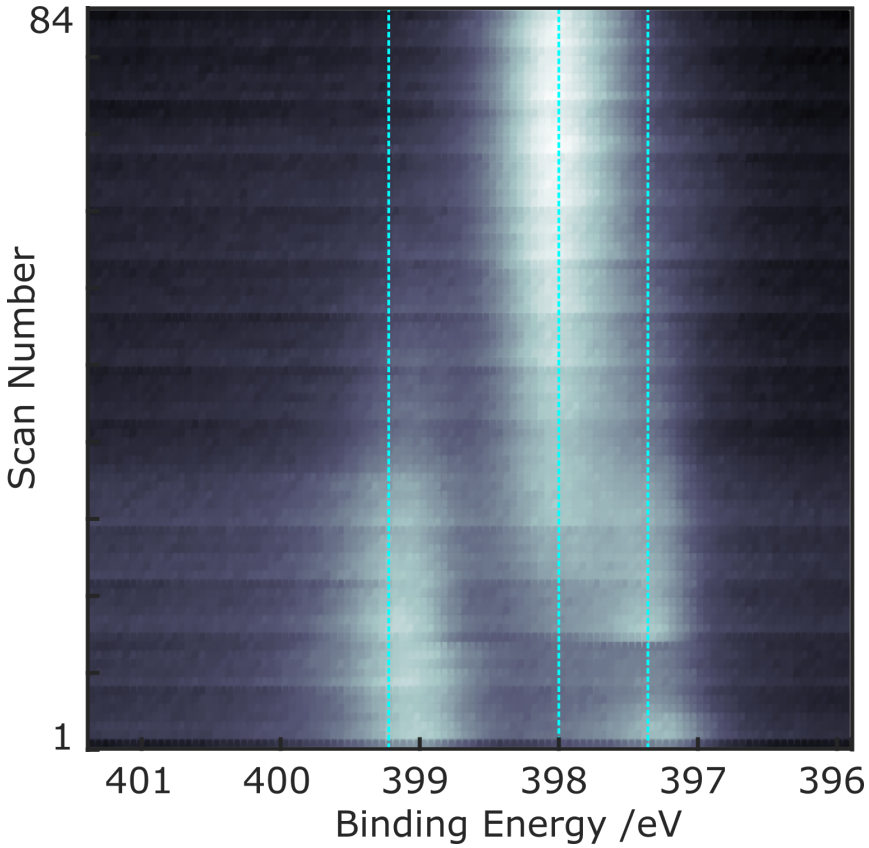

Figure 6.7: Colour gradient showing the change in the proportion of total peak area over each scan, where the intensity of the peak is represented by the intensity of the colour, where the dark areas have less intensity and the bright areas have higher intensity.

The change in the peak size was further analyzed by plotting the change in peak area over time and also temperature. Figure 6.8 shows two graphs, which present the data shown in Figure 6.7 in two seperate ways, 6.8a shows the change in proportion of total peak area over increasing temperature and 6.8b shows the change in proportion of total peak area over time. The change over temperature shows that peaks 1 decreases linearly with increasing temperature, while peaks 2 and 3 are relatively stable up until the temperature reaches 440 °C, where peak 2 rapidly starts

to decrease in area and peak 3 rapidly starts to increase. The change over time shows that the peak areas of Peak 1 and 2 (N and NH) decrease over time, while the peak area of Peak 3 (AuN) increases linearly over time. Another dataset for the N1s transition and two for the C1s transition (taken simultaneously to the N1s) can be seen in Appendix A Initially intensity is lost from the iminic nitrogen peak, (blue line in Figure 6.8) which suggests that the iminic nitrogen groups are the first to start forming an interaction with the gold atoms. It can then be seen as the temperature reached approximately $415 \pm 50^{\circ}C$ that a significant reduction in the aminic nitrogen occurred (pink line in Figure 6.8), this was coupled with an growth in the intensity of the N-Au peak (green line in Figure 6.8). This indicates that the mechanism for the metalation begins with an interaction between the iminic nitrogen atoms and the gold atom, followed by removal of the aminic protons and concluded with full incorporation of the gold atom into the plane of the porphyrin molecule.

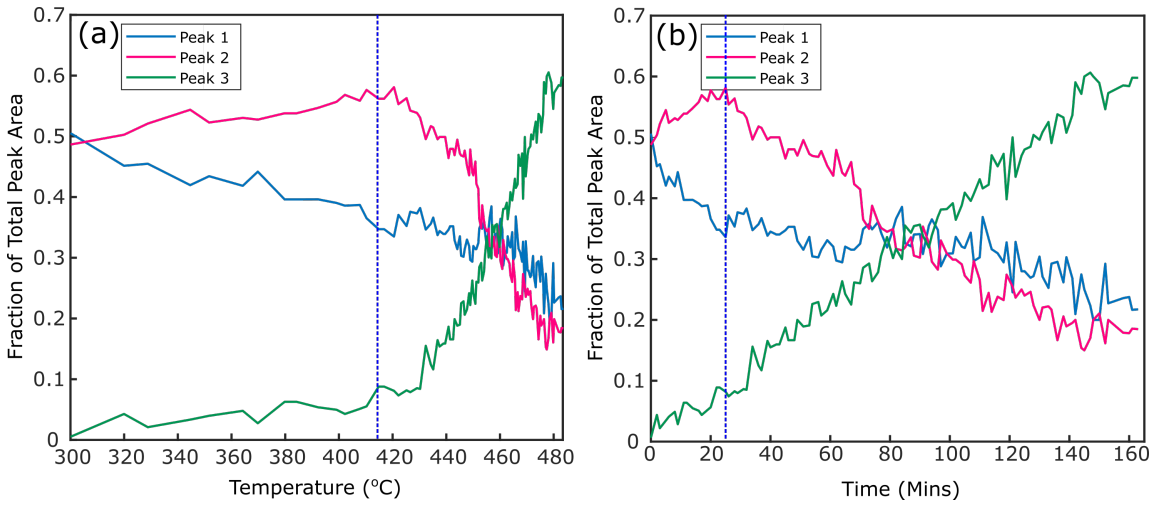

Figure 6.8: (a) shows the change in the area of the data presented in 6.7 with increasing temperature. (b) Shows the change in the area of the of the data presented in 6.7 with time.

6.3 NEXAFS

In contrast to XPS was which is to probe the occupied states in the core levels of molecules, NEXAFS provides insight to the unoccupied molecular states (such as the $\pi*$ and $\sigma*$ anti-bonding MOs). In addition NEXAFS can provide information about the oxidation state of the material and the orientation of the molecular orbitals relative to the surface. By varying the angle of the incident

x-rays relative to the surface plane, excitement of eletrons to different MOs becomes possible. For x-ray exposure at normal incidence (90°) excitation to the $\sigma*$ oribital is primary feature of the spectrum, with almost no contribution from excitation to the $\pi*$ oribital. At grazing incidence (20°in the experiments detailed here) the $\sigma*$ is no longer visible but the $\pi*$ becomes the dominant peak. Both orbitals can be probed at the 'magic angle' (53°).

In this study, spectra were taken at each angle (90°, 53°, 20°) in each phase of TPP (close-packed, diffuse, metalted) at the nitrogen k-edge.

In Figure 6.9a-c each set of spectra can be seen, for the close-packed, diffuse and metalated phases of TPP respectively. The normal incidence (NI) spectrum (blue) shows a σ^* peak, which occurs at 406.5 eV for both the close-packed and diffuse phases. In the metalated phase the energy of the σ^* has shifted to 407.5 eV and the peak itself is broader and less well defined, with a lower intensity. The metalated phase also displays a small peak for the π^* peak at 398.5 eV. The grazing incidence (GI) spectra (green) highlight the π^* peak and the $\pi^* + 1$, $\pi^* + 2$ peaks. The π^* peak is the single peak at the lowest energy in the spectra, which is at 397.8 eV for the close-packed and 397.6 eV for the diffuse. The metalated π^* orbital occurs at a higher energy of 398.5 eV, which mirrors the behaviour of the σ^* (ie. a small shift in both cases).

The grazing incidence spectra change significantly during the transition from close-packed to diffuse to metalated (this is where we expect to be sensitive to π^* features). As previously stated the energy of the π^* orbital shifts higher in the metalated phase (potentially due to the $N-Au$ interaction), however the other peaks in these spectra also display significant changes. The GI close-packed spectrum displays three well defined peaks, including the π^* peak with energies of 397.8, 399.9, 402.1 eV. These three peaks are well spaced and distinct. The form of these peaks changes significantly with the production of the diffuse phase. The π^* peak remained at the same energy, but appeared to lower a little in intensity. The remaining peaks displayed a change in both position and intensity, and evidence for a fourth peak can be seen in between them. The energies of these peaks can be seen in Table 6.3, and generally show that in the diffuse phase they shift towards lower energies. The GI spectra for the metalated phase displays a different arrangement of peaks to both the close-packed and diffuse phase. As previously stated, the π^* orbital shifted to a lower energy while the remaining peaks begin to coalesce and form one major peak with some potentially separate features at the peak. The details of the peak energies can be seen in Table 6.3.

The magic angle (pink) spectra for each phase display peaks for both the π^* and σ^* orbitals and mirror the changes seen across each transition however the intensity is significantly lowered.

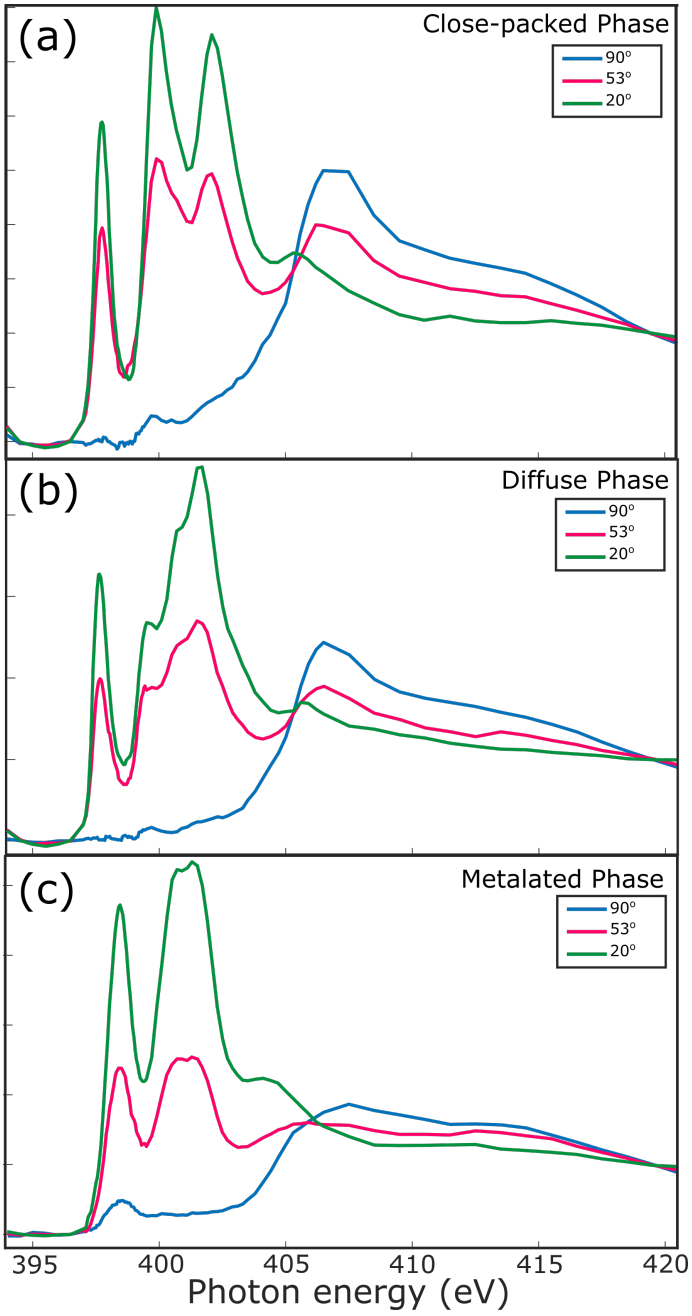

Figure 6.9: NEXAFS Spectra from each phase of TPP on Au(111). (a) NEXAFS Spectra at 90° (blue), 53° (pink) and 20° (green) for the close-packed arrangement of TPP. (b)NEXAFS Spectra for the diffuse phase of TPP. (c) NEXAFS Spectra for the metalated phase of TPP

Phase	Angle	Peak 1	Peak 2	Peak 3	Peak 4	Peak 5
close-packed	NI	399.7	406.5			
	MI	397.8	399.9	401.9	406.3	
	GI	397.8	399.9	402.1	405.3	
Diffuse	NI	399.7	406.5			
	MI	397.6	399.4	400.7	401.5	406.5
	GI	397.6	399.5	400.7	401.7	405.7
Metalated	NI	398.5	407.5			
	MI	398.4	400.7	401.3	405.3	
	GI	398.5	400.7	401.3	404.1	

Table 6.3: NEXAFS Peak Positions in each phase of TPP

This 'fingerprint' of the molecules with the three phases allows comparison with a study performed on TPP and CuTPP, we find similarities between the changes observed in the transition from TPP to CuTPP to the one observed for TPP to AuTPP. A comparison of these spectra can be seen in Figure 6.10, with the MI spectra from this study for the TPP and AuTPP displayed in 6.10a and b and the the experimental and theoretical data from [116] in 6.10c-h, while a comparison of the peak positions can be found in Table 6.4.

The first observation of note is that the spectra for TPP on Au(111) and Cu(111) (6.10a and c) have a similar appearance, with the three peaks seen in the acquired TPP MI spectrum clearly visible in the spectrum reprinted from the literature. The same is true for the metalated phase, where literature spectrum also displays the coalescence of second and third peaks. The LUMO (π^*) for both types of metalated TPP, Au and Cu, are at similar energies 398.5 eV and 398.4 eV respectively.

It is not possible to compare the energies of the LUMO+1, LUMO+2 peaks between the two studies, TPP on Cu(111) displaying a number of peaks between 400.0 eV and 406.0 eV where the data presented here shows a single broad peak. This observation could be due to a substrate induced effect, this study used an Au(111) surface as opposed to a Cu(111) surface, or could be attributed to differences in energy resolution.

From the data shown in Figure 6.10 it can be seen that there is a definite change in the frontier

MOs between each phase. The diffuse phase has undergone a change as there has been a shift in the peak positions and a change in thier intensity. Such a change could be attributed to an on-surface reaction. For example, a consequence of a ring-closing reaction would be a withdrawral of electron character to the core of the molecule, which combined with the change in geometry (planarisation) could produce the observed shift. The metalated phase displays a loss of the peak which occurs at 401.9 eV in the close-packed phase. This could be attributed to a bonding interaction using that particular orbital (eg. N-Au interaction), filling it and resulting in the loss of that feature from the NEXAFS spectrum.

Phase	**Source**	**Peak 1**	**Peak 2**	**Peak 3**	**Peak 4**
close-packed	Au(111) Exp	397.8	399.9	401.9	406.5
	Cu(111) Exp	397.6	399.8	401.6	
	Cu(111) Calc	398.0	400.0	402.2	
Metalated	Au(111) Exp	398.4	400.7	401.3	407.5
	Cu(111) Exp	398.4	400.7	401.3	405.3
	Cu(111) Calc	398.5	400.7	401.3	404.1

Table 6.4: NEXAFS Peak Positions

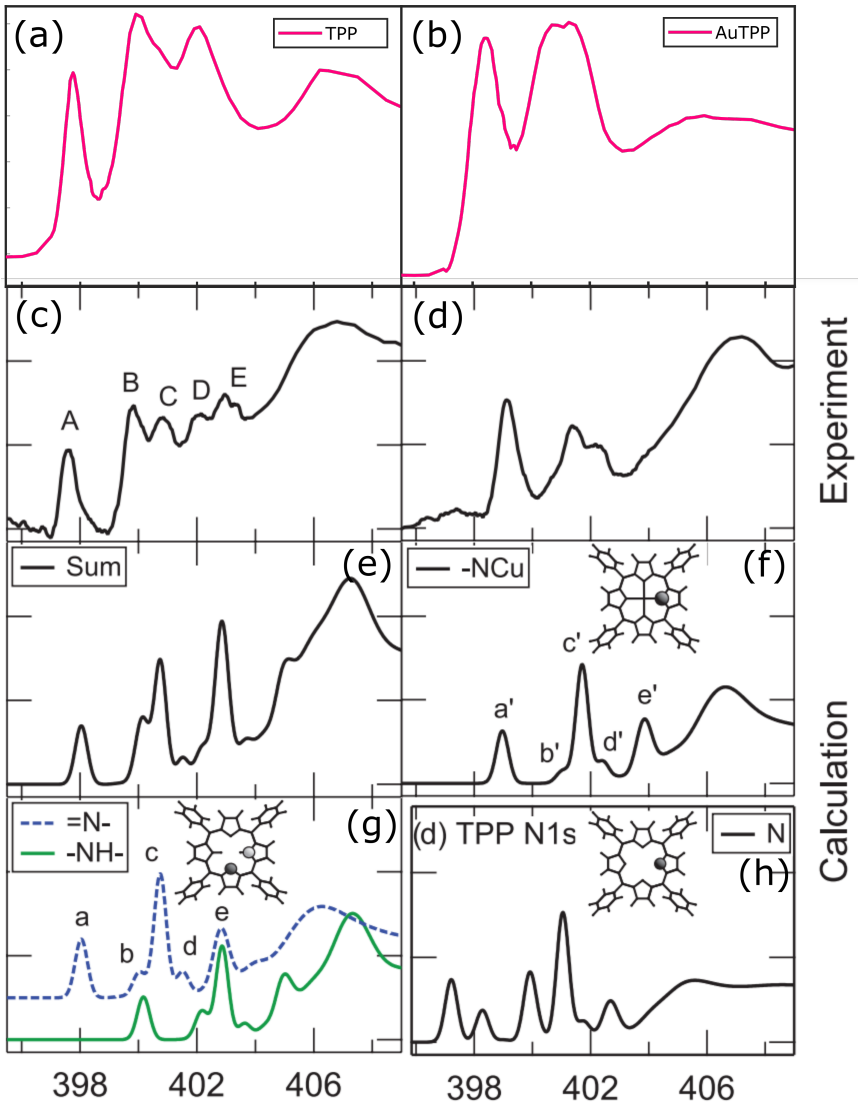

Figure 6.10: Comparison of data from [116] with data taken at 53° for the close-packed and metalated phases of TPP. (a) NEXAFS spectrum of close-packed TPP on Au(111). (b) NEXAFS spectrum of AuTPP on Au(111). (c) NEXAFS spectrum of TPP on Cu(111). (d) NEXAFS spectrum of CuTPP on Cu(111). (e) - (h) NEXAFS spectra predicted by DFT. (c)-(h) taken from [116].

6.4 Conclusion

In this Chapter three different phases of TPP were characterised using XPS, including a third phase which has not been previously seen, assigned to a metalated phase. Two core levels of TPP were analysed using XPS; N1s and C1s.

In the close-packed phase four distinct N1s environments were defined and assigned to N_α, N_β, NH_α and NH_β with binding energies of 397.2, 397.9, 399.4, and 400.0 eV respectively. The α peaks were assigned to the iminic (N_α) and aminic (NH_α) nitrogen atoms of TPP adsorbing onto the gold surface in the saddle conformation, while the β peaks were assigned to the iminic (N_β) and aminic (NH_β) nitrogen atoms of a TPP molecule adsorbed over a gold adatom. The α and β peaks appeared at different ratios in different spectra, which is likely to be due to the ratio of the TPP and aaTPP species varying across the surface as their ratio is highly dependant on the area and sample preparation. The C1s spectrum in the close-packed phase displayed five peaks, which have been assigned to the carbon environments present within TPP, these can be seen in Figure 6.2. The peaks were assigned C_a, C_b, C_c, and C_d, which had binding energies, 285.6, 286.0, 286.3, and 285.2 eV respectively.

In the diffuse phase combinations of two, three and four peaks were seen in the XPS spectra. The two peaks were assigned to the iminic and aminic nitrogen atoms in TPP adsorbing in the saddle conformation and had binding energies of 397.4 and 399.2 eV respectively. The four peaks was assigned to TPP and aaTPP, as seen in the close-packed phase. The peaks were assigned N_α, N_β, NH_α and NH_β with binding energies of 397.4, 397.7, 399.1, and 400.1 eV. The 0.2 eV shift in the N_α peak was linked to the occurrence of the ring closing reaction, causing a change in the electronic state. The spectra with three peaks were assigned to N, NH and N_μ. N and NH belonging to TPP adsorbing in the saddle conformation and having binding energies of 397.4 and 399.2 eV and N_μ belonging to a metalated species of TPP (AuTPP) and displaying a binding energy of 397.9 eV. The C1s spectra in the diffuse phase was fit to two carbon environments, C_a and C_b which had binding energies of 284.0 and 284.9 eV respectively. The reduction in the number of carbon environments was attributed to the ring-closing reaction, and therefore the presence of the 'flattened' TPP derivative.

The metalated phase of TPP was found to display only one peak in the N1s, at 398.0 eV, corresponding to the N_μ environment in which all nitrogen atoms are bonding to a gold atom. The C1s spectrum displayed three peaks, C_a, C_b and C_c at 293.9, 284.4, and 285.9 eV respectively, which can be seen in 6.6.

The XPS data can be summarised be be consistent with two distinct events, the first being the ring closing reaction, and the second being metalation.

The unoccupied frontier orbitals of TPP have been characterised using NEXAFS. Spectra were taken at three different angles (90°, 53°and 20°) for each phase of TPP. A number of changes in the peak structure occurred between the phases of TPP, indicating that chemical transformations have taken place. The change in peak positions and intensities that takes place between the close-packed and diffuse phase is consistent with a chemical reaction having taken place, such as the ring closing. Comparing the acquired NEXAFS spectra with those taken in [116] it can be seen that the peak structure of the close-packed phase is comparable to the spectra of TPP on Cu(111) and the peaks in the metalated phase of TPP on Au(111) are comparable to those of CuTPP on Cu(111).

In order to gain further insight into the mechanisms by which these transformations occur, NIXSW was employed to provide structural information on the specific adsorption geometries of different chemical species. These experiments are discussed in the following chapters.

Chapter 7

A Normal Incidence X-ray Standing Wave Characterisation of the Order to Disorder Transition of TPP on Au(111)

7.1 Introduction

In this chapter experimental results are presented on the structural characterisation of the order-disorder transition displayed by TPP on Au(111) by employing a NIXSW technique.

In previous chapters, the order-disorder transition of TPP on Au(111) has been characterised by employing a variety of surface-based analysis techniques. SPM methods, including STM, STS and KPFM have been used to characterise the following; the surface structure of the different molecular arrangements, the relative abundance and electronic states of the three different surface species, and the CPD of local molecular environments. X-ray methods, such as LEED have been used to characterise the average surface overlayer and its relative orientation to the surface lattice. In addition to LEED, XPS and NEXAFS have utilised x-ray radiation to probe the core and frontier

energy levels of the phases of TPP and characterise an additional, metalated phase of TPP on Au(111). The close-packed and diffuse phases display similar profiles of XPS N1s peaks, two-four peaks of varying intensity, which is dependant on sample preparation, however in the third TPP phase which can be achieved *via* a second annealing step, displays a distinctly different profile of peaks. The metalated phase shows a clear shift from the two-four peaks seen previously in the close-packed and diffuse phases, to a single N1s peak, which indicates that the TPP aminic nitrogens have lost their protons and all N atoms are now in the same environment, which is thought to be bonding with a Au atom uptaken from the surface.

In this chapter, NIXSW is used to determine the position and adsorption sites of the TPP nitrogen atoms on the Au(111) surface and further identify the different surface species and mechanisms through which they are formed.

7.1.1 NIXSW

NIXSW is a technique often employed to characterise the structure of molecule-substrate systems. It may be used to determine adsorption sites of specific atoms within molecules and to estimate the height at which these atoms sit above the surface. This technique can be employed to study structural changes that may be induced by chemical reactions. Tetraphenyl porphyrin has previously been studied by NIXSW, on Cu(111) surface, which was reported by P. Ryan *et al.*. [56] In this study, the adsorption geometry and conformation of the molecule was confirmed using a NIXSW based analysis, with the heights of the nitrogen atoms above the surface found to be 1.88 ± 0.08 Å and 2.15 ± 0.15 Å for the iminic and aminic nitrogens respectively. High coherent fraction C_f values implied that there was a single absorption site for each type of N atom, which was found to be the bridge site for the iminic and the atop site for the aminic.

Metalated porphyrins have also been studied using these methods, Ruthenium metalated TPP (RuTPP) has been studied on Ag(111) by P. Knecht *et al.* [117]. Two forms of this molecule were studied, RuTPP in its original form and also a ring-closed derivative of RuTPP. In the compressed phase of RuTPP the N 1s measurements showed that the nitrogen atoms have an adsorption height of 2.78±0.05 Å. In the planarised RuTPP it was found that the nitrogen atoms had an adsorption height of 2.62±0.05 Å. Both displayed high coherent fractions which implies that there is a preferred adsorption site.

7.2 Normal Incidence X-ray Standing Wave Measurements

NIXSW is employed here to characterise the structural changes that occur for surface confined TPP after annealing. The close-packed, diffuse and metalated phases of TPP have all been studied using this method. By analysing the data produced by this technique the adsorption position for specific atom species and chemical environments may be determined. The results obtained in these experiments are presented in the form of Coherent Fraction (C_f) and Coherent Position (C_p) values (see Chapter 2 for theory). The coherent fraction is an indication of the distribution of adsorption sites, high coherent fraction values indicate atoms of a given type are preferentially adsorbed in a single specific site, a low coherent fraction value therefore indicates there are a number of adsorption sites. The coherent position is an indication of the position of adsorbing atoms above the surface, relative to a set of crystal planes. It is an average of all the positions that atom may be in above the surface so may not directly translate to a specific height (eg. in the case of low C_f and C_p give a value for the mixture of adsorption sites). By looking at LEED and STM data for the close-packed and diffuse phases previously discussed in Chapter 4, it is known that the close-packed phase of TPP presents an incommensurate lattice, this means that the expected coherent fractions for the close-packed phase would be low. Similarly, for the diffuse phase, an over layer lattice is not present and the TPP molecules appear in an amorphous phase, which does not suggest a single binding site. By looking at the STS data presented in chapter 5, it can be seen that in the diffuse phase has a number of different components (TPP, aaTPP, AuTPP), which may mean that any coherent position values produced in the NIXSW are made up a number of different heights (although, as discussed below, in some cases we able to distinguish between =N−, −NH− and Au−N groups). During data acquisition each NIXSW measurement was repeated three times for each phase and the beam was moved to a new areas of the sample each time to limit beam damage. Before and after each measurement N1s and C1s 'soft' XPS spectra were taken to monitor the condition of the sample and check for beam damage. A reflectivity curve was measured prior to each x-ray standing wave measurement, to check the quality of the new areas of the surface and ensure that the energy range of each spectrum is the same with respect to the Bragg energy. The XPS spectra acquired during the XSW measurement are fit using a combination of Gaussian and Doniach-Sûnjiċ line shapes. This extracts the intensities due to each chemically unique species at each photon energy.

The (111) reflection was the focus of this set of experiments and is the XSW reflection presented in the following sections, however data was also taken for the (-111) reflection which can be found in Appendix C.

7.2.1 Fitting the Close-Packed Phase N1s NIXSW Peaks

The (111) reflection was the primary source of information in this system, with the planes lying parallel to the surface and extending up and out from it (nominal Bragg Energy of $E_{bragg} = 2631eV$). Analysing the NIXSW data requires the fitting of XPS peaks corresponding to the chemical environments present. The XPS peaks were fitted in accordance with the soft XPS peaks detailed in Chapter 6. For the close-packed phase two and four peaks were identified within the XPS data. The XPS peak fitting can be seen in Figure 7.1, two peaks in 7.1a and four peaks in 7.1b. Both numbers of peaks appear to fit well to the data. The two peaks are fit at 396.1 eV and 398.1 eV for the aminic and iminic respectively. The four peaks are fit at 396.1, 397.9, 396.6 and 398.5 eV, corresponding to the formerly labelled N_α, NH_α, N_β and NH_β respectively. As discussed previously in this chapter, the β peaks have been assigned to the aaTPP which we saw in Chapter 5 made up a small proportion (9%) of the TPP molecules in the close-packed phase.

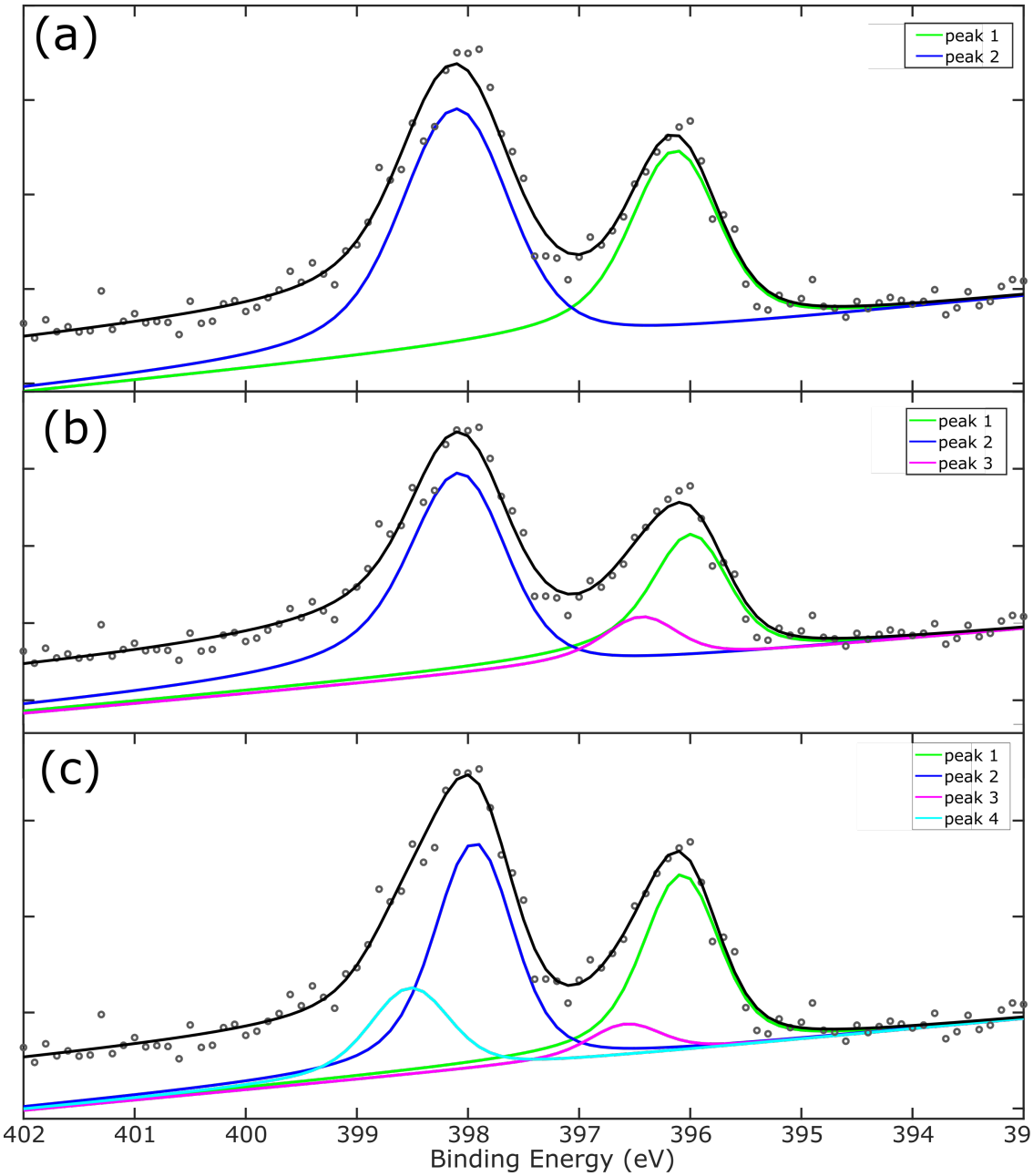

Figure 7.1: Fitting the N1s XPS peaks of the close-packed phase of TPP for N1s data to be used in the XSW. 2, 3 and 4 peaks were attempted to fit the data.

Upon fitting the absorption profiles for each peak, it was found that when using the four-peak fit the minor β peaks gave extremely large errors on the coherent fractions and position values. For this reason the focus was put on the two-peak fit as the errors on the standing wave were

significantly smaller than for the three-peak and four-peak fit. The XSW absorption profiles are shown in Figure 7.2, where 7.2a is for the iminic nitrogen peak and 7.2b is for the aminic nitrogen peak. The C_f and C_p values extracted for these peaks were found to be $C_f = 0.25 \pm 0.08$ and $C_p = 0.25 \pm 0.07$ for the iminic peak and $C_f = 0.21 \pm 0.08$ and $C_p = 0.35 \pm 0.07$ for the aminic peak. C_f is low in both cases, however C_p is potentially different.

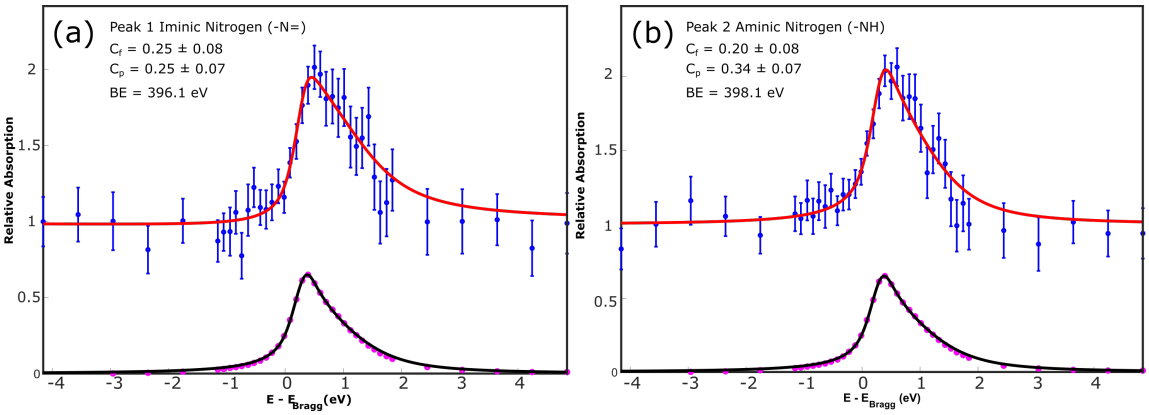

Figure 7.2: NIXSW measurements of the close-packed phase of TPP. NIXSW photoelectron yields obtained using the (111) reflection from the Au(111) crystal for the N1s core orbitals. (a) Peak 1, (b) Peak 2. The reflectively curve is shown below each XSW curve.

After finding the coherent fraction and position values by fitting the XPS peaks and then fitting the absorption profile the result was checked by manually fitting different C_f and C_p values to the XSW absorption profile. A range of C_f and C_p values were fit to the XSW profile, within the error range and then 0.1 either side of it. This data is presented in Figure 7.3, where the blue dots are the individual data points and the red line is the XSW profile fitted using given C_f and C_p values. The calculated fit can be seen in the central white panel, the uncertainty range is described by the light green inner ring of panels. These panels represent possible combinations of coherent fraction and position values within the uncertainty range calculated by the fit to the absorption profile. The outer green panels show the fitting at C_p and C_f values 0.1 outside the uncertainty range. From this figure it can be seen that the central panel, with the calculated C_f and C_p values has the best fit. As C_f and C_p values that differ from this, even within the quoted uncertainty range, are used the fits quickly start to deviate from the data points and outside that range the profiles do not correlate with the data at all. This provides confidence in the fitting parameters obtained for C_f and C_p.

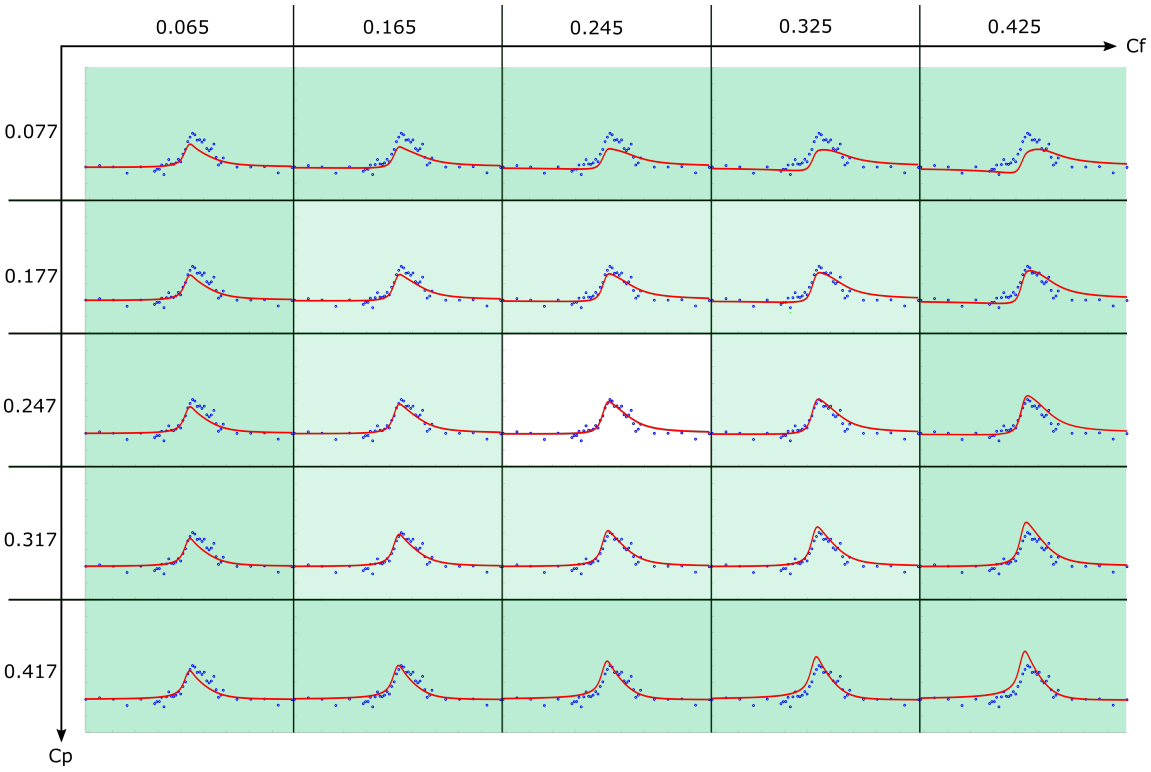

Figure 7.3: Table of XSW profiles with manually chosen C_f and C_p values (red line). Data points are from the (111) reflection for close-packed TPP (blue). The central panel (white, centre) shows the values obtained from the peak fitting, the eight inner panels (light green) show the XSW curve when C_f and C_p are at the limit of the error values, the 16 outer panels (green) are 0.1 outside the quoted error values. The central panel clearly shows the best fit to the data, with the fits outside of this deviating very quickly

7.2.2 Fitting the Diffuse Phase NIXSW Peaks

The XSW measurements for the diffuse phase were fit using the same methods as the close-packed phase. The diffuse phase has a more complex composition than the close-packed phase, in Chapter 5 three different types of STS spectra were identified, each corresponding to a different component of this phase, TPP, aaTPP and AuTPP (ie. unreacted TPP, adatom TPP and the metalted AuTPP species). The XPS peaks in this phase were fit with two, three and four peaks, which can be seen in Figure 7.4a-c. Similar to the close-packed phase none of the combinations showed a significantly better fit to the XPS data. The two peaks were fit at binding energies of 396.1 and 398.0 eV and were assigned to the iminic (N) and aminic (NH) nitrogen atoms respectively. The three peaks were fit at 396.1, 398.0 and 396.6 eV and assigned to iminic nitrogen (N), the aminic nitrogen (NH),

and metal bonded nitrogen (Au−N respectively. The four peaks were fit at 396.1, 397.9, 396.6 and 398.3 eV and were assigned to N_α, NH_α, N_β and NH_β, where the β peaks are due to TPP adsorbing above an adatom (aaTPP)

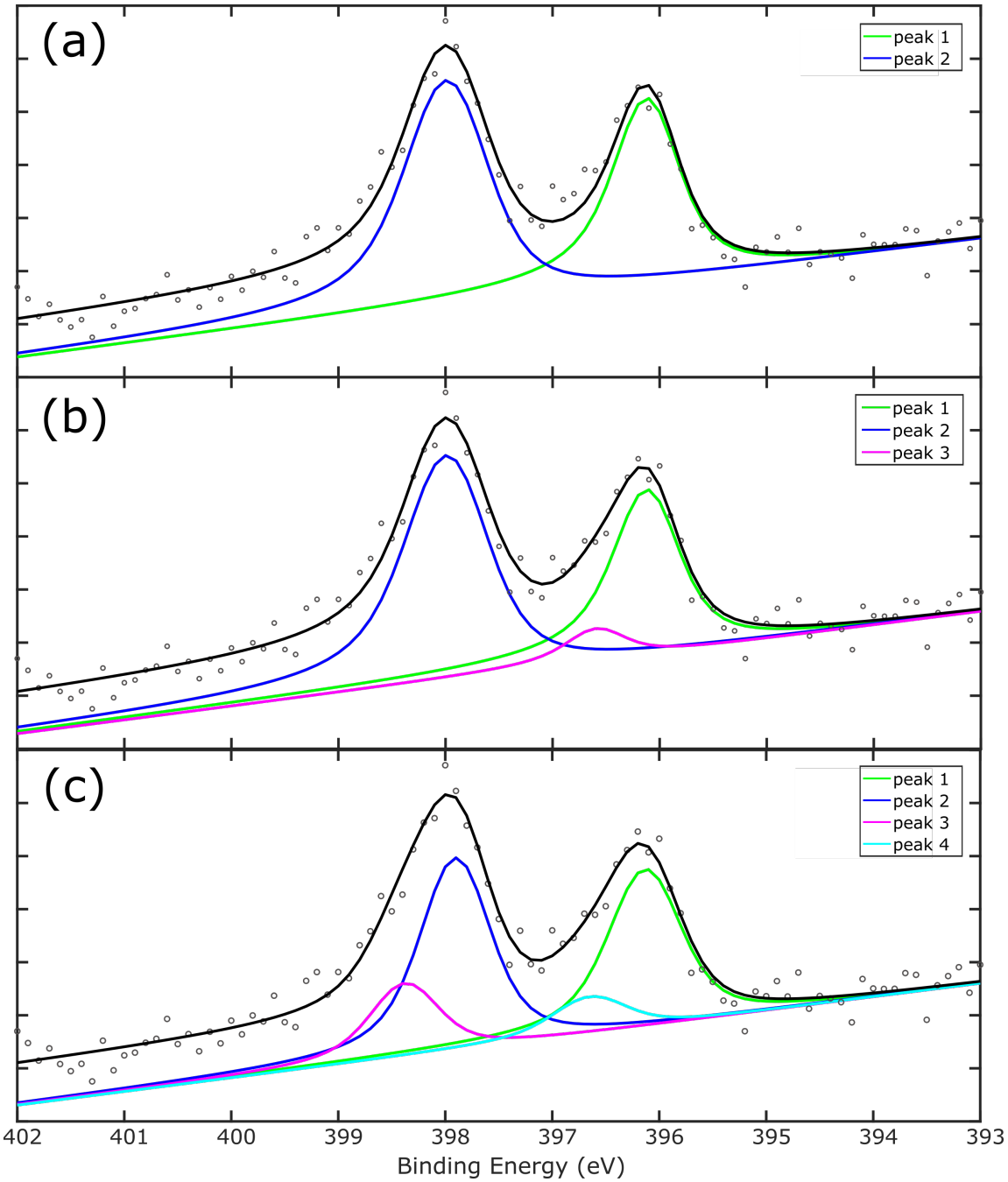

Figure 7.4: Fitting the N1s XPS peaks of the diffuse phase of TPP for N1s data to be used in the XSW. 2, 3 and 4 peaks were attempted to fit the data.

As with the close-packed phase, two peaks were chosen to fit to the absorption profiles as the errors on the third and fourth peaks coherent fractions and positions were very large. These

absorption profiles can be seen in Figure 7.5, where 7.5a is the profile for iminic peak and 7.5b is the profile for the aminic peak. The C_f and C_p values extracted for these peaks were $C_f = 0.41 \pm 0.11$ and $C_p = 0.25 \pm 0.07$ for the iminic nitrogen peak and $C_f = 0.37 \pm 0.10$ and $C_p = 0.27 \pm 0.07$ for the aminic nitrogen peak.

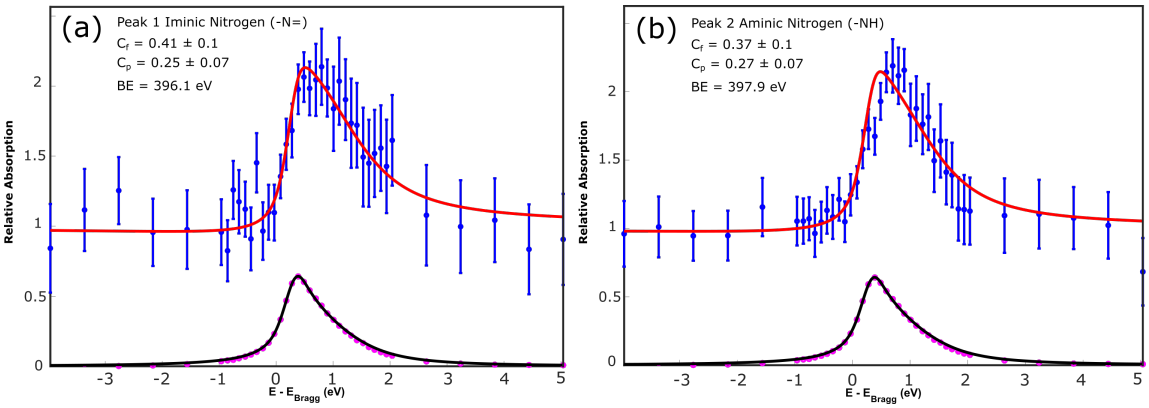

Figure 7.5: NIXSW measurements of the diffuse phase of TPP. NIXSW photoelectron yields obtained using the (111) reflection from the Au(111) crystal for the N1s core orbitals. (a) Peak 1, (b) Peak 2. The reflectively curve is shown below ac XSW curve.

A comparison of these values with those in the close-packed phase can be seen in Table 7.1. In the close-packed phase, both the N and NH peak have low coherent fractions of 0.25 ± 0.08 and 0.21 ± 0.08 respectively. Low coherent fraction values suggest that there is not a preferred adsorption site which is in agreement with the LEED data, which gave an incommensurate lattice. The coherent fractions are also low in the diffuse phase at 0.41 ± 0.11 and 0.37 ± 0.1 for the N and NH peaks respectively. This can be expected as the diffuse phase is a disordered phase, which would not imply that there is a preferential adsorption site. The coherent position values in the close-packed phase are 0.25 ± 0.07 and 0.35 ± 0.07 for the N and NH peaks respectively, which gives a difference of 0.1. TPP is known to adsorb in its saddle conformation [100] in which one set of pyrrole rings points upwards and the other downwards, which would give the two types of nitrogen different heights, therefore it can be expected that C_p values would be slightly different. In the diffuse phase the coherent position values are much similar and are the same within error. This is a clear change from what was seen in the close-packed phase and suggests that a structural change has occurred. It has been previously suggested in Chapter 4 that the transition to the diffuse phase could be facilitated by a cyclodehydrogenation ring closing reaction to form planarised TPP

derivatives. The planarised derivatives of TPP would have their aminic and iminic nitrogen atoms at a similar height above the surface, which would give the same value for C_p in both peaks.

Phase	**Peak**	$\boldsymbol{C_f}$	$\boldsymbol{C_p}$
close-packed	−N=	0.246 ± 0.08	0.246 ± 0.07
	NH	0.205 ± 0.08	0.345 ± 0.07
Diffuse	−N=	0.405 ± 0.11	0.245 ± 0.07
	NH	0.365 ± 0.1	0.265 ± 0.07

Table 7.1: XSW data

7.2.3 Fitting the Metalated Phase NIXSW Peaks

Fitting the metalated phase of TPP on Au(111) was done using the same methods as described previous. However, this phase of TPP gave only one peak in the XPS data. By examining the soft XPS data described previously in Chapter 6, it can be assumed that there is only one component to this phase, which was assigned to a metalated TPP molecule (AuTPP). In this phase all nitrogen atoms are bonding to a gold atom which has been taken into the pore of the molecule, giving a single nitrogen environment, Au−N. The XPS fitting can be seen in Figure 7.6a, with a single peak fit to it at 396.8 eV. The XSW profile is pictured in 7.6b, and gave the coherent fraction and position values as $C_f = 0.44 \pm 0.05$ and $C_p = 0.29 \pm 0.03$. The coherent fraction is slightly higher than those seen previously, but still not high enough to imply that there is a single preferential absorption site.

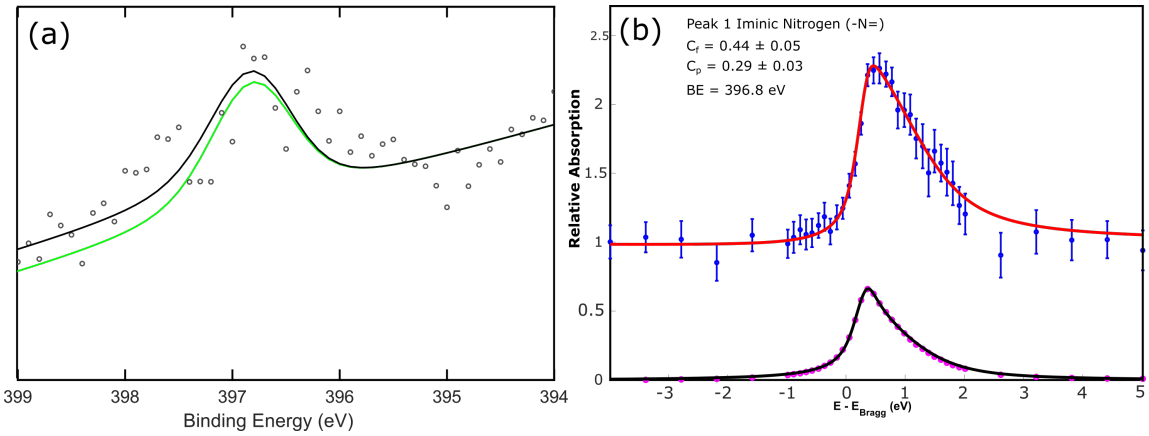

Figure 7.6: (a) XPS spectrum showing the single peak fit to the data. (b) NIXSW measurements of the metalated phase of TPP. NIXSW photo-electron yields obtained using the (111) reflection from the Au(111) crystal for the N1s core orbital. The reflectively curve is shown below the XSW curve.

7.3 Determining the Structure of TPP on Au(111)

The x-ray standing wave results can be used to determine the structure of TPP molecules on Au(111) in each of the phases identified. To understand the structures, the distances from each adsorption site to the relevant atoms in TPP were calculated for all possible types of interactions. There are three high-symmetry adsorption sites in the Au(111) surface, atop, bridge and three-fold hollow.

For a physisorbed molecule it is appropriate to use the Van der Waals radii of the interacting atoms to model the physisorbed dimensions. In the case of the close-packed and diffuse phases, this would be a surface gold atom and a nitrogen atom within TPP. To find the atop position in these phases the Van der Waals (VDW) radi of the N atom (155 pm) and the Au atom (166 pm) are simply added together, as the nitrogen will be sitting directly above the Au atom, this gives a distance of 3.21 Å. This distance can be translated into an equivalent coherent position value to find where it sits between the crystal planes. The interplanar distance in the Au(111) crystal is 2.35 Å, which is smaller distance than the distance calculated for atop adsorption, which shows that the atop adsorption site is in the second plane from the surface. The distance into this second plane that the adsorbing nitrogen would sit can then be used to find its equivalent coherent position. The same process was repeated for the bridge site and the three-fold hollow sites. A model of this can

be seen in Figure 7.7, where the heights and equivalent coherent positions of the different species can be seen in each different high-symmetry site.

In the case of metalated TPP it was assumed that the metal atom had been taken into the plane of the molecule and all nitrogen atoms were in the same plane. This limits the heights of the nitrogen atoms to be the same as the height of the gold atom they are bonding to. The gold atom has a larger VDW radius (166 pm) than the nitrogen (155 pm) so it was used to calculate the adsorption heights for the metalated species. It was found that for the atop species this gave a height of 3.32 Å, slightly higher than the N-Au VDW interaction.

The diffuse phase is thought to consist of a higher proportion of the TPP interacting with adatoms, which meant that the height of the adatom has to be taken into account when finding the positions of the nitrogen atoms above the surface. The gold adatom can be thought of as adsorbing in either the atop site, the bridge site or the three-fold hollow site and its presence can be accounted for in the calculated heights of the nitrogen atoms. It is stated in the study be J. Meilke *et al.,* that a nitrogen atom in TPP forms a coordinate bond with the gold adatom, with a bond length of 2.34 Å. Assuming the TPP sits centrally over the gold adatom, the height above the adatom was calculated and added to the height of the adatom above the surface. [39]

The distances and equivalent coherent positions were also calculated for a TPP N atom bonding to a gold surface atom. The details of each interaction and for each adsorption site can be seen in Table 7.2 and a visual representation of each adsorbing species can be seen in Figure 7.7.

Bond Type	Binding Site	Height Å	Predicted Coherent Position
Au-N VDW	Atop	3.21	0.365
	Bridge	2.87	0.220
	Hollow	2.74	0.166
Au-Au VDW	Atop	3.32	0.413
	Bridge	2.99	0.272
	Hollow	2.87	0.221
Au-Au-N VDW	Atop	4.35	0.852
	Bridge	4.02	0.712
	Hollow	3.90	0.661
Au-N Bond	Atop	2.00	0.851
	Bridge	1.39	0.591
	Hollow	1.11	0.472

Table 7.2: Heights of interacting atoms above the surface, for each adsorption site, in Å and the corresponding coherent position. Distances were calculated using VDW radii for nitrogen and gold atoms, the calculated coordinate bond distance from nitrogen to gold from [39] and the bond length from nitrogen to gold from a metalated TPP molecule from [118]

In Figure 7.7 the VDW radius of the gold surface is marked with a yellow dashed line, while the positions of the atoms are marked by spots, blue where it is a nitrogen atom limiting the distance to the surface and yellow where a gold atom determining to adsorption geometry. The XSW planes are marked with black lines, with the height in angstroms shown on the left and the corresponding C_p on the right. It can be seen that the heights of a TPP nitrogen atoms bonding with a surface gold atom would mean that the TPP molecule would be inside the surface, meaning this is not a viable interaction. The TPP N atom adsorbing at the VDW radii distances is no longer inside the surface and gives equivalent coherent position values close to the ones obtained from the XSW measurements for the close-packed phase. The Au-Au VDW interaction gives a slightly higher position, consistent with the measurements taken in the metalated phase. The TPP interacting with an adatom gives a significantly higher position. The diffuse phase is likely to be a mixture of different species, which we have seen evidence for in the STS and XPS data. The STS data gave a mixture of aaTPP, TPP and AuTPP in the metalated phase, while the XPS data showed different

numbers of peaks at different intensities which have been previously assigned to TPP, aaTPP and AuTPP.

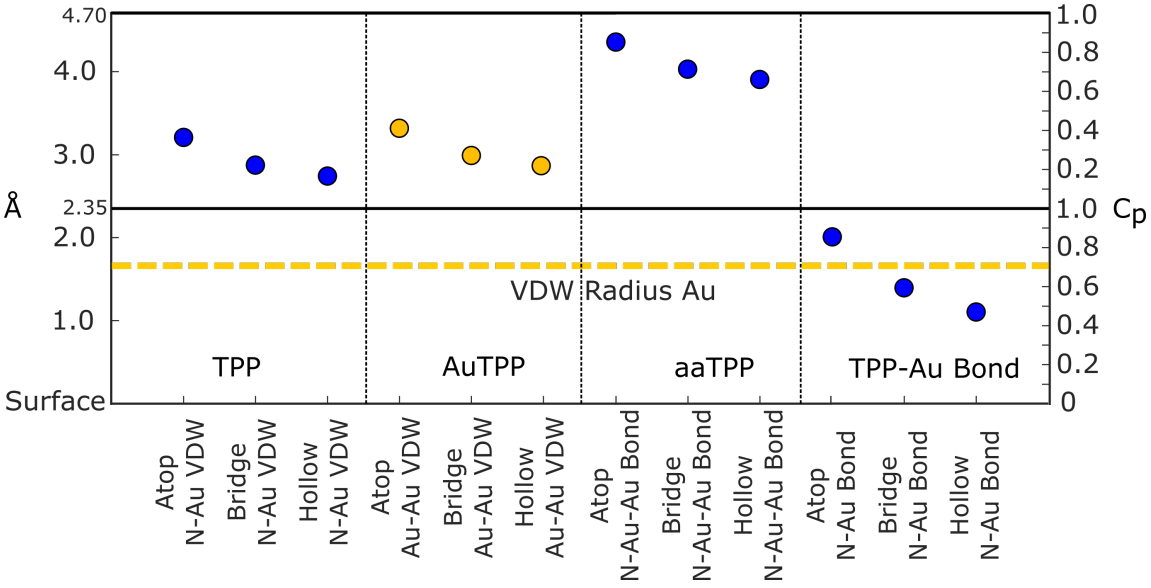

Figure 7.7: Heights of interacting atoms above the surface, for each adsorption site, in Å and the corresponding coherent position, with the VDW radius of gold marked with a dashed yellow line. Distances were calculated using VDW radii for nitrogen and gold atoms, the calculated coordinate bond distance from nitrogen to gold from [39] and the bond length from nitrogen to gold from a metalated TPP molecule from [118].

An adsorption model for molecules on a surface can be obtained using a variety of methods; here two approaches are considered. Firstly, it can be achieved by fitting scaled molecules over STM images and determining if there is a preferred adsorption site. Secondly, it can be acquired using the C_p and C_f parameters obtained from the NIXSW data. The C_f and C_p values and their respective errors can be plotted on an argand diagram using polar coordinates, with the C_f parameter represented by the R value and the C_p parameter represented by θ. A simple model of the adsorbed molecules may then be constructed and plotted on the Argand diagram as a sum of its component vectors. If the sum of the components does not match the experimental C_f and C_p values then the components may be iterated until a self consistent solution is found.

7.3.1 Modelling the Close-Packed Phase

The coherent fraction and position were used to find an adsorption model for each phase of TPP, beginning with the close-packed phase. A number of STM images of the close-packed phase (some shown in Chapter 4) show that the herringbone reconstruction is visible through the layer of TPP molecules. A scaled model of the herringbone may be placed underneath the image, and scaled TPP molecules laid over-top. An image of this can be seen in Figure 7.8, with 7.8a showing the TPP molecules overlaid onto the STM image and 7.8b showing the same arrangement of molecules overlaid onto an atomic model of the herringbone. This method was used to determine which sites the nitrogen atoms in the TPP molecules were adsorbing in on the surface. It was found that there was a random distribution of adsorption sites (predicted by the LEED data, which showed a non-commensurate lattice). The details of the distribution of binding sites for both the aminic and iminic nitrogens can be found in Appendix B. For low coverages ($\ll$ monolayer) the TPP adsorbs preferentially in the FCC regions of the herringbone and forms small islands limited in width by the herringbone, which is driven by surface-molecule interactions. At the full monolayer coverage the packing is driven by molecule-molecule interactions (see Chapter 4), which leads a lack of a specific adsorption site.

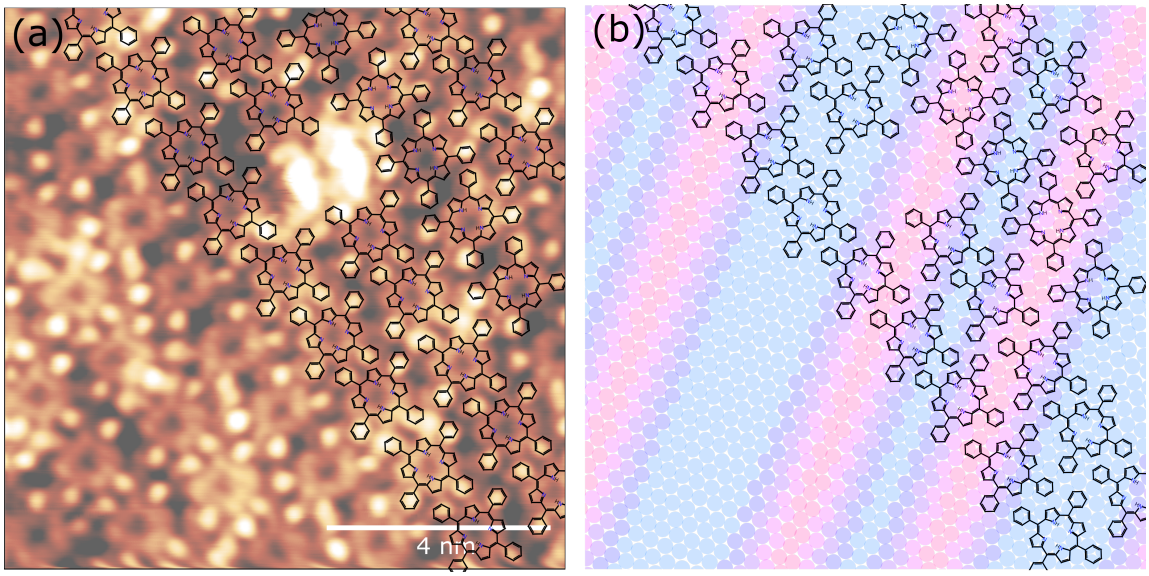

Figure 7.8: Fitting scaled TPP molecules to an STM image. (a) STM image with overlayed TPP molcules. Setpoint = 50 pA, Bias = 0.8 V. (b) Herringbone atoms overlayed with identical scaled lattice of TPP. It can be seen that there is no 'preferential' binding site.

The experimental values of the coherent fraction and position for the close-packed phase were found to be $C_f = 0.25 \pm 0.08$ and $C_p = 0.25 \pm 0.08$ for the iminic nitrogen peak and $C_f = 0.21 \pm 0.07$ and $C_p = 0.35 \pm 0.07$ for the aminic nitrogen peak. These peaks have similar coherent fractions, which is potentially due to having similar distributions of sites across the surface. The aminic peak has a higher coherent position value, which could be attributed to the saddle conformation of the TPP molecules on the surface causing the NH groups to point upwards, therefore being in a higher position above the surface. When fitting vectors to these argand diagram a number of initial assumptions were made. Firstly, it was assumed that there was an equal proportion of N atoms in the atop, bridge and 3 fold hollow sites, this was due to the roughly equal proportions found by fitting the TPP molecules over STM images. Secondly, it can be assumed that there is a combination of TPP and aaTPP on the surface. The ratio of TPP:aaTPP found using the STS spectra was 92%:8%, while the ratio found using the average area ratios of XPS peaks N_α and N_β was 3:1, which gives a significantly larger amount of the aaTPP. The third assumption that was made is that the low experimental C_f values may have been artificially reduced by up to 50% due to a thermal noise contribution [119]. In models 1 and 2 for the close-packed phase we consider the effect of thermal noise and it was assumed that the coherent fraction was reduced by 50%, therefore it can be assumed that the maximum C_f is 0.5.

Model 1

The first model that was attempted used the ratio of TPP and aaTPP found using the STS spectra to fit the iminic nitrogen peak, which can be seen in Figure 7.9a. TPP was taken to account for 90% of the total molecules and aaTPP was taken to acount for 10% and the C_f component used for the TPP vectors (corresponding to the atop, bridge and hollow sites) were equal and set to 0.15, while the C_f components used for the aaTPP was 0.017, to give a total C_f of 0.50. The C_p values used were taken from Table 7.2 for both the TPP and aaTPP. This gave a total of six vectors to be plotted with polar coordinates of (0.15, 0.365), (0.15, 0.220), (0.15, 0.166), (0.017, 0.852), (0.017, 0.712), and (0.017, 0.661). In 7.9a the TPP vectors are seen clearly (blue, green, pink) while it is difficult to see the aaTPP vectors as they make up a very small contribution (yellow, cyan, red). The black vector represents the sum of these six vectors can it can be seen to give a coherent position within the red bounded region ($C_p = 0.25$), however its intensity is too high, which takes

it out in the range for the coherent fraction ($C_f = 0.36$). This indicates that this model has the incorrect proportions of TPP and aaTPP.

Model 2

The proportion of aaTPP is highly dependant on the preparation of the surface, so the second model used the average ratio of the N_α and N_β peaks from all of the XPS data, to give a more accurate ratio for this particular surface. TPP was taken to account for 75% of the total molecules and aaTPP was taken to account for the remaining 25%. From this the C_f components used for TPP and aaTPP were set to be 0.125 and 0.04 respectively. As before, in this model equal parts atop, bridge and three-fold hollow were used for both species to give six sets of polar coordinates; (0.125, 0.365), (0.125, 0.220), (0.125, 0.166), (0.04, 0.852), (0.04, 0.712), and (0.04, 0.661), to be plotted. This can be seen in Figure 7.9b. The vectors representing the three TPP adsorption sites (blue, green, pink) have been reduced in intensity slightly, while the vectors representing the aaTPP have increased in intensity This results in the black total vector being in the centre of the shaded region (experimental value and associated error), indicating a good agreement with the experimental data.

Model 3

An alternate model for this data was constructed in a similar manner. This model used the average ratio of the N_α and N_β peaks from the XPS data however an out-liar was removed when this model was calculated. The data set used can be seen in Appendix C, with the relevant point highlighted. The majority of the XPS spectra displayed ratios of 1:1, 2:1, 3:1 and 4:1 for $N_\alpha : N_\beta$, however one of them displayed an 8:1 ratio, which was removed when calculating this model. Omitting this point changes the ratio of $N_\alpha : N_\beta$ to 9:4 from the previous 3:1, increasing the proportion of the aaTPP species slightly. In this model the C_f values were not artificially reduced based on thermal noise, and summed to a total of one. Using this ratio, the C_f parameters for TPP becomes 0.23 and for aaTPP it becomes 0.1. A total of six vectors were plotted with polar coordinates; (0.23, 0.365), (0.23, 0.22), (0.23, 0.1661), (0.1, 0.852), (0.1, 0.712), and (0.1, 0.661).

An argand diagram for this model can be seen in Figure 7.9c. The vectors representing the TPP adsorption (blue, green, pink) have been reduced in intensity slightly compared to the previous

model, while the vectors representing the aaTPP have increased in intensity (yellow, red, cyan). In this model the black vector sits on the top edge of the shaded region, and gives the total $C_f = 0.34$ and $C_p = 0.25$. This argand diagram shows a significantly better fit, and does not require additional ad-hoc modification (in terms of thermal noise) to achieve agreement with the experimental data.

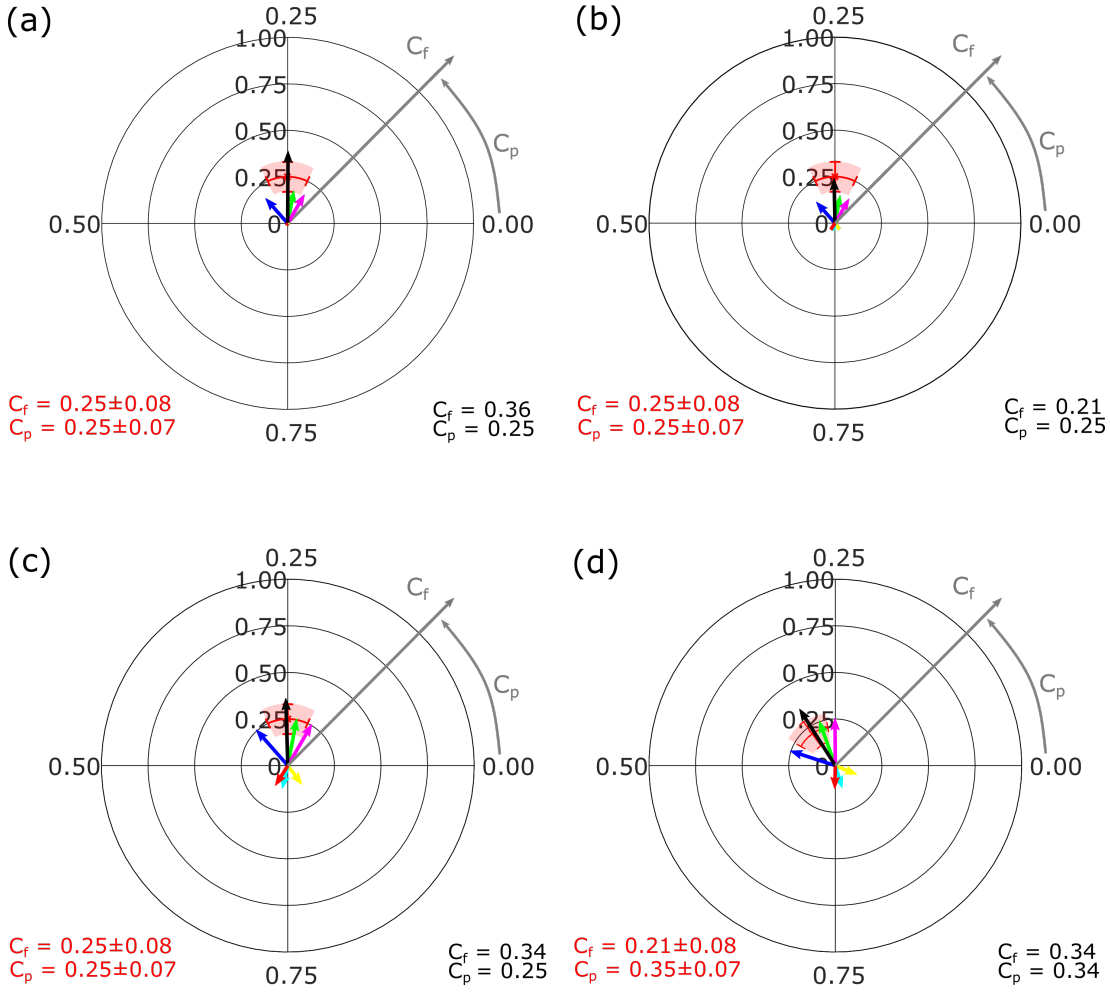

Figure 7.9: Argand diagrams showing C_f and C_p values obtained from XSW measurements from the (111) reflection for the close-packed phase of TPP. The coloured arrows represent vectors showing C_f and C_p values for the different binding sites and modes for the N atom, atop TPP (blue), atop AATP (yellow) bridge TPP (green), bridge AATTP (cyan) 3-fold hollow TPP (pink), three fold hollow aaTPP (red), the black arrow represents a vector which is a sum of the component vectors. (a) Argand diagram for peak 1, using the STS ratio of TPP:aaTPP. (b) Argand diagram for peak 1, using average ratio of peak 1:peak 3 area from the XPS data as TPP:aaTPP. (c) Argand diagram for peak 1, using average ratio of peak 1:peak 3 area from the XPS data, omitting an outlier point, as TPP:aaTPP. (d) Argand diagram for peak 2, using average ratio of peak 1:peak 3 area from the XPS data as TPP:aaTPP.

7.3.2 Modelling the Effect of the Saddle Conformation

TPP is known to adsorp on Au(111) in the saddle conformation [100], which displays different heights for the aminic and iminic nitrogen atoms within the molecule. To account for this in finding a model for this peak a crystal structure of TPP was used to calculate the different heights of the nitrogen atoms. The crystal structure for TPP, taken from [120] shows TPP with a nearly planar core, with phenyl rings rotated ±60°out of plane with the core. However, due to the known adsorption conformation of TPP this was not applicable and a co-crystal structure was chosen instead, with the TPP molecule displaying the saddle conformation [121] which can be seen in Figure 7.10a and b. This saddle conformation is a good match for previous STM based observations. [39] Focusing on crystallography data allows the difference in the heights of the aminic and iminic nitrogen atoms to be calculated. The height difference was found to 0.2 Å, which corresponds to a 0.085 difference in coherent position for the Au(111) crystal. Due to the higher C_p value for the aminic nitrogen peak (0.35), it can be assumed that they are in the higher position relative to iminic nitrogens and that the adjacent hydrogen atoms would be pointing upwards relative to the surface. An adsorption model for the aminic and iminic nitrogen atoms is pictured in Figure 7.10c and d. The iminic nitrogen atoms (7.10c) are located within the second plane above the gold surface, pictured as adsorbed in the atop position at a height of 3.21 Å. The aminic nitrogen atoms (7.10d) are located within the second plane above the gold surface, pictured in a atop site at a height of 3.41 Å.

Using this difference in height, an argand diagram for the aminic nitrogen may be plotted, which can be seen in Figure 7.9d. The input C_p values have been adjusted to account for the difference in height, while the C_f values took the same proportions as seen in the adjusted XPS ratio found for the iminic peak, 9:4 NH_α:NH_β (as pictured in Model 3 above). This gives the set of polar coordinates that were plotted to be (0.23, 0.45), (0.23, 0.305), (0.23, 0.251), (0.1, 0.937), (0.1, 0.797), and (0.1, 0.746).

The component vectors in Figure 7.9d have all been rotated anticlockwise equally but possess the same magnitude as seen previously in 7.10c. The black vector sits in the top centre of the shaded red region and gives the total $C_f = 0.34$ and $C_p = 0.34$. This argand diagram shows a similar fit to the aminic peak and has not been adjusted for thermal noise.

This model is consistent with the know 'saddle' shape adsorption conformation of TPP.

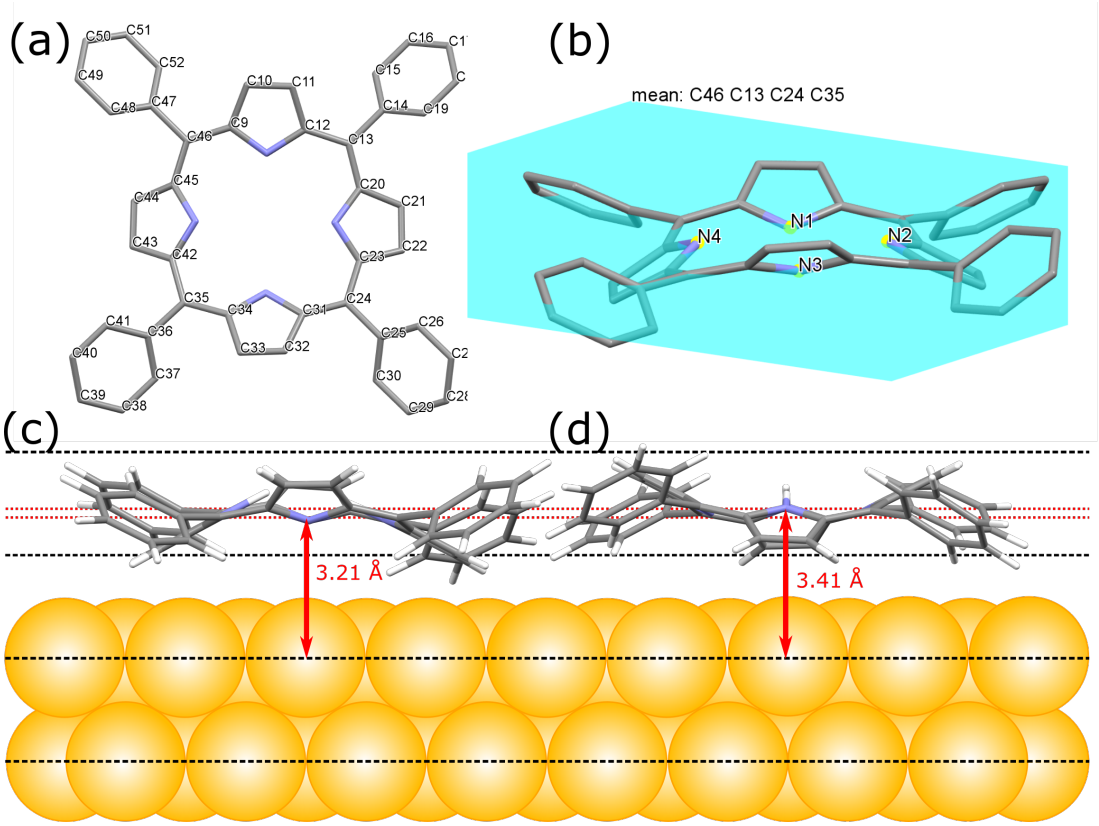

Figure 7.10: Modelling the behaviour of the close-packed phase of TPP on Au(111). (a) A molecule of TPP in its saddle conformation taken from the crystal structure reported in [121] (b) Saddle-shaped TPP with a plane defined using the four *meso*-carbon atoms, shows N1 and N3 lie below the plane and N2 and N4 lie above it. (c) Image showing two layers of surface gold atoms with the 111 crystal planes marked in dotted black lines. TPP can be seen in the second plane with the iminic nitrogen atoms at a height of 3.21 Å above the surface. (d) TPP can be seen in the second plane with the aminic nitrogen atoms at a height of 3.41 Å above the surface.

7.3.3 Modelling the Diffuse Phase

The same procedure of overlaying scaled molecules could not be applied to the diffuse phase as the herringbone reconstruction cannot be seen underneath the molecules. However, due to the disordered nature of the diffuse phase, it may be assumed that there is a random distribution of binding sites across the surface. The argand diagrams for the iminic and aminic nitrogen peaks can be seen in Figure 7.11a and b respectively. The first observation to note about the coherent position is that in comparison with the close-packed phase it is the same within error. As previously stated,

this change could be an indication that a cyclo-dehydrogenation ring closing reaction has occurred, causing the TPP molecules to form a planar TPP derivative. There has also been a change in the coherent fractions, in the diffuse phase they are higher, at 0.41 and 0.36, than in the close-packed where they were 0.23 for both peaks.

When making a model of the diffuse phase, the assumptions made in the close-packed phase are still applicable. The proportion of atop, bridge and three-fold hollow can be assumed to be equal, there may be a mixture of TPP, aaTPP and also AuTPP as seen in the STS and XPS spectra and also that there may be a reduction in C_f due to thermal noise, although as seen above, this may not be a required consideration.

A number of different attempts were made at modelling the diffuse phase, the same parameters for the atom heights were used as in the close-packed phase, with the inclusion of a new species on the surface, the AuTPP species, which is seen in the STS data for the diffuse phase and in a number of the XPS spectra. The first model used the ratio of TPP:aaTPP:AuTPP found using the STS spectra, however this model did not fit the XSW data. The second model attempted used the ratio of the N_α:N_β XPS peaks, and left out the AuTPP species. This model also did not fit with the XSW data. Details of these models and their fitting parameters can be found in Appendix C The model that was found to fit the best for the aminic and iminic nitrogen peaks can be seen in Figure 7.11. The sum of the C_f values for these peaks was taken to be 1, assuming that there is no effect of thermal noise. The iminic nitrogen peak also took into account a possible contribution from the metalated TPP species as the energy of the AuTPP XPS peak is very similar to that of the N_β peak. This was done using the difference in the area of the N_β and NH_β peaks. If both are attributed exclusively to the aaTPP they ought to have roughly equal areas, however this is not the case, and the N_β peak has a larger area, which implies a contribution from the AuTPP. Comparing these peaks, gave a ratio of TPP:aaTPP:AuTPP species as 6:3:1. The C_f components used for this peak were 0.2, 0.1 and 0.03 for TPP, aaTPP and AuTPP respectively, which gave a total of nine vectors. These are shown in Figure 7.11a, however the vectors attributed to the AuTPP are very small, and hard to see. The black vector for the sum of these components sits in the shaded red region, and gives $C_f = 0.34$ and $C_p = 0.27$, these are comparable to the experimental values, $C_f = 0.41 \pm 0.11$ and $C_p = 0.24 \pm 0.07$.

The aminic nitrogen peak was fit using the ratio of the NH_α and NH_β peaks, which was found

to be 2:1 TPP:aaTPP, the same as the TPP:aaTPP ratio from the iminic peaks. There are no contributions to this peak from the AuTPP because it only has one peak, which lies in the region of the N_β peak. The similar coherent position values in these two peaks indicate that the TPP molecules have undergone a ring closing reaction and planarised, causing all the N atoms to lie at similar heights within the molecules, therefore the same values were used for the coherent position as in the iminic peak. The C_f components used for this peak were 0.22 and 0.11 for TPP and aaTPP respectively, which gave a total of six vectors to be plotted, these can be seen in the argand diagram in Figure 7.11b. The black vector lies within the red shaded region indicating that the fit is good, and gave $C_f = 0.29$ and $C_p = 0.26$, which are comparable to the experimental values $C_f = 0.36 \pm 0.1$ and $C_p = 0.27 \pm 0.07$. Similarly to the iminic peak, the calculated coherent fraction value is lower than the experimental one, which could be due to the thermal noise factor.

The proposed composition of the diffuse phase as a mixture of TPP and aaTPP fits well with the data and therefore it may be assumed that the diffuse phase consists of the flattened TPP derivative in a mixture of adsorption heights due to the presence of adatoms. This accounts for the low C_f values observed in this phase.

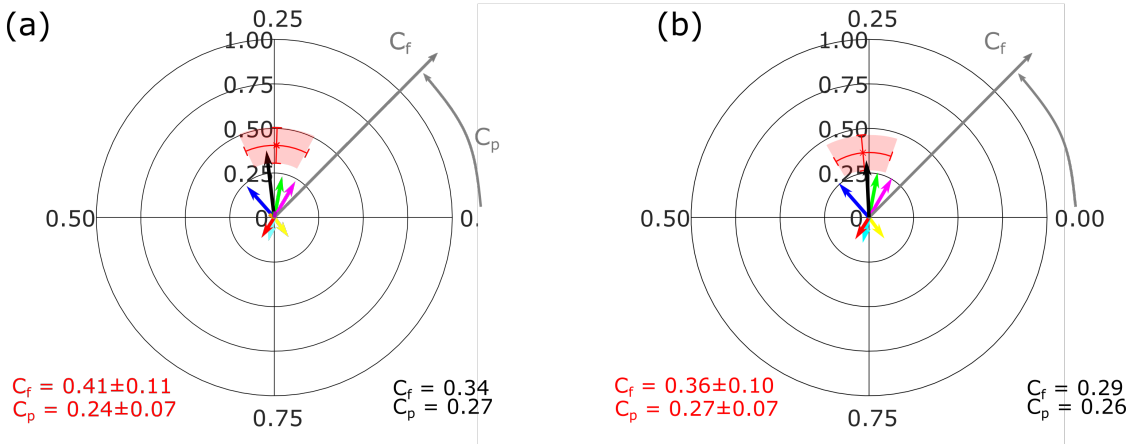

Figure 7.11: Argand diagrams showing C_f and C_p values obtained from XSW measurements from the (111) reflection for the diffuse phase of TPP. The coloured arrows represent vectors showing C_f and C_p values for the different binding sites and modes for the N atom, atop TPP (blue), atop aaTPP (yellow), atop AuTPP (orange) bridge TPP (green), bridge aaTPP (cyan), bridge AuTPP (green), 3-fold hollow TPP (pink), three fold hollow aaTPP (red), three fold hollow AuTPP (purple), the black arrow represents a vector which is a sum of the component vectors. (a) Argand diagram for peak 1, using average ratio of peak 1:peak 3 area from the XPS data as TPP:aaTPP:AuTPP.(b) Argand diagram for peak 2, using average ratio of peak 2:peak 4 area from the XPS data as TPP:aaTPP.(a) and (b) both use C_f summed to 1.

The ring closed TPP derivative is no longer able to form to saddle conformation and is planar, a simulation of this molecule was made using molecular modelling software, Avogadro [99] and used to create a visual representation of this adsorption model which can be seen in Figure 7.12a. A plane can be defined using the *meso*-carbon atoms (7.12b) which shows that each nitrogen atom is in the same plane as the rest of the molecule and is therefore expected to adsorb at the same height.

An adsorption model for the two types of TPP in the diffuse phase is pictured in Figure 7.12c and d. The nitrogen atoms (7.12c) are located within the second plane above the gold surface, pictured in the atop position at a height of 3.21 Å. The remainder of the atoms within TPP would also be at the same height. In 7.12d the adsorption model for aaTPP is pictured. The gold adatom is sitting in a bridge site and the TPP molecule is shown directly above it.

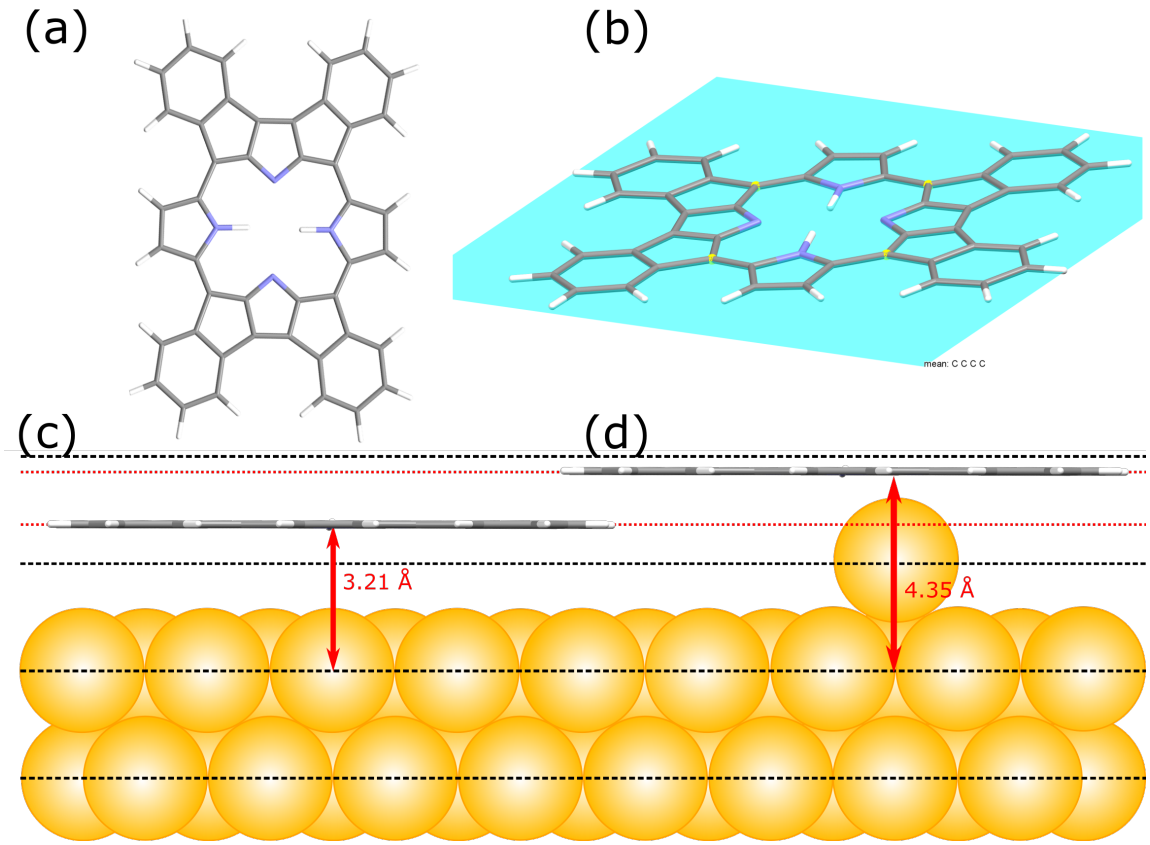

Figure 7.12: Modelling the behaviour of the diffuse phase of TPP on Au(111). (a) The product of the cyclodehydrogenation reaction of TPP, to form a planar ring closed derivative. (b) The ring-close derivative of TPP with a plane defined using the four highlighted carbon atoms, shows the molecule is perfectly planar. (c) Image showing two layers of surface gold atoms with the 111 crystal planes marked in dotted black lines. A simulated molecule of the ring-closed derivative of TPP can be seen in the second plane at a height of 3.21 Å above the surface. (d) A simulated molecule of the ring-closed derivative of TPP can be seen in the second plane interacting with a gold adatom at a height of 4.35 Å above the surface.

Modelling the Metalated Phase

The LEED data for the metalated phase suggests a disordered surface, as there is not a distinct set of spots as seen for the close-packed phase. The pattern appears as a blurred ring, similar to that observed within the diffuse phase. From this it can be assumed that there is an equal distribution of atop, bridge and three fold hollow sites as the surface is in a disordered arrangement. In this phase there is only one peak to fit which is assigned to a nitrogen atom bonding to a gold atom (Au−N), the experimental coherent fraction and position parameters were found to be $C_f = 0.46 \pm 0.06$ and

$C_p = 0.30 \pm 0.04$. The coherent position is higher than in previous phases, which suggests a higher average height, while the coherent position is also slightly higher, which is possibly due to fewer different species present on the surface, and have a higher degree of order.

The first model for this phase assumed equal amounts of atop, bridge and three fold hollow sites and a total C_f of 1. The individual C_f values used for each site were 0.33 and the C_p values were taken from Table 7.2 and were the distances for a Au-Au VDW interaction as all nitrogen atoms are bonded to gold, therefore the height is limited by the Au-Au distance. The resultant argand diagram can be seen in Figure 7.13a, with the black vector showing the sum of the three components. It shows that this model gives the correct coherent position, however the coherent fraction is significantly higher than the experimental value. It was concluded in the modelling of the previous two phases that is is unlikely that there is a thermal noise contribution, hence there must be an alternate model for this phase.

In porphyrin and phthalocyanine metal complexes in which the metalating atom has a large atomic radius it has previously been observed that the metal ion doesn't necessarily sit co-planar with the macrocycle. In a DFT study performed by D. Qin *et al.* it was observed that there are multiple possible positions in which the metalting atom, in this case Sn, can reside within the phthalocyanine macrocycle. The atomic radius of Sn is relatively large, and due to this it was calculated to site just outside the macrocycle, either above or below it relative to the surface. [122] The gold atomic radius (174 pm) is slightly larger than the radius for tin (145 pm), making it likely to exhibit a similar behaviour. Crystallography data has suggested that the Au-TPP complex can be planar, however if this is not the case for 100% of the TPP molecules on the surface there may be an effect on the coherent fraction and position of the phase. Including small amounts of metalated TPP in which the gold atom sits just above or just below the plane of the molecule improves the fitting of the coherent fraction of this phase in particular. An argand diagram displaying the fitting when the co-planar AuTPP accounts for 75% of the total and the deviated TPP accounts for 25% (12.5% either side) can be seen in Figure 7.13b. By using these proportions the calculated C_f and C_p parameters are $C_f = 0.65$ and $C_p = 0.29$. While the fit displayed here is not perfect, it can be seen that by changing the ratio in which these species appear on the surface the fit of the vectors can be improved/worsened.

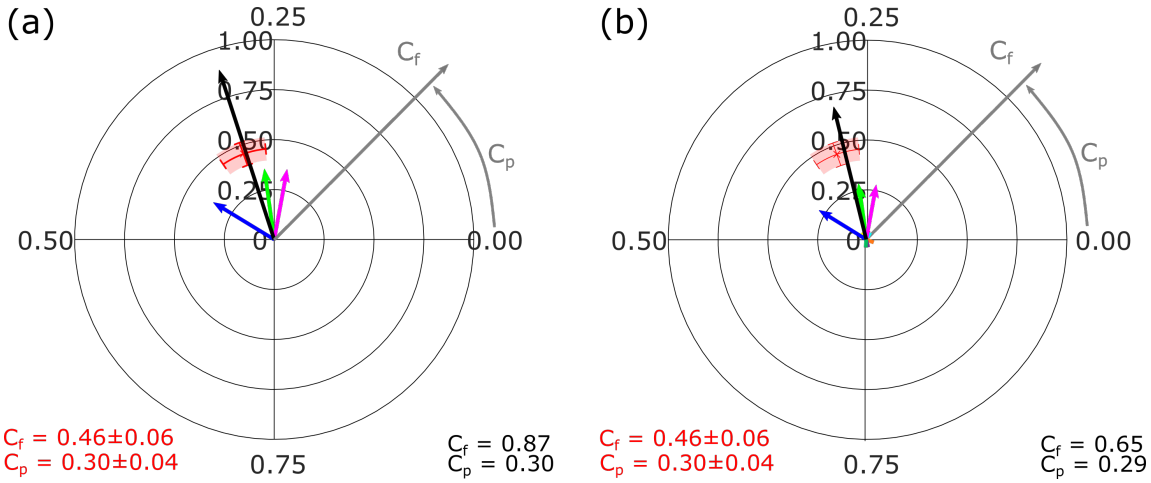

Figure 7.13: Argand diagrams showing C_f and C_p values obtained from XSW measurements from the (111) reflection for the metalated phase of TPP. The experimental values are show by the red error bars with the range enclosed in a lighter red area. The coloured arrows represent vectors showing C_f and C_p values for the different binding sites for the Au atom, atop (blue), bridge (green), 3-fold hollow (pink), the black arrow represents a vector which is a sum of the component vectors. (a) Metalated phase argand diagram where the total C_f is summed to 1. (b) Metalated phase argand diagram where the total C_f is summed to 1, with contributions from the deviated metalated TPP derivative.

The metalated TPP molecule is known to have a planar core, with all nitrogen atoms bonding to the central gold atom [118]. From this it can be assumed that if it is in fact the ring-closed TPP derivative that is metalated, that structure would also be planar. A simulation of this molecule was made using Avogadro [99] to give a visual representation of this, which can be seen in Figure 7.14b. The plane defined using the *meso*-carbon atoms shows that each nitrogen atom is in the same plane as the rest of the molecule and therefore would adsorb at the same height.

An adsorption model for the metalated ring-closed TPP is pictured in Figure 7.14a. The nitrogen atoms are located within the second plane above the gold surface, pictured in the atop position at a height of 3.32 Å. The remainder of the atoms within TPP would also be adsorbing at the same height, limited by the VDW radius of the central gold atom.

A model of the TPP-derivative with the deviated core has also been included, which can be seen in Figure 7.14c. In the case where the gold atom sits slightly above the plane of the molecule the height of the nitrogen atoms is limited by the VDW radii of nitrogen and gold, which has been previously modelled in both the close-packed and diffuse phases. In the case where the gold atoms is below the plane of the molecule the height of the nitrogen atoms is determined by two factors,

firstly the VDW radii of the coordinating gold atoms and the VDW radii of the gold atoms in the surface. The second factor is the Au−N bond length, which limits how far out of plane the gold atom can be. By limiting that distance the maximum distance of the nitrogen atoms above the surface can be determined.

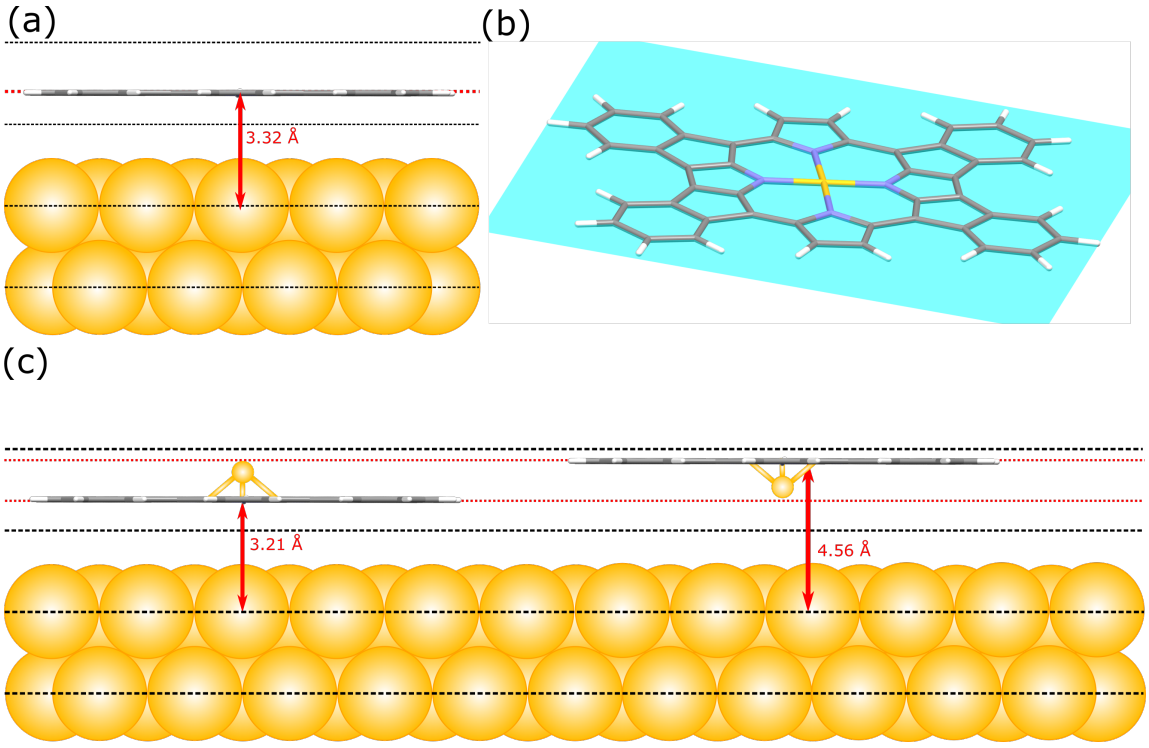

Figure 7.14: Modelling the behaviour of the metalated phase of TPP on Au(111). (a) Image showing two layers of surface gold atoms with the 111 crystal planes marked in dotted black lines. A simulated molecule of the metalated ring-closed derivative of TPP can be seen in the second plane at a height of 3.32 Å above the surface. (b) The metalated ring-close derivative of TPP with a plane defined using the four nitrogen atoms, shows the molecule is perfectly planar. (c) Image showing two layers of surface gold atoms with the 111 crystal planes marked in dotted black lines. A simulated molecule of the metalated ring-closed derivative of TPP can be seen in the second plane, on the left the gold atom is out-of-plane above the molecular and on the right the gold atoms is out-of-plane below the molecule, these give different absorption heights of 3.21 Å, and 4.56 Å.

7.4 Conclusion

Within this chapter NIXSW has been used to characterise the structural changes to the TPP on Au(111) surface in each phase. The coherent fraction and position values (C_f and C_p) have been extracted from the NIXSW information and used to find an absorption model for each phase of

TPP on Au(111).

The close-packed phase could be fit to either two or four NIXSW environments, similar to what was seen in the XPS in Chapter 6. Using four peaks was found to produce large errors on the C_f and C_p values, therefore the fitting was performed with the two peak fit. The two peaks were assigned to the iminic and aminic nitrogen environments, with C_p values of 0.25 and 0.35 and C_f values of 0.25 and 0.20 respectively. From the LEED data presented in Chapter 4 and the low coherent fractions it can be seen that the TPP lattice is incommensurate with the surface lattice and the nitrogen atoms can be found to adsorb in each different high symmetry site, atop, bridge and hollow. The difference in C_p values was attributed to the saddle conformation of TPP, in which the aminic nitrogen atoms are orientated upwards, away from the surface, leading to a higher coherent position. The model for TPP in the close-packed phase comprised of a mixture of TPP and aaTPP, which contributed to the low coherent fractions observed.

The diffuse phase could be fit to two, three or four NIXSW peaks. Similarly to the close-packed phase, the three peak and four peak fits produced large errors, and therefore the two peak fit was selected to model this phase. The two peaks were assigned to the iminic and aminic nitrogen environments, similarly to the close-packed phase. The coherent fractions for these peaks were 0.41 and 0.36, while the coherent positions were 0.24 and 0.27. The change in the coherent position for the aminic peak was attributed to the ring closing reaction taking place in the annealing step, flattening the molecule and therefore equalising the heights of the aminic and iminic nitrogen atoms. This phase was also modelled using a mixture of TPP and aaTPP, as well as AuTPP, which has been seen to appear in small amounts in the first annealing step in the STS and XPS data. The low coherent fractions in this phase indicate that it is also incommensurate with the surface, which is supported by the disordered structure seen in the STM images and in the LEED pattern, seen in Chapter 4.

The metalated phase was fit to one NIXSW peak which were assigned to the nitrogen atoms all bonding to a gold atom. The C_f value for this peak was 0.41 and the C_p value was 0.30. This phase was assigned to the ring-closed TPP derivative, which has been metalated with a gold atom and was modelled using exclusively this component, however the position of the gold atom within the macrocycle was varied.

By employing the methods outlined in this chapter, detailed structural information on the

transitions that occur on the surface can be obtained, which can define the mechanisms that drive on-surface events.

Chapter 8

Conclusion

The work presented within this thesis has focused on understanding the behaviour and reaction pathways which link three phases of TPP molecules on the Au(111) surface. A detailed understanding of the concepts behind these processes allows for the design of systems in which the surface geometry and reaction pathways can be predicted and utilised to produce specific functionalities.

In Chapter 3 the synthesis of porphyrin molecules as subjects for surface studies was presented. A selection of porphyrin isomers were prepared using a statistical synthesis method and their ratio determined using ^1H NMR. The porphyrin molecules selected were tetraphenyl porphyrins functionalised with bromine (Br_XTPP) in different positions. The bromine atom would allow these porphyrins to take part in on-surface Ullmann coupling reactions. STM studies of these isomer mixtures were discussed in Chapter 4. Pure TPP was also synthesised using the Lindsey synthesis for the purpose of surface experiments, which were discussed in Chapters 5, 6, and 7.

In Chapter 4 two different phases, the close-packed phase and the diffuse phase, of TPP on Au(111) were characterised using a combination of STM and LEED. The close-packed phase of as-deposited TPP was found to form an incommensurate lattice with a square unit cell. The structure can be attributed to a combination of VDW forces and C$-$H$\cdots\pi$ interactions, suggesting that the arrangement is stabilised by molecule-molecule interactions as opposed to surface-molecule interactions. The diffuse phase of TPP, which was produced upon annealing the surface was found to be a disordered phase, in which the TPP molecules did not display the same packing arrangement as in the close-packed phase. Instead the TPP molecules has transitioned to a disordered phase, the

observation was linked to the intramolecular ring closing reaction, in which the porphyrin molecules planarise and form a TPP derivative. When the TPP molecules planarise, they lose their ability to form C−H···π interactions, causing the loss of the ordered arrangement. Despite the mixture of Br_XTPP isomers being used only TPP was seen on the surface. The statistical entropy for each surface was calculated using the Voronoi tessellation as a means for quantifying the change that had occurred. In both phases the calculation returned a value that represented the morphology of the surface.

In Chapter 5 additional SPM techniques, STS and KPFM, were used to further characterise the phases of TPP on Au(111). STS data determined that there were two 'types' of TPP molecule present in the close-packed phase, by looking at the positions of the HOMO and LUMO. The two 'types' were assigned to TPP adsorbing the saddle conformation, and also TPP adsorbing over top of an adatom species (aaTPP). STS spectra taken in the diffuse phase showed that there were three different porphyrin species present, TPP, aaTPP and a third species which was assigned to metalated TPP (AuTPP). The STS dataset from the diffuse phase also displayed a significant change in the ratio of TPP and aaTPP present on the surface. While the KPFM data displayed a negative shift between the close-packed and diffuse phases, the results were not indicative of a discernible change (eg. that the transformation was due to the formation of a charged species).

In Chapters 4 and 5 SPM studies determined the local structure of TPP on Au(111) and some of the electronic properties of this system. In Chapters 6 and 7 a chemical and structural characterisation was presented of the different phases of TPP on Au(111). Chapter 6 focused on the analysis of XPS spectra to determine the chemical environments present in each phase. This analysis focused on the N1s and C1s orbitals of TPP. The N1s in the close-packed phase displayed four distinct environments that were assigned to the aminic and iminic environments of TPP and aaTPP. The ratios of TPP and aaTPP peaks changed significantly in different areas of the surface and in different preparations, indicating that the proportion of aaTPP is highly dependant on the preparation and may be linked to the availability of Au adatoms. The diffuse phase displayed 3 different environments, assigned to TPP, aaTPP and AuTPP, these components appeared in various different ratios across the spectra. These experiments saw a new phase of TPP produced, the metalated phase, in which the TPP molecules uptake a gold atom into their cavity. The presence of this phase was monitored using rapid sequential XPS and the change in chemical environments

over the course of the reaction could be directly observed. This phase displayed only one peak, which indicates that all N atoms are in the same environment (bonding to gold). The C1s XPS spectra displayed changes through each of the phases indicative of a reaction having taken place.

Chapter 7 focused on using NIXSW to perform a structural characterisation of the TPP on Au(111) surface. By first extracting the chemical environments present using XPS analysis, the NIXSW peaks were fit and the coherent fraction and position values were extracted. Using these values, models for each phase of TPP on Au(111) were constructed. The close-packed phase gave two nitrogen peaks, with different coherent position values but similar coherent fractions. These values were modelled as TPP in the saddle conformation, in which the nitrogen atoms are at different heights within the molecule, adsorbing on the surface at also over adatoms, giving a large range of possible heights, thus the low coherent fractions. The diffuse phase also gave two peaks, however the coherent position values had equalised, reflecting the planarisation of the molecule, caused by the ring closing reaction, this phase also gave low coherent fraction values. The diffuse phase was modelled assuming that the molecule was planar and that the phase was made up of a combination of TPP, aaTPP and AuTPP (all planarised). The metalated phase only provided one peak, which was fit to a metalated porphyrin sitting on the surface with its height limited by the size of the gold atom inside it.

By employing this variety of surface-sensitive techniques it is possible to perform a full structural and chemical characterisation of these phases. By using STM alone the information available is limited to a visual characterisation of local areas on the surface. By employing a range of techniques there is more information available such that the underlying processes of the system may be understood.

The combination that proved to be particularly valuable was STM and NIXSW. These two techniques combined offer a local characterisation (STM) in which local artefacts can be seen on an atomic scale as well as a picture of the surface in terms of the coherent fraction and position values (NIXSW), from which the specific absorption geometry of the selected atoms can be extrapolated. The methodology is transferable to any on-surface reaction, and allows for the understanding the processes taking place. Furthermore, when applied to studying on-surface reactions, this approach is nearing the point at which mechanistic insight into these pathways is possible. This enables the design, construction and predication that at specific arrangement or reaction will take place,

allowing for the design of systems with increasing levels of complexity.

Appendix A

Additional Temperature Programmed XPS on the Diffuse to Metalated Phases Datasets

A.1 Additional N1s XPS Datasets

An additional dataset for the temperature programmed XPS (N1s region) on the diffuse to metalated phases is presented alongside the one shown in Chapter 6. Similar observations were observed in both datasets. Two peaks, N and NH were seen in the diffuse phase, which reduced over time, to give a single central peak between them. The iminic peak N which appears at 397.4 eV is the first peak to diminish, followed and the aminic peak NH which appears at 399.2 eV. While the third peak, related to Au−N grew at 398.0 eV.

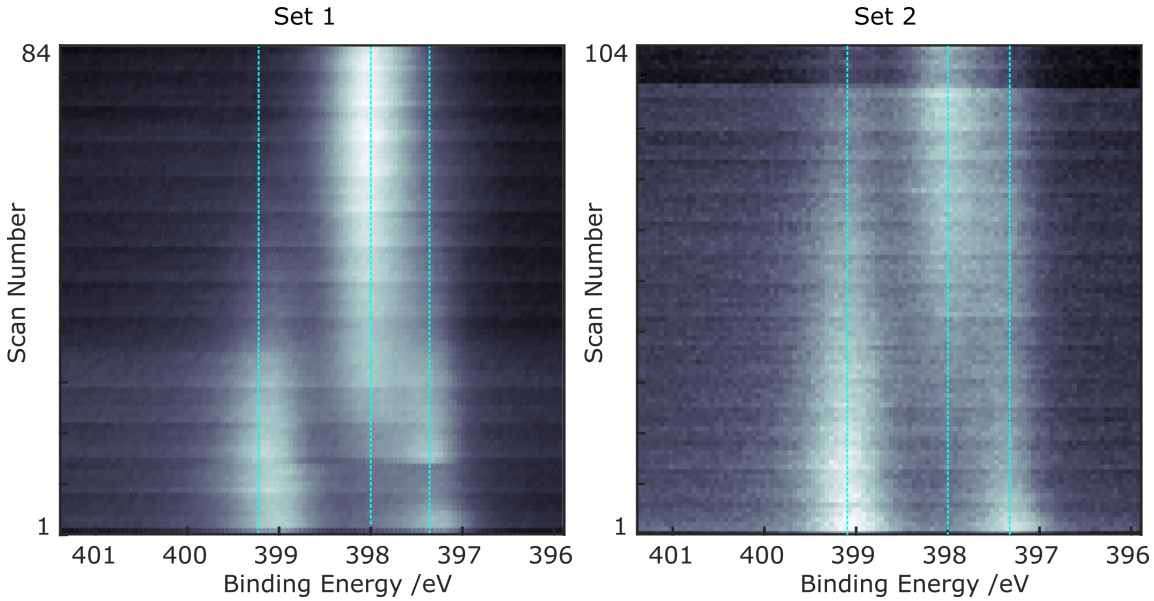

Figure A.1: Colour gradient showing the change in the proportion of total peak area over each scan, where the intensity of the peak is represented by the intensity of the colour, where the dark areas have less intensity and the bright areas have higher intensity.

A.2 Additional C1s XPS Datasets

Two C1s datasets were taken alongside the N1s datasets. Due to the close proximity of the peaks, changes in peak intensity and energy are harder to measure using this method. The changes in peak structure between the diffuse and metalated phases in the C1s were reported in Chapter 6. The only change visible in the heat map visualisation of this data is the small shift of 0.3 eV to a higher binding energy in the main peak structure.

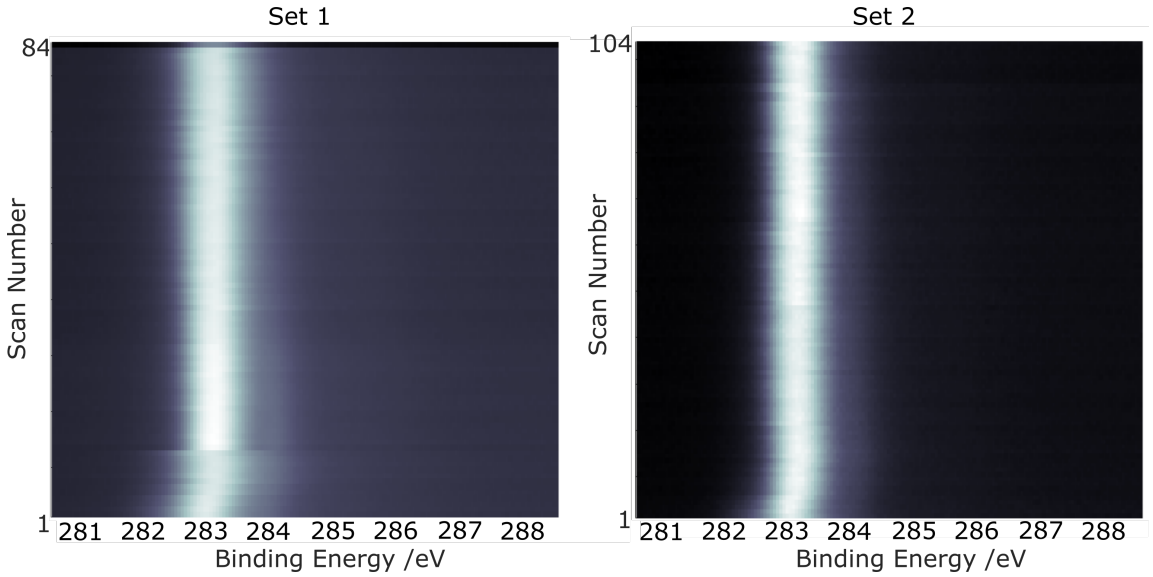

Figure A.2: Colour gradient showing the change in the proportion of total peak area over each scan, where the intensity of the peak is represented by the intensity of the colour, where the dark areas have less intensity and the bright areas have higher intensity.

Appendix B

Distribution of Binding Sites for the Close-packed Phase

B.1 Modelling the Close-packed Phase- Finding a Binding Site

The close-packed phase of TPP was determined by LEED to form an incommensurate lattice with respect to the surface atoms below, meaning that there is not a unit cell which can be defined using both lattices. The presence of a preferential binding site was rejected upon further investigation. This was confirmed by fitting a scaled atomic model of the herringbone reconstructions underneath an STM image in which the herringbone and TPP arrangement are both clearly visible. Scaled models of the TPP molecule were then fit over this image to determine what the binding site of the nitrogen atoms would be. The results are collated in the table below.

TPP Rotation	N			NH		
	Atop	Bridge	Hollow	Atop	Bridge	Hollow
A	34	35	29	25	60	13
B	32	33	31	22	54	20

Table B.1: Binding sites of close-packed phase TPP molecules in rotations A and B

It can be seen in Table B.1, that for the iminic nitrogen the binding sites are distributed evenly across atop, bridge and 3-fold hollow sites for both rotations of TPP. For the aminic there is a slight preference for the bridge sites in both rotations with just over half (58%) of the aminic nitrogens sitting in bridge sites.

Appendix C

Additional NIXSW Data

C.1 The (-111) Reflection

In addition to the (111) reflection, which gives information about the vertical positions of the atoms relative to the surface plane, the (-111) reflection was also measured, this reflection gives information about the lateral positions of the atoms on the surface. This data can be used in conjunction with the (111) reflection data to find the exact positions of the atoms. The data was processed in the same manner as previously discussed, by first extracting the intensities of each chemically unique nitrogen environment by fitting peaks to XPS data. These were then used to fit absorption profiles for each environment, which allowed for the coherent fractions and positions to be extracted. The data acquired in the (-111) direction can be seen to be of a reduced quality in comparison to the (111) data, this is due to the positioning of the analyser; resulting in a reduction in signal intensity. Figure C.1 show the XSW profiles for the N and NH peaks of the close packed phase. The coherent fraction and position for the iminic nitrogen were calculated to be $C_f = 0.40 \pm 0.09$, and $C_p = 0.02 \pm 0.06$, and $C_f = 0.33 \pm 0.07$, and $C_p = 0.97 \pm 0.06$ for the aminic nitrogen. Using these coherent fraction values it can be reasoned that there is not a favourable adsorption site in the lateral direction across the surface. The TPP molecules can be assumed to be adsorbing in a range of positions between the (-111) planes which suggests as we have been previously stated, an incommensurate lattice. Due to the low coherent fraction, it is hard to utilise the coherent position from these scans as there are many different combinations of vectors which could be used to fit to

the coherent fractions.

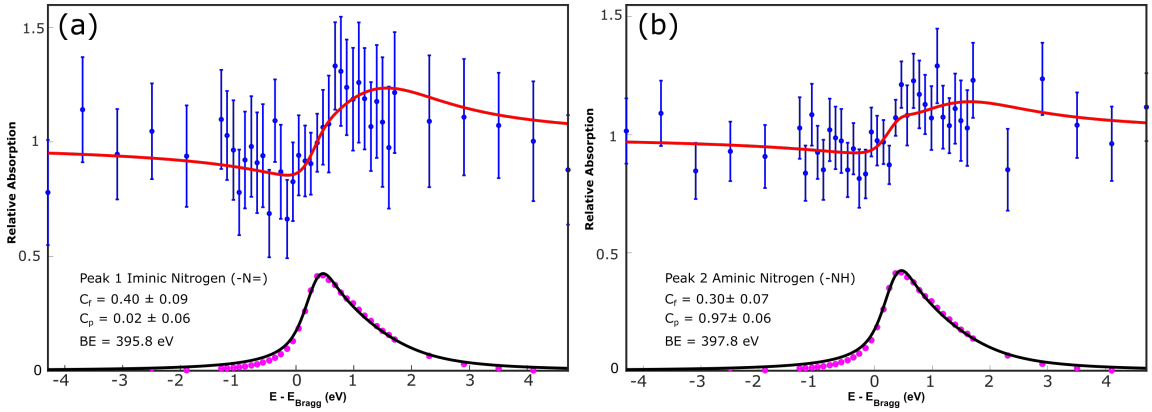

Figure C.1: NIXSW measurements of the close packed phase of TPP. NIXSW photoelectron yields obtained using the (-111) reflection from the Au(111) crystal for the N1s core orbitals. (a) Peak 1, (b) Peak 2. The reflectively curve is shown below each XSW curve.

The only phase in which there could be a regular ordering in this direction would be the close packed phase. The coherent fractions are low in the diffuse and metalated phases as well, which are already known to be disordered. The coherent fractions and positions from the (-111) reflection can be seen in Table C.1.

Phase	**Peak**	C_f	C_p
Close Packed (-111)	−N=	0.395 ± 0.09	0.015 ± 0.06
	NH	0.325 ± 0.07	0.965 ± 0.06
Diffuse (-111)	−N=	0.295 ± 0.08	0.965 ± 0.06
	NH	0.365 ± 0.09	0.965 ± 0.06
Metalated (-111)	Au−N	0.424 ± 0.06	0.987 ± 0.04

Table C.1: Caption

C.2 Modelling the Diffuse Phase

The iminic nitrogen peak was first to be studied. In this phase the first model that was attempted used the ratio of TPP:aaTPP:AuTPP found using the STS spectra. This gave TPP to account for 30% of the total molecules, aaTPP to account for 50% and AuTPP to account for the remaining

20%. Using this ratio and the assumption that the experimental C_f value has been artificially reduced, the C_f component for TPP vectors were equal and set to 0.05, while the C_f components for aaTPP and AuTPP were 0.083 and 0.033 respectively. The C_p values used were taken from Table 7.2, to give a total of nine vectors to be plotted. These are displayed in Figure 7.11a. The blue, green and pink vectors represent the TPP heights and the red, cyan and yellow vectors represent the aaTPP vectors. The AuTPP vectors are orange, purple and dark green, however due to the low proportion of AuTPP in this model it is difficult to see them. The black vector represents the sum of all the components, and gives a total $C_f = 0.09$ and $C_p = 0.60$. From this, it is clear that this model is incorrect as these values do not lie within the shaded red region.

The second attempt to find a model for this phase used the ratio of TPP and aaTPP calculated using the N_α and N_β peaks from the XPS spectra. This ratio gave 60% of the total molecules as TPP and 40% as aaTPP (3:2). This gave a C_f component of 0.1 for TPP and 0.07 for aaTPP, with a total of sixe vectors to be plotted. The resultant argand diagram can be seen in 7.11b. The blue, green and pink vectors represent the heights of TPP and the cyan, red and yellow vectors represent aaTPP. The black vector, representing the sum of the components gives a total $C_f = 0.18$ and $C_p = 0.27$. In this model the coherent position is a much better fit and lies within the uncertainty range of the experimental value, the coherent fraction however, is too low and does not fall within that range.

The low coherent fraction in this model could be due to two reasons; the STS data suggests that the diffuse phase may have a small amount of a metalated species, which has not been accounted for in this model and would affect the total C_f value, the second reason is that the thermal noise may not be reducing the coherent fraction has much as it was previously thought. These factors were accounted for in the finalised fits for this phase.

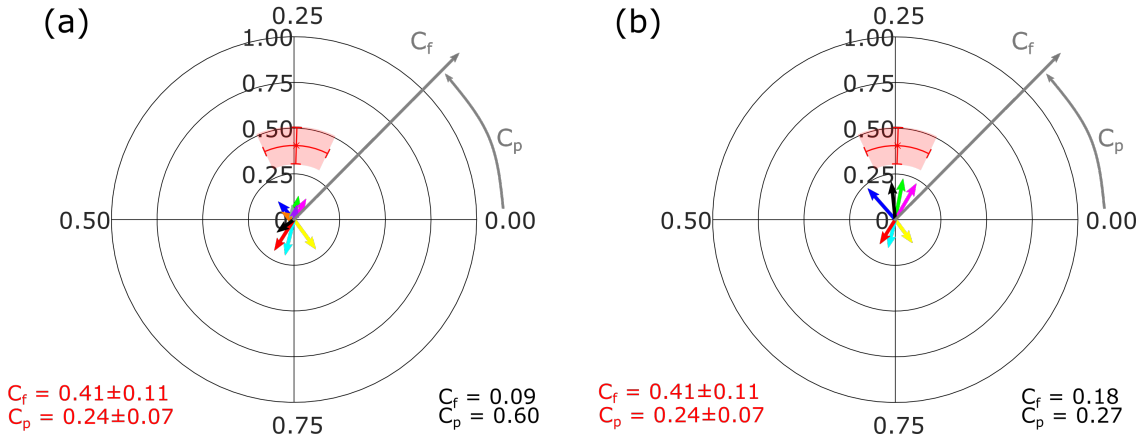

Figure C.2: Argand diagrams showing C_f and C_p values obtained from XSW measurements from the (111) reflection for the diffuse phase of TPP. The experimental values are show by the red error bars with the range enclosed in a lighter red area. (a) Argand diagram for Model 1. (b) Argand diagram for Model 2

Bibliography

[1] Jean-Marie Lehn. Supramolecular chemistry. *Science*, 260(5115):1762–1764, 1993.

[2] Jean-Marie Lehn. Supramolecular chemistry. 1995.

[3] The nobel prize in chemistry 2016. Available at https://www.nobelprize.org/prizes/chemistry/2016/summary/ (2021/07/23).

[4] RP Feynman. There's plenty of room at the bottom, engineering and science 23 (5), 22-36. 1960.

[5] Ludwig Bartels. Tailoring molecular layers at metal surfaces. *Nature chemistry*, 2(2):87–95, 2010.

[6] Jacob N Israelachvili. *Intermolecular and surface forces*. Academic press, 2015.

[7] Dawei Zhang, Tanya K Ronson, You-Quan Zou, and Jonathan R Nitschke. Metal–organic cages for molecular separations. *Nature Reviews Chemistry*, 5(3):168–182, 2021.

[8] Nazir Ahmad, Hussein A Younus, Adeel H Chughtai, and Francis Verpoort. Metal–organic molecular cages: applications of biochemical implications. *Chemical Society Reviews*, 44(1):9–25, 2015.

[9] Robert V Slone, Joseph T Hupp, Charlotte L Stern, and Thomas E Albrecht-Schmitt. Self-assembly of luminescent molecular squares featuring octahedral rhenium corners. *Inorganic chemistry*, 35(14):4096–4097, 1996.

[10] Jackson K Cherutoi, Jace D Sandifer, Uttam R Pokharel, Frank R Fronczek, Svetlana Pakhomova, and Andrew W Maverick. Externally and internally functionalized copper (ii) β-diketonate molecular squares. *Inorganic chemistry*, 54(16):7791–7802, 2015.

[11] Kaho Sugimoto, Yuya Tanaka, Shintaro Fujii, Tomofumi Tada, Manabu Kiguchi, and Munetaka Akita. Organometallic molecular wires as versatile modules for energy-level alignment of the metal–molecule–metal junction. *Chemical Communications*, 52(34):5796–5799, 2016.

[12] Abraham Ulman. Formation and structure of self-assembled monolayers. *Chemical reviews*, 96(4):1533–1554, 1996.

[13] Leslie J Murray, Mircea Dincă, and Jeffrey R Long. Hydrogen storage in metal–organic frameworks. *Chemical Society Reviews*, 38(5):1294–1314, 2009.

[14] Anastasiya Bavykina, Nikita Kolobov, Il Son Khan, Jeremy A Bau, Adrian Ramirez, and Jorge Gascon. Metal–organic frameworks in heterogeneous catalysis: recent progress, new trends, and future perspectives. *Chemical Reviews*, 120(16):8468–8535, 2020.

[15] James A Theobald, Neil S Oxtoby, Michael A Phillips, Neil R Champness, and Peter H Beton. Controlling molecular deposition and layer structure with supramolecular surface assemblies. *Nature*, 424(6952):1029–1031, 2003.

[16] Steven De Feyter, Atsushi Miura, Sheng Yao, Zhijian Chen, Frank Würthner, Pascal Jonkheijm, Albertus PHJ Schenning, EW Meijer, and Frans C De Schryver. Two-dimensional self-assembly into multicomponent hydrogen-bonded nanostructures. *Nano letters*, 5(1):77–81, 2005.

[17] Gangamallaiah Velpula, Takashi Takeda, Jinne Adisoejoso, Koji Inukai, Kazukuni Tahara, Kunal S Mali, Yoshito Tobe, and Steven De Feyter. On the formation of concentric 2d multicomponent assemblies at the solution–solid interface. *Chemical Communications*, 53(6):1108–1111, 2017.

[18] Yuan Fang, Elke Ghijsens, Oleksandr Ivasenko, Hai Cao, Aya Noguchi, Kunal S Mali, Kazukuni Tahara, Yoshito Tobe, and Steven De Feyter. Dynamic control over supramolecu-

lar handedness by selecting chiral induction pathways at the solution–solid interface. *Nature chemistry*, 8(7):711–717, 2016.

[19] Shuhei Furukawa, Hiroshi Uji-i, Kazukuni Tahara, Tomoyuki Ichikawa, Motohiro Sonoda, Frans C De Schryver, Yoshito Tobe, and Steven De Feyter. Molecular geometry directed kagomé and honeycomb networks: toward two-dimensional crystal engineering. *Journal of the American Chemical Society*, 128(11):3502–3503, 2006.

[20] R Decker, U Schlickum, F Klappenberger, G Zoppellaro, S Klyatskaya, M Ruben, JV Barth, and H Brune. Using metal-organic templates to steer the growth of fe and co nanoclusters. *Applied Physics Letters*, 93(24):243102, 2008.

[21] D Ecija, M Marschall, J Reichert, A Kasperski, D Nieckarz, P Szabelski, W Auwärter, and JV Barth. Dynamics and thermal stability of surface-confined metal–organic chains. *Surface Science*, 643:91–97, 2016.

[22] F Ullmann and Jean Bielecki. Ueber synthesen in der biphenylreihe. *Berichte der deutschen chemischen Gesellschaft*, 34(2):2174–2185, 1901.

[23] Weihua Wang, Xingqiang Shi, Shiyong Wang, Michel A Van Hove, and Nian Lin. Single-molecule resolution of an organometallic intermediate in a surface-supported ullmann coupling reaction. *Journal of the American Chemical Society*, 133(34):13264–13267, 2011.

[24] Qitang Fan, Cici Wang, Yong Han, Junfa Zhu, Julian Kuttner, Gerhard Hilt, and J Michael Gottfried. Surface-assisted formation, assembly, and dynamics of planar organometallic macrocycles and zigzag shaped polymer chains with c–cu–c bonds. *Acs Nano*, 8(1):709–718, 2014.

[25] Chris J Judd, Sarah L Haddow, Neil R Champness, and Alex Saywell. Ullmann coupling reactions on ag (111) and ag (110); substrate influence on the formation of covalently coupled products and intermediate metal-organic structures. *Scientific reports*, 7(1):1–7, 2017.

[26] MF Perutz, MG Rossmann, AF Cullis, HILARY Muirhead, G Will, and ACT North. Structure of hemoglobin. In *Brookhaven Symp Biol*, volume 13, pages 165–183, 1960.

[27] Karishma Devi Borah and Jagannath Bhuyan. Magnesium porphyrins with relevance to chlorophylls. *Dalton Transactions*, 46(20):6497–6509, 2017.

[28] Isao Mochida, Katsuya Suetsugu, Hiroshi Fujitsu, and Kenjiro Takeshita. Enhanced catalytic activity of cobalt tetraphenylporphyrin on titanium dioxide by evacuation at elevated temperatures for intensifying the complex-support interaction. *The Journal of Physical Chemistry*, 87(9):1524–1529, 1983.

[29] Abdolreza Rezaeifard and Maasoumeh Jafarpour. The catalytic efficiency of fe-porphyrins supported on multi-walled carbon nanotubes in the heterogeneous oxidation of hydrocarbons and sulfides in water. *Catalysis Science & Technology*, 4(7):1960–1969, 2014.

[30] Hiroshi Imahori. Giant multiporphyrin arrays as artificial light-harvesting antennas. *The Journal of Physical Chemistry B*, 108(20):6130–6143, 2004.

[31] Lu-Lin Li and Eric Wei-Guang Diau. Porphyrin-sensitized solar cells. *Chemical society reviews*, 42(1):291–304, 2013.

[32] Christopher J Wilson, Daniela A Wilson, Ross W Boyle, and Georg H Mehl. The design and investigation of porphyrins with liquid crystal properties at room temperature. *Journal of Materials Chemistry C*, 1(1):144–150, 2013.

[33] Tony E Karam, Noureen Siraj, Jeewan C Ranasinghe, Paulina E Kolic, Bishnu P Regmi, Isiah M Warner, and Louis H Haber. Efficient photoinduced energy transfer in porphyrin-based nanomaterials. *The Journal of Physical Chemistry C*, 124(44):24533–24541, 2020.

[34] Mandeep K Chahal, Habtom B Gobeze, Whitney A Webre, Paul A Karr, Daniel T Payne, Katsuhiko Ariga, Francis D'Souza, and Jonathan P Hill. Electron and energy transfer in a porphyrin–oxoporphyrinogen–fullerene triad, znp–oxp–c 60. *Physical Chemistry Chemical Physics*, 22(25):14356–14363, 2020.

[35] Micheal J. Gottfried. Surface chemistry of porphyrins and phthalocyanines. *Surface Science Reports*, 70(3):256–379, 2015.

[36] Geoffrey Rojas, Xumin Chen, Cameron Bravo, Ji-Hyun Kim, Jae-Sung Kim, Jie Xiao, Peter A Dowben, Yi Gao, Xiao Cheng Zeng, Wonyoung Choe, et al. Self-assembly and properties of

nonmetalated tetraphenyl-porphyrin on metal substrates. *The Journal of Physical Chemistry C*, 114(20):9408–9415, 2010.

[37] Jens Brede, Mathieu Linares, Stefan Kuck, Jörg Schwöbel, Alessandro Scarfato, Shih-Hsin Chang, Germar Hoffmann, Roland Wiesendanger, Roy Lensen, Paul HJ Kouwer, et al. Dynamics of molecular self-ordering in tetraphenyl porphyrin monolayers on metallic substrates. *Nanotechnology*, 20(27):275602, 2009.

[38] Michael Stark, Stefanie Ditze, Martin Drost, Florian Buchner, Hans-Peter Steinrück, and Hubertus Marbach. Coverage dependent disorder–order transition of 2h-tetraphenylporphyrin on cu (111). *Langmuir*, 29(12):4104–4110, 2013.

[39] Johannes Mielke, Felix Hanke, Maike V Peters, Stefan Hecht, Mats Persson, and Leonhard Grill. Adatoms underneath single porphyrin molecules on au (111). *Journal of the American chemical society*, 137(5):1844–1849, 2015.

[40] Leonhard Grill, Matthew Dyer, Leif Lafferentz, Mats Persson, Maike V Peters, and Stefan Hecht. Nano-architectures by covalent assembly of molecular building blocks. *Nature nanotechnology*, 2(11):687–691, 2007.

[41] Leif Lafferentz, V Eberhardt, Carlo Dri, C Africh, Giovanni Comelli, F Esch, S Hecht, and Leonhard Grill. Controlling on-surface polymerization by hierarchical and substrate-directed growth. *Nature chemistry*, 4(3):215–220, 2012.

[42] Leif Lafferentz, V Eberhardt, Carlo Dri, C Africh, Giovanni Comelli, F Esch, S Hecht, and Leonhard Grill. Controlling on-surface polymerization by hierarchical and substrate-directed growth. *Nature chemistry*, 4(3):215–220, 2012.

[43] Alissa Wiengarten, Julian A Lloyd, Knud Seufert, Joachim Reichert, Willi Auwärter, Runyuan Han, David A Duncan, Francesco Allegretti, Sybille Fischer, Seung Cheol Oh, et al. Surface-assisted cyclodehydrogenation; break the symmetry, enhance the selectivity. *Chemistry-A European Journal*, 21(35):12285–12290, 2015.

[44] Borja Cirera, Bruno de la Torre, Daniel Moreno, Martin Ondràčěk, Radek Zboril, Rodolfo Miranda, Pavel Jelínek, and David Ecija. On-surface synthesis of gold porphyrin derivatives

via a cascade of chemical interactions: Planarization, self-metalation, and intermolecular coupling. *Chemistry of Materials*, 31(9):3248–3256, 2019.

[45] C-E. Ha N. V. Bhagavan. *Essentials of Medical Biochemistry*. Elsevier, 2015.

[46] J. K. M. Sanders, N. Bampos, Z. Clyde-Watson, S. L. Darling, J. C. Hawley, H-J Kim, C.C. Mak, and S. J. Webb. The porphyrin handbook vol.3. pages 1–48, 2000.

[47] Kevin M Smith. *Porphyrins and metalloporphyrins*, volume 9. Elsevier Amsterdam, 1975.

[48] Tatyana E Shubina, Hubertus Marbach, Ken Flechtner, Andreas Kretschmann, Norbert Jux, Florian Buchner, Hans-Peter Steinrück, Timothy Clark, and J Michael Gottfried. Principle and mechanism of direct porphyrin metalation: Joint experimental and theoretical investigation. *Journal of the American Chemical Society*, 129(30):9476–9483, 2007.

[49] M Panighel, G Di Santo, M Caputo, C Lal, B Taleatu, and A Goldoni. Review of 2h-tetraphenylporphyrins metalation in ultra-high vacuum on metal surfaces. In *Journal of Physics: Conference Series*, volume 470, page 012012. IOP Publishing, 2013.

[50] Florian Buchner, Veronika Schwald, Karmen Comanici, Hans-Peter Steinrück, and Hubertus Marbach. Microscopic evidence of the metalation of a free-base porphyrin monolayer with iron. *ChemPhysChem*, 8(2):241–243, 2007.

[51] Stefan Müllegger, Wolfgang Schöfberger, Mohammad Rashidi, Lorenz M Reith, and Reinhold Koch. Spectroscopic stm studies of single gold (iii) porphyrin molecules. *Journal of the American Chemical Society*, 131(49):17740–17741, 2009.

[52] Stefan Müllegger, Wolfgang Schöfberger, Mohammad Rashidi, Thomas Lengauer, Florian Klappenberger, Katharina Diller, Kamuran Kara, Johannes V Barth, Eva Rauls, Wolf Gero Schmit, et al. Preserving charge and oxidation state of au (iii) ions in an agent-functionalized nanocrystal model system. *ACS nano*, 5(8):6480–6486, 2011.

[53] Marco Nardi, Roberto Verucchi, Claudio Corradi, Marco Pola, Maurizio Casarin, Andrea Vittadini, and Salvatore Iannotta. Tetraphenylporphyrin electronic properties: a combined theoretical and experimental study of thin films deposited by sumbd. *Physical Chemistry Chemical Physics*, 12(4):871–880, 2010.

[54] J Michael Gottfried, Ken Flechtner, Andreas Kretschmann, Thomas Lukasczyk, and Hans-Peter Steinrück. Direct synthesis of a metalloporphyrin complex on a surface. *Journal of the American Chemical Society*, 128(17):5644–5645, 2006.

[55] Michael Röckert, Stefanie Ditze, Michael Stark, Jie Xiao, Hans-Peter Steinrück, Hubertus Marbach, and Ole Lytken. Abrupt coverage-induced enhancement of the self-metalation of tetraphenylporphyrin with cu (111). *The Journal of Physical Chemistry C*, 118(3):1661–1667, 2014.

[56] PTP Ryan, PL Lalaguna, F Haag, MM Braim, P Ding, DJ Payne, JV Barth, T-L Lee, DP Woodruff, F Allegretti, et al. Validation of the inverted adsorption structure for free-base tetraphenyl porphyrin on cu (111). *Chemical Communications*, 56(25):3681–3684, 2020.

[57] C Bürker, A Franco-Cañellas, K Broch, T-L Lee, A Gerlach, and F Schreiber. Self-metalation of 2 h-tetraphenylporphyrin on cu (111) studied with xsw: Influence of the central metal atom on the adsorption distance. *The Journal of Physical Chemistry C*, 118(25):13659–13666, 2014.

[58] Gerd Binnig and Heinrich Rohrer. Scanning tunneling microscopy. *Surface science*, 126(1-3):236–244, 1983.

[59] Gerd Binnig and Heinrich Rohrer. Scanning tunneling microscopy. *Helvetica Physica Acta*, 55:726–735, 1983.

[60] The nobel prize in physics 1986. Available at https://www.nobelprize.org/prizes/physics/1986/summary/ (2021/07/23).

[61] Nan Yao and Zhong Lin Wang. *Handbook of microscopy for nanotechnology*. Springer, 2005.

[62] John Bardeen. Tunnelling from a many-particle point of view. *Physical Review Letters*, 6(2):57, 1961.

[63] Jerry Tersoff and DR Hamann. Theory and application for the scanning tunneling microscope. *Physical review letters*, 50(25):1998, 1983.

[64] Jerry Tersoff and Donald R Hamann. Theory of the scanning tunneling microscope. *Physical Review B*, 31(2):805, 1985.

[65] Sense Jan van der Molen and Peter Liljeroth. Charge transport through molecular switches. *Journal of Physics: Condensed Matter*, 22(13):133001, 2010.

[66] Roland Wiesendanger. *Scanning probe microscopy and spectroscopy: methods and applications*. Cambridge university press, 1994.

[67] Lord Kelvin. V. contact electricity of metals. *The London, Edinburgh, and Dublin Philosophical Magazine and Journal of Science*, 46(278):82–120, 1898.

[68] Sascha Sadewasser and Thilo Glatzel. *Kelvin probe force microscopy: measuring and compensating electrostatic forces*, volume 48. Springer Science & Business Media, 2011.

[69] F. Sharifi. *Kelvin Probe Force Microscopy on Graphene Thin Films for Solar Cell and Biosensing Applications*. PhD thesis, 2014.

[70] William L. Bragg. V. contact electricity of metals. *Proceedings of the Cambridge Philosophical Society*, 17:43–57, 1912.

[71] Gianangelo Bracco and Bodil Holst. *Surface science techniques*. Springer Science & Business Media, 2013.

[72] Kai Siegbahn. Electron spectroscopy for atoms, molecules, and condensed matter. *Reviews of Modern Physics*, 54(3):709, 1982.

[73] U Gelius, E Basilier, S Svensson, T Bergmark, and K Siegbahn. A high resolution esca instrument with x-ray monochromator for gases and solids. *Journal of Electron Spectroscopy and Related Phenomena*, 2(5):405–434, 1973.

[74] DP Woodruff. Surface structure determination using x-ray standing waves. *Reports on Progress in Physics*, 68(4):743, 2005.

[75] Robert G Jones, ASY Chan, MG Roper, MP Skegg, IG Shuttleworth, CJ Fisher, GJ Jackson, JJ Lee, DP Woodruff, NK Singh, et al. X-ray standing waves at surfaces. *Journal of Physics: Condensed Matter*, 14(16):4059, 2002.

[76] GA Hendry and OT Jones. Haems and chlorophylls: comparison of function and formation. *Journal of medical genetics*, 17(1):1, 1980.

[77] Johan Luwig Thudichum. Haems and chlorophylls: comparison of function and formation. *Report of the Medical Officer*, 1867.

[78] Jianbing Jiang, Jacob A Spies, John R Swierk, Adam J Matula, Kevin P Regan, Neyen Romano, Bradley J Brennan, Robert H Crabtree, Victor S Batista, Charles A Schmuttenmaer, et al. Direct interfacial electron transfer from high-potential porphyrins into semiconductor surfaces: a comparison of linkers and anchoring groups. *The Journal of Physical Chemistry C*, 122(25):13529–13539, 2018.

[79] Yoshio Furusho, Takayuki Kimura, Yukitami Mizuno, and Takuzo Aida. Chirality-memory molecule: Ad 2-symmetric fully substituted porphyrin as a conceptually new chirality sensor. *Journal of the American Chemical Society*, 119(22):5267–5268, 1997.

[80] Kristian M Roth, Narasaiah Dontha, Rajeev B Dabke, Daniel T Gryko, Christian Clausen, Jonathan S Lindsey, David F Bocian, and Werner G Kuhr. Molecular approach toward information storage based on the redox properties of porphyrins in self-assembled monolayers. *Journal of Vacuum Science & Technology B: Microelectronics and Nanometer Structures Processing, Measurement, and Phenomena*, 18(5):2359–2364, 2000.

[81] Xiangdong Xue, Aaron Lindstrom, and Yuanpei Li. Porphyrin-based nanomedicines for cancer treatment. *Bioconjugate chemistry*, 30(6):1585–1603, 2019.

[82] Panagiotis A Angaridis, Theodore Lazarides, and Athanassios C Coutsolelos. Functionalized porphyrin derivatives for solar energy conversion. *Polyhedron*, 82:19–32, 2014.

[83] Lionel R. Milgrom. *The Colours of Life*. Oxford University Press, 1997.

[84] Hans Fischer, Hans Orth, and Adolf Stern. *Die Chemie des Pyrroles*. Johnson Reprint Corporation, 1968.

[85] Hans Fischer and K Zeile. Synthese des haematoporphyrins, protoporphyrins und haemins. *Justus Liebigs Annalen der Chemie*, 468(1):98–116, 1929.

[86] Paul Rothemund. Formation of porphyrins from pyrrole and aldehydes. *Journal of the American Chemical Society*, 57(10):2010–2011, 1935.

[87] Paul Rothemund. Porphyrin studies. iii. 1 the structure of the porphine2 ring system. *Journal of the American Chemical Society*, 61(10):2912–2915, 1939.

[88] Paul Rothemund. A new porphyrin synthesis. the synthesis of porphin1. *Journal of the American Chemical Society*, 58(4):625–627, 1936.

[89] Paul Rothemund and Amel R Menotti. Porphyrin studies. iv. 1 the synthesis of α, β, γ, δ-tetraphenylporphine. *Journal of the American Chemical Society*, 63(1):267–270, 1941.

[90] Alan D Adler, Frederick R Longo, and William Shergalis. Mechanistic investigations of porphyrin syntheses. i. preliminary studies on ms-tetraphenylporphin. *Journal of the American Chemical Society*, 86(15):3145–3149, 1964.

[91] Jonathan S Lindsey, Irwin C Schreiman, Henry C Hsu, Patrick C Kearney, and Anne M Marguerettaz. Rothemund and adler-longo reactions revisited: synthesis of tetraphenylporphyrins under equilibrium conditions. *The Journal of Organic Chemistry*, 52(5):827–836, 1987.

[92] GP Arsenault, Ex Bullock, and SF MacDonald. Pyrromethanes and porphyrins therefrom1. *Journal of the American Chemical Society*, 82(16):4384–4389, 1960.

[93] Tim Hames. *Playing Tetris with porphyrins: the synthesis of porphyrinic materials for self-sssembly studies*. PhD thesis.

[94] Karl Kadish, Kevin M Smith, and Roger Guilard. *The Porphyrin Handbook: Chlorophylls and Bilins: Biosynthesis, Synthesis and Degradation*, volume 13. Elsevier, 2000.

[95] Lionel R Milgrom. Synthesis of some new tetra-aryl porphyrins for studies in solar energy conversion. part 2. asymmetric porphyrins. *Journal of the Chemical Society, Perkin Transactions 1*, pages 1483–1487, 1984.

[96] Diane F Marsh, RaeAnne E Falvo, and Larry M Mink. Microscale synthesis and 1h nmr analysis of tetraphenylporphyrins. *Journal of chemical education*, 76(2):237, 1999.

[97] Diane F Marsh, RaeAnne E Falvo, and Larry M Mink. Microscale synthesis and 1h nmr analysis of tetraphenylporphyrins. *Journal of chemical education*, 76(2):237, 1999.

[98] A Navaza, C De Rango, and P Charpin. 5, 10, 15, 20-tetraphenylporphyrin–bis (trifluoroacetic acid) dioxouranium (vi) trifluoroacetate, c44h30n4. 2c2hf3o2.[uo2][c2f3o2] 2. *Acta Crystallographica Section C: Crystal Structure Communications*, 39(12):1625–1628, 1983.

[99] Marcus D Hanwell, Donald E Curtis, David C Lonie, Tim Vandermeersch, Eva Zurek, and Geoffrey R Hutchison. Avogadro: an advanced semantic chemical editor, visualization, and analysis platform. *Journal of cheminformatics*, 4(1):1–17, 2012.

[100] S Müllegger, M Rashidi, T Lengauer, E Rauls, WG Schmidt, G Knör, W Schöfberger, and R Koch. Asymmetric saddling of single porphyrin molecules on au (111). *Physical Review B*, 83(16):165416, 2011.

[101] René Descartes. *Principia Philosophiae*. Amsterdam: Apud Danielem Elzevirium, 1644.

[102] Thomas M Liebling and Lionel Pournin. Voronoi diagrams and delaunay triangulations: Ubiquitous siamese twins. *Documenta Mathematics, ISMP*, pages 419–431, 2012.

[103] P Moriarty, MDR Taylor, and M Brust. Nanostructured cellular networks. *Physical review letters*, 89(24):248303, 2002.

[104] Adam Dobrin. A review of properties and variations of voronoi diagrams. *Whitman College*, 10(1.453):9156, 2005.

[105] Edward Bormashenko, Mark Frenkel, Alla Vilk, Irina Legchenkova, Alexander A Fedorets, Nurken E Aktaev, Leonid A Dombrovsky, and Michael Nosonovsky. Characterization of self-assembled 2d patterns with voronoi entropy. *Entropy*, 20(12):956, 2018.

[106] Christopher P Martin, Matthew O Blunt, and Philip Moriarty. Nanoparticle networks on silicon: Self-organized or disorganized? *Nano Letters*, 4(12):2389–2392, 2004.

[107] Leo Gross, Fabian Mohn, Peter Liljeroth, Jascha Repp, Franz J Giessibl, and Gerhard Meyer. Measuring the charge state of an adatom with noncontact atomic force microscopy. *Science*, 324(5933):1428–1431, 2009.

[108] Tianchao Niu and Ang Li. Exploring single molecules by scanning probe microscopy: porphyrin and phthalocyanine. *The Journal of Physical Chemistry Letters*, 4(23):4095–4102, 2013.

[109] Fabian Mohn, Leo Gross, Nikolaj Moll, and Gerhard Meyer. Imaging the charge distribution within a single molecule. *Nature nanotechnology*, 7(4):227–231, 2012.

[110] Hagen Söngen, Philipp Rahe, Julia Neff, Ralf Bechstein, Juha Ritala, Adam Foster, and Angelika Kühnle. The weight function for charges—a rigorous theoretical concept for kelvin probe force microscopy. *Journal of Applied Physics*, 119:025304, 01 2016.

[111] Thomas Andreev, Ingo Barke, and Heinz Hövel. Adsorbed rare-gas layers on au (111): Shift of the shockley surface state studied with ultraviolet photoelectron spectroscopy and scanning tunneling spectroscopy. *Physical Review B*, 70(20):205426, 2004.

[112] Peter Craven and Grace Wahba. Smoothing noisy data with spline functions. *Numerische mathematik*, 31(4):377–403, 1978.

[113] Youngu Lee, Shengwen Yuan, Arturo Sanchez, and Luping Yu. Charge transport mediated by d-orbitals in transition metal complexes. *Chemical communications*, (2):247–249, 2007.

[114] Nist x-ray photoelectron spectroscopy database, nist standard reference database number 20, national institute of standards and technology, gaithersburg md, 20899. Available at https://srdata.nist.gov/xps/EngElmSrchQuery.aspx?ETypePE&CSOptRetri_ex_dat&ElmAu (2021/07/23).

[115] Katharina Diller, Anthoula C Papageorgiou, Florian Klappenberger, Francesco Allegretti, Johannes V Barth, and Willi Auwärter. In vacuo interfacial tetrapyrrole metallation. *Chemical Society Reviews*, 45(6):1629–1656, 2016.

[116] Katharina Diller, F Klappenberger, M Marschall, Klaus Hermann, A Nefedov, Ch Wöll, and JV Barth. Self-metalation of 2h-tetraphenylporphyrin on cu (111): An x-ray spectroscopy study. *The Journal of chemical physics*, 136(1):014705, 2012.

[117] Peter Knecht, Paul TP Ryan, David A Duncan, Li Jiang, Joachim Reichert, Peter S Deimel, Felix Haag, Johannes T Küchle, Francesco Allegretti, Tien-Lin Lee, et al. Tunable interface of ruthenium porphyrins and silver. *The Journal of Physical Chemistry C*, 125(5):3215–3224, 2021.

[118] AM Shachter, EB Fleischer, and RC Haltiwanger. The structure of (5, 10, 15, 20-tetraphenylporphinato) gold (iii) tetrachloroaurate (iii). *Acta Crystallographica Section C: Crystal Structure Communications*, 43(10):1876–1878, 1987.

[119] DP Woodruff. Normal incidence x-ray standing wave determination of adsorbate structures. *Progress in surface science*, 57(1):1–60, 1998.

[120] F. Swol and C. Medforth. Structural simulations of nanomaterials self-assembled from ionic macrocycles. 2010.

[121] Paul A Giesting and Peter C Burns. Uranyl-organic complexes: structure symbols, classification of carboxylates, and uranyl polyhedral geometries. *Crystallography Reviews*, 12(3):205–255, 2006.

[122] Dan Qin, Xu-Jin Ge, and Jing-Tao Lü. Tin-phthalocyanine adsorption and diffusion on cu and au (111) surfaces: A density functional theory study. *Surface Science*, 671:6–10, 2018.

List of Figures

List of Abbreviations

STM	Scanning Tunneling Microscopy
SPM	Scanning Probe Microscopy
AFM	Atomic Force Microscopy
STS	Scanning Tunneling Spectroscopy
KPFM	Kelvin Probe Force Microscopy
KPFS	Kelvin Probe Force Spectroscopy
XPS	X-ray Photoelectron Spectroscopy
NEXAFS	Near-Edge X-ray Photoelectron Spectroscopy
NIXSW	Normal Incidence X-ray Standing Wave
XSW	X-ray Standing Wave
LEED	Low Energy Electron Diffraction
UHV	Ultra-High Vacuum
TPP	Tetraphenyl Porphyrin
aaTPP	Tetraphenyl Porphyrin atop an adatom
AuTPP	Gold(III) Tetraphenyl Porphyrin
Br_XTPP	Tetraphenyl Porphyrin with x degree of bromination
VDW	Van Der Waals
MO	Molecular Orbital
HOMO	Highest Occupied Molecular Orbital
LUMO	Lowest Unoccupied Molecular Orbital
LCPD	Local Contact Potential Difference
CPD	Contact Potential Difference
LCAO	Linear Combination of Atomic Orbitals
HCP	Hexagonal Close-Packed
FCC	Face-Centred Cubic
NMR	Nuclear Magnetic Resonance
DFT	Density Functional Theory